

# Large Scale Tunneling Junctions for Electrically Driven Plasmonics

Dissertation

zur Erlangung des akademischen Grades

Doktor-Ingenieur (Dr. Ing.)  
im Fachbereich Technische Physik

vorgelegt dem Rat der Physikalisch-Astronomischen Fakultät  
der Friedrich-Schiller-Universität Jena

von M. Sc. André Dathe  
geboren am 01.07.1988 in Borna



**FRIEDRICH-SCHILLER-  
UNIVERSITÄT  
JENA**

**Gutachter:**

**1. Prof. Dr. Thomas Pertsch**

Institut für angewandte Physik  
Friedrich-Schiller-Universität Jena

**adj. Prof. Dr. Wolfgang Fritzsche**

Department Nanobiophotonik  
Leibniz-Institut für Photonische Technologien e.V. Jena

**2. Prof. Dr. Alfred Meixner**

Institut für Physikalische und Theoretische Chemie  
Eberhard-Karls-Universität Tübingen

**3. Prof. Dr. Lukas Eng**

Institut für angewandte Physik  
Technische Universität Dresden

**Tag der Disputation:** 03. Dec 2019

# Abstract

This work focuses on the fabrication of light emitting tunneling junctions in planar configuration comprised of thin-film material stacks analog to metal-insulator-semiconductor plate capacitors. Electrical and structural properties are studied by different experimental techniques (current-voltage analysis, impedance spectroscopy) and compared to existing theories. Assessment of the junction quality is done in comparison to known features of electrically-driven plasmons, such as the bias dependent cut-off frequency, the dependency of the emission intensity on the tunneling current and tuneability of the spectra by implementation of different materials.

Enhanced scattering and tuneability of light emission features from tunneling junctions by adsorption of chemically-synthesized nanoparticles is demonstrated and localization of the emission hot spots by correlation with measurements in external illumination and topography scans are discussed. Operational stability is increased by decoupling of the fabrication sub-steps, i.e. deposition of high quality thin-film stacks and chemical synthesis of particles with tailored optical properties. The role of nanoparticle geometry and material as hot spots in light emitting tunneling junctions is described and distinguished to reference experiments with external illumination. Emission instabilities in low-frequency regimes from hot spots with uncorrelated phases have been observed and are discussed. Potential transferability of electrically-driven plasmons to established detection schemes is demonstrated exemplary by mimicking a study of a plasmonic nanoruler. Additionally, a first proof-of-principle study on the emission from light emitting tunneling junctions in direct water immersion is described.

- page intentionally left blank -

# Contents

<b>1</b>	<b>Introduction &amp; Motivation</b>	<b>1</b>
<b>2</b>	<b>Fundamentals of Surface Plasmons</b>	<b>3</b>
2.1	Surface Plasmons at Planar Interfaces . . . . .	3
2.2	Multilayer Systems . . . . .	6
2.3	Localized Surface Plasmon Resonances . . . . .	9
2.4	Plasmon Hybridization . . . . .	11
<b>3</b>	<b>State of Knowledge in Electrically Driven Plasmonics</b>	<b>13</b>
3.1	Emission Efficiency . . . . .	14
3.2	Tip-based Excitation . . . . .	15
3.2.1	Emission Characteristics . . . . .	16
3.2.2	Emission Mapping . . . . .	17
3.2.3	Plasmon Propagation, Directionality and Coherence . . . . .	18
3.3	Chip-based Excitation . . . . .	19
3.3.1	Lateral Optical Gap Antennas . . . . .	19
3.3.2	Stacked Systems . . . . .	20
3.4	Junctions involving organic Molecules . . . . .	22
3.5	Scope of this Thesis . . . . .	23
<b>4</b>	<b>Fabrication and Characterization of Thin Film Stacks</b>	<b>25</b>
4.1	Sample Fabrication . . . . .	25
4.2	Reflectance Measurements on Multilayers . . . . .	30
4.3	Current-Voltage Characteristics . . . . .	34
4.3.1	Tunneling Barrier Estimation . . . . .	38
4.3.2	Determination of Sample Reproducibility . . . . .	39
4.4	Impedance Spectroscopy . . . . .	41
4.4.1	Junctions of different Size . . . . .	44
4.4.2	Junctions of different Oxide Thickness . . . . .	46
4.4.3	Junctions at different Bias . . . . .	48
<b>5</b>	<b>Spectra of Planar Light Emitting Tunneling Junctions</b>	<b>49</b>
5.1	Spectral Intensity . . . . .	50
5.2	Cut-off Frequency . . . . .	51
5.3	Role of Electrode Material in Emission . . . . .	53
5.4	Signal Stability & Repeatability . . . . .	54
5.5	Polarity dependent Emission . . . . .	55

---

<b>6 Plasmon Hybridization on Electrically Driven Junctions</b>	<b>57</b>
6.1 Nanoparticles as Emitters . . . . .	59
6.2 Plasmon Coupling in a Particle-Film System . . . . .	61
6.3 Measurement of Organic Layers by Plasmon Coupling . . . . .	65
6.3.1 System Referencing by External Illumination . . . . .	66
6.3.2 Validation by Light Emitting Tunneling Junctions . . . . .	67
6.3.3 Layer Thickness Assignment . . . . .	68
6.4 Emission Localization by Particle Imaging . . . . .	71
6.4.1 Plasmon Scattering on Gold Nanospheres . . . . .	71
6.4.2 Hot Spot Assignment . . . . .	73
6.4.3 Plasmon Scattering on mono-crystalline Goldplates . . . . .	77
6.4.4 Scattering on Metallic and Dielectric Particles . . . . .	80
6.4.5 Investigations of Emission Instabilities . . . . .	84
6.4.6 Emission in Liquid Environment . . . . .	87
<b>7 Summary and Outlook</b>	<b>89</b>
<b>8 Zusammenfassung</b>	<b>91</b>
<b>References</b>	<b>93</b>
<b>Abbreviations</b>	<b>108</b>
<b>Physical Constants</b>	<b>109</b>
<b>Symbols</b>	<b>110</b>
<b>Appendices</b>	<b>i</b>
<b>A Materials &amp; Protocols</b>	<b>i</b>
A.1 Optical Spectroscopy Setup and Calibration . . . . .	i
A.2 Optical Imaging Setup and Procedure . . . . .	ii
A.3 AFM Scan Parameters & Analysis . . . . .	v
A.4 Synthesis of mono-crystalline Goldplates . . . . .	vi
<b>B Supporting Data</b>	<b>vii</b>
<b>C Programming Scripts</b>	<b>xv</b>
<b>D Personal Information</b>	<b>xix</b>

# 1 | Introduction & Motivation

In 1976, Lambe and McCarthy described an up to that point unknown method of light generation in their pioneering experimental work, i.e. light emission by inelastic tunneling (LEIT) that enabled electrical excitation of radiation at frequencies of visible light [1]. After substantial initial attention, the method lost importance due to the low quantum efficiency compared to other light generation techniques.

With today's requirements of point-of-care diagnosis systems, such as miniaturization and the need of smart interlinked devices in the above mentioned fields, the LEIT effect reclaims attention again. The potential to electrically drive surface plasmon polaritons as local, near-field sources by signals and fabrication methods compatible with modern nanoelectronics may widen the available palette in applications substantially [2].

Antennas play an essential role in our everyday life. With the first experimental proof of wireless communication by electromagnetic waves as conducted by Heinrich Hertz in 1886, and based on the theory from James Clerk Maxwell a cornerstone for this branch of modern technology was set. Over the years, many types of electrical antennas have been developed and optimized for different purposes, e.g. for sending or receiving information, signal amplification, specific radiation patterns, or directivity. Until today, the frequency bands of operational antennas were extended to cover a large part of the electromagnetic spectrum, i.e. the low-frequency regime of radio waves up to the mid-range of microwave frequencies as shown in Fig. 1.1 by altering and improving the designs.

A mutuality of all these devices is the conversion of an electrical signal to electromagnetic radiation or vice-versa. Thus, with advancing technology and the progress towards higher operation frequencies, the antenna geometries and feature sizes decreased accordingly. Inherent to the downsizing, both, the radiation efficiency and bandwidth of small electrical antennas are drastically reduced. Nowadays these antennas are mostly increasing in complexity to optimize their properties and pre-designed by numerical methods and simulations.

Sub-micrometer to few-nanometer structures and patterning methods have been made accessible in the last two decades, enabling further developments in antenna technology, i.e. the field of metamaterials comprising nanoantennas, especially by the technological advances in lithographic processes [3, 4]. As pinpointed by their name, these are antennas with few tens of nanometers in feature size, making them suitable for applications that require a resonant band in the frequency range of visible light. With this, a whole

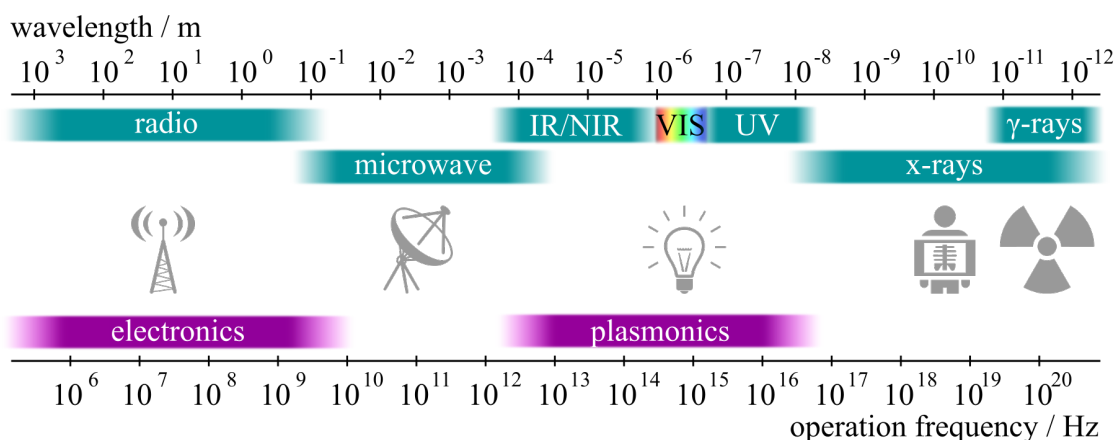


FIGURE 1.1: Part of the electromagnetic spectrum depicting the frequency regimes of different radiation classifications and their application. Classical antennas as used in electronic circuits cover frequencies between the radio up to the microwave regime, whereas plasmonics commonly operates on a light-to-light basis covering the near-infrared to ultraviolet section.

palette of new research and application interests were sparked in nonlinear optics, near-field optics, and plasmonics.

Given by the small dimensions and the high resonance frequencies which coincide with the regime of near-infrared to visible light, interactions of these nanoantennas with surrounding matter correspond to properties on molecular and intra-molecular levels. Thus, analysis in material science, optics, medicine, biotechnology, and many others employ the unique characteristics of these optical antennas to confine and amplify light at the nanoscale and gain information on fundamental material properties and physical effects. Among these, sensing schemes and spectroscopy methods focused on the detection of biological reactions or molecule compositions, such as Raman spectroscopy, refractive index based sensing in plasmonics, and super-resolution microscopy have gained extensively by the field of optical nanoantennas [5–9].

The substantially decreased dimension of optical antennas also entails differences in excitation compared to electrical antennas. Thus, they are usually operated in a purely optical 'light-to-light' approach instead of the previously mentioned conversion of an electric signal to electromagnetic radiation, i.e. optical antennas are driven by an external source of incident radiation. Substantial insights in the field of optical antennas have been transferred from knowledge in classic electrodynamics and electrical antennas [10].

Thus, the LEIT effect might enable the transfer of established analysis and detection techniques of optical sensors based on nanoantennas into highly miniaturized systems based on electrical excitation. This thesis elaborates on the optical interaction of LEIT based samples combined with chemically synthesized particles as nanoantennas and the potential to transfer established light-driven plasmonic sensing protocols into this equivalent electrically-driven system.



## 2 | Fundamentals of Surface Plasmons

Before diving into the details of the state of knowledge in electrically driven plasmonics that employ the LEIT effect, the fundamentals of surface plasmons such as their classification, theoretical description, parameters, and boundary conditions are reviewed briefly. This way all necessary variables for description of plasmonic properties are introduced for the following chapters.

### 2.1 Surface Plasmons at Planar Interfaces

Plasmon polaritons are defined as quanta of charge density oscillations coupled to an external electromagnetic field. For surface plasmon polaritons (SPPs) in particular, they are coupled states between photons and plasma oscillations at the interface between a metal and a dielectric. As implied by its nomenclature SPPs are always non-radiative, surface-bound modes for perfectly flat surfaces.

They can be described by homogeneous solutions of Maxwell's equations that appear for distinct boundary conditions. Mathematically, they represent solutions of a homogeneous wave equation which describe the eigenmodes of the given system

$$\Delta \mathbf{E}(\mathbf{r}, \omega) - \varepsilon(\omega) \frac{\omega^2}{c^2} \mathbf{E}(\mathbf{r}, \omega) = 0 \quad (2.1)$$

with the electric field  $\mathbf{E}$ , the propagation vector  $\mathbf{r}$  the angular frequency  $\omega$ , and dielectric function  $\varepsilon(\omega)$ . For the description and derivation of the fundamentals of an SPP propagating along a metal/dielectric interface, the z-coordinate is chosen to be perpendicular to the interface and the x-coordinate to be the direction of propagation (see Fig. 2.1). Defining the interface between the two media to be at  $z = 0$ , the metal is set to span one halfspace ( $z < 0$ ) and is described by a complex frequency-dependent dielectric function  $\varepsilon_m(\omega)$ , while the dielectric in the other halfspace ( $z > 0$ ) is generally expressed by a real dielectric function  $\varepsilon_d(\omega)$ . The propagation of an SPP wave along the boundary is described by its complex wave vector  $\mathbf{k} = \mathbf{k}' + i\mathbf{k}''$ .

Since SPPs are interface-bound modes, the following boundary conditions have to be fulfilled to find solutions for the given problem:

1. Propagation solely along the boundary (common  $k_x$ ), but no propagation perpendicular to the interface, i.e. the real part of the wavevector  $k'_z$  has to be zero leaving only an exponential decay of the SPP with increasing distance from the boundary determined by the imaginary part of  $k_z$

$$|k'_x| > 0; \quad k'_z = 0. \quad (2.2)$$

2. Continuity of the surface-tangential ( $E_x, H_y$ ) and perpendicular ( $\varepsilon E_z$ ) field components at the boundary

$$\varepsilon_d E_{zd} = \varepsilon_m E_{zm}, \quad (2.3a)$$

$$H_{yd} = H_{ym}, \quad (2.3b)$$

$$E_{xd} = E_{xm}. \quad (2.3c)$$

3. Energy conservation of the wavevector at the interface with  $k_0 = \omega/c$ , where  $\omega$  is the angular frequency and  $c$  the speed of light in vacuum

$$k_x^2 + k_{zd}^2 = \varepsilon_d k_0^2, \quad (2.4a)$$

$$k_x^2 + k_{zm}^2 = \varepsilon_m k_0^2, \quad (2.4b)$$

$$|k_{xm}| = |k_{yd}|. \quad (2.4c)$$

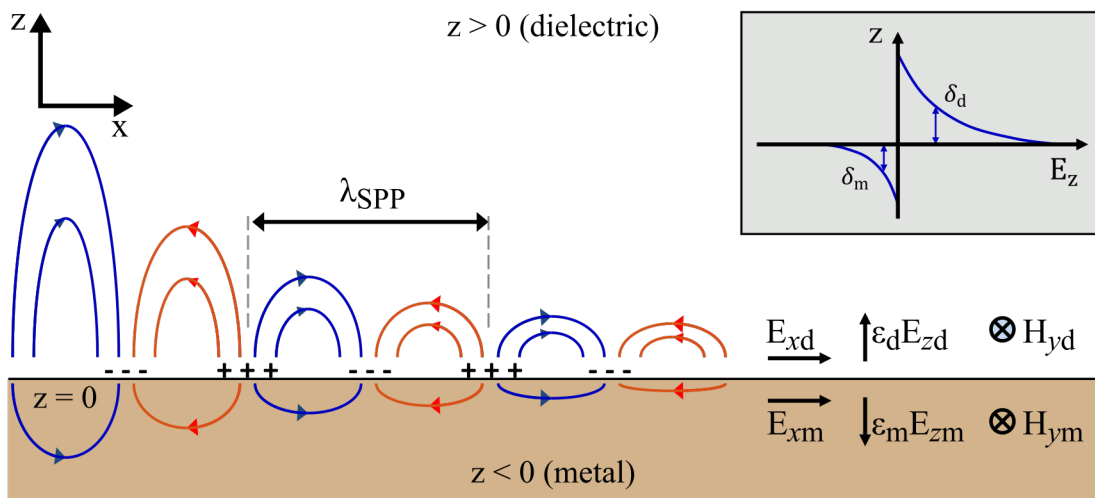


FIGURE 2.1: Surface plasmon polariton with wavelength  $\lambda_{SPP}$  propagating along a metal/dielectric-interface. The propagation length along the boundary  $\delta_{SPP}$  is mainly limited by damping originating in the metal. Inset: Scheme of the exponential decay of the electric field component  $E_z$ . The skin depth  $\delta_{d|m}$  describes how far the field enters into the respective material.

For transverse-electric waves (TE), no solutions exist for the given boundary conditions in Eq. (2.2). Thus, SPP eigenmodes are non-existent in TE polarization. Note, by extension of the given system to inhomogeneous wave equations, solutions do exist.

However, transverse-magnetic waves (TM) in the chosen coordinate system can be expressed in the following form for the interface at  $z = 0$ :

$$z > 0 \begin{cases} \mathbf{E}_d &= \begin{pmatrix} E_{xd} & 0 & E_{zd} \end{pmatrix} e^{i(k_{xd}x + k_{zd}z - \omega t)} \\ \mathbf{H}_d &= \begin{pmatrix} 0 & H_{yd} & 0 \end{pmatrix} e^{i(k_{xd}x + k_{zd}z - \omega t)} \end{cases}, \quad (2.5a)$$

$$z < 0 \begin{cases} \mathbf{E}_m &= \begin{pmatrix} E_{xm} & 0 & E_{zm} \end{pmatrix} e^{i(k_{xm}x + k_{zm}z - \omega t)} \\ \mathbf{H}_m &= \begin{pmatrix} 0 & H_{ym} & 0 \end{pmatrix} e^{i(k_{xm}x + k_{zm}z - \omega t)}. \end{cases} \quad (2.5b)$$

In this case, a trivial solution exists for  $k_x = 0$  which does not describe a propagating wave along the boundary and an additional, non-trivial solution for:

$$\frac{k_{zm}}{\varepsilon_m} = \frac{k_{zd}}{\varepsilon_d}. \quad (2.6)$$

Combined with Eq. (2.4) this yields the so called dispersion relation, i.e. a relation between the surface-parallel wavevector  $k_x$  and the angular frequency  $\omega$

$$k_x = k'_x + ik''_x = \frac{\omega}{c} \sqrt{\frac{\varepsilon_m \varepsilon_d}{\varepsilon_m + \varepsilon_d}}. \quad (2.7)$$

Equivalent descriptions can be derived for the normal components of the wavevector  $k_z$ :

$$k_{zm} = \frac{\omega}{c} \sqrt{\frac{\varepsilon_m^2}{\varepsilon_m + \varepsilon_d}}, \quad (2.8a)$$

$$k_{zd} = \frac{\omega}{c} \sqrt{\frac{\varepsilon_d^2}{\varepsilon_m + \varepsilon_d}}. \quad (2.8b)$$

As shown in Eq. (2.7)  $k_x$  is a complex value with the real part  $k'_x$  being linked to the effective SPP wavelength by  $\lambda_{\text{SPP}} = 2\pi/k'_x$  and the imaginary part  $k''_x$  describing the plasmon propagation length  $\delta_{\text{SPP}} = 1/|k''_x|$  which usually is defined by the distance for which the field strength decayed to  $1/e$  of its original amplitude [11, 12]. The same dependency is given for the skin depths  $\delta_{\text{d|m}} = 1/|k''_z|$ , which describe the decay of the SPP into the respective material perpendicular to the boundary.

The phrased 1. boundary condition (Eq. 2.2) can be stated more precisely by taking the listed equations into account,.  $|k'_x| > 0$  is only fulfilled if the sum and product of the dielectric functions in Eq. (2.7) are both positive or negative and bound solutions only exist, if the denominator sum in Eqs. (2.8) are negative.

Thus, the following must apply:

$$\varepsilon_m(\omega)\varepsilon_d(\omega) < 0, \quad (2.9a)$$

$$\varepsilon_m(\omega) + \varepsilon_d(\omega) < 0. \quad (2.9b)$$

These conditions are mainly met by metals, especially noble metals, since they exhibit large negative real parts of  $\varepsilon_m(\omega)$  combined with small imaginary parts. In summary, SPPs exhibit four characteristic parameters that define their length scales important for SPP based photonics. Namely, the skin depth into the metal  $\delta_m$  and the dielectric medium  $\delta_d$ , in which describe the energy confinement of the mode, as well as the propagation length  $\delta_{\text{SPP}}$  and the surface plasmon wavelength  $\lambda_{\text{SPP}}$  which describe the mode propagation capabilities [13].

## 2.2 Multilayer Systems

For systems with several interfaces the solutions of the previously derived equations are combined to fulfill the additional boundary conditions. A multilayer system with  $M$  domains can sustain  $M - 1$  modes, i.e. one for each boundary. Provided the thickness of the metal film exceeds the plasmon skin depth, oscillations at the interfaces are regarded as decoupled. For thin-film geometries, where the separations of adjacent interfaces are smaller or comparable to the electric fields skin depths  $\delta_{\text{dlm}}$ , interaction and coupling of the respective SPPs have to be considered.

Two geometries can be studied as ideal cases to describe the interaction of modes in multilayer systems [14]. First, Insulator/Metal/Insulator (IMI) structures - a conducting material sandwiched by two dielectric media. Second, Metal/Insulator/Metal (MIM) structures - an insulator sandwiched by two metallic domains. Assuming both outer materials of this model stack to be identical in terms of their dielectric response and thickness, the dispersion relation is split into two branches, where one describes odd modes ( $E_x$  is antisymmetric,  $E_z$  is symmetric) and the other describes even modes ( $E_x$  is symmetric,  $E_z$  is antisymmetric) [15].

The properties of the modes differ for these two geometries. For IMI structures, the odd modes are less confined to the metal with decreasing film thickness leading to higher propagation lengths due to lowered damping, i.e. long-ranged SPPs. For even modes this behavior is inverted. Thus, decreasing  $\delta_{\text{SPP}}$  by thinning of the metal film [16]. In contrast to IMI structures, which only support these two fundamental eigenmodes, MIM waveguides can support many SPP field profiles if the dielectric core is sufficiently thick. Thus, more complex multilayer systems can be described as combinations of the introduced structures in principle. However, the described statements only hold true for the assumption of symmetric, uncoupled structures and bound SPPs.

Derivation of more complex multilayer systems comprised of more films of different thickness, different material combinations, or optical anisotropy significantly change the

situation. Often piecewise analytical expressions of the specific system are studied [17] or numerical approaches are utilized. In the latter case, solutions are found by minimizing the determinant of the set of equations with the previously described boundary conditions. Often, experimentally determined values for the respective film parameters are utilized to properly account for damping effects and technological imperfections [18].

One approach to solve a dispersion relation for such a thin film structure equal to the LEIT supporting junctions as they will be discussed throughout this thesis can be found in Fig. 2.2. A silicon substrate is approximated as an semi-infinite half-space with an alumina layer on top with a thickness of 7 nm and a gold film with a thickness of 30 nm. The superstrate is air with a dielectric constant of unity, while the other materials dielectric functions were taken from experimentally determined values of published reports as shown and referenced in Fig. B.1.

The algorithm was an adaptation based on the model as derived by Dahlin et al. [19]. The solution for eigenmodes of the system is obtained by considering the magnetic and electric field components of a TM polarized wave for each interface as coupled waves. These have to obey the given boundary conditions and continuity requirements as described in the previous section. With this approach and the stated momentum conservation at each boundary Eq.(2.4), all equations can be expressed as functions solely dependent on  $k_x$  as a parameter. Thus, a matrix  $\mathbf{M}(2n - 2, 2n - 2)$  with  $n$  being the number of materials in the structure is obtained. Together with the vector  $\mathbf{v}$ , which describes the respective magnetic and electric field amplitudes at each boundary, the modes can be found by solving for  $|\mathbf{M}\mathbf{v}| = 0$ .

As depicted in Fig. 2.2, the light lines and SPP modes exhibit different propagation constants. Thus, SPPs can not be excited by direct light illumination from the superstrate but additional in-coupling geometries to compensate the mismatch in the wavevector are needed, such as structured surfaces, gratings or prisms [20]. In contrast to the others, mode (II) exhibits no divergence from the light line in alumina, which indicates a photonic mode that is guided along the oxide and confined by the surrounding electrodes.

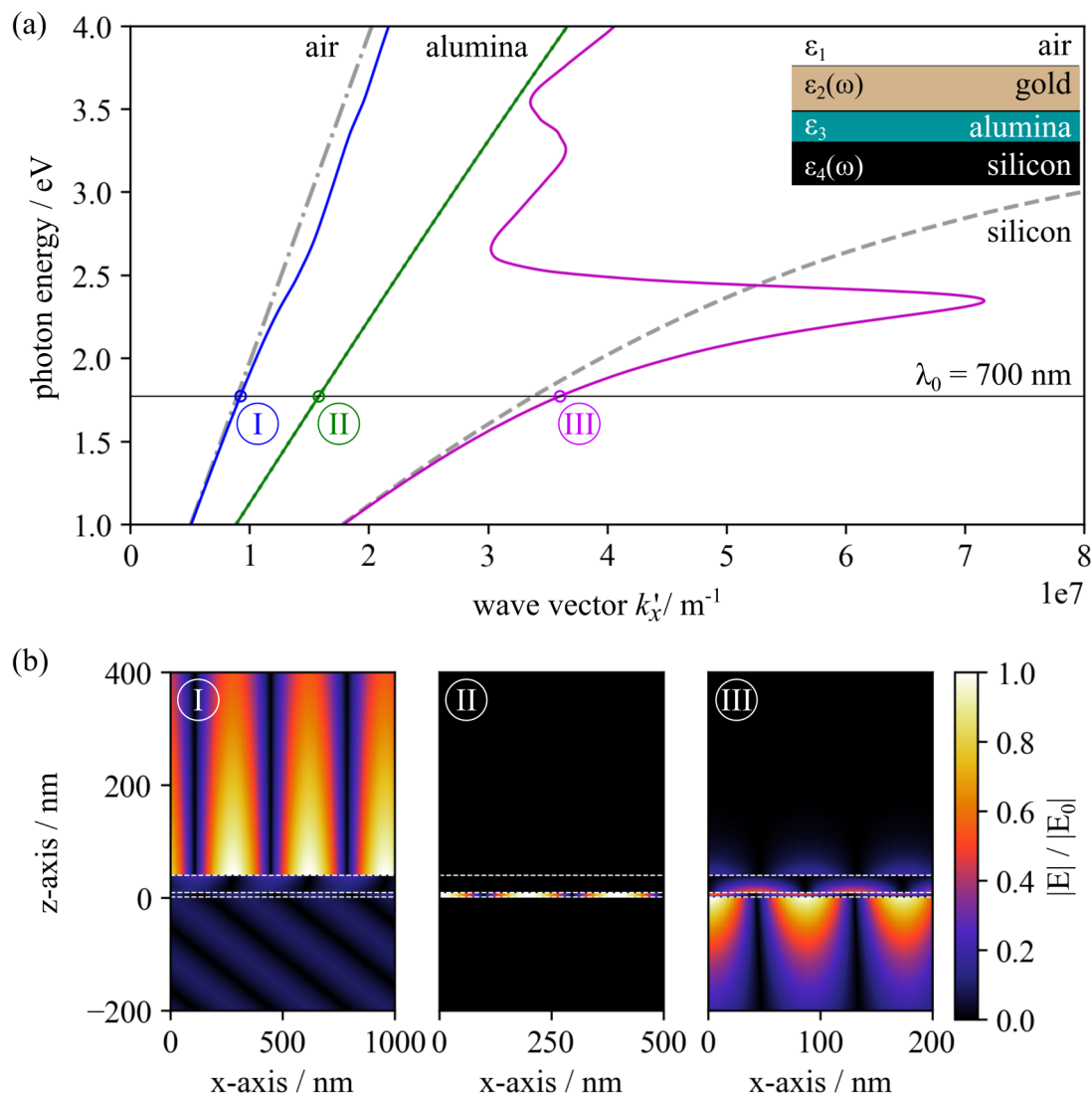


FIGURE 2.2: (a) Dispersion relation for a system composed of air/gold/alumina/silicon (top to bottom). The light lines (grey) for the respective materials are shown for air (dot-dashed), alumina (dotted) and silicon (dashed). Three modes I (blue), II (green) and III (purple) were found and are plotted for an energy corresponding to  $\lambda_0 = 700 \text{ nm}$  (black line). (b) depiction of the total electric field  $|\mathbf{E}| / |\mathbf{E}_0|$  for each found mode. The dashed white lines indicate the position of each interface. (I) corresponds to the SPP mainly located at the air/gold-interface, while the mode partially leaks into the silicon substrate. (II) is located in the alumina thin film. (III) shows the SPP mode inside of the structure exhibiting the highest field intensities at the silicon/alumina interface.

## 2.3 Localized Surface Plasmon Resonances

In addition to the previously described SPPs, another fundamental plasmonic excitation is given if conductive nanostructures, namely particles, in an optically isotropic, surrounding dielectric medium are irradiated by an oscillating electromagnetic field. In that case, direct excitation of plasmons can be observed due to the curvature of the particle/dielectric interface. Within this curved geometry, a restoring force is exerted on the displaced electrons inducing an opposing dipole moment which leads to field enhancements in the vicinity of the particle at its eigenfrequencies. In contrast to SPPs, these highly confined plasmons are non-propagating and hence localized, i.e. Localized Surface Plasmon Resonance (LSPR).

If the particle size is substantially smaller than the wavelength of the incident light, the optical response of a spherical particle to that potential can be described by electrostatics. A particle is considered to be exposed to an uniform electric field  $\mathbf{E}_0 = E_0 e_x$ . To calculate the electric field inside and around the particle, it is necessary to first obtain the potentials by solving the Laplace equation  $\Delta\phi = 0$ , which is linked to the electric field by  $\mathbf{E} = -\nabla\phi$ . The whole derivation is described in detail in [15], while only the solution as shown in Eqs.(2.10) will be discussed here. The electric field inside the particle  $\mathbf{E}_{\text{in}}$  is uniform while the field in the surrounding area  $\mathbf{E}_{\text{out}}$  is a superposition of  $\mathbf{E}_0$  and the field of a electric dipole. Since an electric dipole is described as a pair of two opposite electric charges separated by a small distance  $r$ , its electric field in direction of a point of interest  $P$  with the unit vector  $\mathbf{n}$  is given by  $\mathbf{E}_{\text{DP}}(\mathbf{n})$ .

$$\mathbf{E}_{\text{in}} = \frac{3\varepsilon_d}{\varepsilon_m + 2\varepsilon_d} \mathbf{E}_0, \quad (2.10a)$$

$$\mathbf{E}_{\text{out}}(\mathbf{n}) = \mathbf{E}_0 + \mathbf{E}_{\text{DP}}(\mathbf{n}) = \mathbf{E}_0 + \left( \frac{1}{4\pi\varepsilon_0\varepsilon_m} \frac{3\mathbf{n}(\mathbf{n} \cdot \mathbf{p}) - \mathbf{p}}{r^3} \right). \quad (2.10b)$$

The induced dipole moment  $\mathbf{p}$  is proportional to the external field  $\mathbf{E}_0$  and dependent on the complex polarizability  $\alpha$  of the particle [21]. Note, that this expression exhibits the same functional form as the Clausius-Mosotti relation which connects polarization effects on the nanoscale level with the macroscopic relative permittivity  $\varepsilon_r$

$$\mathbf{p} = \alpha\varepsilon_0\varepsilon_d \mathbf{E}_0 \text{ with } \alpha = 4\pi r_s^3 \frac{\varepsilon_m - \varepsilon_d}{\varepsilon_m + 2\varepsilon_d}. \quad (2.11)$$

Hence, the optical response of a spherical particle can be expressed by an ideal electric dipole. To transfer this approach to general wavelength-dependent light scattering and absorption properties of particles, the uniform electrostatic field is substituted by a time varying electric field  $\mathbf{E}_0 = \mathbf{E}_0 e^{-i\omega t}$ . For a particle with radius  $r_s$  that is smaller than the wavelength  $\lambda$  of the incident light, the phase of this incident wave can be approximated as constant over the whole particle volume, which is known as quasi-static approximation or Rayleigh scattering. With the angular frequency  $\omega = 2\pi c/\lambda$  of the incident field, an oscillating dipole is induced according to Eq.(2.11), in which the frequency dependent response is accounted for by the complex dielectric function of the particle material

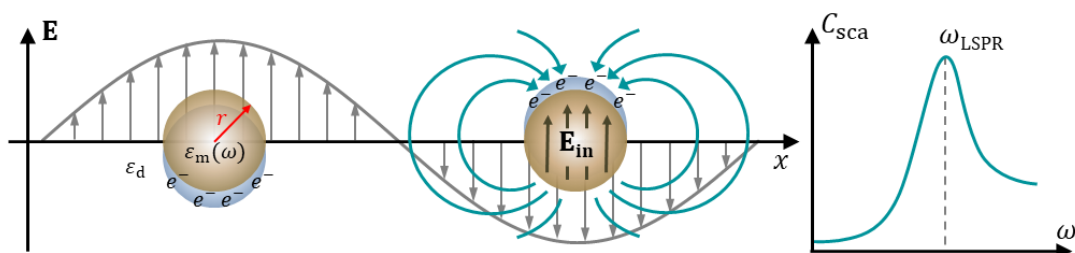


FIGURE 2.3: Depiction of the quasi-static approximation of the Mie theory. An external electric field  $\mathbf{E}_0$  induces a dipole moment dependent on the particle polarizability  $\alpha$  and radius  $r$  that is smaller than the incident wavelength  $\lambda$ . At the particle resonance frequency  $\omega_{\text{LSPR}}$ , which is determined by its material and morphological features, an enhanced scattering occurs which results in the characteristic spectra  $C_{\text{sca}}(\omega)$ .

$\varepsilon_m(\omega)$ . It is apparent that the polarizability exhibits a resonant enhancement if the following condition, known as Fröhlich condition, is fulfilled:

$$\varepsilon'_m(\omega) = -2\varepsilon_d. \quad (2.12)$$

Thus, the particle exhibits enhanced scattering and absorption of the external field at frequencies that satisfy the Fröhlich condition. From this point, the scattering  $C_{\text{sca}}$  and absorption  $C_{\text{abs}}$  cross-sections can be derived by calculating the Poynting vector of the time-dependent electric and magnetic fields [22].

$$C_{\text{sca}} = \frac{k^4}{6\pi} |\alpha|^2 = \frac{8\pi}{3} k^4 r_s^6 \left( \frac{\varepsilon'_m(\omega) - \varepsilon_d}{\varepsilon'_m(\omega) + 2\varepsilon_d} \right)^2, \quad (2.13a)$$

$$C_{\text{abs}} = k \text{Im}[\alpha] = 4\pi k r_s^3 \left( \frac{\varepsilon''_m(\omega) - \varepsilon_d}{\varepsilon''_m(\omega) + 2\varepsilon_d} \right). \quad (2.13b)$$

Note that the parameters which define the LSPR frequency of the particle are its size  $r_s$ , the complex dielectric function of the particle  $\varepsilon_m$ , and the dielectric constant of the surrounding medium  $\varepsilon_d$ . These expressions are also valid for dielectric particles, which exhibit the high local field enhancements [23] with a sixth-order dependency of  $C_{\text{sca}}$  on the particle radius  $r_s$ , whereas the absorption cross-section scales with  $r_s^3$ .

For particles which do not suffice the condition of  $r_s \ll \lambda$ , the description by an electric dipole reaches its limit due to retardation effects and field inhomogeneities in the particle volume. An established method to account for the significant phase-changes that occur and to describe scattering and absorption also for higher modes in spherical particles of arbitrary size is the theory introduced by Gustav Mie [24]. In depth derivations can be found in the work of Bohren and Huffman [22] and will not be discussed further, since no particles that exceeded these criteria were utilized in the course of this work.

The LSPR frequency of anisotropic nanostructures, e.g. morphologically or optically anisotropic particles, can not be described easily by these analytical solutions which is why numerical methods are often utilized to approximate the optical response of such complex systems, e.g. for coupled nanostructures [25].



## 2.4 Plasmon Hybridization

So far, only single plasmonic nanostructures in a homogeneous environment have been discussed neglecting the fact of electromagnetic coupling, if the separation between multiple objects narrows down to values smaller than their plasmon decay length. In this case, the optical response of an individual particle is altered due to the proximity to another structure. Before mentioned analytical solutions are limited to non-perturbed, homogeneous media around single structures, which is not given for this scenario anymore. Thus, different theories have been developed to model the overall optical response of more complex structures, i.e. the almost infinite amount of combinations regarding particle sizes, geometries, materials and separations, whereas in the scope of this work only the most prominent will be introduced briefly.

Plasmon hybridization for particle systems was first described by Prodan et al. [26] and later continued by a list of publications extending and describing the model validity for different plasmonic systems, e.g. dimers [27, 28], nanoshells [29] or particle-film systems [30–33].

Essentially, this model can be regarded as analogy to molecule orbital hybridization, in which the orbitals of individual atoms hybridize at different energy levels, if two or more atoms interact [33].

Similarly, the optical response of complex nanostructures is treated as a result of the interaction between fundamental plasmonic structures, e.g. by introduction of image charges (Fig. 2.4). With this, hybrid plasmon modes with a shifted frequency can be derived as an overlay from the eigenmodes of underlying basic structures with known or optical properties that are easy to calculate. In the example of Fig. 2.4, the plasma frequency of the surface plasmon  $\omega_{\text{SPP}}$  and the LSPR frequencies of a spherical particle  $\omega_{\text{LSPR}}$  are described. The energy levels are asymmetrically split into two levels shifted

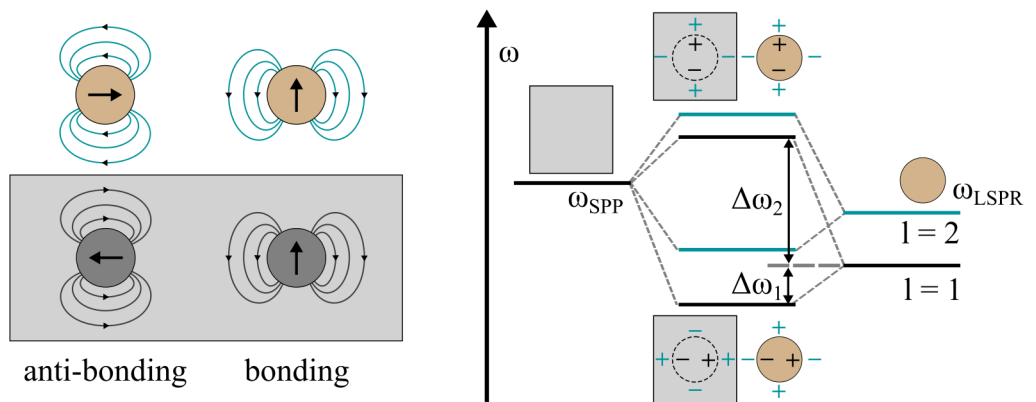


FIGURE 2.4: Scheme of plasmon coupling of a metallic particle-film system. The anti-bonding mode oscillates parallel to the film boundary and is canceled out due to the inverse direction of the induced image dipole, whereas in the bonding mode both charges oscillate in-phase resulting in a coupled mode. This is depicted as a splitting of the fundamental modes between the two basic structures in the energy representation of the plasmon hybridization model. With the corresponding frequency shift  $\Delta\omega$  of the surface plasmon  $\omega_{\text{SPP}}$  and particle plasmon  $\omega_{\text{LSPR}}$ .

by  $\Delta\omega_1$  and  $\Delta\omega_2$ , in which the lower energy fraction is referred to as bonding-mode and the higher fraction as anti-bonding mode. This nomenclature resembles to the in-phase and out-of-phase oscillations between the real and image dipole, respectively. These hybridization effects also occur for higher particles modes as indicated in Fig. 2.4 by the dipole ( $l = 1$ ) and quadrupole ( $l = 2$ ) energies. References on the derivation, explanation on equations, and underlying assumptions of plasmon hybridization can be found in [34, 35]. This coupling effect is also often referred to as gap-mode, due to the restriction to structures in close proximity.

The hybridization effect can also be understood as the combined interaction of the local charge carrier densities from all substructures in proximity. Thus, the overall optical responses of more complex plasmonic nanostructures exhibit interesting properties. Briefly:

**Intensity enhancement** of the electromagnetic fields can be achieved, in which the mode volume is decreased and confined in the gap regime between the structures. This is also known as hot spot formation and is the basis for methods such as surface enhanced raman spectroscopy [36] or tip enhanced raman spectroscopy [37].

**Shifted resonance frequencies** occur as consequence of the collective electron oscillation within the outer boundaries of the respective coupled structures. By changing the gap, splitting of the substructure resonance energies into bonding and anti-bonding modes is influenced, which results in shifted eigenmode frequencies [38] up to white-light continuum spectra by resonant antennas [39].

**Altered decay rates and damping** resulting in line width narrowing caused by hybridization of higher LSPR mode orders and/or SPPs [40, 41].

**Angular dependency** of scattering and absorption radiation patterns can be controlled by geometric or material anisotropy. Thus, by combination of different structural properties the angular scattering cross-section can be tailored [42].

Note, that the challenges in this seemingly easy explanations lie in an adequate description of the components optical properties as well as in the realistic decomposition into contributing substructures [43].

### 3 | State of Knowledge in Electrically Driven Plasmonics

Most concepts of electrically driven plasmons share a common principle, i.e. tunneling of charge carriers through a potential barrier as source of plasmon excitation. However, mechanisms and modeling in tunneling junctions are a field on its own and vastly covered in literature [44–46]. The generic quantum mechanical model of a particle with kinetic energy  $T$  that penetrates a potential barrier  $U$  with a finite probability is applicable for elastic and inelastic tunneling processes. For the study of surface plasmon excitation by inelastic tunneling charge carriers, this can be reduced to the geometry as depicted in Fig. 3.1. By application of a potential  $T = |eV|$ , the fermi levels of region A and B are shifted accordingly, which results in a triangular deformation of the tunneling barrier as described by the WKB approximation.

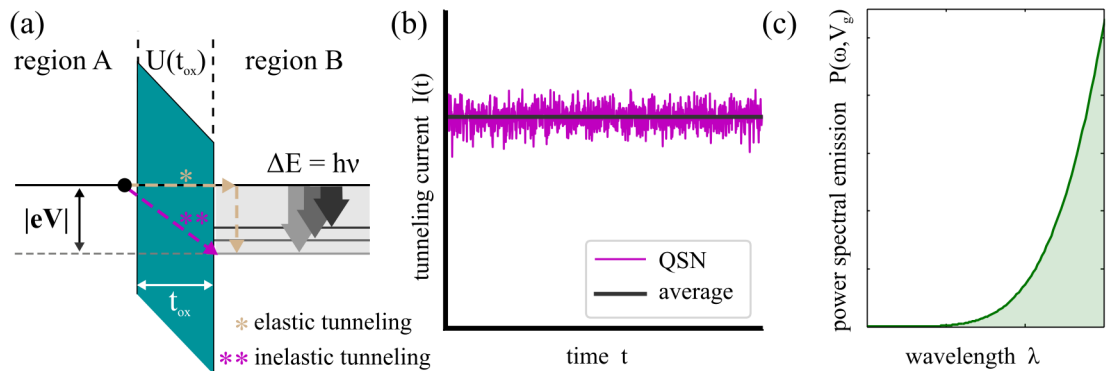


FIGURE 3.1: (a) Scheme of electron tunneling from region A through a potential barrier  $U(t_{ox})$  into the classically forbidden region B. The energy difference  $\Delta E$  between the Fermi levels of the two regions equals the maximum convertible energy of photons emitted by inelastic tunneling. (b) The net tunneling current is accompanied by quantum shot noise (QSN) which is given by the tunneling rate. A fraction of the energy of these fluctuations can cover frequencies up to the visible regime that couple into the boundaries as surface plasmons. (c) Autocorrelation and fourier-transformed depiction of the quantum shot noise for an exemplary tunneling junction at 5 V.

Light emission by inelastic tunneling (LEIT) was first described by the pioneering experimental work of Lambe and McCarthy [1] in 1976 during the investigation of metal-insulator-metal (MIM) thin film stacks. In this mechanism, an inelastic channel for tunneling exists, in which electrons transit from one electrode to the other accompanied by the excitation of surface plasmons that inherit a fraction of the energy loss by the

inelastic tunneling process [47, 48]. It should be emphasized, that this differs from injection processes, where electrons tunnel elastically and decay towards the Fermi level by direct emission of free space radiation. The calculation of the tunneling transition rate can be cast into a form similar to an energy-loss calculation for electron beams [49, 50]. Excitation of surface plasmons by tunneling charge carriers is either induced by the accompanying current fluctuations of inelastic tunneling, i.e. quantum shot noise (QSN) that originates in the stochastic of the tunneling process [51] or directly by relaxation of hot carriers in the electrodes [52–54]. A general description is that the QSN covers energies up to the potential difference between region A and B, eventually including the frequencies of the visible regime. This mechanism can be approximated by an electric dipole situated in the middle of the tunneling barrier oscillating perpendicular to the system boundaries which was derived for planar tunneling junctions by Laks and Mills [55]. For calculation of the emission, the dipole power spectrum often is assumed as a linear function of the photon energy as derived by Hone [56], but also non-linear models [57, 58] have been introduced with experimental support [59]. Regardless of the model, the highest frequencies of the QSN by a single transition are defined by the potential difference  $V_g$  inside the junction. This results in the simple expression for the spectral cut-off  $\hbar\omega_c = |qV_g|$ . However, it is noteworthy that anomalies in this cut-off frequency have been reported for light emission from tunneling junctions utilizing a scanning tunneling microscope tip as one electrode. In that case, the frequency restriction can be exceeded by multi-step Auger-like transitions [60].

### 3.1 Emission Efficiency

Inherent to the effect of light emission by inelastic tunneling is a comparably low quantum efficiency due to the competing processes of elastic and inelastic tunneling. The timescale of elastic tunneling, which is a non-radiative process, is on a femtosecond scale being orders of magnitude smaller than the slower electron-photon interaction in the electric field of the tunneling barrier. In consequence, the efficiency of excitation  $\eta_{\text{exc}}$  as described by Eq. (3.1) is defined by the rate of inelastically tunneling electrons  $\Gamma_{\text{inel}}$  and elastically tunneling electrons  $\Gamma_{\text{el}}$ :

$$\eta_{\text{exc}} \propto \frac{\Gamma_{\text{inel}}}{\Gamma_{\text{inel}} + \Gamma_{\text{el}}}. \quad (3.1)$$

Additionally, the total outcoupled light of a junction is influenced by its property to act as an antenna or emitter and performance to confine, guide, and couple out radiation. Analogous to electrical antennas, this antenna efficiency is dependent on the rate of radiative processes  $P_r$  and non-radiative processes  $P_{\text{nr}}$ :

$$\eta_{\text{ant}} \propto \frac{P_r}{P_r + P_{\text{nr}}}. \quad (3.2)$$

Together with Eq.(3.1) and Eq.(3.2), the overall power spectral emission  $P(\omega, V_g)$  as a function of the applied bias  $V_g$  and angular frequency  $\omega$  can be expressed as given by the following equation [61]:

$$P(\omega, V_g) = \hbar\omega \eta_{\text{exc}}(\omega, V_g) \eta_{\text{ant}}(\omega). \quad (3.3)$$

First theories calculated the maximum achievable efficiency of an ideal tunneling junctions up to 10% [62]. In contrast, experiments in early studies on planar junctions found drastically smaller values in the range of  $10^{-5}$ . This mismatch was attributed to inefficient excitation and conversion to free-space radiation, i.e. low values of  $\eta_{\text{exc}}$  and  $\eta_{\text{ant}}$  mainly given by imperfections and undesired tunneling transitions.

However, recent theories prompt that enhancement of the emission might be achieved by different types of modifications as follows [63]. First, multilayer metal-dielectric systems could create quantum wells and increase the dwelling time of tunneling electrons inside the barriers, leading to an enhanced coupling to SPPs [64] at tunable energy levels [65]. Second, implementation of protruding features inside the insulator of tunneling junction stacks could enhance the conversion of these normally leaky waves into propagating eigenmodes [66]. Both of these modifications aim to amplify  $\eta_{\text{exc}}$ . Third, the implementation of resonant plasmonic nanoantennas to enhance  $\eta_{\text{ant}}$ , e.g. nanostructured surfaces which result in a gain of several orders of magnitude in the efficiency and a narrowing of the spectral emission range [67, 68].

Mainly, three classes of light emitting tunneling junctions can be distinguished in experimental realizations of this effect as depicted by the schemes in Fig. 3.2. These will be differentiated, explained in detail, and summarized with respect to existing literature in the following sections.

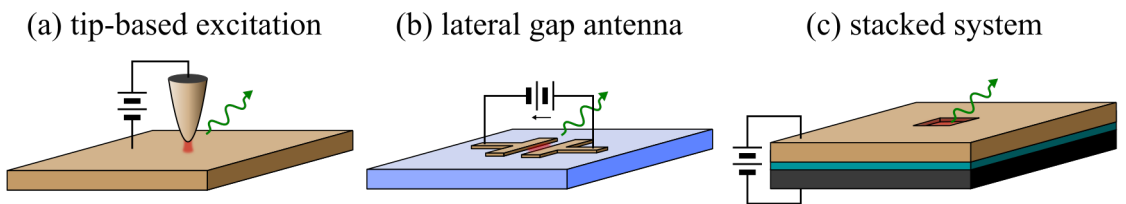


FIGURE 3.2: Depiction of a classification for different types of light emitting tunneling junctions. (a) Scanning tunneling microscopy (STM) as a tip-based excitation source is characterized by a highly localized, point-like excitation of surface plasmons, whereas gap antennas (b) and stacked systems (c) are lithographically structured junctions in lateral or vertical orientation, respectively.

## 3.2 Tip-based Excitation

The highly localized near-field excitation of a surface plasmon polariton by a single, movable, point-like, electrical nanosource will be referred to as “tip-based” excitation.

Scanning tunneling microscopy (STM) fulfills these conditions by utilization of the scanning probe as nanosource of the tunneling current as described in the excellent review of Rossel et al. [69]. STM exhibits a radiative decay of excited gap plasmons between the tip and substrate, in which the tip-sample separation defines the tunneling barrier [70, 71]. Light emission by inelastic tunneling was experimentally shown first for STM in 1988 on a tantalum substrate by Gimzewski [72]. With the experimental proof, the method got immense attention due to the new possibilities in spatially high resolved characterization of the optical properties of plasmon supporting materials. First setups utilized a photon detector directed towards the gap and recorded the emitted energies of the excited states of the sample consisting of mono-crystalline metal films [73, 74]. Gradually, studies on surface defects, grain size and distribution as well as surface roughness for polycrystalline materials were published [75–77].

Setup-wise optimization of the imaging conditions is done in several ways. In the case of opaque samples, tilting impedes shading by the tip, which improves the signal acquisition at the detector. For transparent substrates, another approach is given by the extension of the STM setup by a hemispheric prism coupler at the backside of the substrate. This way, the normally non-radiative slow SPP mode is coupled into free space radiation by the prism. Additionally, Fourier analysis is enabled by imaging the objectives back focal plane. Thus, the angular distribution of STM induced plasmons in thin films is directly detectable as first demonstrated by Takeuchi et al. [78]. A theory to describe the near-field coupling of a point-like dipole source with a thin metallic film resulting in these intensity annuli was derived by Marty et al. [79].

### 3.2.1 Emission Characteristics

The mechanism of light emission from a scanning tunneling microscope has been described in many publications. The junction often is modeled as an ideal sphere in the vicinity of a half-space boundary [51, 56, 71, 80–82]. The tip curvature in the vicinity of the sample surface changes the dispersion relation of the normally non-radiative excitation drastically. This causes a fraction of energy to be emitted directly from the gap, which would be forbidden for an ideal planar system due to momentum selection. Since a fraction of the energy is emitted from the gap directly, the light emission from STM can be distinguished into two compounds. On one hand, the emission of the mode localized between tip and sample (LSPR). On the other hand, propagating plasmons coupled to the sample boundaries (SPP). For genuine probes, the influence of anisotropy and inhomogeneities at the tip apex strongly reinforces the emission process and has to be considered carefully [83–85]. This goes as far as having inverted photon maps of the same nanostructure by modifications of the tip geometry [86]. Hence, mostly tungsten, silver or platinum/iridium tips are used, which offer smooth films and minimize these geometric artifacts. Also, the emission characteristics and spectral position is strongly influenced by the refractive index of the gap. Especially the water bridge forming between the tip and sample can alter the conditions at the tunneling barrier and has to be considered in evaluation of the occurring signals [87]. The model of an intermediate layer can also be transferred to approximate the expected system response from an organic

layer or single molecule at the site of emission. The emitted light from STM was found to be linearly polarized in a set of experiments involving tungsten (W(111)) tips and different single-crystalline substrates [88]. A small, accompanying fraction of circularly polarized light could be attributed to tip asymmetries.

### 3.2.2 Emission Mapping

Surface plasmons are often excited by incident beams of photons, photoelectrons, and electrons as summarized by el Khoury et al. [89]. However, precise focusing of the incident beam represents a major challenge in visualization and imaging of surface plasmons. Tip-based excitation is not directly dependent on the optical diffraction limit but on the geometrical localization of excitation, which is the atom or cluster of the tip closest to the sample surface in the case of STM. Thus, highly precise photon maps with sub-diffraction resolution can be achieved by this technique. A recent example of these capabilities is the study of Yu et al. in which highly resolved photon maps of individual 3-7 nm small gold nanoparticles and dimers were obtained as depicted in Fig. 3.3. Also, the size and shape dependency on the photon emission has been evaluated [90]. Imaging of nanoclusters has been reported multiple times before, where the precision was mostly limited by the setup resolution.

Studies were published for a variety of junctions, involving silver clusters on  $\text{Al}_2\text{O}_3$  [91], on gold [92], and on silicon [93, 94] as well as gold clusters immobilized on graphite [95], on mica [96], and on glass [97]. The manifold experiments with partially different results already represented a main challenge of this technique. The acquired photon maps and emission spectra strongly depend on the effective junction geometry. Consciousness of the given tunneling conditions is crucial. It was shown, that the dominant conduction mechanism not only plays a major role in the emission process, but can alter the origin of information. While the junction is biased in the tunneling regime, radiation is observed correlating to Mie plasmons from the nanostructures. By increasing sample bias, field emission becomes relevant, providing access to other transitions above the Fermi level and thus, the electron density of states. However, the influence of the substrate is

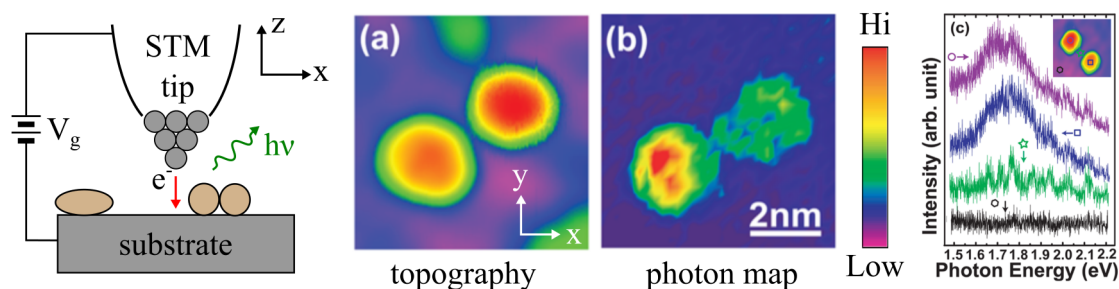


FIGURE 3.3: Schematic of topography and photon emission mapping by scanning tunneling microscopy. The atoms in closest proximity enable tunneling by biasing the STM tip. Emitted photons, changes in the tunneling current and the height information are used to reconstruct the scanned regions. (a) topography of a particle dimer, (b) photon map of this dimer and spectra of a similar dimer structure at different positions. Figure partially reprinted from [90].

increased due to a lower confinement of the intense local electric fields and substrate reflection. This increases complexity of the analysis due to convoluted signal contributions [98] as well as the risk of falsely assigned optical properties to the nanostructures [99]. A promising way to suppress these complex interplays might be enabled by the usage of non-plasmonic STM tips and the restriction to conducting, transparent substrates, e.g. ITO or sapphire. In that way, reflection of the substrate and plasmon coupling of the tip becomes negligible, which might enable deconvolution of the emission and provides the sought after stability in STM photon mapping by trading in surface smoothness [100].

### 3.2.3 Plasmon Propagation, Directionality and Coherence

Despite some of the struggles and complications of the method, it enables unique experiments regarding the propagation of plasmons, their coherence, and the deconvolution of mixed signals from LSPR and SPP. Romero et al. [101] scanned through a range of focal positions above and below the image plane until the contribution of SPP vanished, permitting a strict distinction between LSPR and SPP based radiation. Bharadwaj et al. [102] utilized mono-crystalline gold nanowires with a length of several micrometers for their experiments. The STM tip served as excitation source on one end of the nanowire while simultaneous photon mapping exhibited diffraction-limited emission on both ends of the nanowire, confirming the plasmon based radiation. Wang et al. [103] observed different leakage radiation efficiencies for gap plasmons and SPPs for tungsten and silver tips on gold films, and concluded two independent optical processes. They derived a plasmon decay length of  $10 \pm 5 \mu\text{m}$  for their respective film thickness. Structured surfaces have been investigated extensively by utilizing the highly localized excitation of a point-like, circular SPP in STM. Thus, plasmon propagation, angular distribution and directionality as well as complex nanostructures [104] have been characterized.

Dong et al. [105] enabled a keystone experiment concerning directionality control of launched plasmons on films by utilizing the high spatial precision of excitation by an STM tip. Plasmons excited from a point-like source propagate radially symmetric. By structuring a grating into a gold film with electron beam lithography the propagation was restricted and edge scattering occurs. This lead to interference patterning of the excited SPP. Thus, depending on the position of the tunneling junction, the SPP at the edges can be adjusted to enable directed plasmon propagation due to constructive or destructive interference, respectively. Experiments of 100 nm thin gold slabs on glass substrates showed edge scattering of surface plasmons. Depending on the boundary, strongly directional scattering was observed for the gold-air interface at high angles and diffusive, coherent scattering for the gold-substrate interface at low angles [106]. In a different study, the coherence lifetime of SPPs was found to be mainly dominated by dissipation of the mode into the metal ranging between 5-10 fs, which was achieved by a modified version of the Young double-slit interference experiment [107, 108]. Wang et al. [109] studied the in-plane SPP interference on a thin gold film induced by immobilized nanoparticles and the coincident out-of-plane scattering into free space radiation in which utilization of objectives with different numerical aperture allowed the angular differentiation of the effects.



Active angular control of the STM induced light emission has been shown for electrically excited SPP theoretically and experimentally with truncated bi-tetrahedral gold nanostructures immobilized on ITO. In particular, the angular distribution of emission was altered depending on the position of the STM tip on the particle and the associated tilting of the dipole oscillation. Additionally, by positioning of the tip in different areas of the recorded nanostructure, the spectral distribution of STM-induced light was determined [100, 110]. Focusing capabilities and polarization properties of cylindrical vector beams from plasmonic lenses were investigated, revealing a loss in the cylindrical symmetry of polarization by single, off-centered excitation [111].

### 3.3 Chip-based Excitation

Electrically-driven near-field excitation of surface plasmons in lateral structures with the high potential for easy parallelization will be referred to as “chip-based” excitation. Junctions with a single tunneling transition location will be referred to as optical gap antennas while quasi-infinite, pointlike excitation nanosources of radiation implemented in the tunneling barriers will be described as planar systems.

#### 3.3.1 Lateral Optical Gap Antennas

Inherent to the lateral, freely tunable design, the use of optical gap antennas enables highly stable experimental conditions without the need of sophisticated feedback systems due to the fixed junction geometry as opposed to STM. Fabrication of these devices often is done by electron beam lithography or with focused ion beam structuring. Kern et al. [112, 113] investigated emitted light by electrically connected resonant optical antennas by two facing single-crystalline gold electrodes with a nanoparticle in the gap as shown in Fig. 3.4. Spectral tuning of emission was achieved by changing the antenna geometry with respect to the position of the nanoparticle in between. Similar to the introduced artifacts of a STM tip in measurements by clusters, plasmonic nanostructures that support light emission in the visible regime are comparably small. Thus, a strong influence of the electrical connection on the antenna resonance was described.

Vardi et al. published on the role of the nanoparticle positioning in the vicinity of the gap which enabled electrically-driven emission with Fano resonances as spectral features. The opening angle of this bow-tie shaped electrodes played a minor role in the Fano-resonance strength and spectral position [114]. A detailed investigation of low-biased, electron-fed optical antennas found normally energy-forbidden, spontaneous light emission beyond the quantum limit [115] which can be attributed to a locally elevated hot carrier temperature and corresponding smearing of the Fermi-Distribution [116].

The usage of single crystalline gold flakes from chemical synthesis minimizes artifacts and losses in the medium caused by grains and film inhomogeneities. Thus, they depict an ideal basis for laboratory and high signal-to-noise measurements of the LEIT effect. Most of such studies deploy focused ion beam milling or electron beam lithography for

structuring of the surfaces. However, the high effort in the sample preparation and limited minimal feature size is a major drawback. An alternative fabrication method of lateral gap antennas is the exploitation of electromigration in tunnel junctions. Formation of the tunneling barrier is achieved by deposition of a sacrificing metal layer which is locally oxidized by the intense electric fields at tailored defects [117–119]. Unidirectionality in the radiation pattern has been achieved by this method. Slanted antenna arms were electrically isolated by electromigration in which the unidirectionality is based on the far-field interference of the basic tunneling junction (dipole) emission and the modes supported by the antenna geometry [120]. However, since the gap of an optical antenna is the location of largest field intensity, its properties such as the width, cross sectional area, and the properties of the gap medium are decisive [121]. Reliable fabrication on large scale is an art on its own and subject of several studies [122, 123]. Stacked optical antennas overcome this issue by transiting the lateral optical antenna into a vertical material stack. This renders them highly compatible with standard optical lithography processes and enables precise control of the implemented film thickness.

### 3.3.2 Stacked Systems

Planar tunneling structures consisting of MIM or metal-insulator-semiconductor (MIS) have been studied extensively after discovery of the light emission effect by inelastic tunneling. In contrast to an ideal, planar tunneling junction, all real samples suffer from defects, interstitial layers, or surface roughness. Thus, these imperfections lead to plasmon-based radiation, which normally would be forbidden by momentum selection on ideal surfaces. This enables scattering of the plasmon modes into free space radiation. Since first applications of this effect were supposed to lead to a new light source for compact emitters, spectral tuning by incorporation of all material mixtures of MIM junctions, e.g. aluminum, gold, silver, magnesium, and copper [124–127] was of high interest in early studies. Additionally, characterization of the role of surface roughness in the emission [128–131] was a key aspect for efficiency enhancement to enable competitive yields in comparison with other radiation sources. Detailed studies on intrinsic [132, 133] and artificial surface roughness by a statistically rough sublayer, such as  $\text{MgF}_2$  [134,

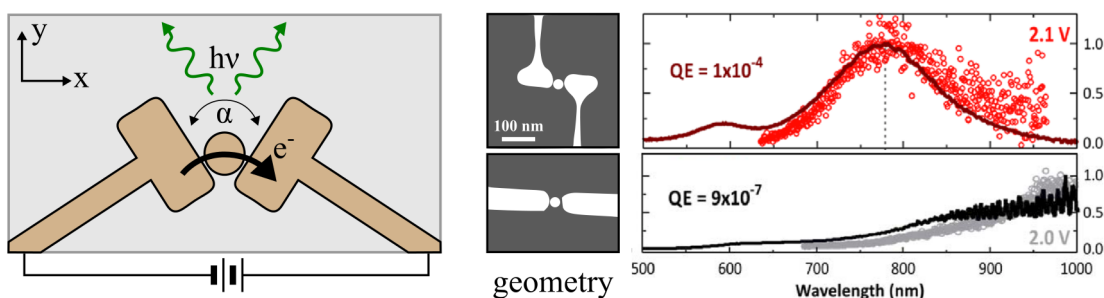


FIGURE 3.4: Illustration of a lateral gap optical antenna featuring a nanoparticle between two slanted arms with an opening angle  $\alpha$ . In this case, a double tunneling barrier was formed. Spectra can be altered by the particle position as well as the geometric features of the antenna arms. Unidirectionality is achieved by tailoring  $\alpha$ .

Figure partially reprinted from [112].

[135], CaF<sub>2</sub> [136–138] and photoresists [139] were published. This approach suffered from the trade-off between higher emission rates and decreased electrical stability of the junctions. Microstructuring of the uppermost and interstitial layers instead of the sublayer enabled to overcome this issue as depicted in Fig. 3.5. The influence of gratings [140, 141], particles [142–145], prism-couplers [146–148], and nanocrystals [149] on light emission efficiency and spectral properties in light emitting tunneling junctions is covered vastly in literature.

An exemplary study utilizing attenuated total reflection measurements found outcoupling efficiencies to be in the range of 5 % for planar silver films, up to 9 % by implementation of CaF<sub>2</sub>, and up to 80 % by holographic gratings in which the thickness of the silver film in the range of 20-60 nm played a minor role [150]. Scattering of the excited surface plasmons is only desired at the uppermost layer. Thus, defect free boundaries are of high interest to increase the quality and lifetime of the underlying tunneling junctions. Due to the lattice mismatch between the implemented oxides and metals, stress induced defects normally degrade the junction and are susceptible to leakage currents which require experimental conditions in ultra-high vacuum or cryostats to prevent electrical breakdown. By the implementation of silicon as substrate, the lattice mismatch between substrate and oxide as well as the silicon crystal orientation are minimized and passed on, resulting in stabilized junctions even in ambient conditions with spectral ranges from NIR to near-UV [151–157]. Nonetheless, calculation and design of these structures is more complex due to the increased influence of temperature, frequency [158], and the tunneling transition zone caused by gradients in the boundaries charge carrier density [159].

Another approach to suppress defects in the oxide induced by top-down deposition is the utilization of single crystalline oxides, e.g. hexagonal boron nitride (h-BN) [160, 161], in which large scale fabrication is problematic due to the necessary oxide transfer methods. Emission features of Au/h-BN/Au junctions exhibit very fast switching capabilities in the emitted light intensity by overlaying the sample bias with an sinusoidal AC signal [162]. The intensity count rate was determined by time-correlated single photon counting. Modulation up to 1 GHz was experimentally proven, whilst this limit was given setup-wise. Theoretically, the frequency of intensity modulation is only limited by the

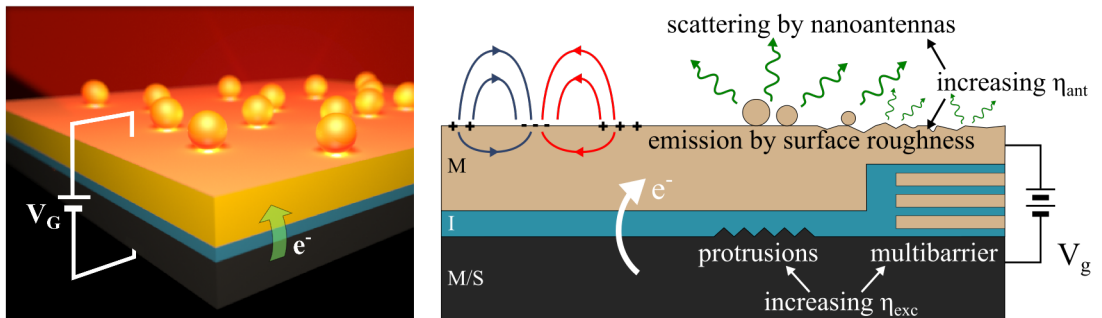


FIGURE 3.5: Stacked LETJ samples feature a palette of parameters to enhance excitation  $\eta_{exc}$ , for example by protruding features in oxides or multibarrier junctions with well defined layers. Nanoantennas or introduced roughness at interfaces can alter and enhance ( $\eta_{ant}$ ) the spectral emission characteristics of these junction types.

tunneling transition time [163], but realistically the limit is given by the RC constant of the junction, which still could enable modulation frequencies up to tens of terahertz [164]. Simultaneously, the gap between optical circuitry and electronics was bridged by integrating structured gap antennas combined with optical waveguides [165] and direct signal transducers [164]. These on-chip devices and junctions exhibit a high potential for direct transfer of electrically generated emission into optical circuitry for long range signal transfer. In combination with optically pumped opto-couplers [166], this might pave the way for complex and ultrafast optoelectronic devices.

### 3.4 Junctions involving organic Molecules

With the technical advances, the steady aim of further miniaturization, and simultaneous need of cheaper devices, molecular and organic structures are getting more and more in focus as seen in recent years [167], which also holds true for studies on plasmon based light emission by electrical excitation. The realized resolutions in light emission STM not only enabled highly resolved mapping of nanostructures but also vibronically characteristic photon imaging of orbital information at the single molecule level [168–171]. Tuning and narrowing of the spectral emission by strain-induced conformational changes in designed chromophores has been demonstrated in cryogenic STM [172, 173].

Self-assembled monolayers (SAMs) have been investigated as tunneling barrier as shown in Fig. 3.6, in which these SAM-based tunneling junctions exhibited characteristic molecular electronic properties [174, 175]. This includes polarized emission dependent on the orientation of the SAM structure, blinking, and the known bias-dependent spectral cut-off. Additionally, non-symmetric molecules can function as diodes, enabling bias-selective light emission due to energetically asymmetric tunneling junctions [176, 177]. Challenges to overcome for molecular junctions often are low breakdown voltages compared to inorganic materials, increased temperature instability, lower device lifetimes, and structural heterogeneities [178, 179]. While the first is an intrinsic material property, the latter three might be overcome by further advances in technology [180]. Alternative methods for contacting of the electrodes are required, such as GaIn-contacting [181], since SAMs are sensitive on strain and temperature [182].

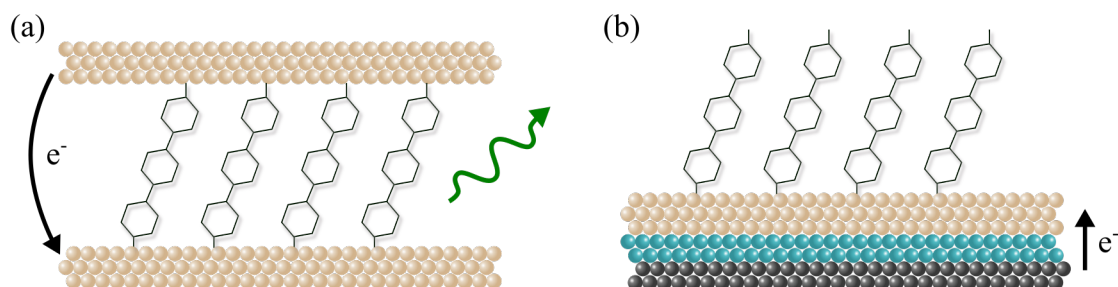


FIGURE 3.6: Scheme of the general applications of molecules in LEIT junctions. (a) MIM junction with the organic layer serving as tunneling barrier with discrete energy levels. (b) adsorption of molecules at the surface of a stacked system to induce a resonance shift similar to detection mechanisms in surface plasmon resonance techniques.

## 3.5 Scope of this Thesis

Derived from the given overview on the literature, this work aims to contribute some insights on missing links in the field of electrically driven plasmonics. The evaluation of theoretical and experimental objectives are listed in the order as handled in the chapters 4 - 6:

### **Fabrication of large scale tunneling junctions**

Planar junctions from thin-film material stacks are fabricated to study their suitability as LETJ. These stacked systems offer a high potential for parallelization by usage of standard lithographic methods on wafer scale. This enables comparability between experiments, easier handling and an upscalable fabrication with a wide range of material combinations and junction geometries for varying emission features.

### **Description of LETJ electrical properties**

Characterization by I-V and impedance spectroscopy with respective models for the estimation of junction parameters are applied to assess the junction quality and structural stability non-destructively.

### **Emission by planar and smooth LETJ systems**

Transfer and equivalency to findings on emission features by micrometersized tunneling junctions towards large scale junctions are investigated. This includes the bias dependent cut-off frequency, the dependency of the emission intensity on the tunneling current and tunability of the spectra by implementation of different electrode materials.

### **Plasmon hybridization between LETJ and adsorbed nanoantennas**

Enhanced scattering and tunability of emission features from electrically driven structures by chemically-synthesized nanoparticles are studied. The distance dependency of these hybrid modes is assessed and a proof-of-principle study similar to plasmonic nanoruler systems as biosensing scheme is described.

### **Imaging of emission features on nanoparticle enhanced LETJ**

The discrimination of metallic and dielectric nanoantennas by LETJ scattering as well as imaging of anisotropic structures at constant operating conditions are discussed. Signals from individual particles are compared at steady-state to assess a correlation between intensity fluctuations. Additionally, the functionality in liquid environment is tested.

- page intentionally left blank -

## 4 | Fabrication and Characterization of Thin Film Stacks

This chapter will focus on the description of the fabrication details of LETJ samples that were used in this work and the influence of individual features in the final chip design is described. Subsequently, the utilized electrical and optical characterization methods for these structures are discussed while comparing the obtained results with theoretical predictions. In the end of this chapter, potential improvements of the current layout will be recommended briefly, followed by suggestions for additional characterization methods that might be interesting for extraction of information on morphological and electrical properties of LETJ samples in general.

### 4.1 Sample Fabrication

For the fabrication of the tunneling structures, a modified procedure of Wang et al. [5] was adapted. The fundamental processes can be divided into four main steps as depicted in Fig. 4.1, while the layout of the LETJ chip is an advanced design based on the first conclusions drawn from previous work on tunneling junctions in the department partially done by myself during my master thesis [183]. An overview on the fabrication details is listed in Tab. 4.5. Reasoning behind this protocol was to ensure reliable operation of the large scale junction and to minimize the risk of electrical breakdown.

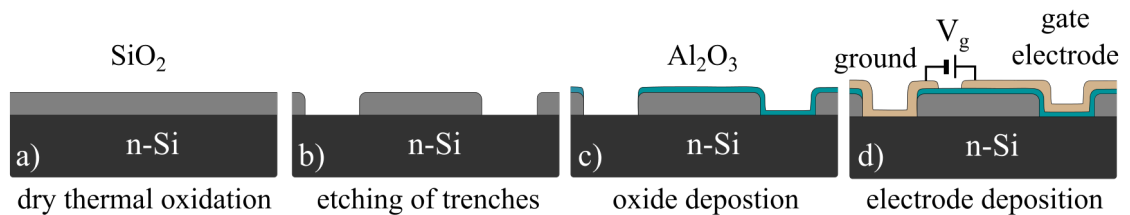


FIGURE 4.1: Scheme of the four main steps in the LETJ sample fabrication as generally used in this work. After dry, thermal oxidation of the whole Si wafer (a), trenches were chemically etched to define the tunneling junction area (b). A thin, high quality isolator was deposited as tunneling barrier by plasma supported atomic layer deposition (c). Top electrodes were deposited followed by an additional etching and deposition step for the bottom electrode. Both were structured by physical vapor deposition (d).

First, a monocrystalline, arsenic doped ( $N_d \approx 10^{19} \text{ cm}^{-3}$ ) silicon substrate with  $\langle 111 \rangle$  orientation was cleansed and thermally oxidized in gaseous environment to grow a 200 nm  $\text{SiO}_2$  thick layer that served as leakage barrier. The wafer was then cut into  $15 \times 15 \text{ mm}^2$  chips and the surface was covered with resist for protection and storage of the chips which allowed for small batch fabrication of individual samples.

Second, all top electrode and ground contacts of a single chip were defined by wet chemical etching of non-masked areas (Fig. 4.2b) into the previously deposited  $\text{SiO}_2$  protection layer down to the silicon substrate.

Third, plasma enhanced atomic layer deposition (ALD) of a high quality tunneling oxide followed. Deposition was done at  $120^\circ\text{C}$ , utilizing the precursor tri-methylaluminum (TMA) combined with gaseous  $\text{H}_2\text{O}$  to ensure ideal conditions for a stable growth of the  $\text{Al}_2\text{O}_3$  tunneling barriers. In this step, the ground contacts were still covered in an additional layer of resist which was removed after the ALD via lift-off to access the silicon substrate again.

As fourth step, the electrode masks were structured into spin-coated resist to deposit the electrodes by physical vapor deposition.

As shown in Fig. 4.2, the contact pads ( $1 \times 1 \text{ mm}^2$  in size to enable easy contacting with micromanipulators) are lying well apart from the junction areas. Thus, weak spots or damaging of the junctions from mechanical contacting are minimized. Additionally, all structures despite the T10 and T100 junctions are placed redundantly on one chip (see Tab. 4.3) for tests regarding chip-wise repeatability of experiments and consistency in additional fabrication steps such as nanoparticle immobilization or surface chemistry.

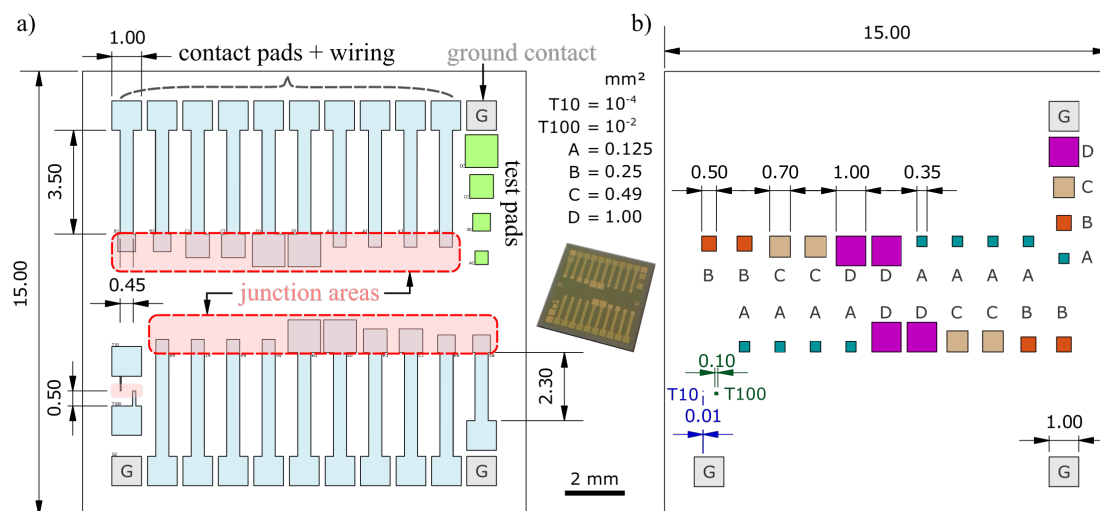


FIGURE 4.2: Lithography design of the LETJ chip layout chromium masks. (a) Mask for the metal electrodes. Crossed areas mark regions of tunneling junctions, while the other outlines indicate locations of wiring and contact pads. (b) Mask for etching of the tunneling areas into the  $\text{SiO}_2$  protection layer. Ground contacts (G) are located at the edges, whereas the junctions (labelled by T10, T100, A – D) indicate different LETJ areas in the center of the chip.



TABLE 4.3: Summary of the available junction types, ground contacts G and wirings W with their sizes on a single LETJ chip.

Type	Size / mm	Area / mm <sup>2</sup>	Redundancy
G	1	1	3
W	3.5x0.45	1.575	N/A
A	0.35	0.1225	8
B	0.5	0.25	4
C	0.7	0.49	4
D	1	1	4
T100	0.1	0.01	1
T10	0.01	1E-4	1

The wiring pad dimensions were chosen to be the best compromise between the introduced parasitic capacitance and the film resistance. Three ground contacts were placed at the edges of the junction for the practical reason of more simple contacting and easier handling of the chips.

One of the most apparent advantages in the usage of photolithography are the capabilities to alter almost all junction parameters between the subsequent manufacturing steps individually but in parallel. By having access to a library of deposition techniques and materials, a variety of junctions was fabricated in the course of this thesis:

A brief summary of the overall fabricated junctions is listed below, in which some structures turned out to be not suitable for the proposed measurements or capable of light emission either inherently by design due to fabrication defects or fast degradation during measurements. Some findings on these configurations, which were studied but rejected after partial characterization due to lack of reliability, will be further discussed in the applicable sections:

**Adhesive thin films** of titanium to improve connection of the electrode films to the oxide layers have been implemented as well as omitted during fabrication. No light emission was observed for junctions with adhesion layer. This might be attributed to the lowered barrier height by the additional layer, introduction of defects and electromigration.

**Al<sub>2</sub>O<sub>3</sub> tunneling oxides with 2, 5, 7 and 10 nm** in thickness have been fabricated, where only 7 nm turned out to be suitable for light emission. The 2 and 5 nm barriers suffered from immediate electrical breakdown upon connection. This was attributed to point defects in the large scale junctions inhibiting characterizations beyond IV-testing. In contrast, the 10 nm oxide resulted in low tunneling currents, which prevented an efficient optical excitation.

**10 nm tunneling oxide of Al<sub>2</sub>O<sub>3</sub> or SiO<sub>2</sub>** have been deposited to study the influence of the tunneling barrier mainly determined by the material electron affinity and breakdown field strength.

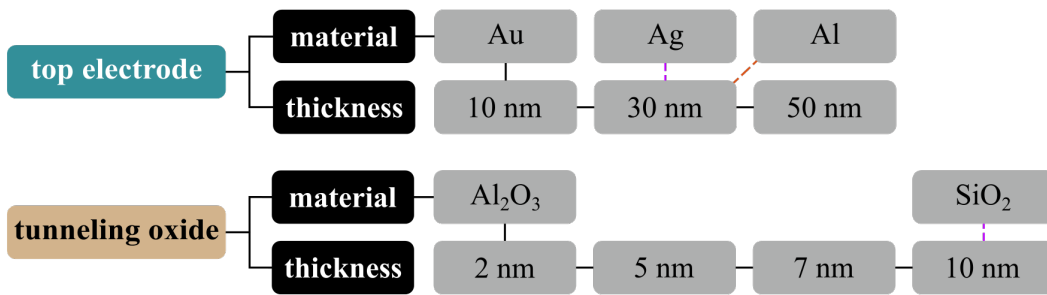


FIGURE 4.4: Overview of the studied junction parameters. By utilizing standard photolithographic processes, a variety of materials and deposition techniques are available to tailor the optical and electrical characteristics of the fabricated samples. Mainly, the material and thickness of the top electrode as well as the oxide material and thickness of the tunneling barrier were investigated for their influence on light emission. Lines mark the variety of fabricated film thickness and material combinations.

**Electrodes of silver, gold and aluminum** were fabricated to alter the barrier heights of the tunneling junction by different work functions while altering the bulk plasmon frequency of the top most material and its influence on light emission.

**10, 30 and 50 nm thick gold electrodes** were assessed for film roughness and influence on light emission. The 10 nm electrodes lacked thickness homogeneity due to island formation, whereas the 50 nm electrodes exhibited no light emission at all. This might be attributed to a preferential mode profile compromising the LETJ process and efficient outcoupling of radiation.

Taking into account the very first findings, the vast majority of measurements were performed on structures with the following parameters:

$$\mathbf{30\text{ nm Au} / 7\text{ nm Al}_2\text{O}_3 / \text{Si}}$$

for the implemented materials in this thesis unless stated otherwise. Other junctions with the parameters as listed in Fig. 4.4 and described before will be brought into the studies and compared in more detail to the 'standard' junction within the respective chapters.

A cross-section of a fully fabricated structure is shown in Fig. 4.6, in which a clear distinction between the junction area and the surrounding protection layer is visible with the transition region between them to mediate the height difference. The focused ion beam (FIB) cut of a similar junction outlines the interfaces of the implemented materials to enable analysis of the grown films.

TABLE 4.5: Generic protocol for the fabrication of the used LETJ structures starting from a blank Si wafer. Figs. 4.1 & 4.2 depict the main processing steps and chip layout.

Process	Description
<b>- Wafer Oxidation -</b>	
Cleaning	cleanse of the wafer in ultrasonic bath
Oxidation	dry oxidation of 190 nm SiO <sub>2</sub>
Resist Application	1,8 μm protective layer of AZ1514E resist
Wafer Dicing	cutting of 15 × 15 mm samples
<b>- Photolithography - Junction Layout -</b>	
Resist Removal	removal of the dicing process damaged resist
Resist Application	1.8 μm of HMDS adhesion layer and <i>AZ1514</i> resist by spin coating at 5000 rpm
Annealing	resist cure for 20 min at 80 °C
Mask Alignment & Development	baking at 120 °C for 2 min and flood exposure defining the tunneling junction layout
<b>- Junction Etching -</b>	
SiO <sub>2</sub> Etching	etching of the protective oxide down to silicon
Resist Removal	removal of the resist residuals
<b>- Photolithography - Tunneling Oxide -</b>	
Resist Application	1.8 μm of HMDS adhesion layer and <i>AZ5214E</i> negative resist by spin coating at 5000 rpm
Annealing	resist cure for 20 min at 80 °C
Mask Alignment & Development	protection of the back electrode region with resist
<b>- Tunneling Oxide Deposition -</b>	
Atomic Layer Deposition	deposition of 2 – 10 nm tunneling oxide by TDMAS or TMA and H <sub>2</sub> O (g) at 120 °C
Lift-Off	lift off back electrode area covering resist
<b>- Electrode Deposition -</b>	
Resist Application	1.8 μm of HMDS adhesion layer and <i>AZ5214E</i> negative resist by spin coating at 5000 rpm
Annealing	resist cure for 20 min at 80 °C
Mask Alignment & Development	baking at 120 °C for 2 min and flood exposure defining the electrode layouts
Physical Vapor Deposition	deposition of gold, silver or aluminum electrodes in different thicknesses by PVD

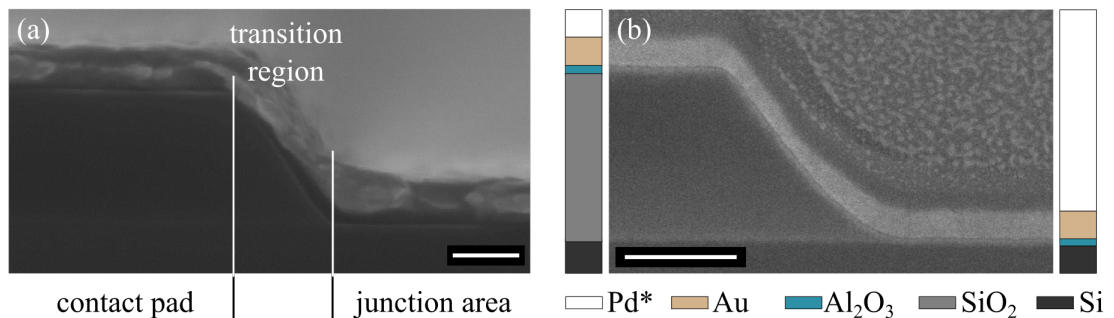


FIGURE 4.6: (a) Scanning electron microscope image of an exemplary LETJ structure. The tunneling junction is located at the righthandside, transitioning into the contact pad, which additionally features a 190 nm thick SiO<sub>2</sub> inhibition layer to prevent leakage currents and simplify electrical contacting of the structures. (b) Focused ion beam cut of a similar structure emphasizing the material contrasts of the junctions. \*The Pd topmost layer was added for enhanced contrast. Scalebars: 50 nm.

## 4.2 Reflectance Measurements on Multilayers

Reflectance spectroscopy is a straight-forward method to assess the structural features of planar thin-film junctions. In contrast to many other methods, it offers the great advantage of non-destructive characterization of samples even in pre-operating conditions. This enabled a quick examination of the devices before first operation.

Fig. 4.7 depicts the self-built experimental setup. A broad-banded tungsten white light source (HL-2000-HP, Ocean Optics) coupled to a reflection probe fiber (300-UV-VIS, Ocean Optics) with y-splitting was used to illuminate the sample surface. At the sampled end of the fiber a collimation lens was attached and mounted perpendicular (angle of incidence - AOI  $\vartheta = 0^\circ$ ) to the sample surface within 1 mm distance. The backward directed fiber collected the reflected light and was connected to a linear CCD spectrometer (Cypher H, BWTEK). Fine-positioning of the junction was achieved by a manual microscopy stage (EK-14, Märzhäuser). Reference measurements to calibrate the system on the lamp spectra were done with a high quality, broadbanded dielectric mirror (BB1-E02, Thorlabs) positioned in the sample spot.

The measurement scheme is shown on the right-hand side of Fig. 4.7. According to the Fresnel equations, an incident beam coming from an angle of incidence  $\vartheta_0$  is partially reflected or transmitted at each interface of the thin-film stack. Depending on the material, also absorption inside the films has to be taken into account. The overall detectable reflected light of a sample is the sum of all interface related fractions of the incident wave leaving the top interface. In experimental setups, the applicability to analyze thin film stacks is limited since the method requires the knowledge of the individual film thickness and planarity of the films in the region of interest (ROI). To discriminate reliably between all implemented films, differences in the material refractive indices are needed as well as a penetration depth of the incident light sufficiently large to reach all interfaces.

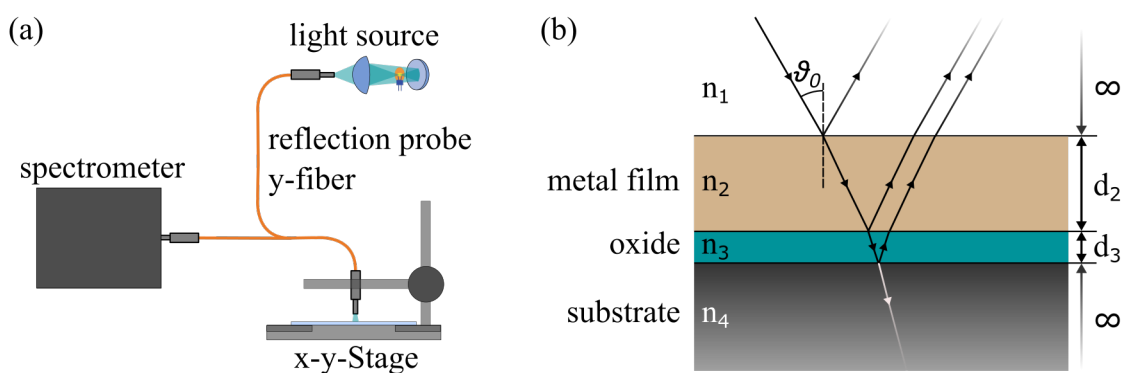


FIGURE 4.7: (a) Setup for reflection measurements. A halogen white light source was coupled into a  $600\ \mu\text{m}$  core diameter y-fiber reflection probe. The fiber end was set 1 mm above the sample surface at an incident angle  $\theta_0 = 0^\circ$ . Sample positioning was done with a manual x-y-stage. (b) Illustration of reflection, transmission and absorption at the boundaries of the thin-film stack with the respective refractive indices  $n_i$  and film thickness  $d_i$  according to the Fresnel transfer-matrix.

The latter can be achieved by using either suitable light sources (e.g. broad-banded halogen sources), restriction to thin-films with low absorption or incident illumination of high power.

Calculations of the theoretical reflectance and absorbance spectra were done by utilizing the Fresnel equations as described by Junesch et al. [184]. The reflection coefficient  $r_j$  and transmission coefficient  $t_j$  at an interface  $j$  for s-polarized light and materials without characteristic magnetic response ( $\mu = 1$ ) are given by the following expressions

$$r_j = \frac{n_j \cos(\vartheta_j) - n_{j+1} \cos(\vartheta_{j+1})}{n_j \cos(\vartheta_j) + n_{j+1} \cos(\vartheta_{j+1})} \rightarrow \vartheta_0 = 0^\circ \rightarrow r_j = \frac{n_j - n_{j+1}}{n_j + n_{j+1}}, \quad (4.1a)$$

$$t_j = \frac{2n_j \cos(\vartheta_j)}{n_j \cos(\vartheta_j) + n_{j+1} \cos(\vartheta_{j+1})} \rightarrow \vartheta_0 = 0^\circ \rightarrow t_j = \frac{2n_j}{n_j + n_{j+1}}. \quad (4.1b)$$

with the angle  $\vartheta_j$  of the incident wave, the transmitted wave angle  $\vartheta_{j+1}$  of the next material and their respective refractive indices  $n_j$  and  $n_{j+1}$ . Note, since absorption is not negligible for various materials, these values might end up to be complex, which is why especially the angles do not necessarily match with the physical angle of incidence (AOI) of the light beam. If the real angle of the incoming beam  $\vartheta_0$  equals to zero, the equations simplify to the terms given in Eqs. 4.1.

The (2x2) transfer matrix  $\mathbf{M}$  as a result of the product of light matter interaction based on the upper equations for an multilayer system composed of an arbitrary number of layers  $m$  and different materials  $n_j$  of thickness  $d_j$  is then defined as given in Eq. 4.2. In this equation, the  $m - 1$  interfaces of adjacent materials are indexed with  $j$  to match the material from which the incident radiation originated. The most outbound layers are assumed to be of infinite thickness. Justifiable for this work, the top layer was defined as air and the bottom layer representing the silicon substrate of the LETJ chips since  $\sum (d_{\text{films}}) / d_{\text{substrate}} \ll 1$ .

$$\mathbf{M} = \prod_{j=2}^{m-1} \left( \frac{1}{t_j} \begin{bmatrix} 1 & r_j \\ r_j & 1 \end{bmatrix} \times \begin{bmatrix} e^{-ik_0 d_j n_j \cos \vartheta_j} & 0 \\ 0 & e^{ik_0 d_j n_j \cos \vartheta_j} \end{bmatrix} \right) \times \frac{1}{t_{m-1}} \begin{bmatrix} 1 & r_{m-1} \\ r_{m-1} & 1 \end{bmatrix} \quad (4.2)$$

To recalculate the total Fresnel coefficients of the multilayer system into the intensity based units for reflectance  $R$ , transmission  $T$  and absorbance  $A$ , the normalization steps as described by Eqs. 4.3 were included:

$$R = \left| \frac{\mathbf{M}(2, 1)}{\mathbf{M}(1, 1)} \right|^2, \quad (4.3a)$$

$$T = \left| \frac{1}{\mathbf{M}(1, 1)} \right|^2 \frac{\text{Re}(n_m)}{\text{Re}(n_1)}, \quad (4.3b)$$

$$A = 1 - R - T. \quad (4.3c)$$

Experimentally obtained reflectance spectra of LETJ chips with different electrode materials in comparison with calculated results are shown in Fig. 4.8. All measurements

were conducted on a self-written software and repeated three times at different areas of the same chip. Every spectrum consisted of 10000 averaged records with an integration time of 1 ms each.

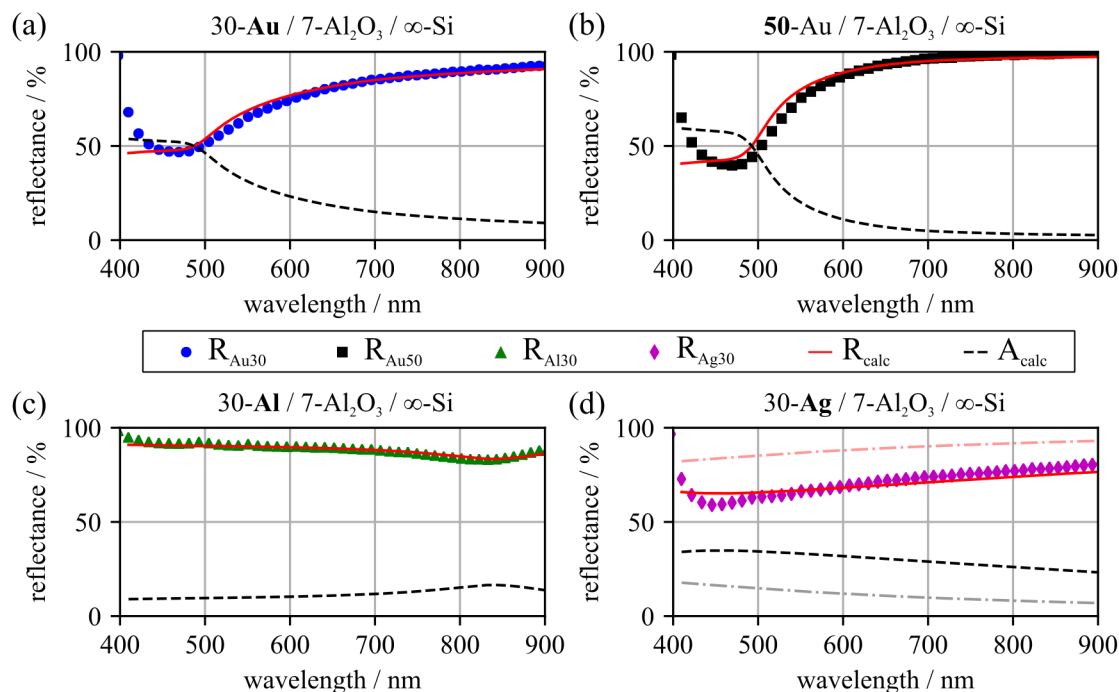


FIGURE 4.8: Measured reflectance spectra of four LETJ stacks with different electrode material and thickness. The calculated results for the reflectances ( $R_{\text{sim}}$ , red line) and absorbance ( $A_{\text{sim}}$ , black dashed) agree well with the experiments. Note, in the case of silver electrode (Ag), the calculated results agree with calculations of a 16 nm thick electrode due to oxidation. The original results for a 30 nm electrode are indicated by the dash-dotted lines. For aluminum (Al) no change is visible since the oxidation is self passivated after  $\approx 1-2$  nm. The silicon substrate is assumed as an infinitely thick medium in the calculations.

The modeled and measured values agreed very well and verified the assumed manufacturing parameters of a 7 nm  $\text{Al}_2\text{O}_3$  tunneling oxide on top of the silicon substrate as basis for the metal electrode layers. As reference, a cross-section of such a junction was imaged in SEM and the film thicknesses were determined to be 31.5-Au / 8.0- $\text{Al}_2\text{O}_3$  / 187-SiO<sub>2</sub>. The subplots outline the potential of this technique to non-destructively verify the fabricated material stacks, especially regarding the layer thickness of the implemented metal electrodes. Three 30 nm thick electrodes of gold - (a), aluminum (c), and silver (d) have been analyzed, while only for gold a second 50 nm thick film (b) was prepared. The spectrum of (a) exhibits the material characteristic dip in the reflection signal at short wavelengths leading to its specific name giving color. By comparison of the two gold samples, reflection only increased for longer wavelengths, if the film thickness was increased. Aluminum exhibited the expected homogeneous reflection in the measured range. For these samples, the experimental results and theory matched very well as listed for selected wavelengths in Tab. 4.9.

Larger deviations occurred in the case of silver, which can be attributed to oxidation of the thin film and therefore a decreased reflectivity. While a film of 30 nm thickness was

TABLE 4.9: Measured ( $R_{\text{exp}}$ ) and calculated ( $R_{\text{sim}}$ ) reflectances of different LETJ stacks at two selected wavelengths of different LETJ stacks. Deviating parameters are indicated bold. \*,\*\* and \*\*\* mark the references for the dielectric functions.

junction	thickness / nm	$R_{\text{exp}}@550$	$R_{\text{sim}}@550$	$R_{\text{exp}}@750$	$R_{\text{sim}}@750$
Au*/Al <sub>2</sub> O <sub>3</sub> **/Si***	30/7/∞	65.2	68.8	87.6	87.1
	<b>50</b> /7/∞	75.2	79.9	97.6	96.0
Ag*/Al <sub>2</sub> O <sub>3</sub> /Si	30/7/∞	66.0	86.8	75.6	91.1
	<b>16</b> /7/∞*	↓	66.8	↓	72.5
Al*/Al <sub>2</sub> O <sub>3</sub> /Si	30/7/∞	86.3	86.9	91.1	90.1

\*McPeak et.al [185] \*\*Dodge [186] \*\*\*Green [187] accessed via refractiveindex.info [188]

deposited, the measured signal only concurred with a calculated thickness of 16 nm after 24 hours in ambient conditions. This effect rendered the usage of uncovered silver films as very problematic for long term applications. Similar could be expected from aluminum, but the self-passivation occurring after 1 - 2 nm oxide thickness inhibited further degradation of the film which is not true for silver. All plots exhibit a larger deviation from theory at low wavelengths, which can be attributed to the low intensity of the light source implemented in the setup as depicted in Fig. B.3.

Drawbacks of these measurements are explicitly visible when the investigated parameters of the thin films are reaching the limits of detection by either very small thickness differences or similar indices of refraction. As shown in Fig. 4.10(a), two different tunneling oxides of 5 and 7 nm were compared, but only marginal differences are emerging for experimental as well as for calculated values. Note, that this was partially caused by the dominance of the topmost metal layer correlated to its skin depth.

Reflectance measurements of the fabricated structures proved to be a fast method to check the chip quality. However, other methods have been deployed for extraction of precise information about the tunneling barrier, as described in the next sections, since these structural information could not resolve reliable correlations on electrical features.

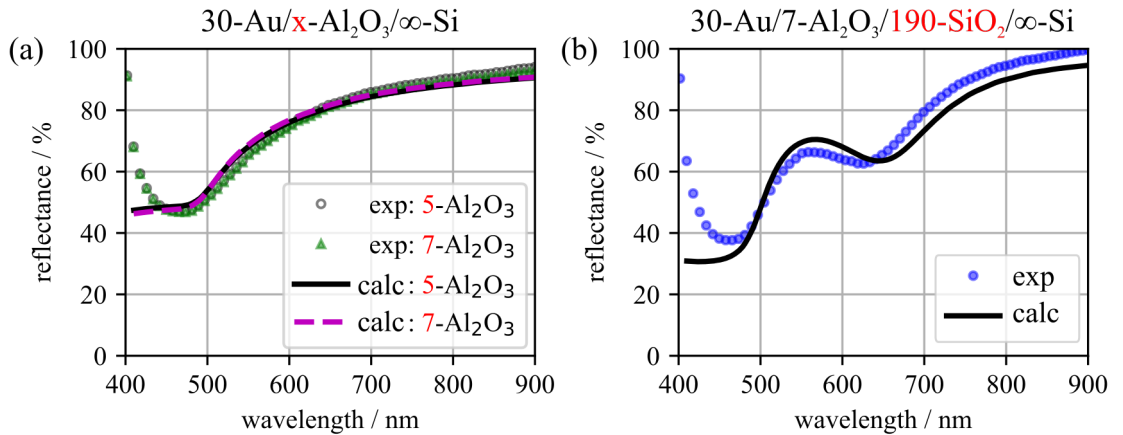


FIGURE 4.10: (a) LETJ chips with two different tunneling oxides of 5 and 7 nm match well with theory, but outline the inapplicability of this technique in respect to minimal changes of the material stacks. (b) Spectrum of a contact area with the underlying 190 nm SiO<sub>2</sub> protection layer (ref. index for calculation taken from [189]).

### 4.3 Current-Voltage Characteristics

The analysis of conduction mechanisms in thin-film junctions with an implemented potential barrier is a well known subject in nanoelectronics [45, 46, 190]. In most of these studies, the scope revolves around gate tunneling effects as leakage source since they take an essential role in the performance of down-scaled CMOS-transistors. In this work, the main objective from these experiments was the distinction of the dominant conduction mechanism at the junction operation points and, with it, the determination of the potential barrier height and thickness.

In Fig. 4.11 the basic experimental setup is depicted as it was assembled in the course of this work at the Nanoscience Center in Jyväskylä, Finland. The sample  $S$  was connected by micro-manipulators inside an electromagnetically shielded vacuum chamber and biased by a stabilized laboratory power supply. Individual precision pre-amplifiers for voltage (1211, DL-Instruments) and current (1201, DL-Instruments) were utilized to acquire the applied voltage  $V_{ds}$  and sample current  $I_{ds}$  while a multipurpose data acquisition card (PXI-6251, National-Instruments) served as channel-wise analog-digital converter. Control software and voltage sweep procedures were written by Assoc. Prof. Dr. Jussi Toppari. As a precautionary measure, a current divider (1:100) was implemented in front of the voltage amplifier to avoid overloading of the device input due to the steep rise of currents in thin-film tunneling junctions.

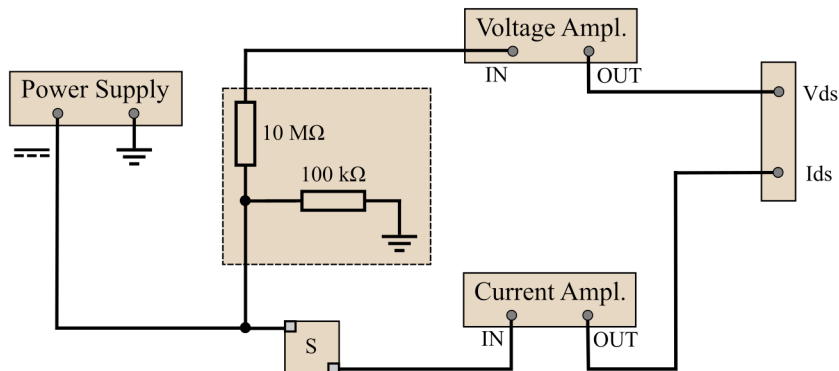


FIGURE 4.11: Schematic of the setup for I-V-measurements. The implemented current divider served as protection of the amplifier input due to the limited dynamic range of the device. Voltages  $V_{ds}$  and currents  $I_{ds}$  are logged by a high precision data acquisition card. The DC voltage ( $\equiv$ ) was fed by a laboratory power supply.

For hetero-junctions, i.e. junctions with different electrode materials, the band energy diagram exhibits an asymmetry due to the difference in the material work functions. Thus, in contrast to homo-junctions which are energetically symmetric, a forward and backward direction can be distinguished inherently since the potential barrier height for charge carrier tunneling differs with the direction of the applied electric field [191]. An exemplary current voltage (I-V) curve of this effect is shown in Fig. 4.12 (a). By forward biasing ( $V_g > 0$ ), the MOS-structure is driven into the accumulation state (b) with electrons being transported from the semiconductor to the semiconductor-insulator interface. This application of a sample bias across the junction is a non-equilibrium



state. Thus, the Fermi level of the positive electrode is shifted from its original energy  $E_{f0}$  to  $E_{fm}$ . The resulting electrical field inside the tunneling stack is compensated by the insulator and semiconductor, while the insulators electric field is interpreted as a deformation of the barrier energy and the semiconductor field by a band bending  $\varphi_s$ . Given by the degenerated doping concentration of the silicon substrate, energy losses in the semiconductor are considered marginal compared to the electric field inside the tunneling barrier [44].

For reverse biasing ( $V_g < 0$ ) the energy diagram goes into depletion and the energy diagram is shifted inversely (Fig. B.4a). Hence, the initial potential barrier faced by electrons for each sample polarity is given by the difference in the material work functions, i.e. at the metal-insulator  $\phi_{Bm}$  or the semiconductor-insulator  $\phi_{Bs}$  interface [46]. With this, substantially different tunneling rates are expected by changing of the polarity, as visible in the I-V curve. Note, that for insulators and semiconductors, work functions in the classical understanding are not given, but the electron affinity  $\chi$ . At larger negative bias, the junction would switch into inversion state, which is not considered here due to the high semiconductor doping of the fabricated stacks.

As soon as the applied potential suffices and very thin films are implemented, conduction mechanisms occur for classically forbidden charge carrier transitions. A large variety of classifications is described in literature [192]. Distinction is mostly done by the charge carrier transition such as electron valence band (EVB) or conduction band tunneling (ECB) and hole valence band tunneling (HVB) (Fig.B.4a). Here, only the most likely models will be introduced, which are dominantly ECB processes for the fabricated junctions in accumulation state. Thus, the distinction by developed models for the description of dominant conduction mechanisms is a more suitable approach.

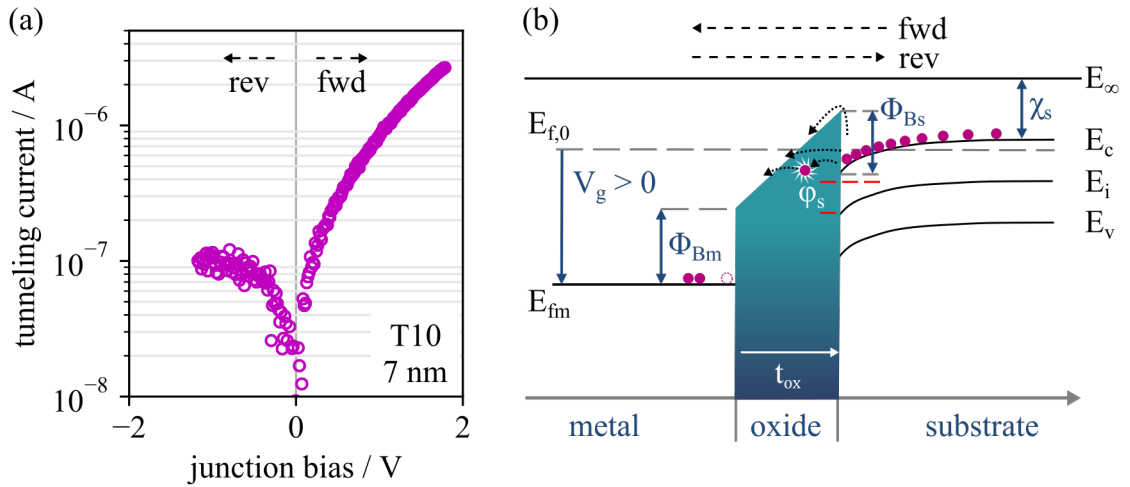


FIGURE 4.12: (a) I-V curve of a T10-type junction with 7 nm  $\text{Al}_2\text{O}_3$  in forward (fwd) and reverse (rev) bias. (b) Energy band diagram of such a MOS structure in accumulation state (fwd bias) with the potential barrier. The barrier is defined by the oxide with thickness  $t_{ox}$  and the work function differences between the oxide and adjacent materials, i.e.  $\Phi_{Bm}$  on the metal and  $\Phi_{Bs}$  on the semiconductor interface. Tunneling rates are changed by deformation of the barrier, band bending  $\varphi_s$  and fermi energy level shifts  $E_{fm} - E_{f0}$  which are controlled by application of a sample bias  $V_g$ .

In Fig. 4.13 the experimentally obtained current density vs. voltage (J-V) curve of a tunneling junction with a 10 nm SiO<sub>2</sub> tunneling barrier is depicted. Two regions can be discriminated. The low field interval of region I and the regime of high internal electric fields ( $E > 1 \text{ MV}(\text{cm})^{-1}$ ) as in region II upwards. In the latter, Fowler-Nordheim tunneling (FN) is dominating the occurring conduction mechanisms, since the deformation of the barrier is strong enough to form a triangular potential profile. This results in an energetically smaller effective oxide thickness and thereby an increased tunneling rate.

Extraction of tunneling barrier information from the Fowler-Nordheim current  $I_{\text{FN}}$  is a straight forward, well established method [193, 194]. The first equation as given in Eq. 4.4 with its subterms states that a mono-exponential dependency is expected. Thus by plotting  $J/E^2$  vs.  $1/E$ , the so called Fowler-Nordheim plot is obtained (as shown in Fig. B.5). A linear regression was used to determine the slope and intercept of the function [195, 196]. From these, the barrier height  $\phi_{\text{B}}$  was calculated directly as given in the Script C.3. Together with the known material parameters or literature values as given in Tab. 4.14, the barrier height for tunneling from the cathode into the oxide was determined to  $\phi_{\text{B}} = 2.94 \text{ eV}$  which is in good agreement with the expected value of 3.1 eV [197].

$$I_{\text{FN}} = SK_1 E^2 \exp\left(-\frac{K_2}{E}\right) \quad (4.4a)$$

$$K_1 = \frac{m_0}{8\pi h m_{\text{ox}}^*} \frac{q^3}{\phi_{\text{B}}} \quad (4.4b)$$

$$K_2 = \frac{16\pi m_{\text{ox}}^*}{3h^2} \frac{\phi_{\text{B}}^{3/2}}{q} \quad (4.4c)$$

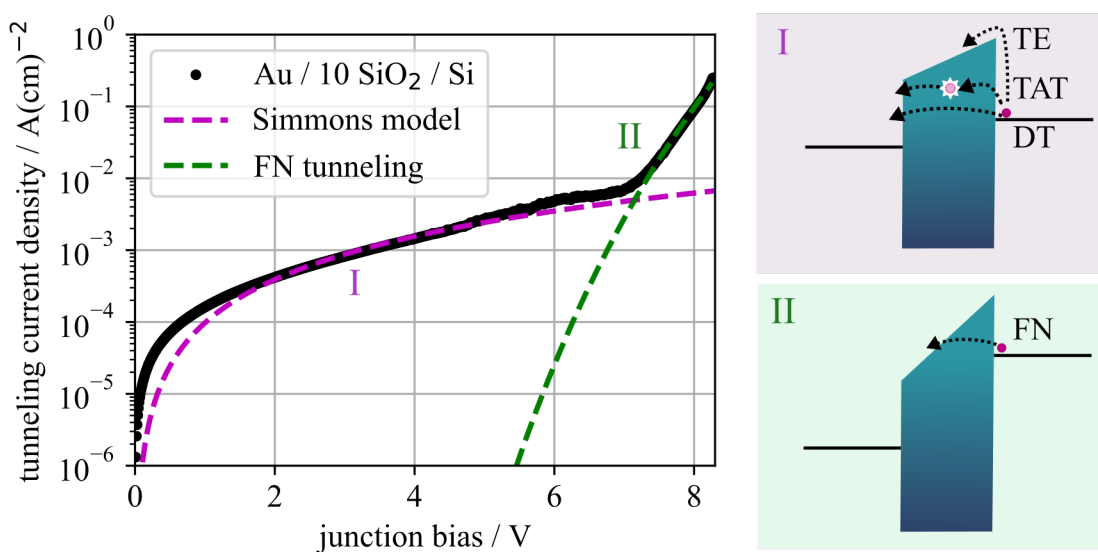


FIGURE 4.13: I-V characteristic of a LETJ with a 10 nm SiO<sub>2</sub> tunneling oxide. Two different regimes of low (I) and high (II) electric field applied to the oxide can be distinguished. Region I is dominated by mechanisms such as direct tunneling (DT), thermionic emission (TE) or trap-assisted tunneling (TAT). Region II is dominated by Fowler-Nordheim tunneling (FN). The dashed lines indicate calculated curves for DT (purple) and FN (green) tunneling for such a junction, respectively.

However, the high electric fields necessary for FN tunneling induce high stress in the oxide, which often leads to electrical breakdown, introduction of defects, leakage pathways, and ion diffusion. All these processes decrease the long-term stability at these operation conditions.

By implementation of few nm thick films, tunneling processes at lower electric fields, such as in region I of Fig. 4.13, dominate which induce less stress at the interfaces and in the insulator. Conduction mechanisms in this regime are superpositioned as follows; Direct tunneling (DT) describes tunneling through the whole barrier thickness  $t_{\text{ox}}$  and is dominant for very thin oxides. Thermionic emission (TE) is a transition over the barrier by thermal excitation and becomes relevant for low tunneling barriers. Trap-assisted tunneling (TAT) and Frenkel-Poole emission (FP) are mechanisms, in which the total oxide thickness is degraded by impurities or defects which introduce discrete energy levels inside the insulator band gap. This allows tunneling in stepwise or hopping-like transitions.

In practice, mostly a combination of all mechanisms is present, especially for tunneling junctions with large active areas as utilized in this work. For this reason, a semi-empirical model for the intermediate voltage range ( $V_g \approx \phi/e$ ) as developed by Simmons [198] was chosen to fit the data instead of the idealized, analytic extensions for direct tunneling to account for these mixed conduction mechanisms. Along with the previously extracted potential barrier by the FN-plot, the curve in Fig. 4.13 (I) was calculated to verify the validity of this model. The model expression is a third order expansion of the tunneling model  $I_{\text{inter}}$  as given in Eq. 4.5.

$$I_{\text{inter}} = S \left( \frac{q}{h} \right)^2 \sqrt{\frac{C_1 \phi_B}{t_{\text{ox}}}} \cdot \exp \left( \frac{2t_{\text{ox}} \sqrt{C_1 \phi_B}}{\hbar} \right) \cdot (V_g + C_2 + C_3) \quad (4.5)$$

with the subterms in Eqs. 4.6, the effective mass  $m_{\text{ox}}^*$ , electron rest mass  $m_0$ , elementary charge  $q$ , Planck constant  $h$ , junction area  $S$ , barrier thickness  $t_{\text{ox}}$ , barrier height  $\phi_B$  and applied bias  $V_g$ :

$$C_1 = 2m_{\text{ox}}^* m_0 q, \quad (4.6a)$$

$$C_2 = \frac{t_{\text{ox}}}{24\hbar} \sqrt{\frac{C_1 \phi_B^3}{q^2}} V_g^2, \quad (4.6b)$$

$$C_3 = \frac{t_{\text{ox}}^2 C_1}{12\hbar^2 \phi_B} V_g^3. \quad (4.6c)$$

An implementation of this model for fitting to experimental data is appended as Python function in Script C.4. The applicability of the described mixed model approach is an element of the following sections. Good agreement was found for assessment the tunneling barrier without the need of characterizations at high internal fields.

TABLE 4.14: Parameter used for calculation of I-V characteristics and extraction of information on the potential barrier in MIS-structures [44, 151, 199].

Parameter	Value	Parameter	Value
$\chi_{\text{Si}}$	4.05 eV	$\phi_{\text{Au}}$	5.1 eV
$\chi_{\text{SiO}_2}$	0.9 eV	$\chi_{\text{Al}_2\text{O}_3}$	1.8 eV
$N_{\text{D}}$	$2 \cdot 10^{19} \text{ cm}^{-3}$	$n_i$	$1.45 \cdot 10^{10} \text{ cm}^{-3}$
$T$	293 K	$m_{\text{SiO}_2}^*$	$0.33 \cdot m_0$
$m_{\text{Al}_2\text{O}_3}^*$	$0.23 \cdot m_0$		

### 4.3.1 Tunneling Barrier Estimation

The results for the dominantly utilized junctions with  $\text{Al}_2\text{O}_3$  oxide of different thickness are shown in Fig. 4.15. As shown, by increasing the oxide thickness from 2 up to 10 nm, a substantial decrease of the tunneling current is observable. For junctions with 2 nm, the current densities were high enough to cause electrical breakdown even at low voltages. This might be attributed to defects, leakages and residual surface roughness that prevented a full enclosure of the oxide film on the silicon substrate. Thus, no valid information on the tunneling barrier were extracted since the optimization algorithm failed to converge in the given low-voltage datasets.

For junctions with expected oxides of 5, 7 and 10 nm, the extracted barrier heights ranged from 2.0 to 2.6 eV. The ideal value of the tunneling barrier is given by  $\chi_{\text{Si}} - \chi_{\text{Al}_2\text{O}_3} = 2.2 \text{ eV}$  meaning that the obtained value of 2.6 eV for 5 nm is overestimated. Since real junctions in general suffer from parasitic interfacial charges, defects, and inhomogeneities

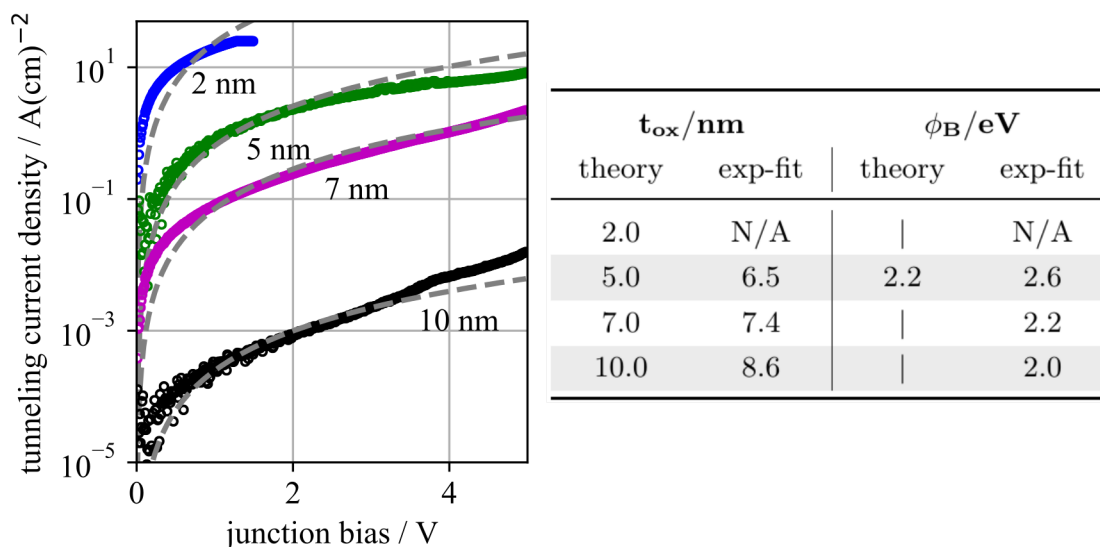


FIGURE 4.15: I-V curves of junctions with  $\text{Al}_2\text{O}_3$  oxide with varying thickness between 2, 5, 7 and 10 nm. The grey dashed lines depict fitted results according to the empirical model for direct tunneling, respectively. Calculated values for the barrier thickness  $t_{\text{ox}}$  and height  $\phi_{\text{B}}$  are listed in the table righthandside. The barrier height is only dependent on the material and thus expected to be constant for all junctions.

in the oxide thickness, the barrier height should be lower than that for an ideal junction. This is especially important for the large scale tunneling junctions fabricated in this thesis, since the probability of defects in the junction is also increased with the junction area. Thus, overestimation of the junction quality is introduced by the model to some extent, yet it still enabled validation of the underlying conduction mechanism.

LETJ samples with the same oxide thickness, but different junction sizes should exhibit identical potential barrier heights. A set of measurements was performed on junctions of type T100, A, B, C and D with 7 nm  $\text{Al}_2\text{O}_3$  as depicted in Fig. 4.16. The reduced Fowler-Nordheim depiction ( $I/V_g^2$  vs.  $1/V_g$ ) in (a) represents a simple method to evaluate the threshold voltage  $V_t$  from which the conduction mechanism is dominated by tunneling effects and was found to be  $1.2 \pm 0.3$  V. The linear section of the depiction is shown in (b) in which the curves exhibit the expected offset while the slope is similar. Utilizing the tunneling model, the barrier height was determined to be  $\phi_B = 2.15 \pm 0.1$  eV and the thickness to be  $t_{\text{ox}} = 7.5 \pm 0.2$  nm.

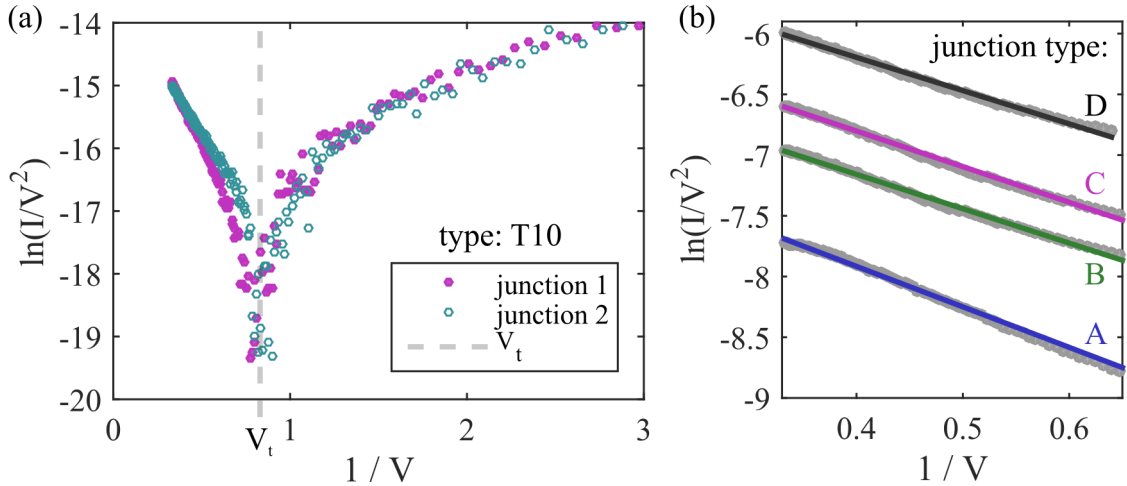


FIGURE 4.16: Fowler-Nordheim plots of two T10-junctions. (a) The dashed line indicates the threshold bias at which the conduction mechanism is dominated by tunneling (left side from  $V_t$ ). By linear regression of the data correlated to tunneling the barrier parameter can be extracted. (b) FN plot (tunneling domain) for junctions of the types A,B,C and D with different sizes.

### 4.3.2 Determination of Sample Reproducibility

In addition to the previously discussed methods, another approach for fast assessment of the sample and chip repeatability was used. As shown in Fig. 4.17 (a), junction currents shift accordingly to changes in the oxide thickness (color) and junction area (linestyle). By calculating the tunneling current density, dependencies on the junction area are normalized and the oxides are clearly discriminated. In case of the chip reproducibility, junctions at several positions along the chip were measured and the insulator film homogeneity was verified over the whole chip. Furthermore, full functionality of the junction areas were verified simultaneously, since parasitic influences would scale differently with the varying junction geometries.

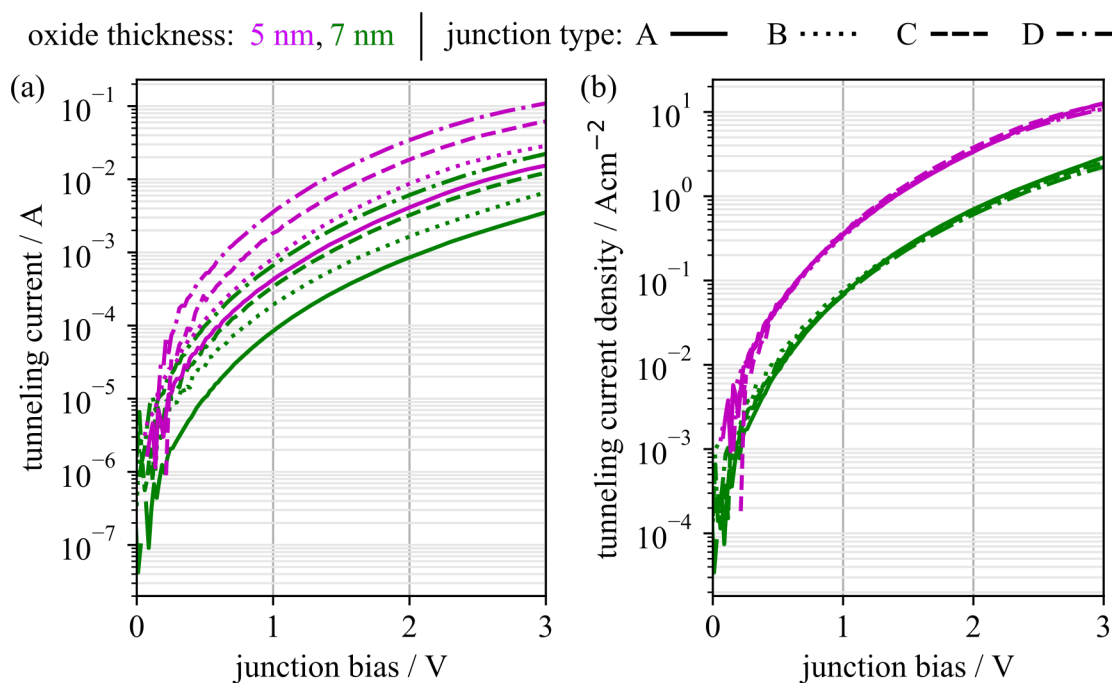


FIGURE 4.17: (a) IV-Characteristics of LETJ samples with an oxide thickness of 5 (purple) and 7 nm (green) for four different junction sizes each (linestyle). (b) Tunneling current densities for the same LETJ. The overlap of the experimental values by the area normalization verifies the film homogeneity and full-area functionality of the individual junctions over the whole chip.

Despite the reasonably good agreement with theory, the main cause for failures in large scale tunneling junctions are defects from pinholes in the insulator and hot spot effects due to residual surface roughness [200]. In the course of this thesis, samples that exhibited high drifts, electrical breakdown, or deviating characteristics were discarded. This was necessary for approximately 40% of all tested junctions, while the fraction of non-functional samples increased with the LETJ size, up to 80% for type D.

Among the fabricated samples in the course of this work, it was found that  $\text{Al}_2\text{O}_3$  films of 5 to 7 nm exhibited the most stable and reproducible results. They exhibited well defined properties over the whole chip layout, in which especially the small junctions T10, T100 and A proved to be well functioning. Larger junctions, such as B, C and D-type emitted steadily but to were more likely damaged by electrical breakdown during operation.

To improve the mentioned performance of the  $\text{Al}_2\text{O}_3$  films, thermal annealing would be a recommended option either during fabrication or as a post-processing step. The overall LETJ functionality might also be improved by exchanging the initial fabrication step of dry-thermal substrate oxidation by direct deposition of the ALD-layer on the non-etched, polished silicon substrate and only subsequent deposition of the leakage protection layer. That way, the high surface quality of a wafer would be fully utilized, while only a limited risk of parasitic lateral channels along the material interfaces would remain. Another improvement might be to experiment with the semiconductor doping concentration and doping type to tailor the I-V curves to be optimized for LETJ samples.

## 4.4 Impedance Spectroscopy

Per definition, electrical impedance  $Z$  is the effective opposition of an electric circuit or component to alternating current (AC), arising from the combined effects of ohmic resistance  $R$  and reactance  $X$  as shown on the lefthandside of Fig.4.18. In contrast to purely ohmic resistivity, it can account for phase shifted and frequency dependent components such as capacitors and inductors. The overall impedance as a function of the input signal frequency  $f$  is given by the summed up interplay of all components. This renders impedance spectroscopy a mighty tool for analysis of electrical circuitry, given that the type of contributing elements is known. Alternatively to the cartesian indication of the impedance derived from the complex plane, polar description is often used by defining the impedance magnitude  $|Z|$  and phase angle  $\vartheta$  as given in Eq.4.7 and shown in Fig.4.18 (a). Both notations are established depending on the field of application.

$$Z = |Z|e^{i\vartheta} = R + iX \quad (4.7)$$

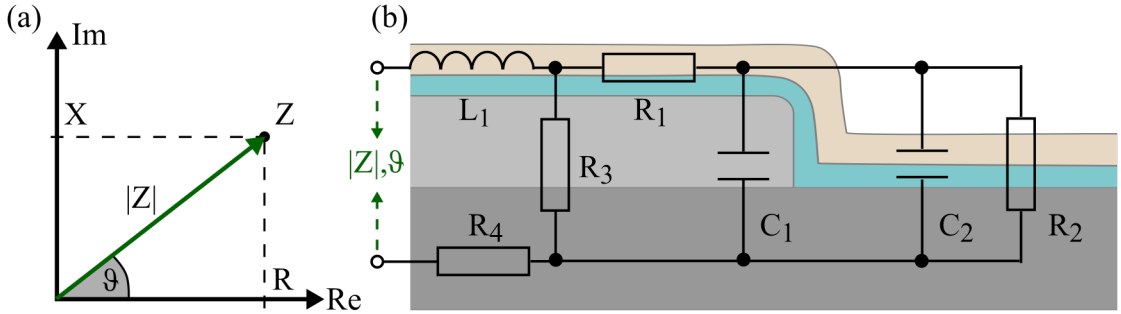


FIGURE 4.18: (a) The total impedance  $Z$  is given by the linear combination of resistance  $R$  and reactance  $X$ . (b) Equivalent circuit of the LETJ samples with all dominant components as given by the material stack and junction geometry. The individual resistive  $R_j$ , inductive  $L_j$  and capacitive  $C_j$  components contribute to the total impedance  $Z$  with the measurable magnitude  $|Z|$ .

Inherent by the design of the fabricated LETJ samples, only the equations to describe the three fundamental impedances of resistors  $Z_R$ , inductors  $Z_L$  and capacitors  $Z_C$  at frequencies  $f$  as given in Eq. 4.8 were needed to reconstruct an equivalent circuit as depicted in Fig. 4.18 (b).

$$Z_R = R \quad Z_L = i2\pi fL \quad Z_C = \frac{1}{i2\pi fC} \quad (4.8)$$

As previously stated, the total frequency response of the junction is governed by the summed signals of all contributing elements. Thus, by describing the whole equivalent circuit as a network composed of  $k$  sub-circuits with either  $n$  interlinked series  $Z_s$  or  $m$  parallel connections  $Z_p$ , it is possible to derive the calculated impedance  $Z_{\text{calc}}$  as

summarized in Eqs. 4.9 without violating Kirchhoff's rules:

$$\text{serial: } Z_s = \sum_{j=1}^n Z_j, \quad (4.9a)$$

$$\text{parallel: } \frac{1}{Z_p} = \sum_{j=1}^m \frac{1}{Z_j}, \quad (4.9b)$$

$$\text{total: } Z_{\text{calc}} = \sum_{j=1}^k (Z_{s,j} \vee Z_{p,j}). \quad (4.9c)$$

Based on the introduced equations (Eqs. 4.7-4.9), a general programming script for the frequency response estimation  $|Z_{\text{calc}}|$  of an arbitrary network of resistors, inductors and capacitors was developed as given in APP. C.5, in which the given script contains the equivalent circuit of the described LETJ sample as an example already. If experimentally acquired values  $|Z_{\text{exp}}|$  are available, the script can be utilized to fit the individual component parameters (inductance  $L_j$ , resistivity  $R_j$  and capacitance  $C_j$ ) of the respective equivalent circuit to minimize the residual  $Y$  at  $l$  frequencies according to Eq. 4.10 by deploying the limited-memory Broyden-Fletcher-Goldfarb-Shanno optimization algorithm with boundary conditions (L-BFGS-B) [201].

$$Y = \sum_{j=1}^l \left( |Z_j^{\text{calc}}| - |Z_j^{\text{exp}}| \right)^2 \quad (4.10)$$

In the specific case of the fabricated junctions, seven circuit components had to be described, in which the determination of the tunneling barrier thickness  $t_{\text{ox}2}$  was the main parameter of interest as extracted from the capacitor  $C_2$ .

The following assumptions were made to approximate initial guesses for some of the parameters and to confine the boundary conditions to physically plausible values:

- **L<sub>1</sub>** describes the inductivity of the setup coaxial cables [202] and was fixed to  $L_1 \approx 10^{-7}$  H as estimated by  $L = (\mu_0 \mu_r l) / (2\pi) \cdot \ln(D/d)$  with the cable length  $l$  and the inner and outer core diameter,  $d$  and  $D$ .
- **R<sub>1</sub>** expresses the combined contact and film resistance of the top electrode. The gold film resistance was calculated by  $R = (\rho l) / A$  and the whole electrode geometry ( $\rho = 2.21 \cdot 10^{-8}$  Ωm with  $l = 3.5$  mm and  $A = 13.5 \cdot 10^{-6}$  mm<sup>2</sup>) to  $R_1 = 5.7$  Ω. Due to the variability of the contact resistance from measurement to measurement  $R_1$  was limited to  $[0, 5000]$  Ω nonetheless.
- **R<sub>2</sub>** represents the tunneling resistance of the junction and was fixed to the experimentally determined value at the lowest frequency of the measurement as initial value and set to range freely between  $[0, \infty]$  for the optimization process.
- **R<sub>3</sub>** corresponds to the resistance of the 190 nm leakage protection layer and was usually set to  $\infty$  since it was expected to range in  $[G\Omega, \infty]$ .



- $\mathbf{R}_4$  is the silicon substrate resistance and was handled similar to  $R_1$ . The resistance was calculated as  $R_4 = 7.2 \Omega$  from  $\rho = 6 \cdot 10^{-5} \Omega\text{m}$  as given by the doping concentration. With the maximum chip edge length  $l = 15 \text{ mm}$  and contact area of a type A junction  $S = 0.125 \text{ mm}^2$  to assess the maximal resistance residing from the substrate. See Fig. B.6 for experimental references.
- $\mathbf{C}_1$  describes the capacitance of the  $\text{SiO}_2$  leakage protection layer and was estimated to the value of a plate capacitor by  $C = (\epsilon_0 \epsilon_r S) / t_{\text{ox}1}$  with  $\epsilon_r = 3.9$ ,  $S = 2.6 \text{ mm}^2$  and  $d = 190 \text{ nm}$  to  $C_1^{\text{init}} = 475 \text{ pF}$  with the limits  $[0.8C_1^{\text{init}}, 1.2C_1^{\text{init}}]$ .
- $\mathbf{C}_2$  as the dominating capacitance defined by the tunneling area was estimated similarly to  $C_1$  for the initial guess  $C_2^{\text{init}}$  with the respective parameters for  $\text{Al}_2\text{O}_3$  oxides dielectric constant  $\epsilon_r = 9.6$ , the thickness  $t_{\text{ox}2}$  and area  $S$  for each junction type but left with large tolerances in the boundaries to be determined within  $[0.8C_2^{\text{init}}, 1.2C_2^{\text{init}}]$ .

The experimental setup as used in this work and schematically shown in Fig. 4.19 is situated at the Nanoscience Center, Jyväskylä in the laboratories of Assoc. Prof. Dr. Jussi Toppari to whom I am very grateful for giving me the opportunity to use and assemble his equipment independently during a one-month research stay while giving me access to all of his self-developed LabVIEW measurement routines.

The core components of this setup are the synchronized Lock-In Amplifiers (SR830, SRS) which provide the AC signal (SINE OUT  $\pm 30 \text{ mV}$ ) and enable the detection of the frequency response of the connected sample S by tracking the complex valued, differential current  $dI$  and voltage  $dV$  signals, respectively. To enable measurements of LETJ chips at different tunneling conditions, mixed inputs with overlapping AC signals

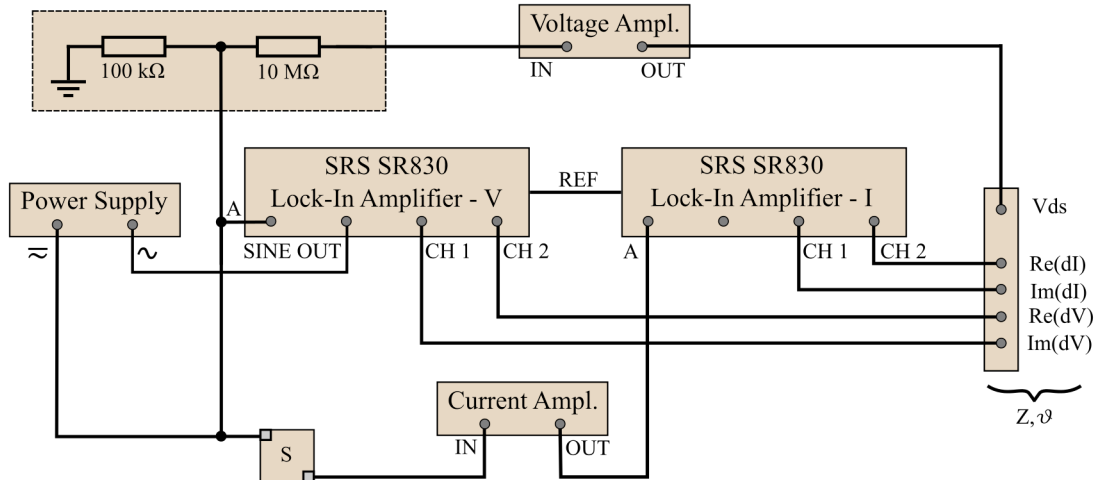


FIGURE 4.19: Wiring diagram of the setup for impedance measurements. The AC/DC mixed input signal ( $\approx$ ) was fed to the sample S by two synchronized Lock-In amplifiers overlaid which detect the differential signals of the complex valued current  $dI$  and voltage  $dV$ . All outbound, acquired signals are amplified by current or voltage amplifiers and logged by a in-house developed LabVIEW routine via a high resolution data acquisition card.

and constant bias (DC) were provided by an in house built power supply . A current preamplifier (1211, DL-Instruments) was interposed between sample and  $dI$ -detection to account for the very low signals, especially at  $DC = 0\text{ V}$ , in which the gain factor was selected individually for each connected tunneling junction. Logging of the junction bias  $V_g$  was enabled by a voltage amplifier (1201, DL-Instruments) with a current divider (ratio 100:1) in front of the input to protect it from overload in its most sensitive configurations. Since the whole setup was located in an electromagnetically shielded room (ETS Euroshield), all signals were transmitted out of the enclosure by opto-coupled wirings which were then reconnected to a data acquisition card (PXI-6251, National Instruments). Note, that the reliability of obtained information from known circuitry by this technique also depends on the complexity of the inaccessible underlying sub-circuits ('black-boxes') and the available number of access points at different positions for probing [203].

Depiction of the frequency response is usually done in one of three established methods, i.e. Nyquist plots ( $X \rightarrow f(R)$ ), Nichols plots (similar to Nyquist but in polar instead of cartesian coordinates), and Bode diagrams ( $\log_{10}(|Z|) \rightarrow \log_{10}(f(\omega))$  and  $\vartheta \rightarrow \log_{10}(f(\omega))$ ). Despite being the more frequently used Nyquist plots, double-logarithmic scaling of the data would be necessary for proper depiction which is neither common nor an intuitive measure. Thus, Bode diagrams were chosen for plotting of acquired LETJ data since the investigated parameters span several orders of magnitude at different tunneling conditions.

#### 4.4.1 Junctions of different Size

In Fig. 4.20 results of experiments on tunneling junctions at bias  $V_g = 0\text{ V}$  with different junction areas are shown and the corresponding extracted parameters are listed in Tab. 4.21. Two different sections of the plot can be distinguished. The low frequency area  $< 10\text{ Hz}$  runs into a resistance plateau which can be assigned to the dominating effect of the tunneling resistance of the junction, since the phase plot alters accordingly to low angles. At higher frequencies ( $10^2 - 10^4\text{ Hz}$ ), the differences in the capacitances are manifested in the offset between the graphs at highest slope.

Both fitted capacitances  $C_1$  and  $C_2$  agree well with the calculated results with a deviation of less than 3% for the  $\text{SiO}_2$  protection layer capacitance  $C_1$ . The resistances  $R_1$  and  $R_4$  were combined due to their low values which are dominated by the additional contact resistance. All other parameters were evaluated for plausibility, whereas the inductivity  $L_1$  seemed to play no essential role in the fitting algorithm since the initial guess was not altered in most cases. This is in agreement with the negligible small inductance introduced by the coaxial wirings for this frequency regime.

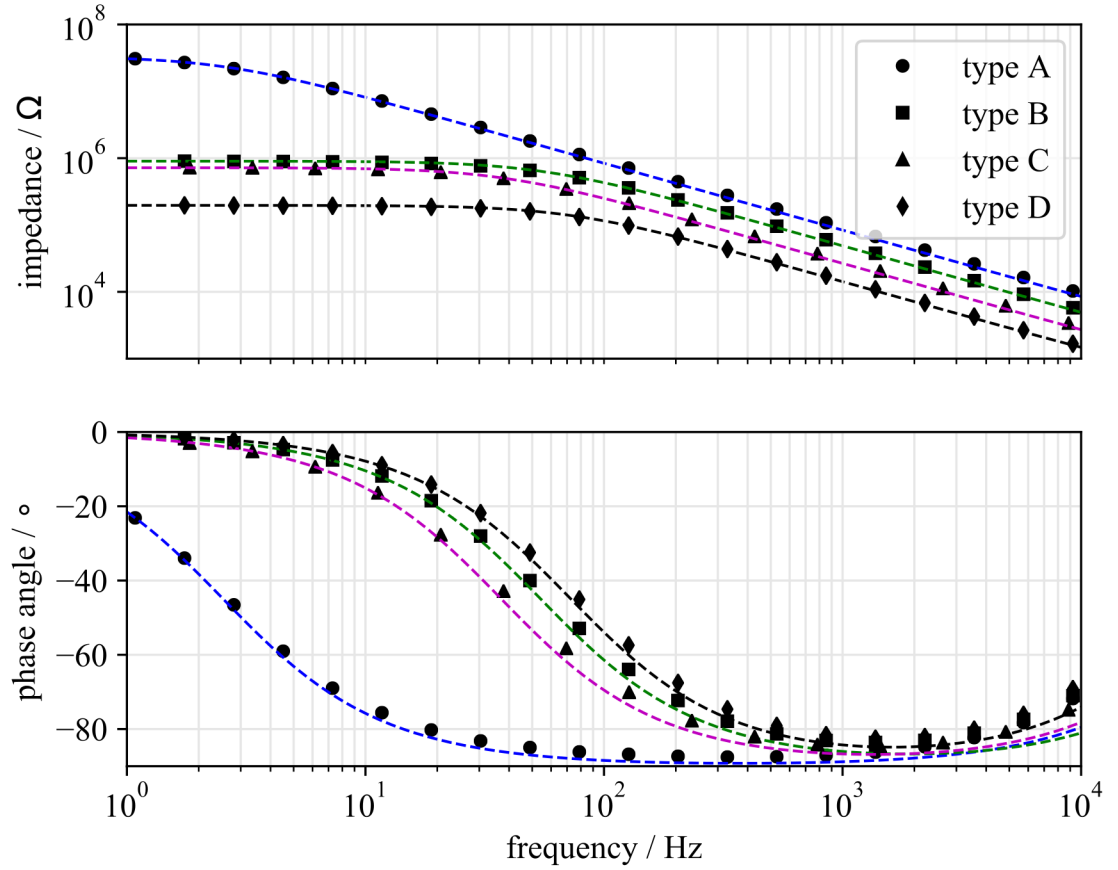


FIGURE 4.20: Bode diagram of the LETJ samples with the impedance amplitude (top) and phase (bottom) for different junction areas with the fitted model (dashed lines) as given by the equivalent circuit. Starting from A, the area doubles for each junction (A – 0.125 mm<sup>2</sup>; B – 0.25 mm<sup>2</sup>; C – 0.5 mm<sup>2</sup>; D – 1 mm<sup>2</sup>).

The determined capacitances of all performed measurements on chips of the type 30 nm Au / 7 nm Al<sub>2</sub>O<sub>3</sub> / Si are depicted in Fig. 4.22. Since the area doubles between each junction type, the y-axis was normalized to the capacitance of the smallest junction and plotted on log<sub>2</sub>-basis. With this, the gridlines depict the expected capacitances of the other junctions. Repeated measurements of  $\#_{\text{samples}}$  enabled determination of the standard deviation.

A systematic offset  $\Delta C$  in the experimentally determined capacities  $C_{\text{exp}}$  from the calculated ideal capacitor values  $C_{\text{calc}}$  can be seen in Fig. 4.22 right. This can be assigned to either a slightly thicker tunneling oxide or edge effects at the transition regime of the

TABLE 4.21: All parameters of the equivalent circuit as determined from the least-square fitted functions to experimental data.

Junction	$L_1$ / nH	$R_1 + R_4$ / kΩ	$R_2$ / kΩ	$R_3$ / Ω	$C_1$ / pF	$C_2$ / nF
type A	100	1.55	33103	∞	471	1.43
type B	100	0.74	900	∞	469	2.79
type C	100	0.55	719	∞	468	5.48
type D	89	0.39	196	∞	467	10.7

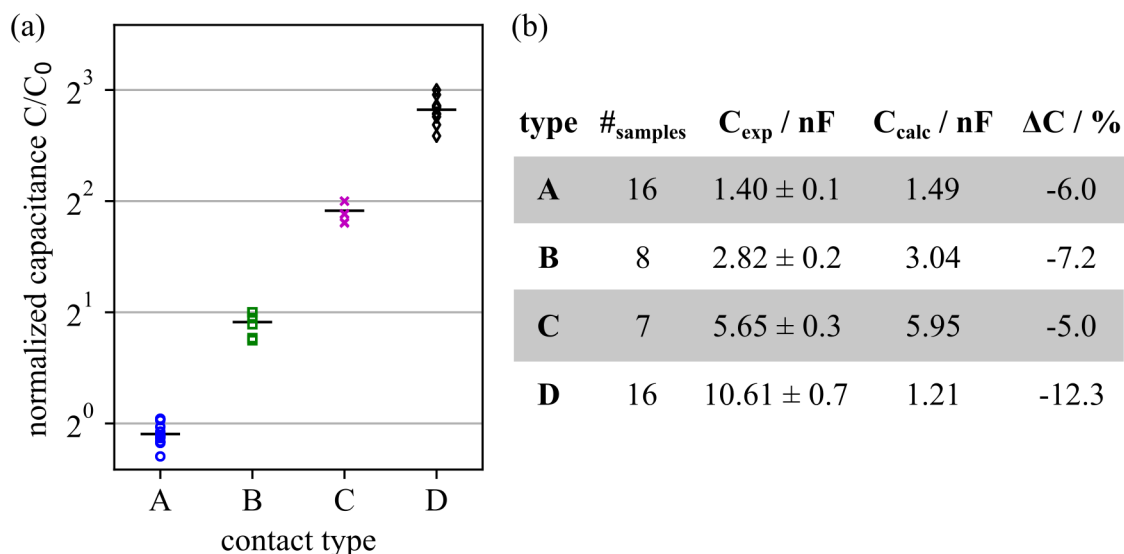


FIGURE 4.22: (a) Determined capacitances  $C$  for the different junction types normalized to the expected capacitance of an ideal type A junction  $C_0$ . The area dependency is clearly visible while having a systematic offset to the expected values (given by the grid). (b) Theoretical values of an ideal capacitor with same dimension  $C_{\text{calc}}$ , extracted experimental capacitances  $C_{\text{exp}}$  and their deviation  $\Delta C$ .

tunneling area towards the  $\text{SiO}_2$  leakage protection layer. The latter can be ruled out since the capacity offset should inversely scale with the junction edge-to-area ratio in this case, which was not observable in the data.

The oxide thickness of all junctions with the  $\text{Al}_2\text{O}_3$  tunneling barrier in these measurements was expected around 7 nm from fabrication. It has been experimentally determined to be  $t_{\text{ox}} = 7.6 \pm 0.6$  nm. This was derived with the relation of an ideal, plate capacitor as given in Eq. 4.11 from 40 measurements of several chips, in which outliers (7 in total) were programmatically tossed out by the script in APP.C.2 if the fitting algorithm failed to converge and the capacitance deviated more than two times from the median  $\tilde{C}_{\text{exp}}$  of all samples of the same type.

$$t_{\text{ox}} = \varepsilon_0 \varepsilon_r \frac{S}{C_{\text{exp}}} \quad (4.11)$$

#### 4.4.2 Junctions of different Oxide Thickness

Tunneling junctions (size A) with planned oxides of 5 nm and 7 nm  $\text{Al}_2\text{O}_3$  were measured without bias ( $V_g = 0$  V) as shown in Fig. 4.23 and compared with their 7 nm oxide equivalent. In contrast to the previous analysis, an intersection point between the graphs is present which indicates the difference in the tunneling resistance and capacitance of these junctions. The tunneling resistance of the thinner oxide was  $R(5 \text{ nm}) = 375 \text{ k}\Omega$ , being almost two orders of magnitude smaller than the thicker oxide  $R(7 \text{ nm}) = 33 \text{ M}\Omega$ .

Two subsequent experiments for each junction type are plotted to assess the repeatability exhibiting a fairly stable reproducibility in the measurements accuracy. This is an important consideration since the thinner oxides deviated strongly from the theoretical expectations. Junctions with the expected 5 nm oxide layer thickness have been determined from seven independent measurements of different samples to a capacitance of  $C_{\text{exp}} = (6.33 \pm 1.4) \cdot 10^{-9}$  F compared to the calculated value of ( $C_{\text{calc}} = 3.04 \cdot 10^{-9}$  F). With the equation of a plate capacitor (Eq. 4.11), an effective oxide thickness of only  $1.7 \pm 0.4$  nm was estimated.

The phase angle of the 5 nm measurement should drop to  $0^\circ$  asymptotically but showed fluctuations. These large deviations indicate a leakage current impaired tunneling junction [200] or a junction suffering from ion motion or interface and oxide charges. This led to the conclusion, that 5 nm samples suffered from inhomogeneities of the electrical properties of the oxide at constant operation. Measurements on samples with 2 and 10 nm oxide did not result in employable results. Electrical breakdown during operation was the main cause of failure in the determination of the thinner barriers. For the 10 nm pendants, substantial problems in the lock-in process of the low currents and signal phases prevented clean frequency and voltage sweeps by the setup. These findings led to preferential usage of the substantially more stable 7 nm junctions ( $C_{\text{exp}} = 1.40 \pm 0.1 \cdot 10^{-9}$  F) with ( $C_{\text{calc}} = 1.49 \cdot 10^{-9}$  F) as described in the previous section.

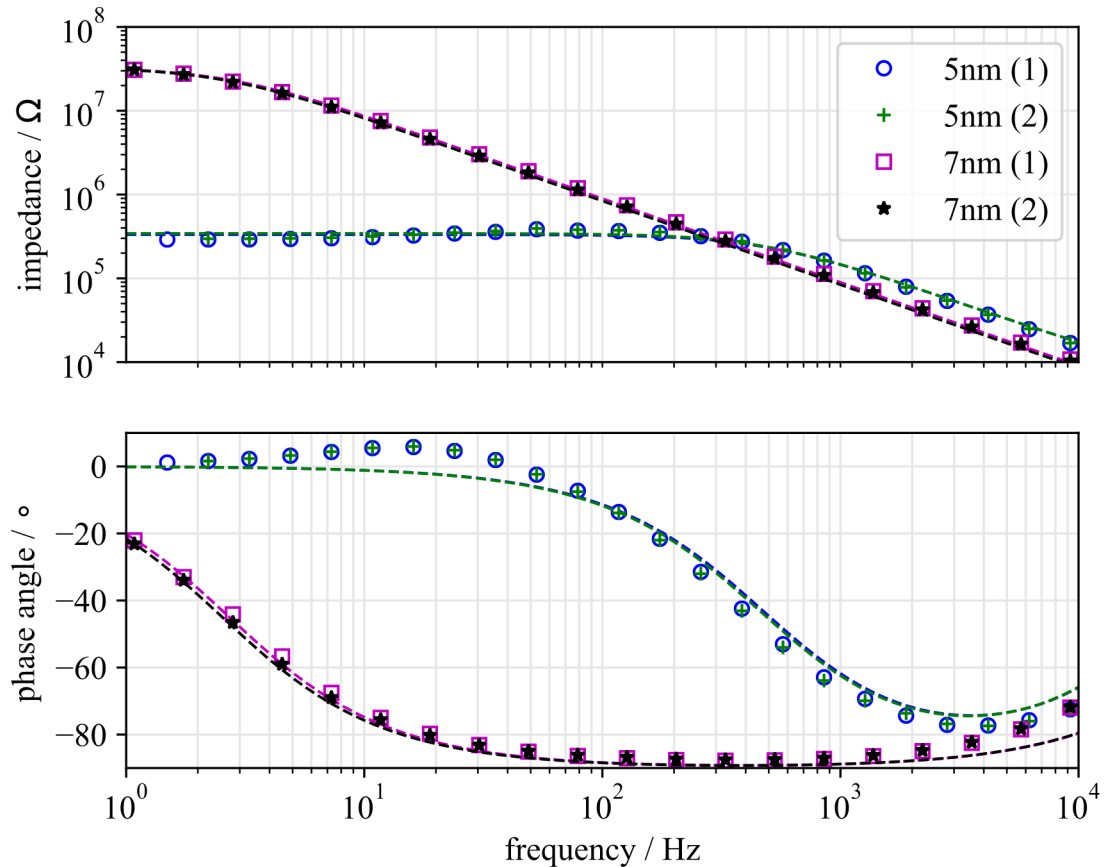


FIGURE 4.23: Bode diagram of the LETJ samples with the impedance amplitude (top) and phase (bottom) for an oxide thickness of 5 and 7 nm with two measurements each.

### 4.4.3 Junctions at different Bias

Analysis of the junction stability at several operation conditions for an individual sample was performed by sweeping the direct current component of the setup between [0,3] V with the AC sinusoidal component still being fixed to 30 mV as shown in Fig. 4.24.

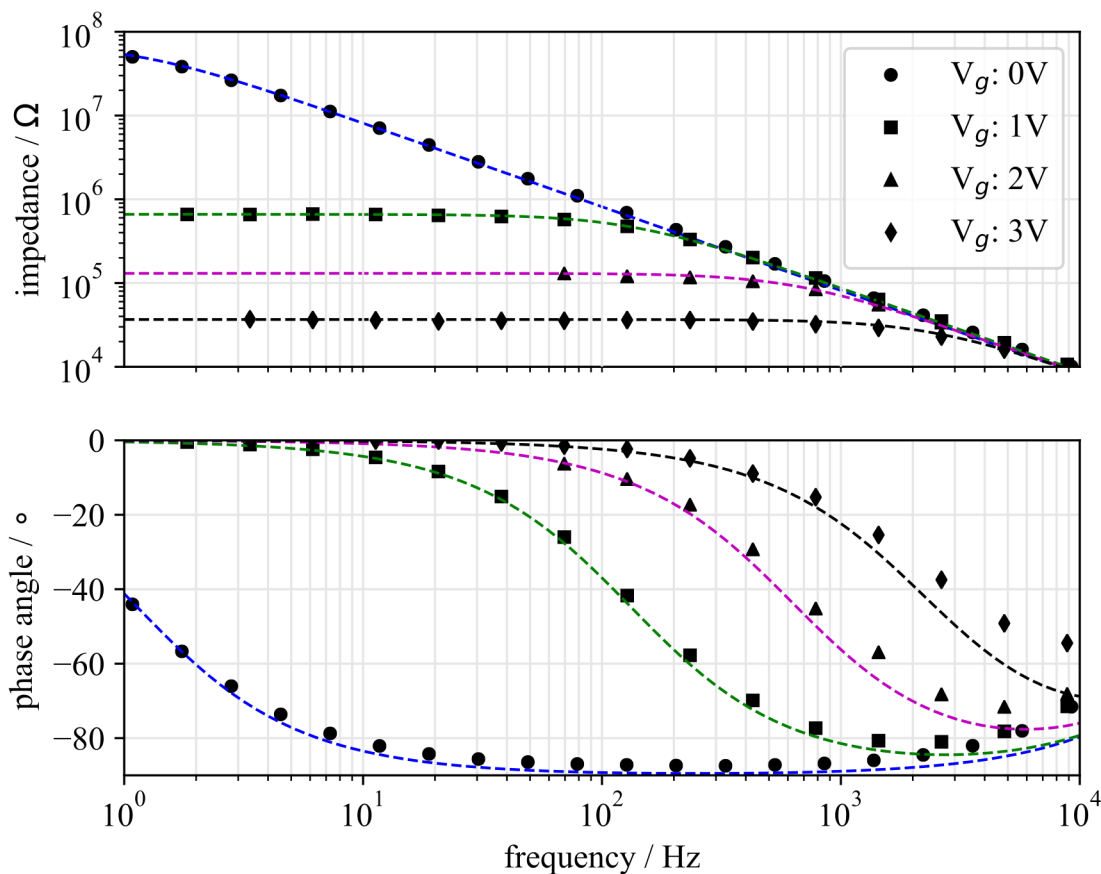


FIGURE 4.24: Bode diagram of the LETJ impedance amplitude (top) and phase (bottom) for a junction (type A) biased at potentials with the respective fits as given by the equivalent circuit.

The tunneling resistance  $R_2$  decreased drastically with increasing bias as expected due to the triangular deformation of the tunneling barrier potential, while the capacitance  $C_2$  stayed constant as given in Tab. 4.25. Measurements of individual graphs at each bias state took approximately 10 min, proving reasonably stable operation conditions for the analyzed voltage range.

TABLE 4.25: Junction (Type A) parameters extracted at different bias.

$V_g / \text{V}$	$L_1 / \mu\text{H}$	$R_1 + R_4 / \text{k}\Omega$	$R_2 / \text{k}\Omega$	$R_3 / \Omega$	$C_1 / \text{pF}$	$C_2 / \text{nF}$
0.0			32642			1.48
1.0	$96 \pm 0.7$	$1.45 \pm 0.13$	660	$\infty$	$467 \pm 7$	1.36
2.0			129			1.45
3.0			35.5			1.46

## 5 | Spectra of Planar Light Emitting Tunneling Junctions

The general emission features of planar light emitting tunneling junctions are known from results from plenty of studies as reviewed in Chapter 3. Here, sets of experiments were performed to cross-check and validate the functionality of the fabricated large scale junctions regarding their light emission characteristics. This included measurements on the emission intensity as a function of the tunneling current and the cut-off frequency given by the applied bias. Additionally, the emission efficiency was tested for both sample polarities as well as the role of the implemented gate electrodes on the emitted spectral bandwidth and center wavelength. The chapter will end on considerations about the emission stability and reproducibility of the designed junctions.

As described before, the excitation of SPPs in a LETJ can be approximated by an oscillating electric dipole with magnitude  $|\mathbf{E}_0|$  situated in the insulating layer of the tunneling junction. This approach is depicted in Fig. 5.1 for a flat junction in air consisting of a 30 nm gold electrode, 10 nm  $\text{Al}_2\text{O}_3$  barrier and a semi-infinite silicon substrate at two

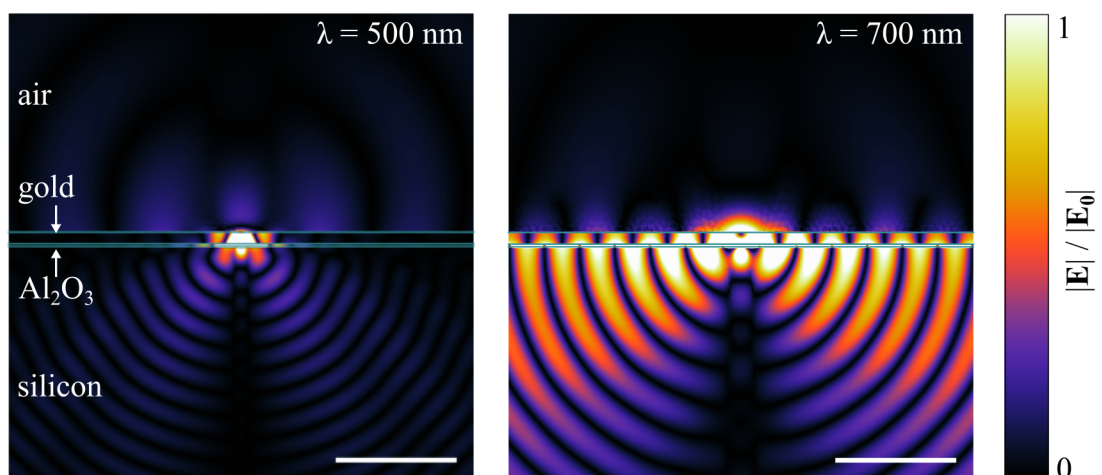


FIGURE 5.1: Electric field  $|\mathbf{E}|/|\mathbf{E}_0|$  of an exemplary LETJ junction (air/Au/ $\text{Al}_2\text{O}_3$ /Si). Excitation of surface plasmons is modeled by an electric dipole oscillating perpendicular to the material boundaries as formulated by Uehara et al. [57] for two wavelengths at 500 nm (left) and 700 nm (right). In both cases SPP are coupled along the boundaries, where a large fraction radiates into the silicon substrate. Scalebars: 300 nm.

dipole wavelengths  $\lambda = 500$  and  $700$  nm. The normalized electric field  $|\mathbf{E}|/|\mathbf{E}_0|$  depicts the propagation of surface plasmons exclusively along the boundaries, in which a fraction of energy is dissipated into each material. For ideal, planar junctions, light emission would be forbidden, since momentum conservation would not allow for decoupling of the excited SPPs. However, in reality, emission is observable due to surface roughness, crystal imperfections, grains and other inhomogeneities. Thus, the emitted light on these underlying junctions depicts scattering on artifacts and could basically be viewed as a measure of non-ideal electrodes and interfaces.

Experiments were done on a self-built optical setup which allowed for the detection of the integral emission from single junction areas individually. Applied bias and tunneling current and the detection spectra were controlled and logged by a self-written software. Details on the utilized equipment and components are depicted and listed in APP. A.1.

## 5.1 Spectral Intensity

The emitted spectral intensity of LETJ is dependent on the tunneling rate. An intuitive interpretation is given, if the tunneling rate is regarded as quantity of charge carriers transiting through the potential barrier. Thus, with higher rates of tunneling electrons, also an increased rate of inelastic tunneling and SPP excitation are expected.

A D-type junction was measured as shown in Fig. 5.2 (a) with an integration time of 60 s per spectrum at the labeled currents. Note, that these junctions had to be driven at the highest possible operation conditions to enable these extensive currents, which were necessary to measure reliable signals.

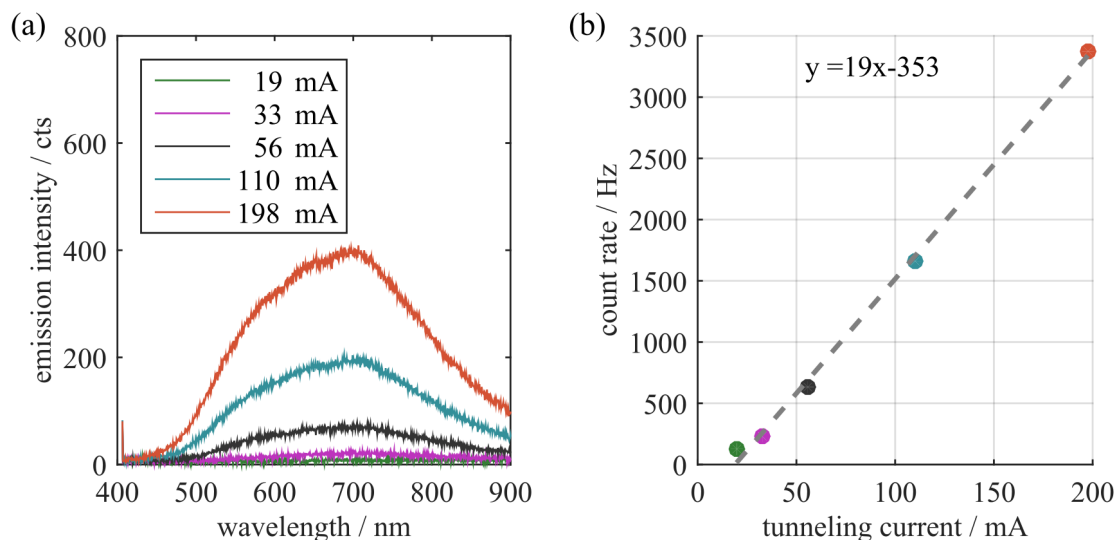


FIGURE 5.2: (a) Emission from a D-type LETJ in dependency of the tunneling current. The broad banded emission can be controlled in terms of intensity by increasing the tunneling current. (b) Total count rate over the spectral range of 450-900 nm. A linear dependency can be approximated and an average emission rate of 19 Hz/mA was determined by the slope of the linear regression (dashed line).



All measured intensities scaled with the respective tunneling current as predicted from theory, by plotting the integrated signal over the spectral range (450-900 nm) as total count rate over the average tunneling current during the measurement. This approach is only valid as long as the selected integration interval coincides with the spectral bandwidth of the junction at that applied bias.

The linear regression has a negative intercept which would represent implausible values, since the intersection with the x-axis does not pass in the origin. This should not be mistaken as threshold current from which emission is possible, but for the setup limit of detection. Hence, the limiting factor here is the low quantum efficiency of the junctions and the losses in the setup. However, the average emission rate  $\gamma_r$  was determined from the slope of a fitted linear approximation to be 19 Hz/mA. This rather low value allows two assumptions. First, the quantum efficiency of the planar LETJ is low, which is explained by the introduced theory and is subject of Chapter 6. Second, the morphological properties of the thin films are very homogeneous and the intrinsic surface roughness is low enough to minimize emission by scattering artifacts. AFM imaging was used to measure the electrode surface roughness. A value of  $\sigma_{\text{RMS}} = 0.9$  nm was determined, as taken from Fig. B.7, which underlines the assumption. Thus, a low emission efficiency of a planar junction also depicts a high quality of the deposited films.

## 5.2 Cut-off Frequency

LETJ with an applied bias exhibit a broad spectral bandwidth. Emission at low frequencies is enabled since the QSN covers several orders of magnitude of different frequencies arising from the tunneling current with varying emission efficiencies. When pushing into the regime of visible radiation, the highest emittable frequency is limited by several quantities as follows:

**Applied bias**  $V_g$  defines the maximal kinetic energy of the electrons transiting through the potential barrier. Thus, the shortest emittable wavelength  $\lambda_c$  from radiation driven by inelastic tunneling is given by  $\lambda_c = hcq|V_g|^{-1}$ .

**Non-radiative processes** are dominating at higher bias, such as intraband oder indirect interband transitions resulting in absorbance and loss effects in the media. These transitions are material characteristics and exhibit varying onsets for the implemented materials in the tunneling stack.

**Breakthrough voltage** of the implemented tunneling barrier is an essential parameter in the electrical solidity of the junction. For inorganic barriers it is seldomly a limiting factor, while it has to be considered for organic potential barriers.

The latter two are intrinsic material properties, whereas the first is an accessible variable for parametric sweeps. Experiments on  $\lambda_c$  were performed again on D-type junctions of the chip. The largest junction type was chosen since it exhibited the highest risk to be non-functional. Hence, they were regarded as plausible representation for all samples

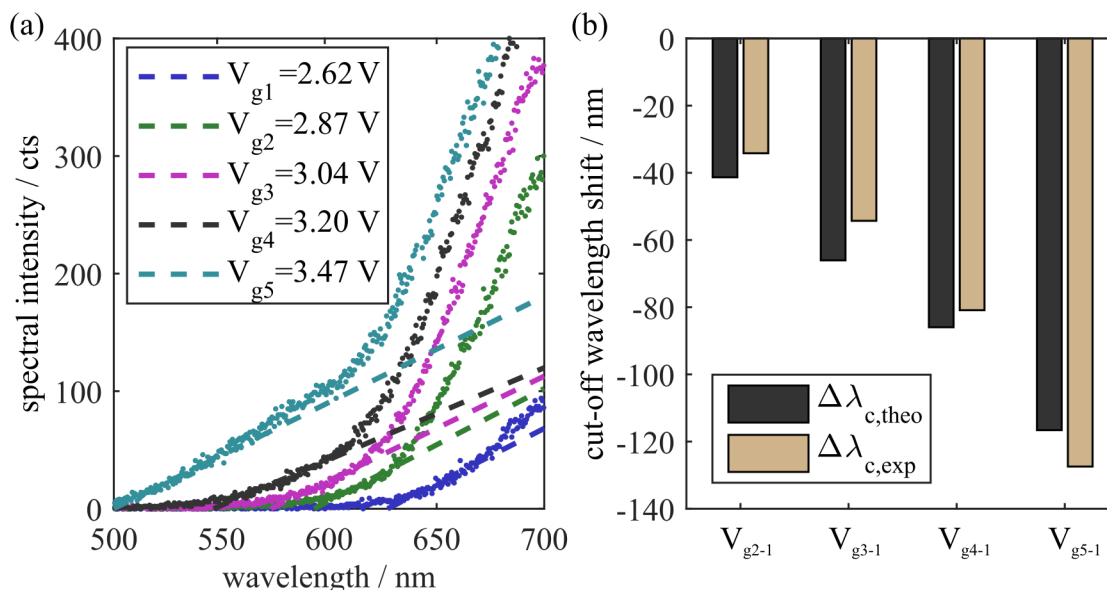


FIGURE 5.3: (a) Shift of the spectral cut-off wavelength by increased bias. The offset is obtained by linear regression of the emission of a D-type tunneling junction. (b) Respective shifts are in agreement with the expected values originating from the voltage difference between each measurement. However, the overall determined cut-off wavelengths are substantially longer than the predicted values.

with smaller size. A LETJ was biased between 2.62 and 3.47 V as shown in Fig. 5.3 (a), in which the bias represents an average value of the 60 s integration time for each spectrum. Lower voltages were not possible for measurements as no reliable emission was detected for these cases. The shortest emittable wavelengths for the tested bias according to the introduced equation are listed in Tab. 5.4. Since this basic equation does not account for the other effects as given above, the theoretical cut-off wavelengths ( $\lambda_{c,theo}$ ) were shorter than achievable in reality. This can be attributed to the limitation by the intraband transitions of the implemented gold electrode that arise at energies higher than 2.5 eV [204]. Experimental values were extracted by a linear regressions intercept with the x-axis. A systematic offset of 155 nm between theory and experiment was found and is probably caused by the detection efficiency of the setup. It would need a single photon detection to account for this artifact. Hence, the spectral shifts  $\Delta\lambda_c$  induced by  $\Delta V_g$  were compared as alternative approach to compensate for this offset. These values were normalized on the data at lowest bias and exhibit good agreement with the theory.

TABLE 5.4: Absolute cut-off wavelength as estimated by theory  $\lambda_{c,theo}$  and experimentally  $\lambda_{c,exp}$  as well as the relative cut-off shifts for the given applied bias.

$V_g / V$	Absolute Value $\lambda_c / nm$		$\Delta V_g / V$	Relative Shift $\Delta\lambda_c / nm$	
	Theory	Experiment		Theory	Experiment
2.62	473	627	-	-	-
2.87	432	593	0.25	-41	-34
3.04	407	573	0.42	-66	-54
3.20	387	546	0.58	-86	-80
3.47	357	499	0.85	-117	-127

### 5.3 Role of Electrode Material in Emission

Since the cut-off wavelength is dependent on the inter- and intraband transitions of the implemented materials, two additional electrode materials have been deposited on similar underlying chips with a 10 nm  $\text{Al}_2\text{O}_3$  tunneling barrier. Supplementary to the already investigated gold electrodes, silver and aluminum films of 30 nm thickness were also deposited on equivalent chips to investigate the influence of these materials on the emission. Measurements were done with 300 s integration time and are depicted in Fig. 5.5 as normalized intensities to remove the influence of different emission efficiencies of the junctions.

The high bias drove the gold junction at the saturation cut-off wavelength limited by the interband transitions as derived from the experiment in the previous section. Silver and aluminum exhibited a different spectral center as the gold electrode, where the expectation would be a cut-off at shorter wavelengths due to lower losses in this interval. However, the experimental results contradicted this assumption. A possible explanation could be the difference in the material work functions of gold (5.1 eV), silver (4.2 eV) and aluminum (4.0 eV) since the potential barrier heights are decreased accordingly. If the applied bias increases to a point that thermionic emission slowly start to dominate, non-radiative conduction mechanisms would prevent a further shift of the cut-off wavelength. Thus, it could additionally be limited by the tunneling barrier height at the cathode interface. This would define the limits for gold ( $\phi_B = 3.3$  eV,  $\lambda_c \approx 375$  nm), silver ( $\phi_B = 2.4$  eV,  $\lambda_c \approx 515$  nm), and aluminum ( $\phi_B = 2.4$  eV,  $\lambda_c \approx 565$  nm). Note, that despite the possibility of spectral tuning of the emitted wavelength by selection of the implemented materials, emission was unstable in consecutive measurements for silver due to oxidation, while aluminum junctions often suffered from electrical breakdown. These restrictions lead to omission of both junction types for further investigations in the course of this thesis. However, passivation layers or metal alloys might enable stabilization of these material stacks as LETJ and spectral tuning by material selection.

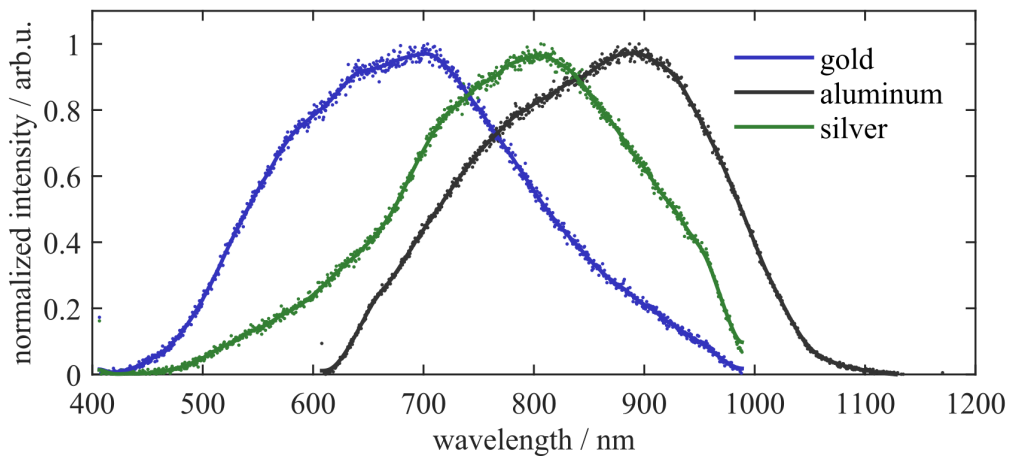


FIGURE 5.5: Normalized emission of LETJ with various electrode materials at 5 V bias. The change in the barrier potential due to differences in the electrode work functions cause shifted emission characteristics as visible for gold electrodes, aluminum and silver with 30 nm film thickness ( $t_{\text{ox}}: \text{Al}_2\text{O}_3 = 10$  nm).

## 5.4 Signal Stability & Repeatability

To assess the quality of the optical spectra emitted by the fabricated LETJ, experiments on the stability and repeatability were conducted. Ten subsequent measurements (integration time 60 s) of a junction at 4.5 V are depicted in Fig. 5.6 (a). A delay of 60 s was inserted between measurements to exclude influences of the measurement procedure for instance by capacitive discharging or thermal gradients. Outliers induced by background radiation or other noise sources were removed by a median-based filter (Hampel Filter [205]) and are indicated accordingly (orange markers). The mean intensity  $\bar{x}$  and the threefold standard deviation  $3\sigma$  was found to be less than 20% of  $\bar{x}$  which represents a good measure due to the contribution of the setups dark current at this low signal-to-noise ratio (SNR).

In Fig. 5.6 (b) spectra at three different tunneling currents of a sweep (80 → 140 → 200 → 200 → 140 → 80 mA) are shown. The overlap of the emitted light is in agreement with the determined standard deviation and thus also valid at various operation conditions. Residual variances in the intensities might have been caused by degradation of the tunneling barrier during operation. The structures had no titanium adhesion layer implemented since tests even with a 2 nm thin layer lead to no emission of the junctions at any applied bias. Thus, a higher risk of instabilities in emission due to the weakened connection between the materials could be responsible for drift effects and are topic of Section 6.4.5. However, tested samples were found to be fully functional even after 12 month of storage in sealed shrink-wrapping. Storage in ambient conditions decreased lifetime to a few months, as blistering of the topmost film occurred.

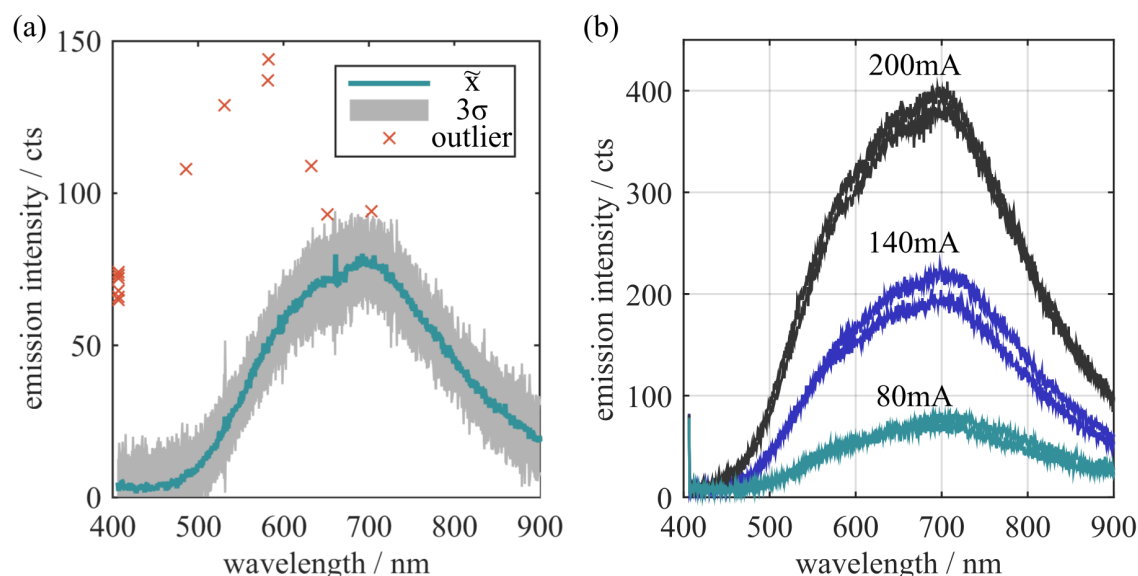


FIGURE 5.6: (a) Stability of the spectra from LETJ at 4.5 V with a 7 nm tunneling barrier at 10 subsequent measurements. The averaged intensity  $\bar{x}$  is shown (line) with its 99.73% standard deviation  $3\sigma$  (area) and is less than 20% of  $\bar{x}(\lambda)$ . The markers (x) are outliers from background radiation and were removed by analyzing the data with a Hampel filter. (b) Repeatability of signals at different operating conditions was verified by a sweep of tunneling currents (80 → 140 → 200 → 200 → 140 → 80 mA).

## 5.5 Polarity dependent Emission

An experiment to verify whether the detected emission from LETJ was indeed based on the underlying effect of inelastic tunneling was the comparison of the spectra towards both bias polarities. The possible processes which have to be distinguished are the intended LEIT effect and elastic tunneling with subsequent recombination of hot electrons into lower energy levels. While the first process is dependent on the QSN of quantum tunneling, the second is primarily dependent on the available states in the anode. In consequence, the spectral bandwidth and center position should vary for elastic tunneling since the energy band diagrams of the electrodes are different in hetero-junctions. For the LEIT effect, both spectra are expected to be equivalent and only differ in the intensity due to the difference in the tunneling rate at each polarity.

The results of this experiment are shown in Fig. 5.7 for an Au / 7 nm Al<sub>2</sub>O<sub>3</sub> / Si junction at  $\pm 3.0$  V, the integration time was set to 60 s again. Both spectra exhibited the same spectral bandwidth and a central wavelength at around 720 nm. At the same time, a difference in the integrated spectra by a factor of 2.4 was determined. The tunneling currents differed only by a factor of 0.92. For an energetically symmetric junction both factors should be equal, but the tunneling direction might also entail a decreased emission efficiency by additional effects of the implemented materials, i.e. changes in the charge carrier majority at the insulator/semiconductor interface and different density of states.

The inset of Fig. 5.7 depicts the normalized spectra to emphasize the spectral overlap for both operation conditions. A well defined overlap between both states was found which strongly indicates the LEIT effect as dominant contribution in the emitted radiation. Note, that this junction had plasmonic nanoparticles incorporated on top of the gold electrodes which drastically changed the spectral shape in contrast to a basic LETJ sample. The influence of these nanoparticles will be subject of the next chapter.

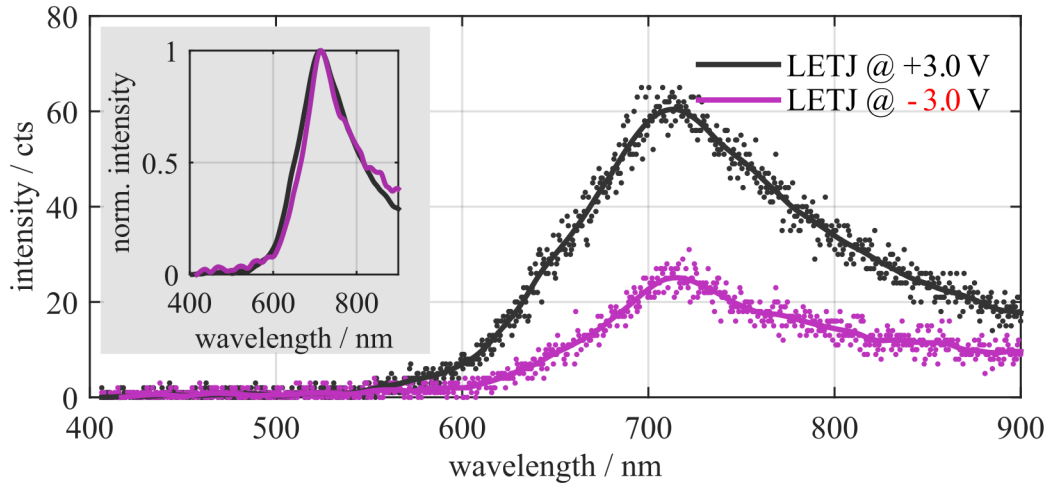


FIGURE 5.7: Emission in dependency of the bias polarity at  $\pm 3.0$  V, respectively. The spectral characteristics are equal regarding spectral bandwidth and peak position. Intensities differ according to the present tunneling currents. As shown in the insets, spectra are equivalent if normalized.

- page intentionally left blank -

## 6 | Plasmon Hybridization on Electrically Driven Junctions

So far, experiments on the electrical properties of the fabricated thin-film stacks established their suitability as LETJ by the prominent conduction mechanism of electron tunneling. The experimentally supported verification of the general spectral features in the last chapter was congruent with theory and published results as summarized in Chapter 3. Based on these findings, this part of the thesis will focus on the influence of post-fabrication deposited nanoparticles on top of the LETJ stack.

From the theory of plasmon hybridization in optically excited systems, at least two effects are expected to influence the SPP mode eigenfrequencies of the LETJ. First, if the nanoparticles are simply regarded as scattering centers, outcoupling of the excited SPP and thus the emission efficiency should increase. Second, plasmon hybridization effects caused by interaction between the excited SPP on the chip and the adsorbed nanoparticles should occur, resulting in changes of the resonance frequencies if they are positioned within the nanometer range as described in Section 2.4. Experimental proof on the equivalence between externally illuminated and electrically driven junctions was verified by several reference measurements.

A set of nanoparticle geometries and materials in interaction with LETJ was studied as exemplary shown in Fig. 6.1. All utilized nanoparticles were either purchased or

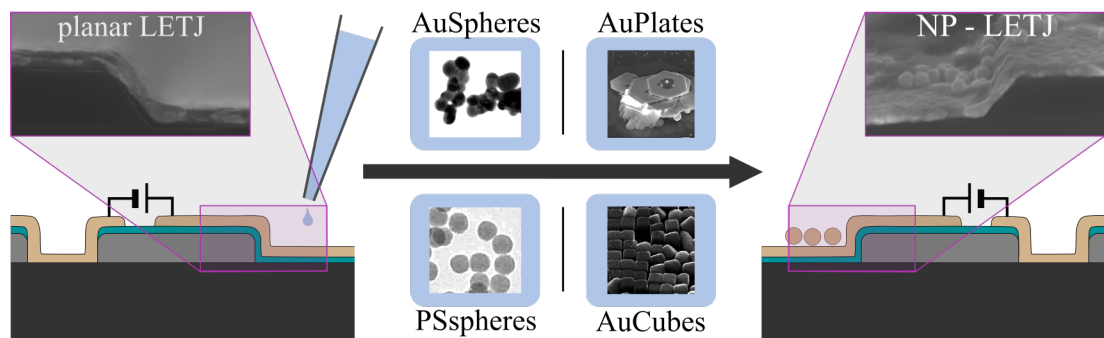


FIGURE 6.1: Planar junctions were modified with chemically synthesized gold and polystyrene nanoparticles of different geometry by drop-casting from colloidal solutions to investigate their influence on scattering, emission features, and spectral tunability of the LETJ samples.

chemically-synthesized in-house and deposited by simple drop-casting on the junction area. This approach promised some advantages to other techniques:

- Since all LETJ chips are fabricated with pre-defined properties by photo lithography, the underlying junctions profit from the high standards established in these processes as well as from the parallel completion of equivalent chips at the wafer-scale. Thus, good film homogeneity and precision in the junction parameters are given and ensure the comparability between experiments.
- In contrast to lateral gap antennas, vertical tunneling junctions exhibit better control on the resulting tunneling barrier due to precise control of the junction thin-film properties.
- By using of chemically-synthesized particles, tailored properties defined by the synthesis parameters enable a whole palette of geometries and materials. These would be hardly realizable in top-down approaches or go beyond the current limitations of structuring methods while being easily accessible in bottom-up approaches.
- The separation of the fabrication steps into bottom-up and top-down sections offers the potential to optimize the individual components of the experiments independently from each other.

Naturally, some drawbacks are encountered in this method, which are listed below. The evaluation of the given advantages and drawbacks may differ depending on the scope of the experiments and applications:

- In contrast to lateral gap antennas, vertical stacks are not easily accessible in the tunneling barrier which prevents a direct alteration of the tunneling barrier by post-fabrication procedures.
- Regular patterns of plasmonic nanoantennas are not realizable, since the immobilization of the utilized chemically-synthesized particles by drop-casting is of statistical nature, which also incorporates agglomeration effects.
- Colloidal solutions have to be purified carefully to remove solvent components, detergents, and other residuals before drop-casting to exclude undesired effects on the tunneling junctions.

All known alternative techniques which circumvent these drawbacks require either tremendous instrumentational efforts, piecewise fabrication by FIB or electron-beam structuring as introduced in Chapter 3.



## 6.1 Nanoparticles as Emitters

Enhancement of the emission efficiency from LETJ can be expected by adsorption of nanostructures since they serve as artificial scattering centers or emitters. These contribute to the overall roughness of the electrode and support outcoupling of the electrically driven SPP.

An example for this efficiency enhancement is described in Fig. 6.2 (a). For an ideally flat interface, no scattering would occur due to momentum conservation, confining the energy in the bound mode as visible by the magnetic field component  $H_z^b$ . By addition of a nanoparticle, the introduced defect allows scattering of a fraction of the surface plasmon energy (represented by  $H_z^{sc}$ ).

The experimental proof of this concept is shown in Fig. 6.2 (b). The spectrum of a bare LETJ junction at a bias of 3.5 V and a integration time of 60 s is compared with the same junction after nanoparticle immobilization. 3  $\mu\text{l}$  of spherical gold nanoparticles (EM.GC80, BBI Solutions) with radius  $r_{s,1} = 40$  nm from a stock solution with an optical density (OD) of 1 ( $c_1 = 1.1 \cdot 10^{10}$  particles/ml) were immobilized on the chip. Integration of the spectra yielded an average emission rate  $\gamma_r = 425$  Hz/mA. By comparison on the emission rate of a bare junction  $\gamma_0$ , an amplification factor  $A_F$  was defined by the ratio  $\gamma_r/\gamma_0$  and determined to  $A_F = 22.4$ .

The grey curve displays a scattering spectrum of a similar experiment without applied bias and in external excitation which was realized by a halogen whitelight source in a dark-field configuration. While the peak positions overlap for both systems at approximately  $\lambda_{\text{max}} = 720$  nm, the optically driven spectrum was more narrow (FWHM = 117 nm) than the LETJ spectrum (FWHM = 231 nm). This may either be caused by a different nanoparticle concentration or by the difference in the SNR of the two excitation schemes.

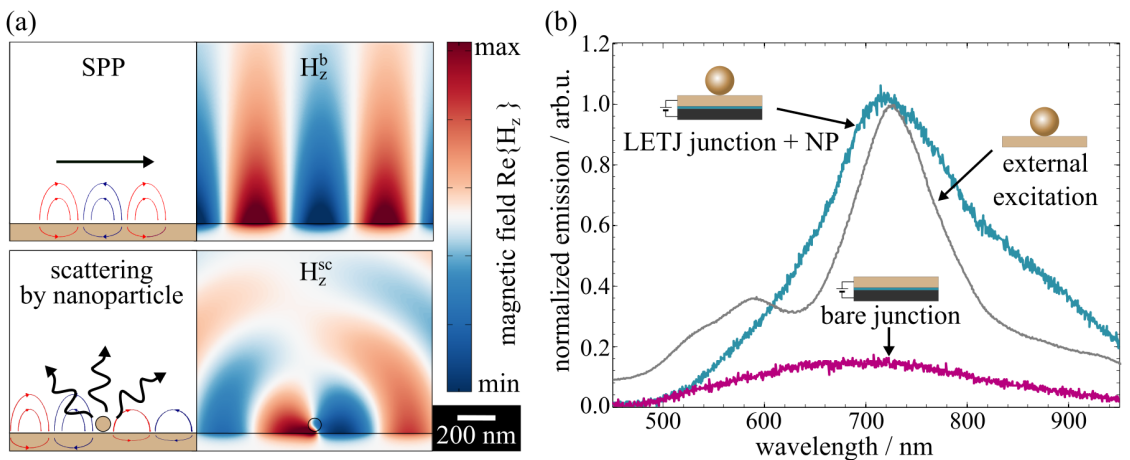


FIGURE 6.2: Emission enhancement of LETJ by nanoparticles. (a) The normally bound SPP is partially scattered into free-space radiation by an adsorbed nanoparticle ( $r_s = 40$  nm). (b) LETJ emission spectra (@3.5 V) without (purple) and with adsorbed nanoparticles (teal), normalized on the intensity maximum of the latter, emphasizing the emission enhancement between both junctions. For comparison of the overall spectral shape, a DF scattering spectrum of this system is shown (black).

A second experiment with a substantially higher concentration of larger particles was conducted to address both questions - the nature of the broadband emission as well as a more reliable determination of the amplification factor based on more measurements. Gold nanoparticles (EM.GC100, BBI Solutions) with  $r_{s,2} = 50$  nm and OD 1 ( $c_2 = 0.56 \cdot 10^{10}$  particles/ml) were centrifuged and redispersed to 10x of the original concentration and drop-casted on a junction. After immobilization, a sweep for different tunneling currents similar to the procedure in Section 5.1 was performed and is depicted in Fig. 6.3 (a). Substantially lower currents were necessary for the reference experiment to obtain signals. Additionally, a more pronounced peak was observed (FWHM = 76 nm), emphasizing the role of the nanoparticle concentration in the emission.

As before, the average emission rate  $\gamma_r = 8239$  Hz/mA was determined from the slope of a linear regression of the integrated count rates as function of the tunneling current (Fig. 6.3(b)). With this, an amplification value of  $A_F = 433$  was obtained.

These results indicated, that a correlation might be given by the ratio of the expected amplifications  $A_r$  from experiments that incorporate different nanoparticle types by considering their surface concentration and scattering cross-sections as given in Eq. 6.1.

$$A_r \propto \frac{\eta_{\text{ant},2}}{\eta_{\text{ant},1}} \propto \frac{c_2}{c_1} \cdot \frac{C_{\text{sca}}(r_{s,2})}{C_{\text{sca}}(r_{s,1})} \quad (6.1)$$

Hence, with the given equation and the known parameters, an ideal gain of  $A_{r,\text{theo}} = 20.4$  was expected between the experiments. The experimentally obtained value was  $A_{r,\text{exp}} = 433/22.4 = 19.3$  which matches well with the calculated value. Therefore, a strong indication for the importance of the implemented plasmonic nanostructures as Rayleigh scattering centers for enhanced emission efficiency in LETJ devices was found.

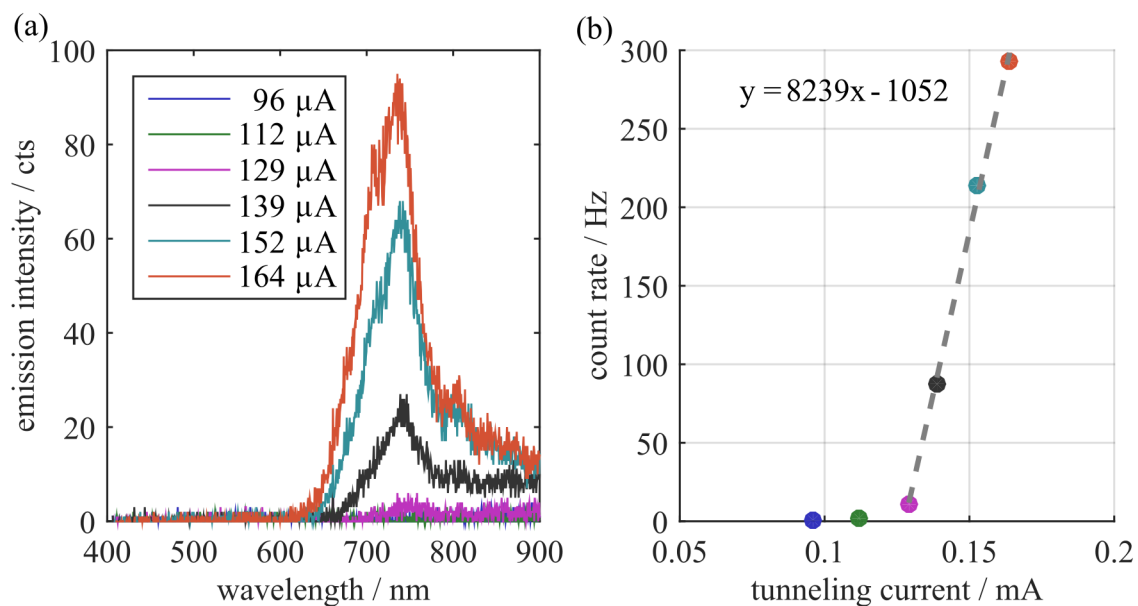


FIGURE 6.3: Current dependency of LETJ emission. (a) D-type junction measured with an integration time of 60s per spectrum at the labeled currents. (b) integrated intensity as total count rate. Above the detection threshold ( $\approx 130$   $\mu\text{A}$ ), the average emission rate was determined from the slope of a linear regression (dashed line).

## 6.2 Plasmon Coupling in a Particle-Film System

To evaluate the determined influence of adsorbed nanoparticles on the emission of a LETJ *in silico*, a two-dimensional numerical model was set up in finite element methods calculations (COMSOL Multiphysics). The LETJ process is described as a two stage process of inelastic tunneling and subsequent scattering of the excited surface plasmons at the junction interfaces. Thus, to simplify the approach, restriction to the second step was done by assuming an incoupled SPP propagating along the dielectric-metal interface as initial state. The SPP was described according to the analytic expressions in Eqs. 2.5 and as given by Dionne et al. [206] with the respective material parameters. More details on the domains and triangular meshes of the model are given in Fig. B.8.

An exemplary depiction of the normalized scattered electric field of such a particle-film system is shown in Fig. 6.4. In the described case, strong coupling between the gold substrate and a gold particle ( $r_s = 50$  nm) occurs with enhanced scattering in the region around the particle with a hot spot in the particle-film gap ( $s = 2$  nm). This distance was chosen as an exemplary value as valid for a biological film in a sensing scheme.

Since the penetration depth as well as the SPP propagation length are wavelength dependent values, the infed electric field  $\mathbf{E}(\omega)$  was normalized on the field magnitude  $\mathbf{E}_N(\omega)$  at the model origin. This was defined as the location at the dielectric-metal interface below the particle, resulting in the background electric field  $\mathbf{E}_b(\omega)$  as given in Eq. 6.2.

$$\mathbf{E}_b(\omega) = \frac{\mathbf{E}(\omega)}{|\mathbf{E}_N(\omega)|} \quad (6.2)$$

After numerically solving for the full field components, the scattered fields were obtained by subtracting the background fields from the results:

$$\mathbf{E}_{\text{sca}}(\omega) = \mathbf{E}(\omega) - \mathbf{E}_b(\omega) \quad (6.3a)$$

$$\mathbf{H}_{\text{sca}}(\omega) = \mathbf{H}(\omega) - \mathbf{H}_b(\omega) \quad (6.3b)$$

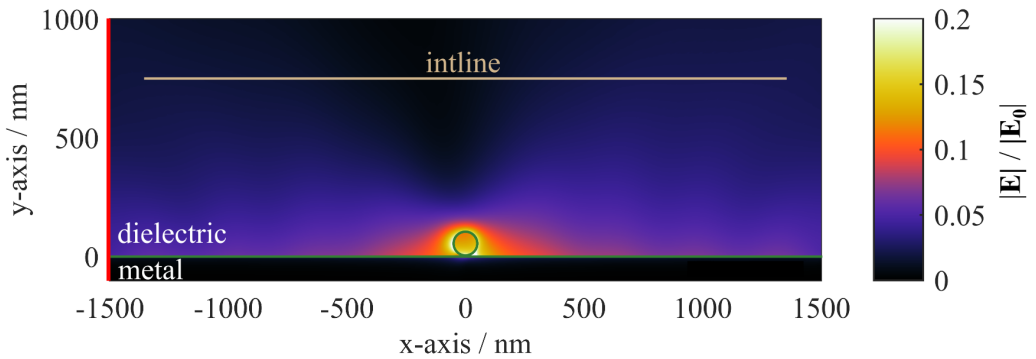


FIGURE 6.4: Two-dimensional model geometry to simulate the optical response of a metallic nanoparticle (gold) in the vicinity of a metallic film (gold). The scattered electric field is plotted, which is integrated at the line (yellow) resulting in the total scattered power over an detection angle of  $\vartheta = 120^\circ$ .

Calculation of the scattered power of such a system is often done by the surface-integrated flux of all relevant boundaries. However, a different method was chosen to approach the far-field detection of real instrumentations, which exhibit a limited detection angle  $\vartheta$  in contrast to the full-angle integration of idealized studies. The implemented "intline" in Fig. 6.4 covers  $\vartheta \approx 120^\circ$ . With the resulting distance from the interface, edge artifacts from the numerical calculations and residual near-field contributions of the SPP are minimized. By integration of the Poynting vector components as given in Eq. 6.4

$$S_x = 0.5 \operatorname{Re}(E_{y,\text{sca}} H_{z,\text{sca}}^*) \quad (6.4a)$$

$$S_y = 0.5 \operatorname{Re}(-E_{x,\text{sca}} H_{z,\text{sca}}^*) \quad (6.4b)$$

and summation of the individual components by Eq. 6.5, the scattered power  $P_{\text{sc}}$  is obtained. The last step is a necessary addition in the used software to account for the field components perpendicular and parallel to the implemented integration line.

$$P_{\text{sc}} = n_x S_x + n_y S_y \quad (6.5)$$

The optical response of the particle-film system in this model was evaluated by a parametric study with the particle radius  $r_s$ , the refractive index of the surrounding medium  $n_m$  and the particle-film separation  $s$  as shown in Fig. 6.5(a). The dielectric function of the gold film and particle was taken from published values as before (see Fig. B.1).

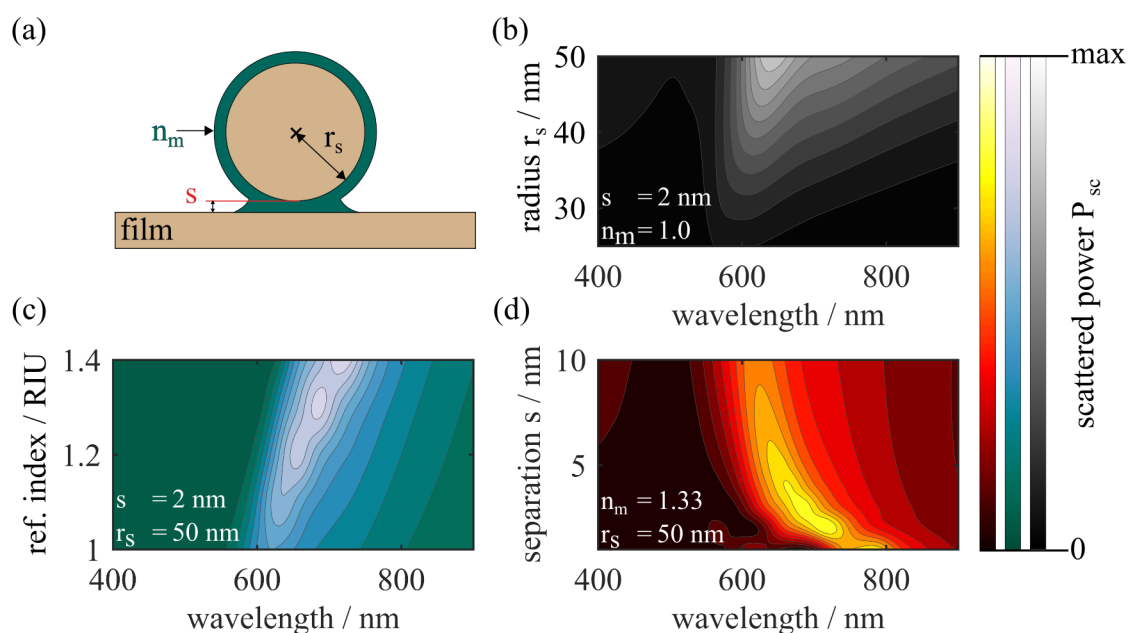


FIGURE 6.5: (a) Scheme of a gold particle with radius  $r_s$ , surrounding shell with thickness  $s$  and refractive index  $n_m$  coupled to a 100 nm thick gold film surrounded by air. The contour plots show scattering spectra of this system in dependency of these three parameters, respectively; (b) Scattering spectra map as function of particle radius  $r_s$  ( $s = 2$  nm,  $n_m = 1.0$ ); (c) Scattering spectra map as function of refractive index  $n_m$  ( $s = 2$  nm,  $r_s = 50$  nm); (d) Scattering spectra map as function of shell thickness  $s$  ( $r_s = 50$  nm,  $n_m = 1.3$ ).

Spectra for different particle radii are depicted in Fig.6.5(b) for a fixed separation of 2 nm and an air shell ( $n_m = 1.0$ ). By increasing the particle radius, the scattered power is increased together with a redshift of the resonance wavelength. This is similar to the expectations from Mie theory, while a systematic offset to longer wavelengths of the resonances is observable which originates from electromagnetic coupling with the metallic film and the correlated splitting of resonance energy levels. The influence of the particle shell refractive index is shown in (c) with a linear dependency of the resonance wavelength on  $n_m$ . This dependency is also known from Mie theory and is heavily used in refractive index based sensing methods with plasmonic nanoparticles. In (d), a strongly non-linear behavior of the scattering maxima on the separation is observed which is correlated to the near-field effects of coupled plasmonic structures as introduced in Section 2.4. All effects contribute simultaneously in the overall signal of such a described system.

The near-field coupling by hybridization of the film and particle plasmon for different separations is depicted in Fig. 6.6. Intense electromagnetic fields are confined in the gap region, while these coupling effects are only present for separations in the few nanometer range. The occurring shifts in the systems eigenfrequency are also the largest in this regime. For this reason they are also known as gap modes.

Note, that the obtained spectra and field distributions are approximations with bias given by the method and due to the assumptions and restrictions that were made in the model. Separations smaller than 1 nm were not simulated since the underlying electromagnetic equations do not account for quantum corrections [207, 208] that are necessary at the sub-nanometer scale such as non-local responses and tunneling of charge carriers [209–211]. Hence, with the lowest calculated separation of 1 nm the limits in the validity of this approach are reached. Additional bias in the results is given by the calculations of the scattered field over an restricted angle, the finite geometry and the limitation to one single boundary of the stack. Other scattering contributions may arise in real samples as well, since the fabricated LETJ structures in the experiments undergo various complex processes at the different interfaces of the material stack simultaneously. However, reasonably good approximations are obtained by the procedure as validated by the experiments in the next sections.

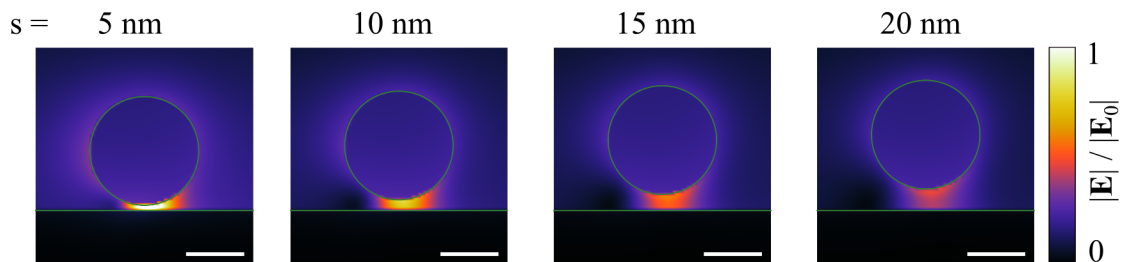


FIGURE 6.6: Normalized electric fields  $|\mathbf{E}|/|\mathbf{E}_0|$  of a gold particle with  $r_s = 50$  nm in air ( $n_m = 1.0$ ) above a gold film for different separations ( $s = 5, 10, 15$  and  $20$  nm). The bonding mode of the particle-film-interaction decreases nonlinearly with increasing separation leading to lower scattering intensities. Scalebar: 50 nm.

The quality of the model was assessed by fabricated reference samples. A 30 nm thick gold layer was deposited on top of a glass substrate and covered by  $\text{Al}_2\text{O}_3$  ALD spacer layers of different thickness ( $s = 1, 2$  and 5 nm). The refractive index of the deposited films was determined by ellipsometry to  $n = 1.58$  at 633 nm probing wavelength. As last step, the gold particles with  $r_s = 50$  nm were drop-casted onto the samples. Thus, a fully described system for comparison with the calculated results was available and measured by a darkfield microscopy setup as depicted in Fig. A.4 with an integration time of 10 s per spectrum.

The depicted experimental spectra in Fig. 6.7 are averages of 10 measurements each. Resonance shifts for the different spacer layers are observed as well as pronounced peaks for bonding and anti-bonding mode. While the resonances of the bonding modes are evaluated well by the simulations with a slight overestimation at longer wavelengths, the anti-bonding resonances are underestimated. To cross-check this and rule out the influence of the SPP excitation scheme, an equivalent model was set up, deploying excitation by a planar wave with an angle of incidence of  $60^\circ$  as given in Fig. B.9. Similar spectra were obtained for both approaches which indicates the suppressed detection of the transverse dipole mode by the integration line of the model.

However, since the observable, separation dependent resonance shift is governed by the longitudinal axis of the particle-film system, the reasonably well description of that mode was prioritized and accepted as is.

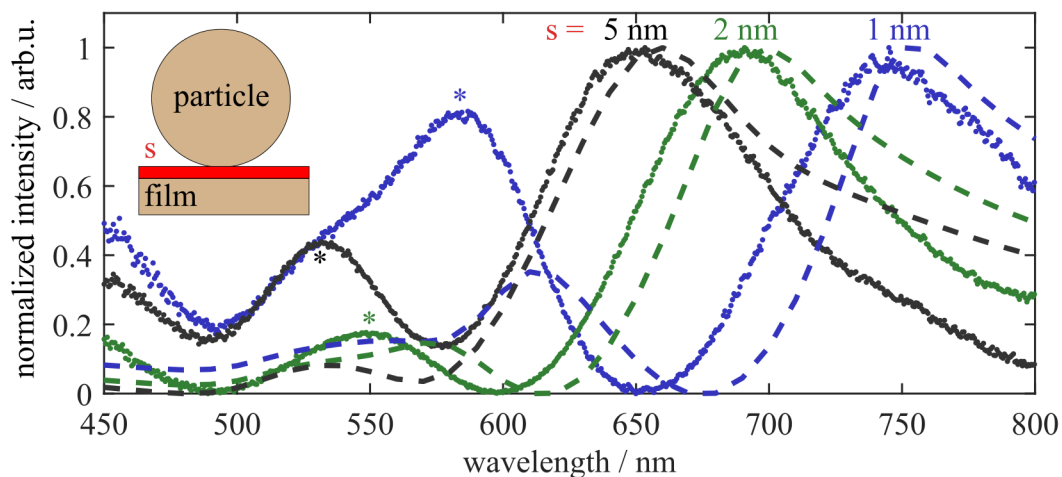


FIGURE 6.7: Darkfield scattering spectra of gold nanoparticles with  $r_s = 50$  nm on top of a 30 nm gold substrate with a separation  $s$  of 1, 2 and 5 nm (dotted) are shown. The reference spacer layers consisting of  $\text{Al}_2\text{O}_3$  were deposited by ALD ( $n = 1.58$ ). The corresponding spectra calculated from the model as developed in the beginning of the chapter is shown by the dashed lines. The bonding-mode exhibits a good agreement with the experiments, while having a small systematic offset induced by the spacer refractive index and film thickness deviations. Intensities in the anti-bonding mode at shorter wavelengths (asterisks) are underestimated by the model.

### 6.3 Measurement of Organic Layers by Plasmon Coupling

With the tremendous sensitivity of the resonance splitting into bonding and anti-bonding mode arising from sub-nanometer changes in the separation, the effect of gap-modes has been demonstrated as sensing scheme in biological reactions and nanoanalytics. The probing of conformational changes in molecules, DNA-origami, or detections on reactions with exchanging ligands of similar refractive index are potential fields of application by gap-mode structures as plasmonic nanorulers [212, 213].

A proof-of-principle study of such a detection scheme on LETJ based chips was in the scope of the next experiments. One of the main advantages of the chosen junction geometry and fabrication method becomes apparent, since organics are involved in this detection scheme. Organic spacer layers of varying thickness mimicking the conformational change of a molecule were assembled by functionalization of nanoparticles in solution before immobilization on the sample surface. Spherical gold NP with a radius  $r_s = 40$  nm (EM.GC80, BBI Solutions, Cardiff, UK) were deposited by drop-casting from an aqueous solution ( $c \approx 1.1 \cdot 10^{10}$  particles/ml).

Three types of nanoparticles were functionalized as depicted in Fig. 6.8, in which all types were based on the previous functionalization step:

**Type I:** consisted of trisodiumcitrate-stabilized nanoparticles, resulting in a densely functionalized surface layer with thickness  $s_{\text{CITR}}$ .

**Type II:** BSA (Bovine Serum Albumine, Fluka Biochemika) was injected into Type I up to a concentration of 375  $\mu\text{M}$  into the solution and incubated for 24 h to guarantee full coverage of the NP according to the procedures of Dominiguez-Medina et al. [214, 215] resulting in layer thickness  $s_{\text{BSA}}$ .

**Type III:** obtained by centrifuging the solution of Type II at 6000 rpm for 300 s, prior to the addition of 10  $\mu\text{l}$  of anti-BSA IgG (IgG<sub>2a</sub> light chain Antibody (7A9), Santa Cruz Biotechnology, Dallas, TX) which specifically binds to BSA as described in Chaïet et al. [216], incubation for 2 h, and a second centrifugation step for purification to achieve a double layer with thickness  $s_{\text{IgG}}$ .

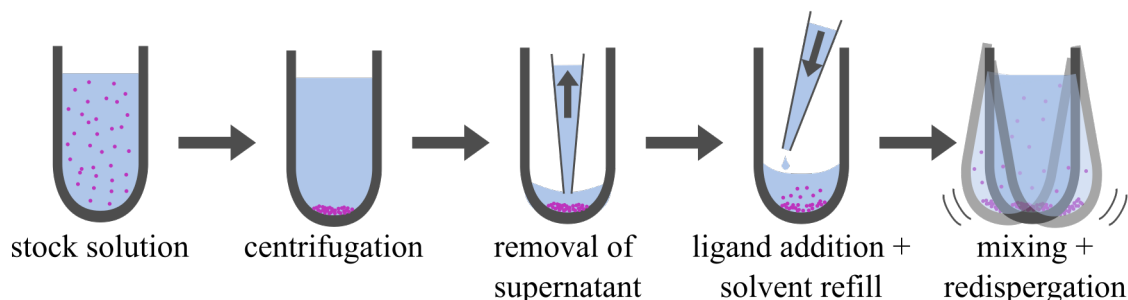


FIGURE 6.8: Illustration of the nanoparticle treatment for the functionalization with organic layers around the particle in subsequent steps, starting from a colloidal stock solution.

### 6.3.1 System Referencing by External Illumination

A reference experiment was done first to validate the chemical protocols and feasibility of the experimental procedure. Glass substrates coated with a 30 nm gold film were drop-casted with 3  $\mu\text{l}$  of the colloidal solutions and dried under ambient conditions. Measurements were done at the microspectroscopy-setup as depicted in Fig. A.4 with an microscope objective (EC Epiplan 20x/0.4 HD, Zeiss) in darkfield configuration and an integration time of 10 s for each spectrum. The signals  $I_{\text{raw}}$  were additionally corrected for the background  $I_{\text{bg}}$ , the setup dark current  $I_{\text{dc}}$  and light source  $I_{\text{ls}}$  by the relation  $I = (I_{\text{raw}} - I_{\text{bg}})/(I_{\text{ls}} - I_{\text{dc}})$ .

Experimentally recorded spectra of all three nanoparticle types are depicted in Fig. 6.9. Signals were normalized to the peak maximum due to deviations in the nanoparticle concentrations from losses by the prior mentioned functionalization steps. The peak position of the resonance band was determined by a polynomial fit of the data and calculation of the center of gravity  $\lambda_{\text{cog}}$  to account for asymmetries in the peaks. Resonance wavelengths of 722 nm for type I particles (CITR), 707 nm for type II (BSA) and 694 nm for type III (IgG) were determined to verify the practicability of the functionalization protocol.

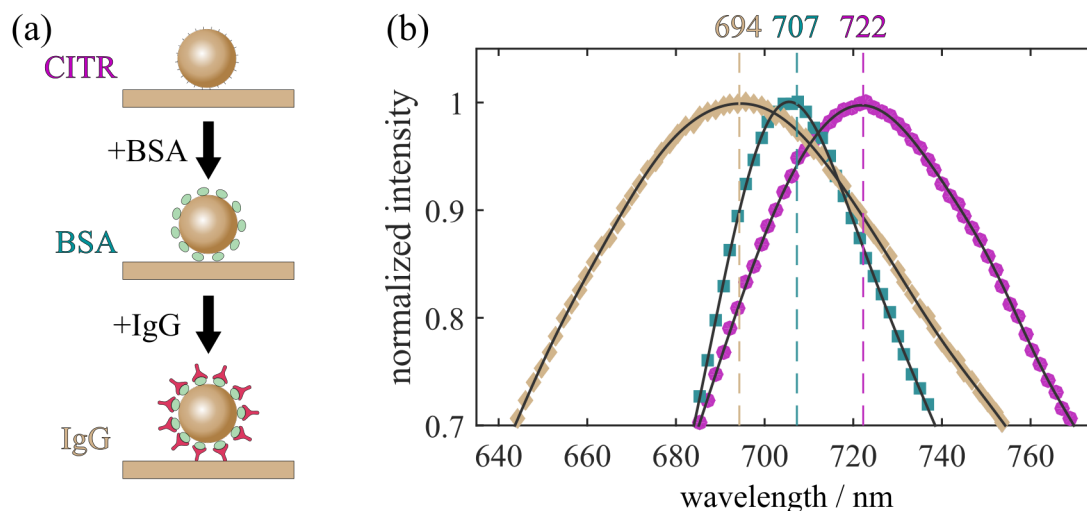


FIGURE 6.9: (a) Scheme of the experiment to demonstrate the different cappings of three previously described nanoparticle types. Colours of the plots in (b) correspond to the capping-agents. The resulting spectral shifts are caused by an increased distance between particle and metallic substrate. Peak positions were determined by polynomial fitting and calculation of the center of gravity.

Interestingly, differences in the resonance bandwidths are encountered which can be attributed to the averaging of the data, effects of varying backgrounds, and probably inhomogeneities in the organic layer comprised of proteins. Nonetheless, peak positions are clearly discriminated by this approach and the chosen analysis.



### 6.3.2 Validation by Light Emitting Tunneling Junctions

After successful testing by the reference experiments, the same protocol was repeated for measurements on LETJ chips. Fig. 6.10(a) shows the raw spectra for three different junctions with the functionalized particles biased at 3.3 V. All junctions were located on the same chip to minimize chip-to-chip deviations. A well defined shift of the broad-banded emission was observable, while the cut-off frequency stayed constant as expected for equally biased structures according to theory. In sub-graph (b), the average power consumptions of the measured D-type junctions are shown for the preliminary experiment before nanoparticle immobilization (initial) and after immobilization on the same junctions (final). Constant input powers for both states of all three junctions were determined in which the average of all measurements (66 mW, red dashed line) with a 5% confidence interval (grey area) is given for better comparability. The seemingly high powers are attributed to the sample areas which are orders of magnitude larger than the single transition junctions used in other studies.

Stability of the junctions was proven by these measurements even after wet-chemical treatment, that is the drop-casting process of the nanoparticle immobilization. During development of the experimental procedure, it was found that purification of the colloidal solutions by centrifugation and redispersion in dH<sub>2</sub>O directly before the measurements increased the quality of the obtained results substantially.

The peak maxima were determined as described before and yielded a  $\lambda_{\text{cog}}$  (dashed lines) of 723 nm for type I, 709 nm for type II and 690 nm for type III particle. The evaluated peak caps are shown in Fig. 6.11 and emphasize the advantage of polynomial fitting (black) over single Gaussian or Lorentz functions which are not able to account for the

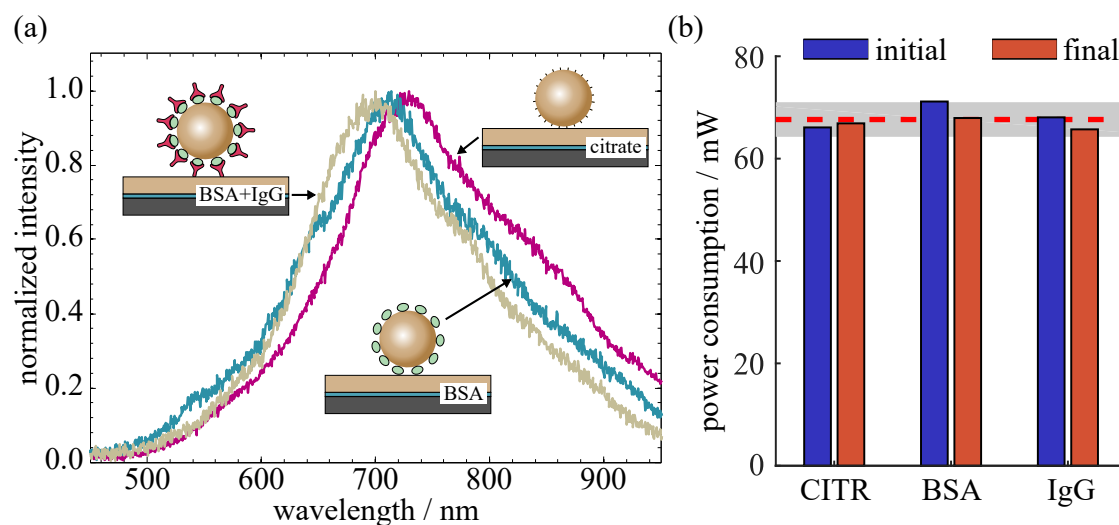


FIGURE 6.10: (a) LETJ emission spectra for different functionalized particles. The particles were prepared prior to measurements by capping with CITR (purple), BSA (teal) or a BSA/IgG double layer (beige). (b) Power consumption of the junctions before (blue) and after nanoparticle adsorption (red) within a confidence interval of 5% (grey area) from the average of all measurements (red dashed).

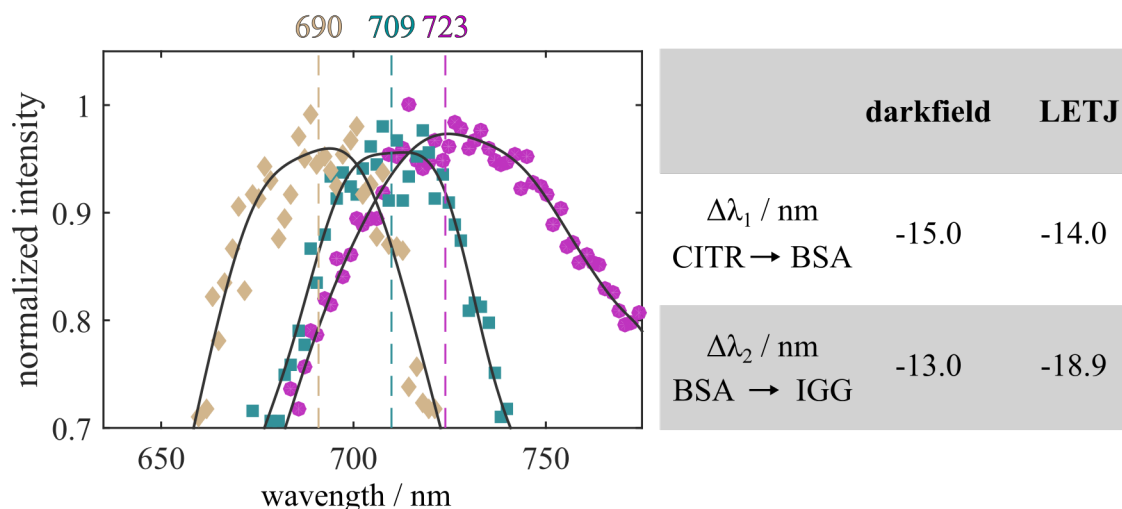


FIGURE 6.11: Bonding-mode peak position for different particle cappings. Peaks were fitted with polynomials after removal of outliers by hampel filtering to denoise the experimental data from background signals. The peak wavelengths were obtained by calculating the center of gravity of the polynom within a range of  $\pm 40$  nm from the polynomial maximum. The determined peak maxima for the different experiment stages exhibit the same trend as references by darkfield measurements.

asymmetric and superpositioned contributions in the signals. Relative shifts  $\Delta\lambda$  between the different functionalization steps are listed for both methods in Fig. 6.10(b) and exhibited the same trend. The obtained shifts achieved for BSA capped particles matched well (deviation  $< 7.5\%$ ) for both techniques. For the double layer experiment dissimilar shifts in darkfield  $\Delta\lambda_{2,DF} = -13$  nm and  $\Delta\lambda_{2,LETJ} = -18.9$  nm for the LETJ experiment were obtained, which indicated batch-to-batch inhomogeneities of the adsorbed organic films. The correlation of these peak shifts to the actual layer thickness was in scope of the next analysis.

Despite a lower SNR arising from the efficiency of the LETJ samples, an unambiguously distinguishable peak shift and position determination was possible from the experimental results. This proves the feasibility of the investigated LETJ structures as potential sensors similar to plasmonic nanorulers compatible with nanoelectronics [213].

### 6.3.3 Layer Thickness Assignment

To assign the physical layer thickness of the organics around the particles from the determined peak positions, the model from the previous section was deployed again. A set of separations ( $s = [1,20]$  nm) between a gold particle ( $r_s = 40$  nm) and a gold film was calculated with a refractive index for the molecular layers of  $n_m = 1.4$  as taken from Vörös et al. [217]. Note, that measurements were performed in dry environment which had to be taken into account in this study since the refractive index differs from liquid phase experiments. Additionally, the molecular weights of the two proteins BSA and IgG are comparable with 65 kDa and 150 kDa, respectively. This allowed for the assumption of equal refractive indices between the individual functionalization steps.

Hence, spectral shifts were attributed solely to changes in the separation between the particles and gold film induced by the larger protein cappings around the particle [218].

The simulated signals as partially shown in Fig. 6.12 (a) were calculated at distinct points (black dots), in which the peaks were then interpolated (teal) and fitted by the same procedure as in the previous cases resulting in the depicted  $\lambda_{\text{cog}}$  values (purple cross).

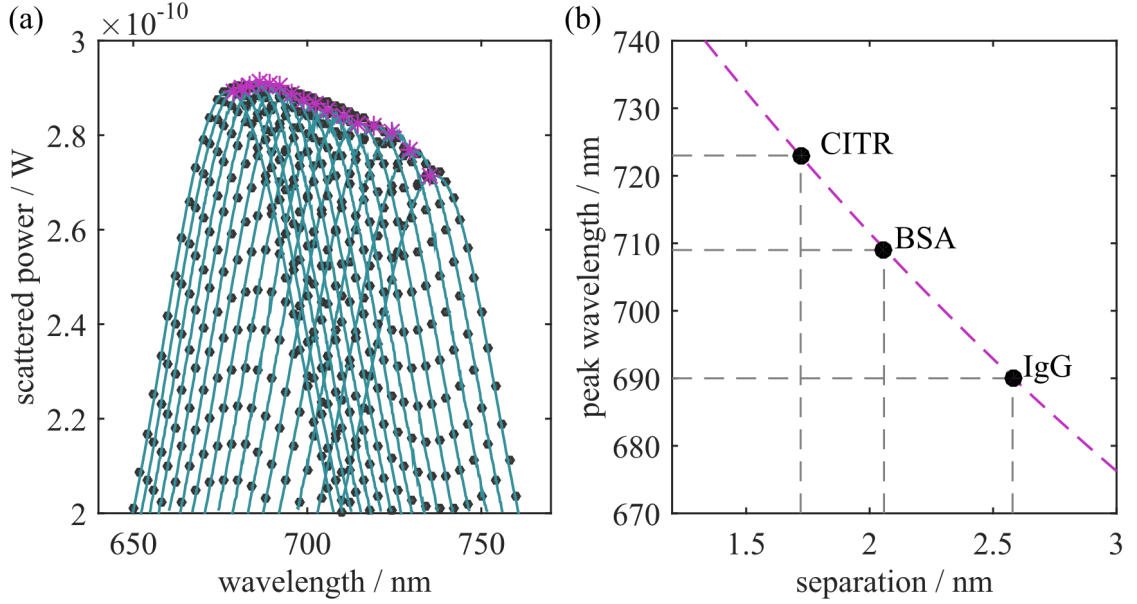


FIGURE 6.12: (a) Calculated scattering spectra for a gold particle ( $r_s = 40$  nm) on a gold substrate for separations ranging from 1 to 4 nm (dots) and their polynomial interpolations (teal) with a surrounding organic shell ( $n_m = 1.4$ ). The peak positions were determined as center of gravity values (purple cross). (b) Derived decay function of the resonance wavelength vs separation (purple) used for assignment of organic layer thickness from the experimentally determined peak values.

Validity of a simple mono-exponential dependency of the peak position to the separation was found by Reinhard et al. [219] and implemented for this study. Since only distinct experimental values were available, the obtained values from simulations were fitted to this equation as given in Eq. 6.6 with the parameters  $a$ ,  $b$  and  $c$ .

$$\lambda_{\text{cog}} = a \cdot e^{(-s/b)} + c \quad (6.6)$$

The constant  $c$  defining the function offset was fixed to  $\lambda_{\text{max}} = 572$  nm. This value was chosen as it corresponds to a decoupled particle at an infinite separation from the substrate. Thus, the peak position  $\lambda_{\text{max}}$  of such a particle was calculated by Mie theory as shown in Fig. B.10 (a). Both constants,  $a$  and  $b$ , were determined to 247.4 nm and 3.485 nm, respectively. The full range of the exponential function is listed in Fig. B.10(b).

A reassignment of the measured peak positions to the organic layer thickness from the exponential function was achieved as shown in Fig. 6.12(b) and as listed for both experiments in Tab. 6.13. Thus, the earlier determined, rather large peak shift of the double layer experiments only depicts a physical variation of the organic film thickness in the sub-nanometer range around the particle.

TABLE 6.13: Determined organic layer thickness  $s$  from the measured peak positions  $\lambda$  for both experiments in darkfield (DF) and electrical excitation (LETJ).

	$\lambda_{\text{DF}} / \text{nm}$	$s_{\text{DF}} / \text{nm}$	$\Delta s_{\text{DF}} / \text{nm}$	$\lambda_{\text{LETJ}} / \text{nm}$	$s_{\text{LETJ}} / \text{nm}$	$\Delta s_{\text{LETJ}} / \text{nm}$
CITR	722	1.74	-	723	1.72	-
BSA	707	2.11	0.37	709	2.06	0.34
BSA/IgG	694	2.47	0.36	690	2.58	0.52

The full spectra shown in Fig. 6.14 by external excitation in darkfield configuration and LETJ are depicted for the type I (CITR) and type III (IgG) particle studies with the corresponding calculated signals. LETJ spectra were normalized by their emission in initial state (w/o particles). The individual, unnormalized experiments for the LETJ samples are shown in Fig. B.11. All three spectral features overlap very well indicating transferability of the known detection schemes from optical excitation into electrically driven plasmonics.

The extracted values support the high potential of the measurement scheme as plasmonic nanorulers with sub-nanometer resolution, in which the proof-of-principle was shown for the first time for electrically driven structures. Sub-nanometer changes could be detected by this approach which could be utilized in sensing schemes. Also, refractive index changes in media with constant film thickness could be measured with high precision.

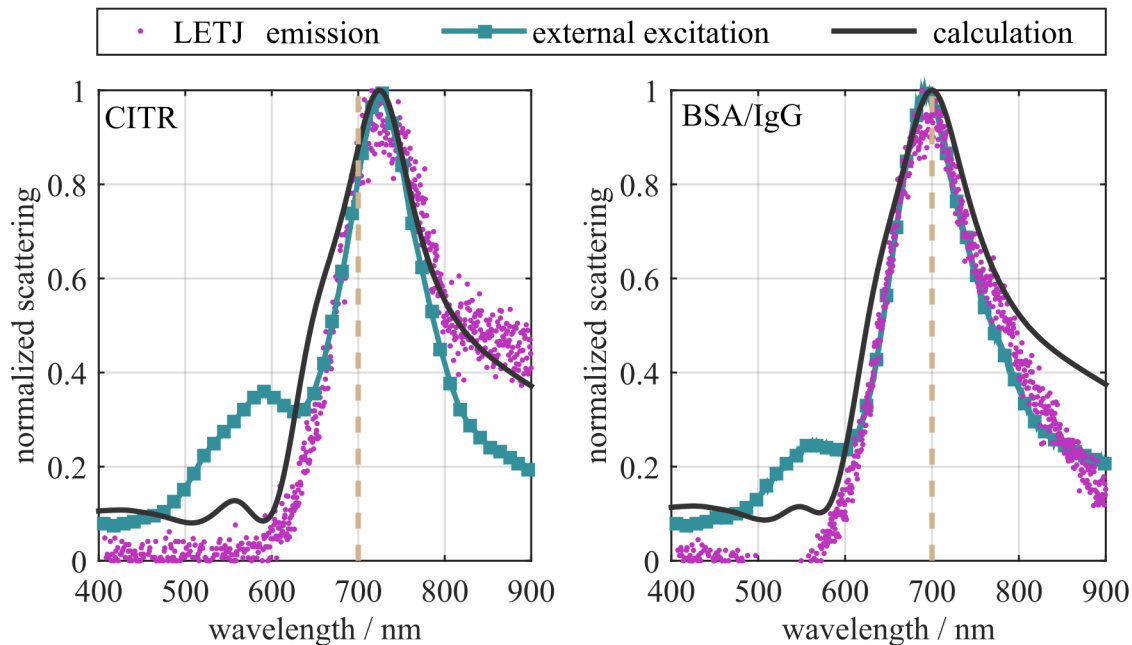


FIGURE 6.14: Scattering spectra of the performed bioanalytical measurements from darkfield measurements (square, teal), LETJ emission (dotted, purple), and calculations (line, black). All spectra are normalized to account for the differences in signal intensity caused by different amounts of contributing nanoparticles. A reference line at 700 nm (dashed, gold) is shown to emphasize the spectral shift between the different states of the experiment.

## 6.4 Emission Localization by Particle Imaging

After the evaluation of the spectral emission observed from electrically driven tunneling junctions, examinations of the topographical features and locations of increased emission were carried out. The enhanced scattering caused by the near-field effects in plasmon coupling should result in drastically increased emission rates from the locations of immobilized nanoparticles. Individual contributions leading to the total signals that were measured in the previous chapters will be elucidated. Different gold particle geometries will be described on their emission features as well as dielectric particles. The utilized setup for these measurements is given in Fig. A.4 with the listed general measurement procedure unless stated otherwise.

### 6.4.1 Plasmon Scattering on Gold Nanospheres

The nanoparticles under scope were spherical gold particles since all previous results incorporated these plasmonic nanostructures. Imaging of a T100-type junction was conducted in darkfield configuration as depicted in Fig. 6.15 (left) after adsorption of gold spheres ( $r_s = 50$  nm). The field of view shows edge scattering at the tunneling area (inner rectangle) and the overlapping gold electrode (outer rectangle) with statistically distributed scattering centers comprised of the adsorbed particles and agglomerates as well as larger objects over the whole junction area.

The right side of Fig. 6.15 shows the acquired data of the same junction at electrical excitation of 3.3 V. Increased count rates were only obtained in the region of the tunneling area. Outer edges were not visible since they overlapped with the protection oxide and were located at an elevated position. Thus, no scattering at the electrode edges was

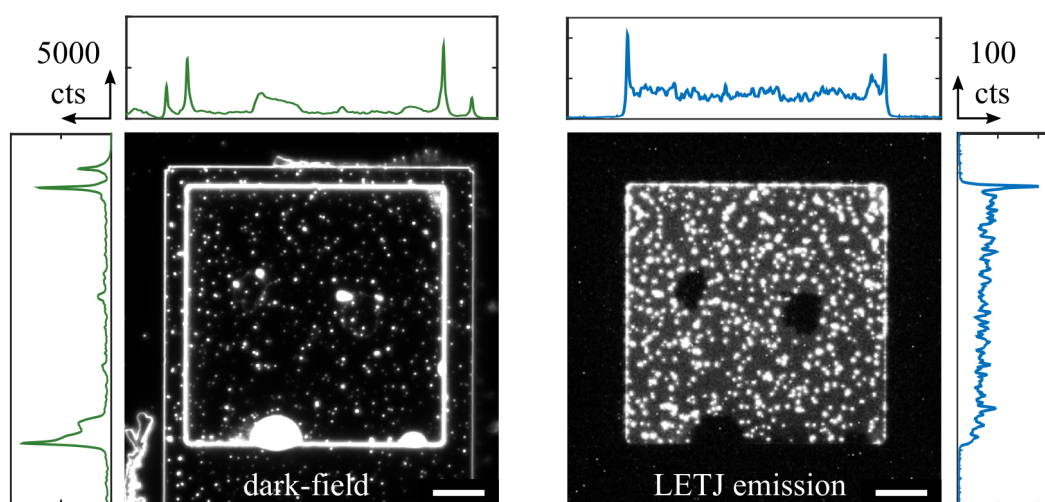


FIGURE 6.15: Measured signals of a junction - type T100 - with immobilized gold nanoparticles ( $r_s = 50$  nm) in darkfield illumination (left) and under electrical excitation (right). The intensity profiles (mean) are plotted on the outer edges. Note the different z-scalings for both measurements. Lateral scalebars: 10  $\mu\text{m}$ .

observed since propagating SPP are scattered at the sidewalls of the etched junction trenches. Additionally, inactive areas located inside the tunneling area indicated an ablated electrode due to the lack of an adhesive layer at the interfaces. Emission hot spots were distributed statistically on the active areas of the LETJ sample. The outer plots depict the line- or row-wise intensity profiles, respectively. Both images were corrected by subtracting the average dark count rate acquired separately with a covered detector and exhibit differences in the retrieved signals. While the large objects and side walls are regions of highest intensity in the darkfield image, electrically driven emission yielded a homogeneous emission pattern with hot spots and side walls as maxima.

Fig. 6.16 depicts the intensity histogram of LETJ image pixel intensities with partially superpositioned peaks before background correction. The total intensity (a) was expected to be comprised of three contributions. The dark count rate determined by the system noise  $y_{BG}$ , the direct emission from scattering of SPP by surface roughness  $y_{DE}$ , and the emission hot spots located inside the junction area  $y_{PAR}$ . Labeled areas in the corresponding images were obtained by simple bandpass-filtering over the width of the illustrated distributions and allow for an initial identification of the signal origins as shown in the subgraphs in Fig. 6.16(b-d). A least-square fit was applied on the histogram to extract the background and direct emission as a result of multiple normal distributions (red, purple). The extracted amplitudes  $a_i$ , mean intensities  $\mu_i$ , and bandwidths  $\sigma_i$  are listed in Tab. 6.17. The particle mediated emission  $y_{PAR}$  was fitted with a exponential pulse function to exclude the influence of the other signal fractions. The ratio of the integrated signals of  $y_{DE}$  and  $y_{PAR}$  yielded 0.63. This weighted the emission features arising from direct emission and particle enhancement for this junction. Thus, the rather large resonance bandwidth of emission spectra from LETJ with nanoparticles as found in prior experiments might be explained by the fact, that both processes contributed comparably to the total intensity at the given nanoparticle concentration.

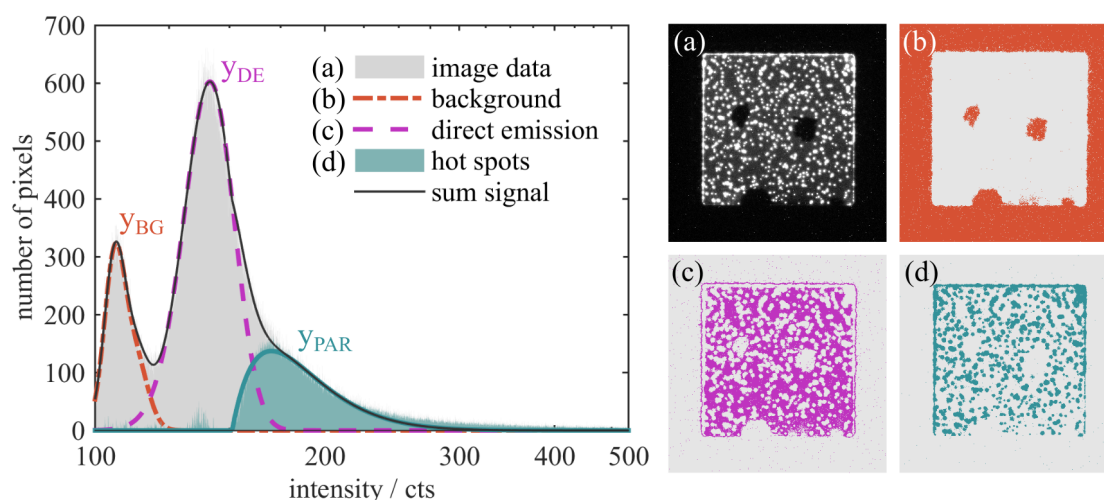


FIGURE 6.16: Histogram of the measured intensities of a biased LETJ with nanoparticles. Different contributions in the signal can be extracted straight from the full emission (a) by bandpass-filtering of the underlying distributions. The first peak corresponded to the background (b), the second was attributed to direct emission by surface roughness mediated scattering and (c) to hot spot emission (d).

TABLE 6.17: Determined values of the distributions as fitted from the intensity histogram of a LETJ biased at 3.3 V. Three signals were assumed to the sum of intensities.

Gaussian	$a_i$	$\mu$	$\sigma$
dark current	246	105.8	7.46
direct emission	602.9	141.4	25.27
Exp. Pulse	$a_i$	$\tau_1$	$\tau_2$
hot spots	548.8	151.2	27.45

### 6.4.2 Hot Spot Assignment

The remaining question of which structural features are involved in the formation of emission hot spots has not been addressed up to this point. In previous experiments the correlation to nanoparticles as scatterers was found by measurements on the emission features before and after immobilization, thus, only depicting an indirect proof by exclusion rules. To directly verify the correlation between adsorbed nanoparticles and emission hot spots, two approaches were chosen as described in the following.

Atomic force microscopy (AFM) was utilized on junctions after imaging their emission. T10 and T100-type junctions were used since their edge length of 10 and 100  $\mu\text{m}$  narrows the region of interest down to a size suitable for AFM measurements. Fig. 6.18 summarizes the experiment by depicting a partial image of a T100 junction. Areas of increased emission are shown in the underlying pseudo-colormap. An 20 x 20  $\mu\text{m}$  height map (green) of this junction is overlaid in the outlined ROI. Hot spots are unambiguously assigned to the locations of immobilized nanoparticles. Also the scattering events at the side walls exhibited an increased emission rate where nanoparticles are adsorbed. Interestingly, not all objects recognized in the AFM image contributed to the emission. By extraction of the height profiles, it was found that these objects had a flat slope and lower height than the nanoparticles and were identified as regions of ablated electrode material. Additionally, a mixture of individual particles and multi-particle agglomerates was determined in the active hot spots (see Fig. B.12).

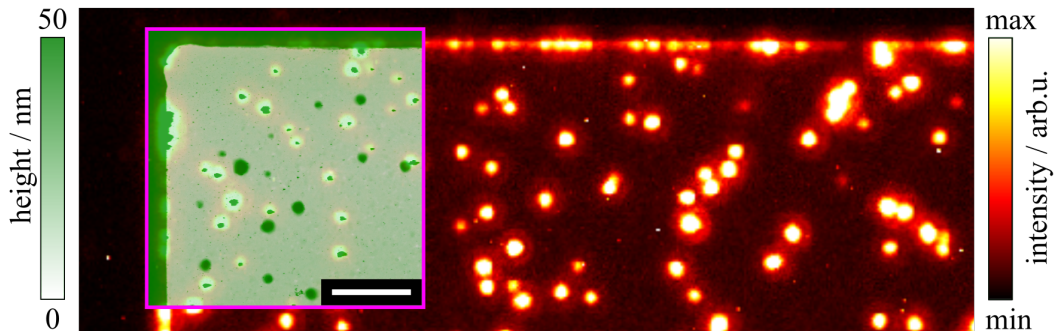


FIGURE 6.18: LETJ emission (right colormap) of a T100 junction biased at 3.3 V with gold nanoparticles ( $r_s = 50 \text{ nm}$ ). The overlaid ROI (purple frame) depicts a 20x20  $\mu\text{m}^2$  AFM topography scan (left colormap) exhibiting a well defined overlap of nanoparticle locations and emission hot spots. Note, that the height colormap was cropped to 50 nm to enhance contrast (see Fig. B.12 for full range). Scalebar: 5  $\mu\text{m}$ .

After the assignment of nanoparticles to the acquired emission rates, a comparison between the obtained darkfield and LETJ data was done. The image of the previously studied junction was cropped to the region of the tunneling area and corrected for slight shifts and rotations along the x-y-axis by affine transformations. Afterwards, a threshold value was set to create a labeling mask which only included the particle areas. From these labeled masks (see Fig. B.13), the individual center of gravity coordinates  $(x_i, y_i)$  were calculated for both images and are plotted in Fig. 6.19 (a). Overall, 419 objects for darkfield (circles) and 357 objects for the LETJ (crosses) ROI were identified, whereby the highest deviation occurred at the locations of the ablated electrode. In these inactive areas (brown), no LETJ emission was possible as determined before, while the external excitation still exhibited signals from scatterers. Additionally, deviations due to false identifications by the obtained mask were minimized by manual cross-checking for implausible objects, e.g. single-pixel objects.

To evaluate the overlap between particle locations, the nearest neighbor distance  $r_{\text{NN}}$  of all DF objects  $i$  to a LETJ object was determined by Eq. 6.7. Hence, the shortest distance to another particle was identified by the approach as schematically depicted in Fig. 6.19(b).

$$r_{\text{NN},i} = \min \sqrt{(x_i - x_{\text{LETJ}})^2 + (y_i - y_{\text{LETJ}})^2} \quad (6.7)$$

As illustrated, hotspot locations for both excitations are largely identical within a narrow range of 10 pixels (purple dashed). This range was set since it converts to 650 nm lateral resolution (see Fig. A.7) and therefore represents a diffraction limited discrimination of the nanoparticles from imaging. 82.3% of all compared objects were found to overlap within the diffraction limit. An even higher correlation of 87.6% was determined when the inactive areas were excluded from the procedure.

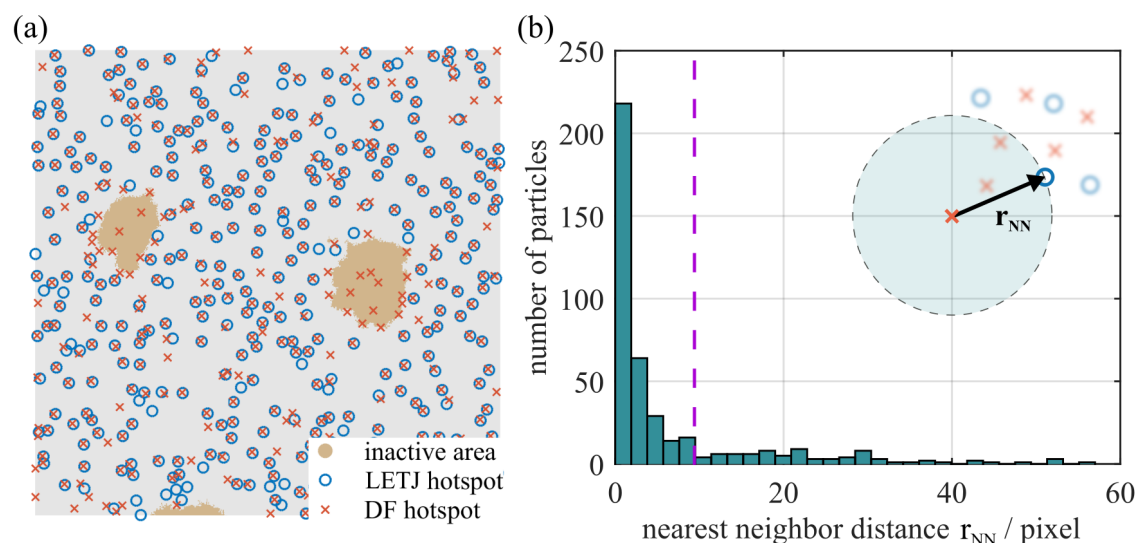


FIGURE 6.19: (a) Central positions of the emission hot spots. The center of gravity locations are plotted for darkfield scattering (DF, cross) and electrical excitation (LETJ, circles). Inactive area (brown) indicate areas of the junction with defect surface electrode. (b) Correlation of the nearest neighbor distance between darkfield and LETJ signals allowing for a comparison of overlapping hot spot locations.



Beside the localization and comparison of the hot spots, their correlation regarding the emitted intensities was studied. Fig. 6.20 shows the relative intensities of 25 randomly selected particles from DF and LETJ emission normalized to the highest signal among them, respectively. Since the particle intensities exhibited a fairly good agreement for individual label numbers, it is appropriate to assume a common physical property of the particles, determining the scattering signal, i.e. the particle/agglomerate size.

The particle label size (area) and mean count rate were calculated and are plotted in Fig. 6.20. Only the objects which were found to coincide for both excitations were used from the labeled masks (357 particles) to remove the influence of non-correlated mask regions. Naturally, the average count rate increases with the label size, stating that larger objects contribute stronger in the emission. The data clearly shows that the LETJ emission is increasing with the increasing scattering efficiency of the particle. This proves that the optical properties of the scattering structures play an important role in the LETJ emission. In this case, it is most probably caused by particle agglomerates on the junction as observed before from AFM measurements. Note, that the offset between both excitation methods is given by the differences in input powers and integration times of the measurements. Thus, it can not be utilized to estimate differences in the emission efficiencies of DF and LETJ. However, a large divergence between both processes regarding the intensity distribution can be seen. While the darkfield particles varied in a large intensity range, the LETJ labels were distributed within a narrow interval. Uncertainties by the measurements were minimized as each underlying image was averaged 100 times in the case of external excitation and 6 times for electrical excitation during exposure. Another explanation is the substantially higher count rate and corresponding broader Poisson distribution of the illumination, but this would entail a homogeneous widening over all particle sizes, whereas the experimental data is distributed rather inhomogeneously over all label sizes.

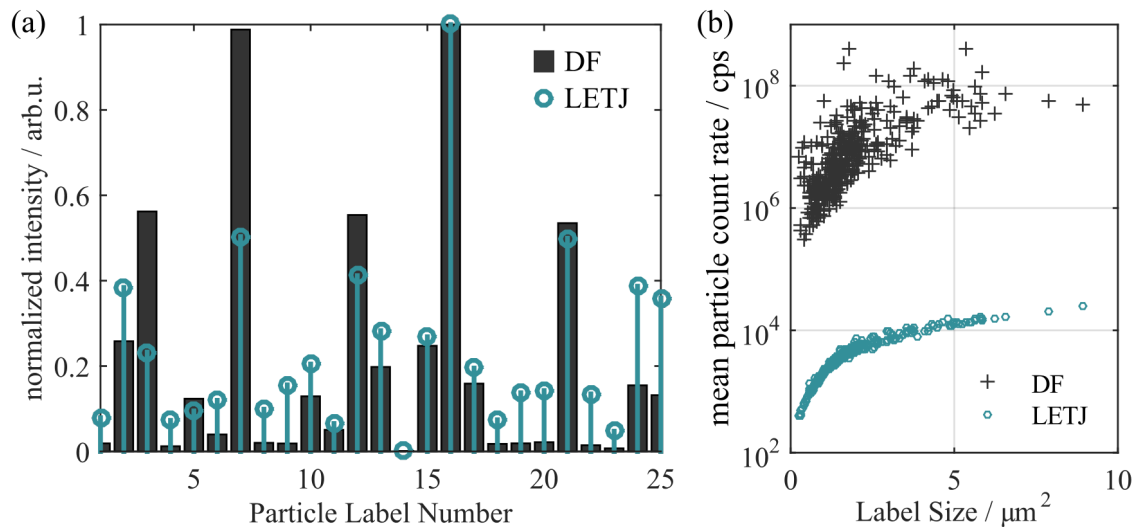


FIGURE 6.20: (a) Comparison of the scattering intensity normalized to the highest intensity for each excitation schemes (DF, LETJ) on 25 randomly selected particles. (b) Mean particle intensities as count rates in dependence of the label size. Increased scattering with larger label sizes is prominent for both mechanisms.

Direct comparison of these particles was done by plotting their intensities for each excitation method against each other. Perfectly identical measurements would result in a linear function with a slope of 1 and a coefficient of determination  $R^2$  equal to 1, whereas uncorrelated processes with a random distribution would have  $R^2$  fluctuating around zero. However, system noise as well as statistical uncertainty always decrease this limit. As indicated in Fig. 6.21, the data exhibited a correlation which was determined by a power series fixed at intercept in the origin. Since the excitation methods were not identical, the slope was determined to 0.52 which describes the difference in the detected intensities but not the emission efficiencies of both mechanisms. However, it still enables a qualitative correlation analysis between individual emission hot spots of the same junction.

Two coefficients of determination were tested with different weighting methods in the presence of outliers. The residuals by weighted bisquares yielded a  $R_{\text{bi}}^2 = 0.841$ , while the coefficient of determination for least-absolute residuals (LAR) was calculated to  $R_{\text{LAR}}^2 = 0.993$ . While the first emphasizes the role of outliers in the data, the latter minimizes the total residual by underrating of outliers. Since a clear definition of outliers is hardly realizable in this case, both values were given. No matter which representation is preferred, a correlation between DF and LETJ intensities was demonstrated, completing the experiment in localization and correlation of hot spots detected from both excitation methods with nanoparticles smaller than the diffraction limit.

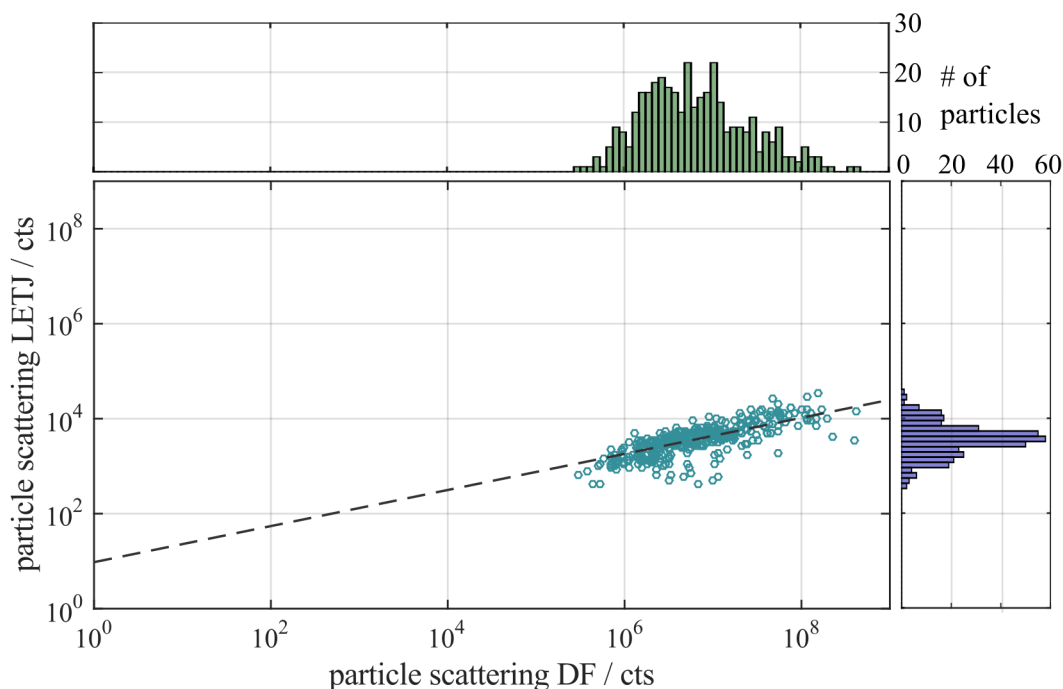


FIGURE 6.21: Correlation of summed scattering intensity (per second) mediated by 100 nm spherical gold particles (357 in total) for darkfield (DF) illumination and electrical excitation (LETJ). The fitted power series was constrained to intersect with the origin and yielded in an least-absolute residual of  $R_{\text{LAR}}^2 = 0.993$ .

### 6.4.3 Plasmon Scattering on mono-crystalline Goldplates

Next, the LETJ emission pattern was extended from arbitrary point-like plasmonic particles to more complex geometries. Thus, objects with well-defined shapes and edge lengths larger than the diffraction-limit were chosen. Mono-crystalline gold flakes were chemically-synthesized at the Leibniz-IPHT according to the protocol given in APP. A.4. These flakes have long edges defined by the crystal orientation and a thickness of around  $110 \pm 40$  nm. Due to their size, these plates do not support localized plasmons in contrast to the previously implemented nanoparticles, but exhibit the properties of macroscopic gold. Thus, they scatter or sustain plasmons at their edges and support SPP on their flat surfaces. Gold flakes were centrifuged twice at 3000 rpm for 5 min to remove residual detergents (CTAB) and redispersed in dH<sub>2</sub>O to minimize effects on the junction from chemicals. Directly before deposition on the samples, the solutions were vortexed for 10-20 s to dissolve precipitates and obtain individual flakes.

Similar to the creation of gap-modes in the particle-film system, the flake edges nearly touching the electrode can support hybridized plasmons. The AFM scan, LETJ and DF image of a LETJ were recorded and are presented in Fig. 6.22 for different junction regions. (a) and (b) depict single flakes of different heights (127 and 81 nm) and geometry, in which the resulting LETJ emission pattern traced the edges of these flakes perfectly and form continuous emission lines with some hot spots. As expected the edges were also visible in the DF image of the flakes and matched equally well with the other methods.

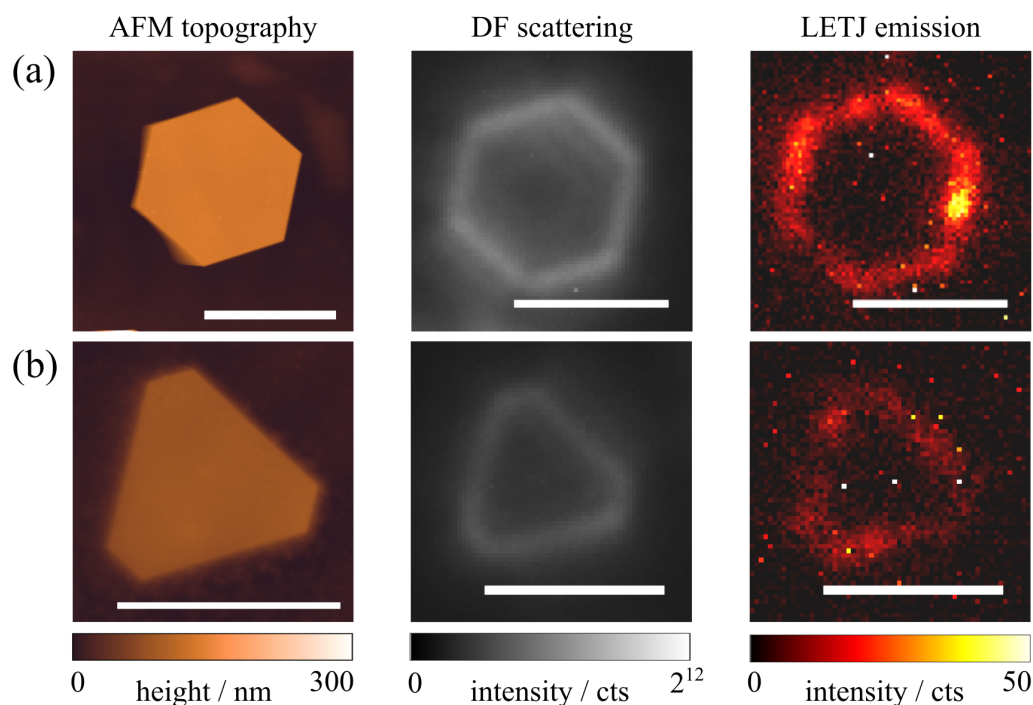


FIGURE 6.22: LETJ with immobilized gold nanoflakes. (a) and (b) depict single flakes of different heights (127 and 81 nm) and geometry. Left - atomic force microscopy scans of single-crystalline flakes with different height and morphologies. Center - darkfield images (DF) of these structures with scattering at the structural edges. Right - LETJ emission of the same flakes at applied bias 3.3 V. The intensity mappings correspond to the morphological features of the flakes. Scalebars: 5  $\mu$ m.

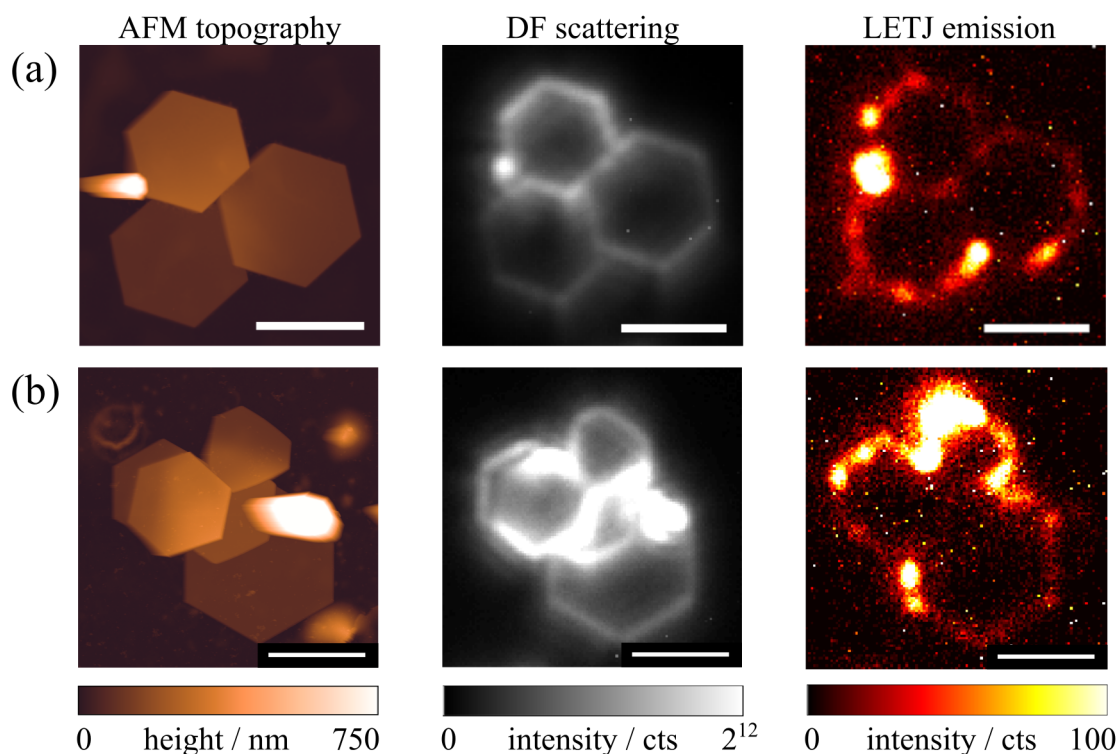


FIGURE 6.23: LETJ with immobilized gold flake aggregates with a flat assembly (a) and a stack of several flakes (b). Left - AFM topography scans. Center - darkfield images (DF) of the scattering signals outline all edges of the stack due to the angle of incidence in illumination. Right - LETJ emission at 3.3 V exhibit enhanced signals only at the outermost edges of the piled particle stack. This is in corresponds the expectation of propagating SPPs at the gold-air interface of the underlying LETJ that are scattered at the outer flake edges. Scalebars: 5  $\mu\text{m}$ .

Aggregates of flakes are shown in Fig. 6.23. Such formations were often found since large particles as these flakes tend to aggregate within seconds after vortexing. Some of the flakes were in direct contact with the gold electrode, others were piled over the bottom flakes and partially on the electrode. Emission was not fully uniform along the edges but showed heterogeneity and some hot spots. This could be attributed to the complex geometry of the stacks forming localized plasmons or interference of the differently faceted flake edges with the gold film [220].

The flakes in (a) were not fully stacked on top of each other but lied densely packed with a small overlap (flake heights: 76, 94, 149 nm). All structural features of the flakes were observable with some hot spot formation at distinct regions. Outer edges exhibited higher intensities than the inner edges of the total geometry. In contrast to this, the inner edges of the stacked pile in (b) were not visible for LETJ samples, but only the edges of the flakes that were in direct contact with the gold electrode, which is in agreement with LETJ emission process. In the case of DF, all accessible edges were observed due to the angle of the incident illumination.

A comparison of the scattering and hot spot formations is shown in Fig. 6.24. Flakes stacked on top of each other (250 nm in height) outline the difference in the scattering effects of both excitation methods. Since darkfield utilizes incident illumination of large

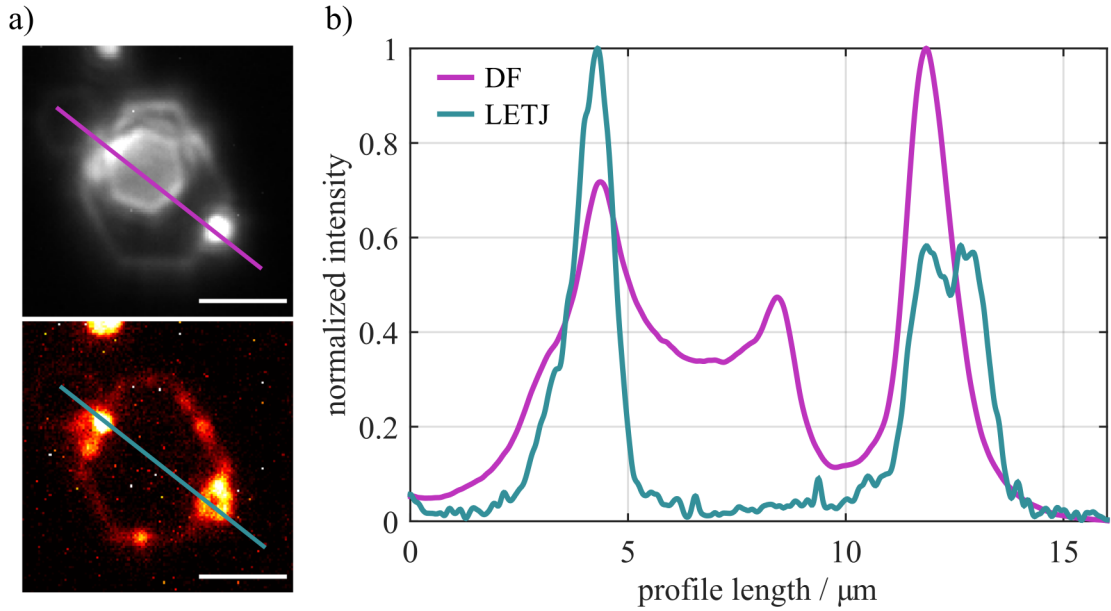


FIGURE 6.24: (a) Edge scattering on a gold nanoflake stack with maximum height of 250 nm in DF illumination and electrical excitation. The profiles as shown in (b) highlight the difference of the scattering intensities. Due to the oblique angle of the DF illumination, scattering was observable at all edges, whereas the scattered surface plasmons in electrical excitation were scattered only at the outmost edges close to the sample surface. Scalebars: 5  $\mu\text{m}$ .

angles, all scattering features and sidewalls of the stack were observable. For the LETJ process, only the outermost edges were visible since scattering of the SPP occurs only at steps in the vicinity of the electrode surface. Hot spot formations were found at similar accessible sides since the formation of these locations is independent of the excitation mechanism. The plotted profiles depict a cross-section of the detected intensities along the indicated lines from the images. While the DF image exhibited high signals from the flake on top of the junction due to tilting, the LETJ intensity was decreased down to the background signal at that point since the uppermost flake was out of range for excitation.

To demonstrate the potential of miniaturization of these chips as compact SPP sources, a small reference experiment was conducted by biasing junctions with a clock battery instead of a stabilized laboratory power supply (see Fig. B.14). However, after proof-of-principle these tests were dropped since comparability was of utmost interest in this work and batteries suffer from discharging.

These experiments showed that it is possible to extend the LETJ emission to line light sources, enabling the design of arbitrarily shaped light emitting pattern at the nanoscale. In contrast to pointlike sources with intensity profiles governed by the diffraction limit, the emission profiles of the flakes are unique in shape and intensity. With these findings, all remaining parasitic radiation processes in question, such as emitting pinning centers or interband transitions of the junctions or degradation effects were ruled out.

#### 6.4.4 Scattering on Metallic and Dielectric Particles

The following experiment aimed at the relation between the properties of the scattering objects and the LETJ emission intensities. In detail, the influence of the nanoparticle material was investigated by implementing plasmon-supporting (metallic) and non-supporting (dielectric) structures. Hence, gold particles ( $r_s = 50$  nm, EM.GC100, BBI solutions) and polystyrene particles ( $r_{PS}=100$  nm, PPs-0.2, Kisker Biotech) were chosen for the study. A solution containing a mixture of both particle types was prepared by diluting the stock solutions of the PS particles (1:1000) and the Au particles (1:10) in dH<sub>2</sub>O. The particles were immobilized by drop-casting 3  $\mu$ l of the solution onto the junction. The subsequent experimental protocol consisted of three analysis steps:

First, an LETJ emission image from the chip with nanoparticles was recorded with the applied voltage, then the voltage was switched off and the scattering properties were characterized with DF microscopy. Afterwards, the topography of the surface was obtained by AFM measurements. The size of the PS and Au particles was intentionally chosen to be different in order to identify them in the topographic AFM scans as presented in Fig. 6.25. Note, that the shown AFM scan was taken after electrical breakdown of the junction as visible from deformed electrode areas and introduced defects.

The LETJ image revealed six point-like emission centers with higher intensities and no

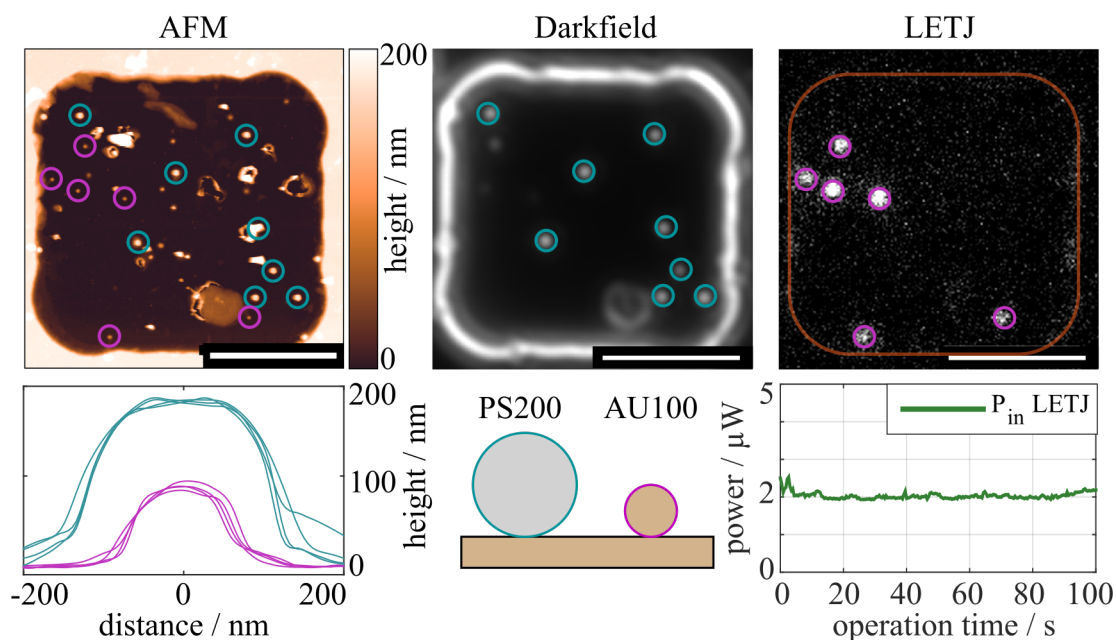


FIGURE 6.25: LETJ junction with metallic nanoparticles (gold,  $r_s = 50$  nm) and dielectric particles (polystyrene,  $r_{PS} = 100$  nm). Height profiles and locations of the immobilized particles were extracted from AFM data (left). Imaging in DF (top, center) exhibited highest scattering at the locations of PS particles and the outer edges of the junction, while LETJ emission (top, right) was only observed at locations of metallic nanoparticles (violet circles – Au NP, blue circles – PS NP). Constant power consumption of the chip during LEIT (bottom, right). Scalebars: 5  $\mu$ m.

outline at the edge of the LETJ area. For the DF image, completely different information were obtained, as the highest signals were recorded at the junction edges and the locations of PS particles. The latter are visible as distinct scattering centers, which do not coincide with any feature of the LETJ image. The locations of the metallic particles were also obtained in the DF image but their intensities were orders of magnitude lower than the maximal values. Assignment of the features in the optical images was done by AFM as before and allowed for the identification of gold and PS particles based on their height. By combining the structural and optical information, it was found that only the gold nanoparticles contributed effectively to the emission of the LETJ sample. In contrast, the DF image showed much stronger signals for the larger PS particles by scattering, which resulted in a high visibility of these particles due to their size, depicting the opposite case of the LETJ image.

Additionally, it had to be considered that the obtained signals could be impaired by the spectral profile of the excitation mechanisms. These would entail selective excitation of the different particles. Unfortunately, measurements of the electrically driven spectra from individual particles was not achieved, due to the low intensities in LETJ emission. This impeded a direct analysis of the emitted light, but an alternative deduction method was used. Spectra of these nanoparticle types were recorded by a Sagnac interferometer based hyperspectral system (SpectraCube, Applied Spectral Imaging) attached to the imaging setup (see Fig. A.4) in darkfield configuration with an integration time of 100 ms per point. One measurement is depicted in Fig. 6.26, in which both spectra in (a) are 10 averages of the particles as shown in (b). The gold particles exhibited gap-modal features, resulting in the specific bonding ( $\approx 730$  nm) and anti-bonding ( $\approx 585$  nm) mode peaks. In contrast, the polystyrene nanoparticles on the gold-film showed a broad scattering spectrum with a single peak ( $\approx 630$  nm). Note, that also dielectric particles on a metallic film exhibit altered spectral properties compared to the  $1/\lambda^4$  scattering dependency as valid for dielectric substrates [221] (see Fig. B.15). Since the spectral features were clearly distinguishable, a classification was also possible by calculating the intensity ratio of the resonance bands by  $(\int_{F_1} I + \int_{F_2} I) / \int_G I$  with the bandpass filters  $F_1$ ,  $F_2$  and  $G$ . The masks of the assigned particles are shown in (c).

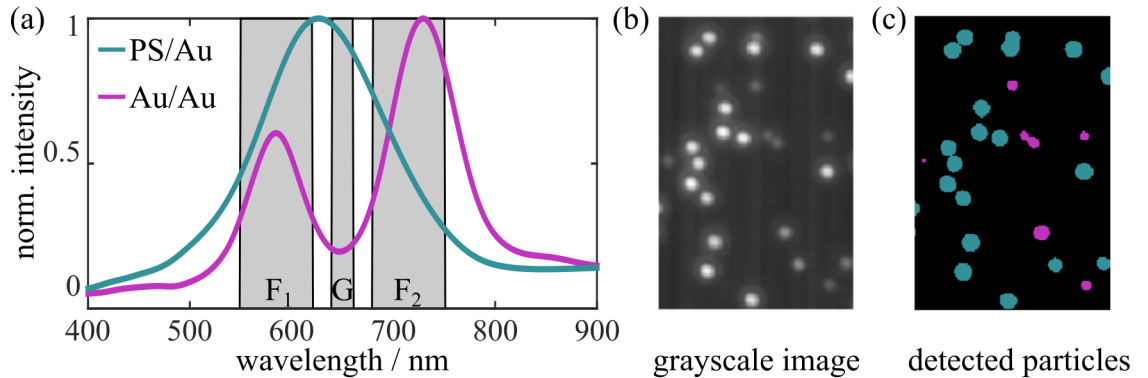


FIGURE 6.26: (a) Experimentally determined scattering spectra of gold particles  $r_s=50$  nm (purple) and PS particles (teal) with radius 100 nm located on top of a gold substrate. The grey areas depict the filter regions to assign the type of particle. (b) Grayscale image with a mixture of Au and PS particles. (c) Particle classification obtained by spectral bandpass filtering with  $F_1, F_2$  and  $G$  as depicted in (a).

Although, the spectra for both particle types are not identical, they were still in a wavelength range that both excitation mechanisms should be capable of interaction with the chosen particles. Together with the results from Section 5.1 that underlined the broadband nature of electrically driven plasmons and Section 5.2 in which the cutoff frequency of LETJ was determined, the spectral bandwidth is comparable to a halogen light source as used in the DF detection to some extent. Thus, the strong signal differences in acquired DF and LETJ experiments as in Fig. 6.25 can not simply be explained by the different excitation intensity profiles, but rather based on the differences in the scattering process of free propagating photons (DF) and of electrically driven coupled plasmons to the top electrode (LETJ). These results strongly indicate that resonant plasmon scattering on the gap-modes plays an important role in the LETJ emission process.

The AFM image in Fig. 6.25 also shows the presence of debris on the surface of the sample and defects of the top gold electrode, which presumably arose from degradation of the top layer during the experiment. On the bottom area of the chip, the top electrode was ablated, which can be seen in the AFM and DF images. These defects as well as other non-scattering objects and the edges can not be seen in the LETJ imaging. Therefore, LETJ samples might be potential sources for plasmon imaging with excellent background suppression.

In an additional experiment, which incorporated different nanoparticle materials, the influence on particle aggregation on the intensity of the LETJ emission was elucidated. Gold cubes [222] with an edge length of 70 nm and PS nanoparticles ( $r_{\text{PS}} = 100$  nm) were deposited on a T10 sample which exhibited a different junction geometry due to overexposure in the fabrication process. The advantage of these cubes over spherical metallic particles is their capability to form well defined dimers. Experimental data is presented in Fig. 6.27 with a topographical overview obtained from SEM imaging and an AFM scan together with the emission map acquired by LETJ imaging. Distinct emission spots with different intensities were visible in the junction area with low edge scattering at the junction sidewalls as observed before.

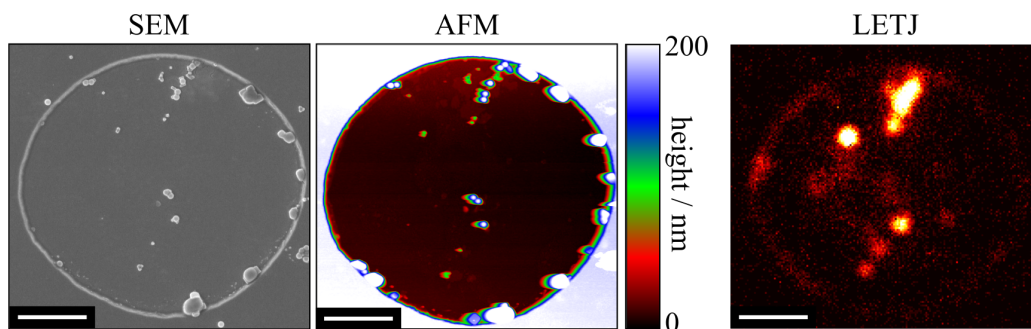


FIGURE 6.27: left/center - SEM/AFM image of a T10 junction with two types of sparsely immobilized nanoparticles: polystyrene spheres ( $r_{\text{PS}} = 100$  nm) and gold cubes with edge length 70 nm. right - LETJ emission image at 3.3 V recorded with 10 s exposure. The nanoparticle positions are correlated well with hot spots, but not all particles contributed to the emission. Mainly agglomerates formed hotspots. The junction edges scattered very weakly and non-plasmonic particles were not observable due to the lack of hybrid plasmon modes. Scalebars: 2.5  $\mu\text{m}$ .



SEM was used to distinguish between individual cubes, closely separated cubes, and multimers. These three groups were identified and their corresponding LETJ emission spots assigned as shown in Fig. 6.28. Polystyrene beads were immobilized as reference. Cube dimers (green frame) strongly increased the intensity of the LETJ emission in comparison to single cubes (blue frame). This effect was also observed for separated cubes in vicinity of each other (purple frame). Thus, the assumption of just two emitters placed closer than the diffraction-limit of the optical system is not sufficient to describe this effect, but it has to be induced by the complex coupling of plasmons between the cubes and gold layer.

These results demonstrated that objects made of dielectric materials are ineffective LETJ emitters in contrast to the objects which support plasmons such as metallic nanoparticles. Additionally, it was found that coupling between plasmonic particles occurs for particle-film systems as well as for agglomerates of these particles, substantially enhancing the emission process. This has been established by cubic nanoparticles promoting the formation of suitable, defined gaps between the particles. These features could be especially interesting in energy guiding, confinement, and localization or line sources of emission by controlled stacking and alignment of similar anisotropic particles.

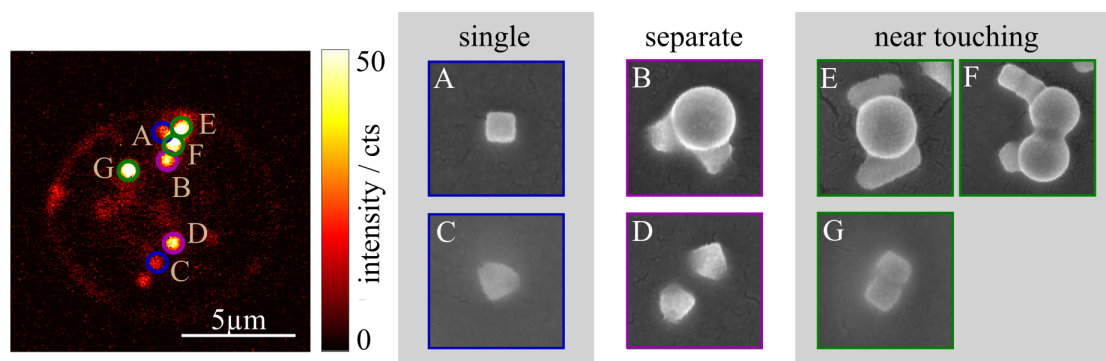


FIGURE 6.28: LETJ emission image of a 10  $\mu\text{m}$  junction with PS200 and cubic AU80 particles (left). Emission hot spots were found for all locations where plasmonic particles were immobilized. These regions of increased emission were correlated by SEM imaging (right). Emission hot spots were formed by single gold structures (A,C), separated particles (B,D), in which highest intensities were found for clusters and agglomerates of particles (E,F,G).

### 6.4.5 Investigations of Emission Instabilities

Next, the short temporal stability of the LETJ emission was investigated. Gold spheres were adsorbed on a chip and then a sequence of images in electrical excitation was recorded for a total time of 30 s with 2 fps (integration 500 ms) biased at 3.0 V. Some of the individual particles exhibited significant fluctuations in their emission intensity in the timeseries, whereas others seemed to emit steadily. An example of such an fluctuating emitter is given in Fig. 6.29 with the sum signal of an individual particle over the measurement time, the power consumption of the whole junction (bottom), and selected images at times of highest intensity fluctuations (top). Points  $P$  depict lowest intensities, in which  $Q$  represent states of highest emission. The measurement revealed that the intensity changed in a range of 50 to 250 kcps for this particle, depicting a relative change of 5x the original signal. During the experiment, the electrical power consumption was monitored and it exhibited stable functionality. Hence, the blinking behaviour seems to be an induced effect (more intense after few seconds), but it does not damage the LETJ junctions or nanoparticle emitters macroscopically. In contrast to degradation, their signals do not simply decay or stay dark, but resemble an oscillation.

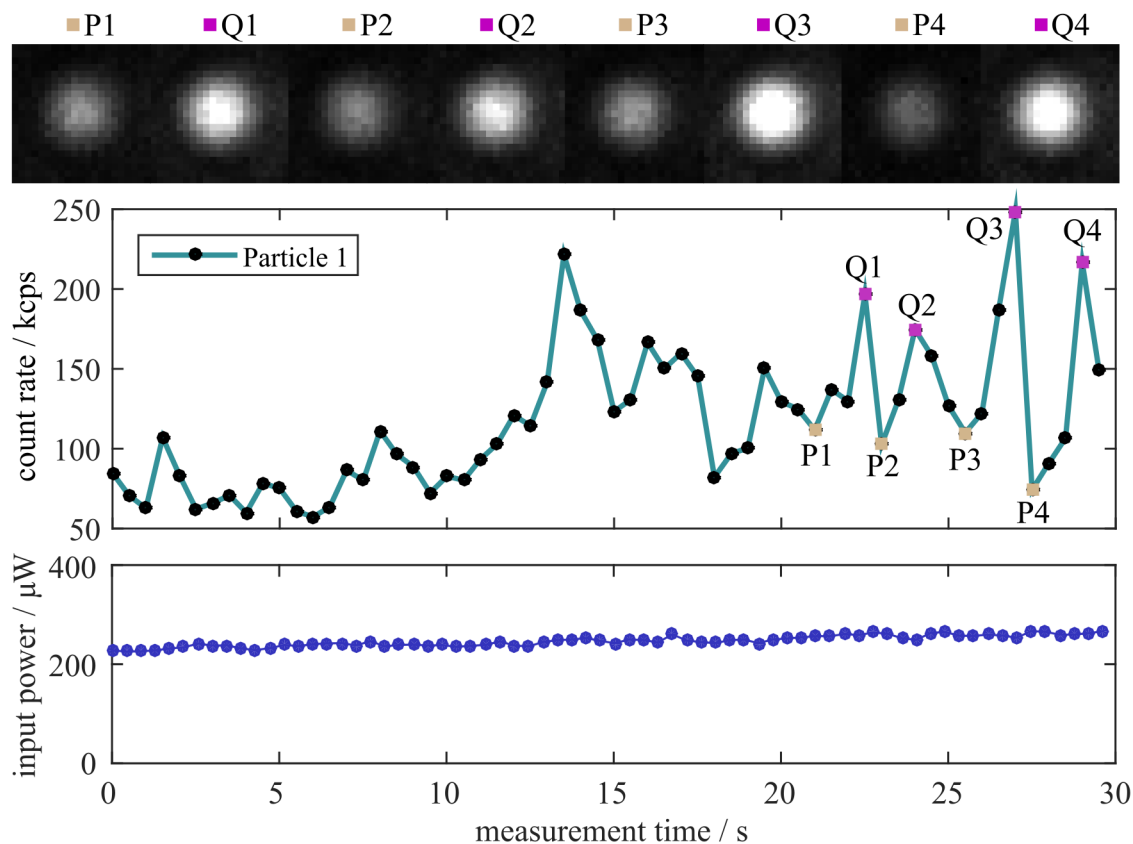


FIGURE 6.29: Intensity fluctuations in LETJ emission by a chip biased at 3.0 V. A steady count rate is observed for the first 10 s. With longer operation time, fluctuations occurred, which did not correspond to decreasing efficiencies or electrical breakdown. Intensity modulations were in the frequency regime of less than 1 Hz.

Four examples of such blinking effects of single emitters are depicted in Fig. 6.30 (a). The data shows that the intensity fluctuations between the LETJ hot spots are not correlated and differ strongly in their amplitude (scaling factors given at right border). To outrule any external mechanical or electrical perturbations which could negatively influence the interpretation, the power spectral density for the whole junction area was calculated (Fig. 6.30 (b)). With this, the average LETJ emission power was split into its frequency components. It was found that the integrated signal of the junction did not exhibit any specific oscillation (peak only at zero frequency) and therefore indicated stable measurement conditions. At the same time, it can be concluded that only a fraction of particles was affected by these fluctuations, as a high energy fraction should have been observable in the power spectral density. This implies that emission instabilities at this level are neither coherent nor due to setupwise modulations, e.g. by vibrations.

However, to investigate this further, autocorrelations of the emission centers were conducted for ROIs from the image. These ROIs were cropped down to sizes that only individual spots were included. Some representative autocorrelation functions (ACF) that were obtained are shown in Fig. 6.31. In total, 92 of the 463 analyzed emitters exhibited low-frequency blinking as given in the graphs. The entirety of particles was recorded in the same measurement, thus excluding mechanical instability of the setup, since a correlated fluctuation would be observable. The main frequency component  $f$  from the ACF was extracted by fitting a sinoidal function (Eq. 6.8) to the data:

$$y = a \cdot \sin(2\pi ft + \phi) + c. \quad (6.8)$$

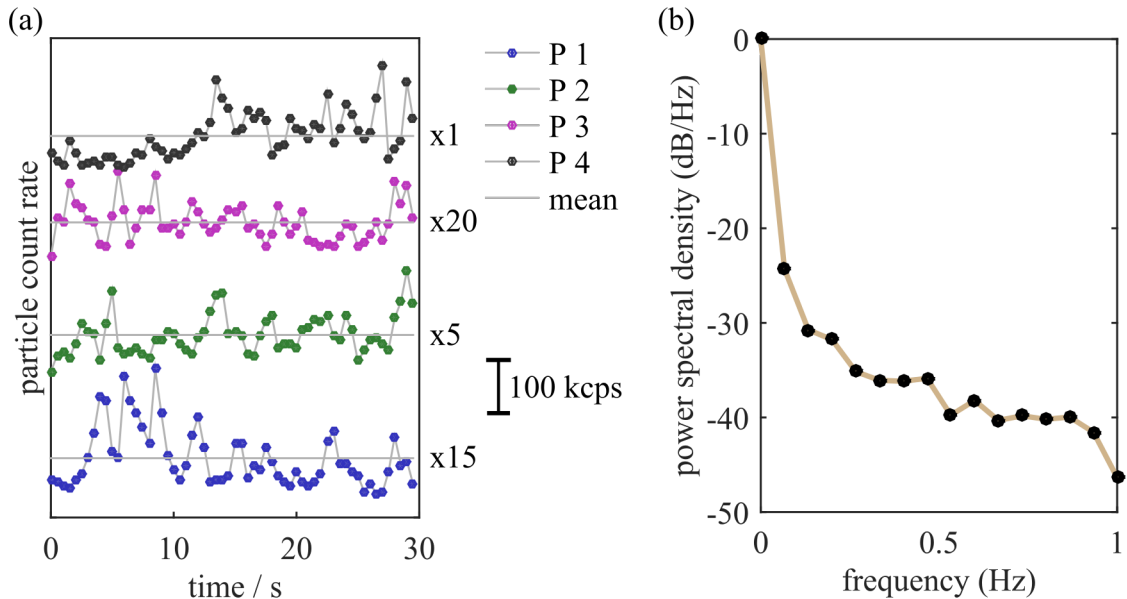


FIGURE 6.30: (a) Exemplary intensity time trace of four individual gold particles excited at 3.3 V. Curves are offset and multiplied by the factor listed on the right side for better visibility. (b) Power density spectrum for scattering timeseries averaged over all detected particles. No pronounced low frequency oscillation can be extracted despite the constant (0 Hz) emission.

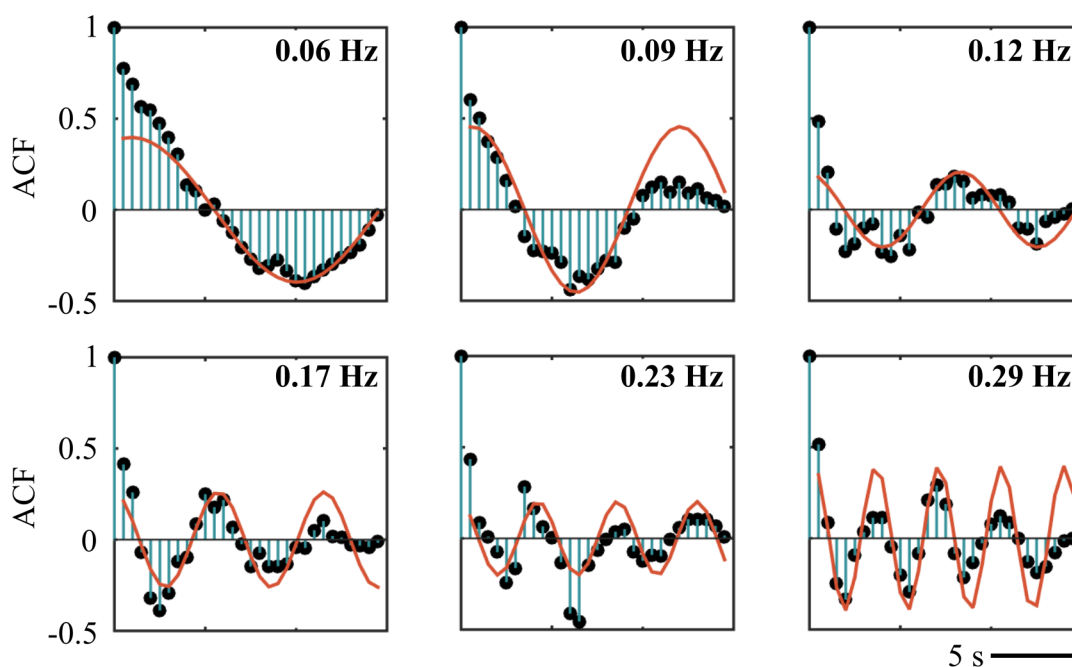


FIGURE 6.31: Autocorrelation functions of different emission hot spots formed by nanoparticles from the same experiment. Different low-frequency components were determined which indicate a non-correlated process in the junction causing emission fluctuation similar to blinking effects in optics.

Different low frequency components were found ranging from 0.06 Hz to 0.29 Hz. The underlying effect of the fluctuations is most certainly not limited to these frequencies, but given by the minimal integration time of the experimental setup. Hence, a maximal detection limit of 1 Hz was set by Nyquist theorem, while a reliable limit was further reduced by the noisy data. Nonetheless, a set of non-correlated frequency components was found from the exact same measurement in which the sample was fed by a constant bias and no alternating current. High frequency components obtained by controlling the amplitude of an AC signal overlayed on the DC have been demonstrated by another study [162] which differs fundamentally from this process.

Possible explanations could lie in the characteristics of gap-mode plasmons (intensity, spectral position) and their high sensitivity on the NP- substrate distance. Moreover, the nanoparticles have thin organic layers to increase their stability in solution. Dissipated thermal energy in the junction could modify this organic layer or influence the junction density of states locally due to heating at defects. Such induced particle-film distance variations or changes in the available states are the most plausible explanations for the observed LETJ emission blinking effect next to nanoscopic defects in the oxide which are promoted during operation. However, since no clear correlation for this effect was deducted, further studies should be conducted with time correlated single photon detection schemes to deconvolve and analyze the individual aspects of these observations and solve the issue of undersampling. Additionally, conductive AFM or STM measurements could complement interpretations of the underlying structural origins.

### 6.4.6 Emission in Liquid Environment

In the final experiment, the capability of LETJ emitters to work in aqueous environment was investigated. This is of special interest for certain sensoric applications, such as in biosensing. A drop of aqueous solution of gold spheres was placed on the active area of the LETJ chip. The chip was mounted on the stage of the optical microscope with a water immersion objective (N-Achroplan W, 63x, NA 0.9, Zeiss). It formed a water meniscus between the sample and the objective. Spherical nanoparticles could freely diffuse in the aqueous environment and some of them adsorbed over time on the active area of the chip. The objective itself was prepared by pipetting a droplet of deionized water on the lens and fitting of kitchen foil on the droplet to prevent nanoparticle adsorption on the objective itself. Two acquisitions with and without applied bias at the junction were recorded with an integration time of 10 s and are presented in Fig. 6.32. The power consumption of the junction was measured prior and after the experiment and found to be functional, but the power rose to  $\approx 150\%$  of the initial state at the same time. This indicates degradation of the junction to some extent. However, emission hot spots were observed in the images and exhibited the same characteristics of localized point-like emitters as in section 6.4.1. These results show the potential transferability of such LETJ and electrically-driven plasmons into biologically relevant environments.

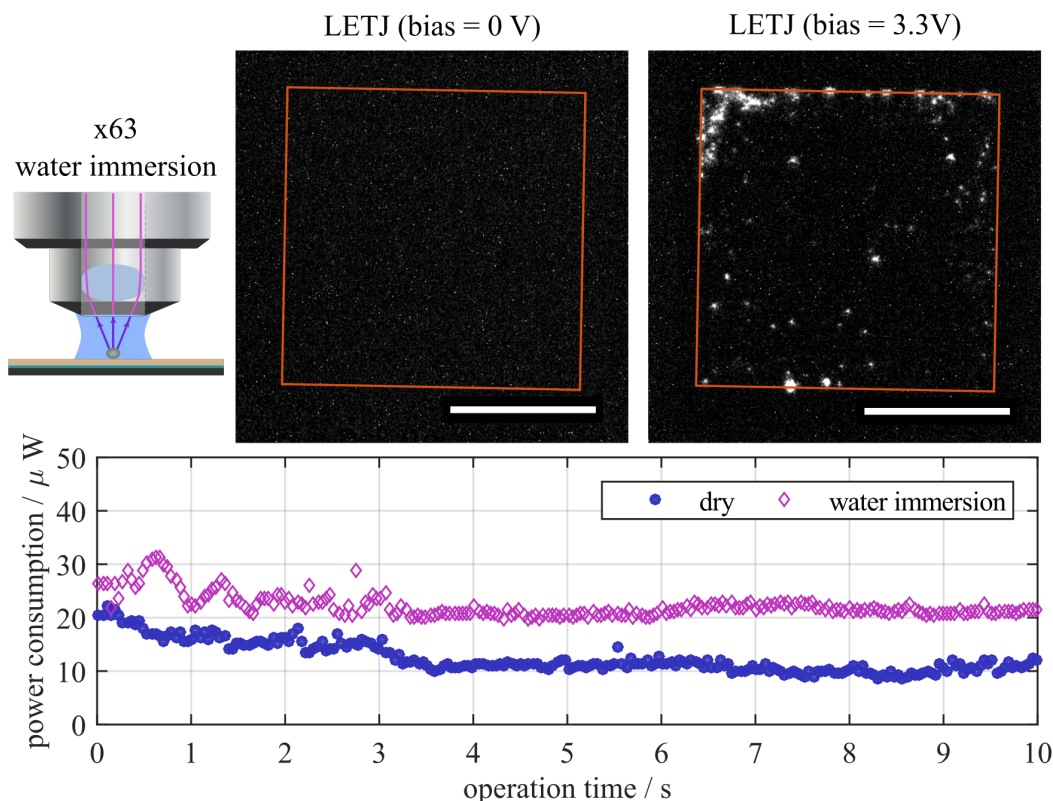


FIGURE 6.32: LEIT emission measured in liquid environment with a water immersion objective. 100 nm gold particles were immobilized on the sample surface before the experiment. The intensity was mapped without sample bias ( $V_g = 0\text{ V}$ , left) and at ( $V_g = 3.3\text{ V}$ , right). The junction outline is labeled (orange). Emission hot spots were mainly located at the edges of the LETJ junction. Scalebars: 50  $\mu\text{m}$ .

- page intentionally left blank -

## 7 | Summary and Outlook

The aim of this thesis was the fabrication of functional, large scale tunneling junctions and the investigation of their light emission features based on inelastic tunneling. In recent years, these junctions sparked new interest since they represent a potential candidate to bridge gaps between optics and electronics, e.g. by local, electrical launching of plasmons, as single photon sources or electrically-tunable, self-emitting metamaterials in sensing or ultrafast opto-electronics.

Planar junctions were fabricated from thin-film material stacks based on a heavily n-doped silicon substrate and atomic layer deposition for the tunneling barrier. By the usage of standard photolithographic methods and corresponding masks, a parallelized fabrication on wafer scale was achieved. This depicts the potential for upscaled production of such junctions similar to nanoelectronics, since the utilized light emitting tunneling junction geometry is based on the design of a thin-film plate capacitor. With this, experimental characterization methods regarding the electrical properties of these junctions were described by established theories of current-voltage characteristics and impedance spectroscopy. Thus, reproducible and straight-forward comparable results to other studies were obtained and enabled a direct estimation of junction parameters such as the tunneling barrier potential and effective oxide thickness.

Functionality of the samples was found to be dependent on the size of the junctions as well as the thickness of the tunneling oxide. This was attributed to the increased chance of pinning centers, surface charges at interstitial layers and defects per unit area. Spectral emission features for these junctions were analyzed and determined for a set of parameters. It was found that the spectra exhibit the bias dependent cut-off frequency and the emission intensity as function of the tunneling current as described by theory. Implementations of different electrode materials yielded a shifted spectral central position and shape, in which the cut-off frequency was shifted, which strongly indicates the influence of the potential barrier at the anode-insulator interface. With experiments on the emission at different bias polarities, the underlying effect of inelastic tunneling as source of the detected radiation was proven. Experiments on the signal stability exhibited stable operation at applied bias in the range of few volts compatible with modern electronics.

The interaction with chemically-synthesized nanoantennas adsorbed on the junction surface was simulated numerically by finite element methods and experimentally verified. Immobilized nanoparticles resulted in enhanced scattering of the propagating

surface plasmons to free-space radiation and an increased emission rate depending on the nanoparticle surface concentration. Simultaneously, these particle-film systems exhibited a distance dependency of the resonance energy as valid for plasmon hybridization. This was verified for electrically-driven plasmons from light emitting tunneling junctions by an experiment comprising different organic spacer layers made from proteins as capping at the nanoparticle surface. Comparison with theory demonstrated the potential transferability of the gap-mode detection scheme as known from optical excitation schemes (plasmon nanoruler [212]) and possibly other sensing methods based on plasmonic interactions.

Localization of emission hot spots was compared for darkfield scattering, electrical excitation and was correlated to topographic scans by atomic force microscopy. Electrically-driven structures exhibited enhanced emission at locations of adsorbed nanoparticles and a minimization of non-plasmonic background contributions compared to dark-field illumination. Different geometries and materials of nanoparticles demonstrated the role of plasmon hybridization by the nanoparticles in emission. Gold nanospheres exhibited strong coupling and scattering, whereas dielectric particles did not contribute in the overall signal. Intensity fluctuations of individual particles were found at steady-state operation conditions and found to oscillate at low frequencies. Additionally, a proof-of-principle experiment of a light emitting tunneling junction in liquid environment was done. With this, the potential applicability of these junctions in sensing schemes was shown.

During the course of this work fundamentally new understandings on the underlying theory light emission from inelastic tunneling and its description by the density of states as defined from the involved material parameters have been published [61, 223]. With these, also the main obstacle of low emission efficiencies might be overthrown. Rendering these junctions useful in manifold applications due to their spectral versatility by the choice of incorporated materials and structuring methods.

Future research could handle further improvements on longterm stability of large area junctions by thermal annealing during fabrication. Analysis methods from semiconductor physics might give additional insights, such as deep-level-transient-spectroscopy or secondary ion mass spectrometry. Especially with the usage of a semiconductor as substrate, the parameters of doping concentration and type depict interesting fields of research in electrically driven plasmonics. Future studies could advance on light emitting tunneling junctions as plasmonic biosensor operating in liquid environment based on the described results and transferred to other sensing approaches.

With the vast amount of materials and structuring methods from nanoelectronics that are compatible with this approach, also the electronic structure and resulting energy band diagram of the multilayer thin-film stack should be almost freely tunable. In combination with chemically-synthesized nanostructures or lithographically structured metasurfaces, substantially increased device performances and broad-banded applications are to be expected in the future.



## 8 | Zusammenfassung

Zielstellung dieser Arbeit war die Herstellung funktionsfähiger, großflächiger Tunnelstrukturen sowie die Untersuchung der, auf dem inelastischen Tunneleffekt basierenden, spektralen Emissionscharakteristika.

Planare Tunnelstrukturen, bestehend aus Dünnschicht–Materialstapeln, wurden im Zuge dieser Arbeit gefertigt, wobei ein stark n-dotiertes Siliziumsubstrat als Ausgangsmaterial und Atomlagenabscheidung zur Herstellung der Tunnelbarriere diente. Durch die Nutzung Photolithographietechniken und den dazugehörigen Strukturierungsmethoden konnte eine hochparallelisierbare Herstellung der Strukturen im Wafermaßstab erreicht werden. Da die Schichtstapel technologisch einem Dünnschicht-Plattenkondensator entsprechen, sind somit ähnliche Skalierungen in Stückzahlen und Dimensionen denkbar. Weiterhin wurden etablierte Analysemethoden, wie Strom–Spannungs–Analysen und Impedanzspektroskopie, um die hergestellten Strukturen hinsichtlich ihrer elektrischen Eigenschaften zu untersuchen. Über Rekonstruktion und Analyse des Ersatzschaltbildes oder Regression der Tunnelströme wurden Informationen über die Tunnelbarriere und -oxiddicke gewonnen.

Funktionalität und Stabilität der Proben sind abhängig von der Tunnelfläche und Oxiddicke, was einer erhöhten Wahrscheinlichkeit von Oberflächenladungen, Defekten und sogenannten "Pinning"-Zentren zugeordnet werden konnte. Die spektralen Eigenschaften wurden hinsichtlich mehrerer, aus anderen Studien, bekannter Parameter untersucht. Dabei wurden die Strukturen hinsichtlich ihrer maximalen Emissionswellenlänge und spannungsabhängigen Emissionsintensität evaluiert. Durch die Implementierung unterschiedlicher Elektrodenmaterialien wurden, von der Theorie abweichende, Emissionsfrequenzen ermittelt, welche mit hoher Wahrscheinlichkeit durch die Potentialhöhe an der Anoden-Isolator-Grenzfläche und den damit verbundenen, veränderten Tunnelbedingungen, definiert ist. Experimente an Tunnelstrukturen bei positiver und negativer Polarität wurden genutzt um inelastisches Tunneln von sogenanntem "hot electron decay" zu unterscheiden. Zusätzlich konnte eine Reproduzierbarkeit und Signalstabilität im Bereich niedriger Spannungen gezeigt werden, welche die Kompatibilität mit aktueller Elektronik unterstreicht.

Die elektromagnetische Kopplung lichtemittierender Tunnelstrukturen mit chemisch synthetisierten, oberflächenimmobilisierten Nanopartikeln, wurde mittels Finite-Elemente-Methoden simuliert und experimentell nachgewiesen. Hybridisierungseffekte elektromagnetischer Nahfeldkopplung für Partikel–Film–Systeme sind durch Studien mittels

externer Anregung bekannt. Dieser Effekt wurde für elektrisch-angeregte Plasmonen verifiziert und in einem Experiment mit organischen Proteinmonolagen als Partikelhülle genutzt. Dabei konnte die Äquivalenz optisch und elektrisch angeregter Oberflächenplasmonen für dieses System aufgezeigt werden.

Areale erhöhter Emissionsintensität (engl. *hot spots*) auf nanopartikelverstärkten Strukturen wurden in elektrischer Anregung lokalisiert und mit Streulichtexperimenten in Dunkelfeldkonfiguration sowie Topographieaufnahmen mittels Rasterkraftmikroskopie verglichen. Über die Korrelation der Daten wurden die Positionen der Emissionsmaxima mit denen von adsorbierten Nanopartikeln in beiden Anregungsmethoden zugeordnet. Weiterhin konnte über Experimente an verschiedenen Nanopartikelmaterialien und -formen gezeigt werden, dass Emissionsmaxima an plasmonisch aktiven Materialien auftreten und elektrische Anregungen im Vergleich zu Dunkelfeld-Konfigurationen weniger Hintergrundsignalen durch dielektrische Streuzentren unterliegen. Erstmals wurde die Emission lichtemittierender Tunnelstrukturen in flüssiger Umgebung über ein Wasserimmersionsobjektiv detektiert, was speziell für potentielle Anwendungen in der Biosensorik relevant ist. Während der Bearbeitung dieser Monographie wurden neue Publikationen veröffentlicht, welche die zugrundeliegenden Mechanismen der Lichtemission durch den inelastischen Tunneleffekt mit den lokalen Zustandsdichten der Tunnelstruktur in Verbindung bringt [61, 223]. Mittels dieser neuen Erkenntnisse kann einer der größten Nachteile solcher Strukturen, die niedrige intrinsische Quanteneffizienz, systematisch bearbeitet. Somit könnten elektrische Anregungsmechanismen für Plasmonenresonanzen vielfältige Anwendungen finden, da sie über die Wahl der implementierten Materialien und Strukturierungsmethoden in ihren optischen Eigenschaften eingestellt werden können.

Weiterführende Studien sollten sich mit der weiteren Verbesserung der Langzeitstabilität von großflächigen Tunnelstrukturen beschäftigen; beispielsweise über thermische Behandlungsschritte der einzelnen Schichten während der Herstellung. Analysemethoden aus der Halbleiterphysik könnten dabei zusätzliche Einsichten in die Funktionsweise der Strukturen liefern, indem Störstellen mittels DLTS (engl. "deep level transient spectroscopy") untersucht oder präzise Profile der Materialzusammensetzung mittels Sekundärionen Massenspektrometrie korreliert werden. Durch die Nutzung eines Halbleiters als Substrat kommt der zusätzliche, frei einstellbare Parameter der Dotierkonzentration ins Spiel, um die Strom-Spannungcharakteristika weiter zu optimieren. Analysen über Kapazitäts-Spannungs-Kennlinien und temperaturabhängigen Strom-Spannungskennlinien gaben einen experimentellen, quantitativen Aufschluss über die dominanten Leitungsmechanismen und deren Beitrag in der Lichtemission. Zusätzliche Kerngebiete weiterer Studien, könnten die Weiterentwicklung der Strukturen hinsichtlich ihrer biosensorischen Nutzung in wässriger Umgebung und der Überführung zusätzlicher Sensorprotokolle sein, sowie die Bestimmung der quantitativen Detektionslimits.

Aufgrund der Vielfalt an einsetzbaren Materialien und Strukturierungsmethoden die, mit dem in dieser Arbeit vorgestellten Ansatz, kompatibel sind, sollte die resultierende Energiebandstruktur mehrschichtiger Systeme flexible Einstellmöglichkeiten bieten. Somit könnten lichtemittierende Strukturen die limitierenden Faktoren der geringen Quanteneffizienz weiter überwinden und Einzug in vielfältige Anwendungen finden.

# References

- [1] J. Lambe, S. L. McCarthy, “Light emission from inelastic Electron tunneling”, *Phys. Rev. Lett.* **1976**, *37*, 923–925.
- [2] L. Novotny, “From near-field optics to optical antennas”, *Physics Today* **2011**, *64*, 47–52.
- [3] S. Walia, C. M. Shah, P. Gutruf, H. Nili, D. R. Chowdhury, W. Withayachumnankul, M. Bhaskaran, S. Sriram, “Flexible metasurfaces and metamaterials: A review of materials and fabrication processes at micro- and nano-scales”, *Applied Physics Reviews* **2015**, *2*, 011303.
- [4] Y. Lee, S.-J. Kim, H. Park, B. Lee, “Metamaterials and Metasurfaces for Sensor Applications”, *Sensors* **2017**, *17*, 1726.
- [5] K. A. Willets, A. J. Wilson, V. Sundaresan, P. B. Joshi, “Super-Resolution Imaging and Plasmonics”, *Chemical Reviews* **2017**, *117*, 7538–7582.
- [6] P. Bon, N. Bourg, S. Lécart, S. Monneret, E. Fort, J. Wenger, S. Lévêque-Fort, “Three-dimensional nanometre localization of nanoparticles to enhance super-resolution microscopy”, *Nature Communications* **2015**, *6*, 7764–7771.
- [7] M. E. Stewart, C. R. Anderton, L. B. Thompson, J. Maria, S. K. Gray, J. A. Rogers, R. G. Nuzzo, “Nanostructured Plasmonic Sensors”, *Chemical Reviews* **2008**, *108*, 494–521.
- [8] M. Li, S. K. Cushing, N. Wu, “Plasmon-enhanced optical sensors: a review”, *The Analyst* **2015**, *140*, 386–406.
- [9] Z. Li, H. Xu, “Nanoantenna effect of surface-enhanced Raman scattering: managing light with plasmons at the nanometer scale”, *Advances in Physics: X* **2016**, *1*, 492–521.
- [10] L. Novotny, “Effective Wavelength Scaling for Optical Antennas”, *Physical Review Letters* **2007**, *98*, 266802.
- [11] L. Novotny, B. Hecht, *Principles of Nano-Optics*, **2006**.
- [12] M. Parzefall, *Optical antennas driven by quantum tunneling*, ETH Zürich, **2017**.
- [13] W. L. Barnes, A. Dereux, T. W. Ebbesen, “Surface plasmon subwavelength optics”, *nature* **2003**, *424*, 824–831.
- [14] R. Zia, M. D. Selker, P. B. Catrysse, M. L. Brongersma, “Geometries and materials for subwavelength surface plasmon modes”, *JOSA A* **2004**, *21*, 2442–2446.

- [15] S. Maier, *Plasmonics: Fundamentals and Applications*, Springer, **2007**.
- [16] B. Prade, J. Vinet, A. Mysyrowicz, “Guided optical waves in planar heterostructures with negative dielectric constant”, *Phys. Rev. B* **1991**, *44*, 13556–13572.
- [17] E. N. Economou, “Surface Plasmons in Thin Films”, *Physical Review* **1969**, *182*, 539–554.
- [18] V. J. Sorger, R. F. Oulton, R.-M. Ma, X. Zhang, “Toward integrated plasmonic circuits”, *MRS Bulletin* **2012**, *37*, 728–738.
- [19] A. B. Dahlin, M. Mapar, K. Xiong, F. Mazzotta, F. Höök, T. Sannomiya, “Plasmonic Nanopores in Metal-Insulator-Metal Films”, *Advanced Optical Materials* **2014**, *2*, 556–564.
- [20] H. Raether, *Surface plasmons on smooth and rough surfaces and on gratings*, red. by Springer-Verlag Berlin Heidelberg, Springer-Verlag Berlin Heidelberg, **1988**.
- [21] W. Nolting in *Grundkurs Theoretische Physik 3*: Springer, **2001**.
- [22] C. F. Bohren, D. R. Huffman, *Absorption and scattering of light by small particles*, Wiley, New York, **1983**, 530 pp.
- [23] D. Zopf, *Optimization and LSPR-based sensoric Test of a Fourier Transform Imaging Spectrometer*, Universität Leipzig, **2013**.
- [24] G. Mie, “Beitrage zur Optik trueber Medien speziell kolloidaler Metalloesungen”, *Ann. Phys.* **1908**, *25*, 377–445.
- [25] M. I. Mishchenko, J. W. Hovenier, L. D. Travis, “Light Scattering by Nonspherical Particles: Theory, Measurements, and Applications”, *Measurement Science and Technology* **2000**, *11*, 1827.
- [26] E. Prodan, C. Radloff, N. J. Halas, P. Nordlander, “A Hybridization Model for the Plasmon Response of Complex Nanostructures”, *Science* **2003**, *302*, 419–422.
- [27] E. Prodan, P. Nordlander, “Plasmon hybridization in spherical nanoparticles”, *The Journal of Chemical Physics* **2004**, *120*, 5444–5454.
- [28] P. Nordlander, C. Oubre, E. Prodan, K. Li, M. I. Stockman, “Plasmon Hybridization in Nanoparticle Dimers”, *Nano Letters* **2004**, *4*, 899–903.
- [29] F. Le, N. Z. Lwin, N. J. Halas, P. Nordlander, “Plasmonic interactions between a metallic nanoshell and a thin metallic film”, *Physical review B* **2007**, *76*, 165410.
- [30] P. Nordlander, E. Prodan, “Plasmon Hybridization in Nanoparticles near Metallic Surfaces”, *Nano Letters* **2004**, *4*, 2209–2213.
- [31] F. Le, N. Z. Lwin, J. M. Steele, M. Kall, N. J. Halas, P. Nordlander, “Plasmons in the metallic nanoparticle - Film system as a tunable impurity problem”, *Nano Letters* **2005**, *5*, 2009–2013.
- [32] P. Kliuiev, “Gap modes-coupling of plasmonic nanoparticles with a gold film”, Master Thesis, Master Thesis, Jena, **2014**.
- [33] J. J. Mock, R. T. Hill, A. Degiron, S. Zauscher, A. Chilkoti, D. R. Smith, “Distance-dependent plasmon resonant coupling between a gold nanoparticle and gold film”, *Nano letters* **2008**, *8*, 2245–2252.

- [34] D. Brandl, *Plasmon hybridization in generalized metallic nanostructures*, Rice University, **2008**.
- [35] M. Pelton, G. W. Bryant, *Introduction to metal-nanoparticle plasmonics*, Wiley : Science Wise Publishing, Hoboken, New Jersey, **2013**, 275 pp.
- [36] M. Fleischmann, P. Hendra, A. McQuillan, “Raman spectra of pyridine adsorbed at a silver electrode”, *Chemical Physics Letters* **1974**, *26*, 163–166.
- [37] R. M. Stöckle, Y. D. Suh, V. Deckert, R. Zenobi, “Nanoscale chemical analysis by tip-enhanced Raman spectroscopy”, *Chemical Physics Letters* **2000**, *318*, 131–136.
- [38] I. Romero, J. Aizpurua, G. W. Bryant, F. J. García De Abajo, “Plasmons in nearly touching metallic nanoparticles: singular response in the limit of touching dimers”, *Optics Express* **2006**, *14*, 9988.
- [39] P. Mühlischlegel, H.-J. Eisler, O. J. F. Martin, B. Hecht, D. W. Pohl, “Resonant Optical Antennas”, *Science* **2005**, *308*, 1607–1609.
- [40] G.-C. Li, Y.-L. Zhang, J. Jiang, Y. Luo, D. Y. Lei, “Metal-Substrate-Mediated Plasmon Hybridization in a Nanoparticle Dimer for Photoluminescence Line-Width Shrinking and Intensity Enhancement”, *ACS Nano* **2017**, *11*, 3067–3080.
- [41] C. Sönnichsen, T. Franzl, T. Wilk, G. von Plessen, J. Feldmann, O. Wilson, P. Mulvaney, “Drastic Reduction of Plasmon Damping in Gold Nanorods”, *Physical Review Letters* **2002**, *88*, 077402.
- [42] D. Y. Lei, A. I. Fernández-Domínguez, Y. Sonnefraud, K. Appavoo, R. F. Haglund, J. B. Pendry, S. A. Maier, “Revealing Plasmonic Gap Modes in Particle-on-Film Systems Using Dark-Field Spectroscopy”, *ACS Nano* **2012**, *6*, 1380–1386.
- [43] K. Bao, H. Sobhani, P. Nordlander, “Plasmon hybridization for real metals”, *Chinese Science Bulletin* **2010**, *55*, 2629–2634.
- [44] S. M. Sze, K. K. Ng, *Physics of semiconductor devices*, John wiley & sons, **2006**.
- [45] J. C. Ranuárez, M. J. Deen, C. Chen, “A review of gate tunneling current in MOS devices”, *Microelectronics reliability* **2006**, *46*, 1939–1956.
- [46] H. Bentarzi, *Transport in metal-oxide-semiconductor structures*, Springer, **2011**.
- [47] R. A. Volkov, A. F. Chuiko, “Tunneling-Assisted Photon Emission in MIM Junctions”, *physica status solidi (b)* **1991**, *163*, 311–320.
- [48] R. A. Volkov, A. F. Chuiko, M. V. Dmitriev, “Tunneling-Assisted Photon Emission in MIS (p+) Junctions”, *physica status solidi (b)* **1993**, *175*, 93–102.
- [49] L. C. Davis, “Theory of surface-plasmon excitation in metal-insulator-metal tunnel junctions”, *Physical Review B* **1977**, *16*, 2482.
- [50] R. H. Ritchie, “Plasma Losses by Fast Electrons in Thin Films”, *Physical Review* **1957**, *106*, 874–881.
- [51] Y. Uehara, Y. Kimura, S. Ushioda, K. Takeuchi, “Theory of visible light emission from scanning tunneling microscope”, *Jpn. J. Appl. Phys. Part 1 - Regul. Pap. Short Notes Rev. Pap.* **1992**, *31*, 2465–2469.

- [52] P. Canet, C. Laurent, “Electroluminescence from radiative decay of surface plasmons in aluminum-insulator-indium tin oxide structures”, *Journal of Applied Physics* **1994**, *75*, 7460–7464.
- [53] J. R. Kirtley, T. N. Theis, J. C. Tsang, D. J. DiMaria, “Hot-electron picture of light emission from tunnel junctions”, *Phys. Rev. B* **1983**, *27*, 4601–4611.
- [54] D. Diesing, D. Kovacs, K. Stella, C. Heuser, “Characterization of atom and ion-induced internal electron emission by thin film tunnel junctions”, *Nuclear Instruments and Methods in Physics Research Section B: Beam Interactions with Materials and Atoms* **2011**, *269*, 1185–1189.
- [55] B. Laks, D. L. Mills, “Photon emission from slightly roughened tunnel junctions”, *Phys. Rev. B* **1979**, *20*, 4962–4980.
- [56] D. Hone, B. Mühlischlegel, D. J. Scalapino, “Theory of light emission from small particle tunnel junctions”, *Appl. Phys. Lett.* **1978**, *33*, 203–204.
- [57] Y. Uehara, J. Watanabe, S. Fujikawa, S. Ushioda, “Light-Emission Mechanism of Si-MOS Tunnel-Junctions”, *Phys. Rev. B* **1995**, *51*, 2229–2238.
- [58] N. Asli, M. I. Vexler, A. F. Shulekin, P. D. Yoder, I. V. Grekhov, P. Seegebrecht, “Threshold energies in the light emission characteristics of silicon MOS tunnel diodes”, *Microelectronics Reliability* **2001**, *41*, 1071–1076.
- [59] N. L. Schneider, G. Schull, R. Berndt, “Optical Probe of Quantum Shot-Noise Reduction at a Single-Atom Contact”, *Physical Review Letters* **2010**, *105*, 026601.
- [60] R. Pechou, R. Coratger, F. Ajustron, J. Beauvillain, “Cutoff anomalies in light emitted from the tunneling junction of a scanning tunneling microscope in air”, *Applied Physics Letters* **1998**, *72*, 671–673.
- [61] M. Parzefall, P. Bharadwaj, L. Novotny in *Quantum Plasmonics, Vol. 185*, (Eds.: S. I. Bozhevolnyi, L. Martin-Moreno, F. Garcia-Vidal), Springer International Publishing, Cham, **2017**, pp. 211–236.
- [62] A. Downes, M. E. Taylor, M. E. Welland, “Two-sphere model of photon emission from the scanning tunneling microscope”, *Physical Review B* **1998**, *57*, 6706.
- [63] A. V. Uskov, J. B. Khurgin, M. Buret, A. Bouhelier, I. V. Smetanin, I. E. Protsenko, “Biased Nanoscale Contact as Active Element for Electrically Driven Plasmonic Nanoantenna”, *ACS Photonics* **2017**, *4*, 1501–1505.
- [64] A. V. Uskov, J. B. Khurgin, I. E. Protsenko, I. V. Smetanin, A. Bouhelier, “Excitation of plasmonic nanoantennas by nonresonant and resonant electron tunnelling”, *Nanoscale* **2016**, *8*, 14573–14579.
- [65] M.-X. Wang, C.-X. Sun, “Light emission from the double-barrier Al/Al<sub>2</sub>O<sub>3</sub>/Al/Al<sub>2</sub>O<sub>3</sub>/Au tunnel junction”, *Thin Solid Films* **2000**, *371*, 191–194.
- [66] W. K. Phua, Y. Akimov, L. Wu, H. S. Chu, P. Bai, A. Danner, “Highly efficient tunable and localized on-chip electrical plasmon source using protruded metal-insulator-metal structure”, *Optics Express* **2016**, *24*, 10663.
- [67] F. Bigourdan, J.-P. Hugonin, F. Marquier, C. Sauvan, J.-J. Greffet, “Nanoantenna for Electrical Generation of Surface Plasmon Polaritons”, *Physical Review Letters* **2016**, *116*, 106803.

- [68] K. Braun, F. Laible, O. Hauler, X. Wang, A. Pan, M. Fleischer, A. J. Meixner, “Active optical antennas driven by inelastic electron tunneling”, *Nanophotonics* **2018**, *7*, 1503–1516.
- [69] F. Rossel, M. Pivetta, W.-D. Schneider, “Luminescence experiments on supported molecules with the scanning tunneling microscope”, *Surface Science Reports* **2010**, *65*, 129–144.
- [70] P. Johansson, R. Monreal, P. Apell, “Theory for light emission from a scanning tunneling microscope”, *Physical Review B* **1990**, *42*, 9210–9213.
- [71] P. Johansson, “Light emission from a scanning tunneling microscope: Fully retarded calculation”, *Physical Review B* **1998**, *58*, 10823.
- [72] J. K. Gimzewski, B. Reihl, J. H. Coombs, R. R. Schlittler, “Photon emission with the scanning tunneling microscope”, *Zeitschrift für Physik B Condensed Matter* **1988**, *72*, 497–501.
- [73] J. K. Gimzewski, J. K. Sass, R. R. Schlitter, J. Schott, “Enhanced photon emission in scanning tunnelling microscopy”, *EPL (Europhysics Letters)* **1989**, *8*, 435.
- [74] R. Berndt, J. K. Gimzewski, P. Johansson, “Inelastic tunneling excitation of tip-induced plasmon modes on noble-metal surfaces”, *Physical Review Letters* **1991**, *67*, 3796.
- [75] P. Dawson, M. G. Boyle, “Light emission from scanning tunnelling microscope on polycrystalline Au films—what is happening at the single-grain level?”, *Journal of Optics A: Pure and Applied Optics* **2006**, *8*, S219–S226.
- [76] I. I. Smolyaninov, D. L. Mazzoni, J. Mait, C. C. Davis, “Experimental study of surface-plasmon scattering by individual surface defects”, *Physical Review B* **1997**, *56*, 1601.
- [77] D. Walmsley, T.-S. Tan, P. Dawson, “Light emission from gold and silver thin films in a scanning tunneling microscope: role of contamination and interpretation of grain structure in photon maps”, *Surface Science* **2004**, *572*, 497–520.
- [78] K. Takeuchi, “Prism-coupled light emission from a scanning tunneling microscope”, *Journal of Vacuum Science & Technology B: Microelectronics and Nanometer Structures* **1991**, *9*, 557.
- [79] R. Marty, C. Girard, A. Arbouet, G. Colas des Francs, “Near-field coupling of a point-like dipolar source with a thin metallic film: Implication for STM plasmon excitations”, *Chemical Physics Letters* **2012**, *532*, 100–105.
- [80] M. Sakurai, C. Thirstrup, M. Aono, “New aspects of light emission from STM”, *Applied Physics A* **2005**, *80*, 1153–1160.
- [81] R. W. Rendell, D. J. Scalapino, “Surface plasmons confined by microstructures on tunnel junctions”, *Physical Review B* **1981**, *24*, 3276.
- [82] V. Kalathingal, P. Dawson, J. Mitra, “Scanning tunneling microscope light emission: Effect of the strong dc field on junction plasmons”, *Physical Review B* **2016**, *94*, 035443.

- [83] Y. Uehara, Y. Suda, S. Ushioda, K. Takeuchi, “Tip shape dependence of the light emission efficiency for the scanning tunneling microscope”, *Applied Physics Letters* **2001**, *79*, 1718.
- [84] T. Wang, *Electrical excitation of surface plasmons with a scanning tunneling microscope*, Université Paris Sud-Paris XI, **2012**.
- [85] X. Wang, K. Braun, D. Zhang, H. Peisert, H. Adler, T. Chassé, A. J. Meixner, “Enhancement of Radiative Plasmon Decay by Hot Electron Tunneling”, *ACS Nano* **2015**, *9*, 8176–8183.
- [86] R. Branscheid, V. Jacobsen, M. Kreiter, “STM induced light from nontrivial metal structures: Local variations in emission efficiency”, *Surface Science* **2008**, *602*, 176–181.
- [87] M. G. Boyle, J. Mitra, P. Dawson, “The tip-sample water bridge and light emission from scanning tunnelling microscopy”, *Nanotechnology* **2009**, *20*, 335202.
- [88] D. T. Pierce, A. Davies, J. A. Stroscio, R. J. Celotta, “Polarized light emission from the metal-metal STM junction”, *Applied Physics A: Materials Science & Processing* **1998**, *66*, S403–S406.
- [89] P. Z. El-Khoury, P. Abellan, Y. Gong, F. S. Hage, J. Cottom, A. G. Joly, R. Brydson, Q. M. Ramasse, W. P. Hess, “Visualizing surface plasmons with photons, photoelectrons, and electrons”, *The Analyst* **2016**, *141*, 3562–3572.
- [90] A. Yu, S. Li, G. Czap, W. Ho, “Tunneling-Electron-Induced Light Emission from Single Gold Nanoclusters”, *Nano Letters* **2016**, *16*, 5433–5436.
- [91] N. Nilius, N. Ernst, H.-J. Freund, “Photon emission spectroscopy of individual oxide-supported silver clusters in a scanning tunneling microscope”, *Physical Review Letters* **2000**, *84*, 3994.
- [92] A. Taleb, A. O. Gusev, F. Silly, F. Charra, M. P. Pileni, “Local photon emission of self-assembled metal nanoparticles”, *Applied surface science* **2000**, *162*, 553–558.
- [93] M. Sakurai, M. Aono, “Scanning tunneling microscope-induced light emission from nanostructures formed by Ag clusters”, *Physical Review B* **2001**, *64*, 045402.
- [94] T. Arai, K. Nakayama, “STM-induced photon emission from sputter-deposited Ag nanoclusters”, *Applied Surface Science* **2005**, *246*, 193–198.
- [95] T. Umeno, R. Nishitani, A. Kasuya, Y. Nishina, “Isochromat photon map induced by scanning tunneling microscopy from gold particles”, *Physical Review B* **1996**, *54*, 13499.
- [96] N. Venkateswaran, K. Sattler, J. Xhie, M. Ge, “Photon emission from nano-granular gold excited by electron tunneling”, *Surface science* **1992**, *274*, 199–204.
- [97] M. M. J. Bischoff, M. Van der Wielen, H. Van Kempen, “STM-induced photon emission spectroscopy of granular gold surfaces in air”, *Surface science* **1998**, *400*, 127–133.



- [98] S. A. Nepijko, A. Chernenkaya, K. Medjanik, S. V. Chernov, A. A. Sapozhnik, L. V. Odnodvoretz, I. Y. Protsenko, W. Schulze, G. Ertl, G. Schönhense, “Spectral Measurement of Photon Emission from Individual Gold Nanoparticles Using Scanning Tunneling Microscopy”, *Journal of Nano- and Electronic Physics* **2016**, *8*, 02039.
- [99] P. André, F. Charra, M. P. Pileni, “Resonant electromagnetic field cavity between scanning tunneling microscope tips and substrate”, *Journal of Applied Physics* **2002**, *91*, 3028–3036.
- [100] E. Le Moal, S. Marguet, D. Canneson, B. Rogez, E. Boer-Duchemin, G. Dujardin, T. V. Teperik, D.-C. Marinica, A. G. Borisov, “Engineering the emission of light from a scanning tunneling microscope using the plasmonic modes of a nanoparticle”, *Physical Review B* **2016**, *93*, 035418.
- [101] M. J. Romero, J. Lagemaat, G. Rumbles, M. M. Al-Jassim, “Plasmon excitations in scanning tunneling microscopy: Simultaneous imaging of modes with different localizations coupled at the tip”, *Applied Physics Letters* **2007**, *90*, 193109.
- [102] P. Bharadwaj, A. Bouhelier, L. Novotny, “Electrical Excitation of Surface Plasmons”, *Phys. Rev. Lett.* **2011**, *106*, 226802.
- [103] T. Wang, E. Boer-Duchemin, Y. Zhang, G. Comtet, G. Dujardin, “Excitation of propagating surface plasmons with a scanning tunnelling microscope”, *Nanotechnology* **2011**, *22*, 175201.
- [104] S. Egusa, Y.-H. Liao, N. F. Scherer, “Imaging scanning tunneling microscope-induced electroluminescence in plasmonic corrals”, *Applied Physics Letters* **2004**, *84*, 1257.
- [105] Z. Dong, H.-S. Chu, D. Zhu, W. Du, Y. A. Akimov, W. P. Goh, T. Wang, K. E. J. Goh, C. Troadec, C. A. Nijhuis, J. K. W. Yang, “Electrically-Excited Surface Plasmon Polaritons with Directionality Control”, *ACS Photonics* **2015**, *2*, 385–391.
- [106] Y. Zhang, E. Boer-Duchemin, T. Wang, B. Rogez, G. Comtet, E. Le Moal, G. Dujardin, A. Hohenau, C. Gruber, J. R. Krenn, “Edge scattering of surface plasmons excited by scanning tunneling microscopy”, *Optics Express* **2013**, *21*, 13938.
- [107] T. Wang, G. Comtet, E. Le Moal, G. Dujardin, A. Drezet, S. Huant, E. Boer-Duchemin, “Temporal coherence of propagating surface plasmons”, *Optics Letters* **2014**, *39*, 6679.
- [108] T. Wang, E. Boer-Duchemin, G. Comtet, E. Le Moal, G. Dujardin, A. Drezet, S. Huant, “Plasmon scattering from holes: from single hole scattering to Young’s experiment”, *Nanotechnology* **2014**, *25*, 125202.
- [109] T. Wang, B. Rogez, G. Comtet, E. Le Moal, W. Abidi, H. Remita, G. Dujardin, E. Boer-Duchemin, “Scattering of electrically excited surface plasmon polaritons by gold nanoparticles studied by optical interferometry with a scanning tunneling microscope”, *Physical Review B* **2015**, *92*, 045438.

- [110] E. Le Moal, S. Marguet, B. Rogez, S. Mukherjee, P. Dos Santos, E. Boer-Duchemin, G. Comtet, G. Dujardin, “An Electrically Excited Nanoscale Light Source with Active Angular Control of the Emitted Light”, *Nano Letters* **2013**, *13*, 4198–4205.
- [111] S. Cao, E. Le Moal, E. Boer-Duchemin, G. Dujardin, A. Drezet, S. Huant, “Cylindrical vector beams of light from an electrically excited plasmonic lens”, *Applied Physics Letters* **2014**, *105*, 111103.
- [112] J. Kern, R. Kullock, J. Prangma, M. Emmerling, M. Kamp, B. Hecht, “Electrically driven optical antennas”, *Nature Photonics* **2015**, *9*, 582–586.
- [113] J. C. Prangma, J. Kern, A. G. Knapp, S. Grossmann, M. Emmerling, M. Kamp, B. Hecht, “Electrically Connected Resonant Optical Antennas”, *Nano Letters* **2012**, *12*, 3915–3919.
- [114] Y. Vardi, E. Cohen-Hoshen, G. Shalem, I. Bar-Joseph, “Fano Resonance in an Electrically Driven Plasmonic Device”, *Nano Letters* **2016**, *16*, 748–752.
- [115] M. Buret, A. V. Uskov, J. Dellinger, N. Cazier, M.-M. Mennemanteuil, J. Berthelot, I. V. Smetanin, I. E. Protsenko, G. Colas-des-Francis, A. Bouhelier, “Spontaneous Hot-Electron Light Emission from Electron-Fed Optical Antennas”, *Nano Letters* **2015**, *15*, 5811–5818.
- [116] N. L. Schneider, P. Johansson, R. Berndt, “Hot electron cascades in the scanning tunneling microscope”, *Physical Review B* **2013**, *87*, 045409.
- [117] M. Frimmer, G. Puebla-Hellmann, A. Wallraff, L. Novotny, “The role of titanium in electromigrated tunnel junctions”, *Applied Physics Letters* **2014**, *105*, 221118.
- [118] A. Dasgupta, M. Buret, N. Cazier, M.-M. Mennemanteuil, R. Chacon, K. Hammani, J.-C. Weeber, J. Arocas, L. Markey, G. C. des Francis, A. Uskov, I. Smetanin, A. Bouhelier, “Electromigrated electrical optical antennas for transducing electrons and photons at the nanoscale”, *Beilstein Journal of Nanotechnology* **2018**, *9*, 1964–1976.
- [119] T. Taychatanapat, K. I. Bolotin, F. Kuemmeth, D. C. Ralph, “Imaging Electromigration during the Formation of Break Junctions”, *Nano Letters* **2007**, *7*, 652–656.
- [120] S. P. Gurunaryanan, N. Verellen, V. S. Zharinov, F. James Shirley, V. V. Moshchalkov, M. Heyns, J. Van de Vondel, I. P. Radu, P. Van Dorpe, “Electrically Driven Unidirectional Optical Nanoantennas”, *Nano Letters* **2017**, *17*, 7433–7439.
- [121] D. W. Pohl, S. G. Rodrigo, L. Novotny, “Stacked optical antennas”, *Applied Physics Letters* **2011**, *98*, 023111.
- [122] M. Manheller, S. Trelenkamp, R. Waser, S. Karthäuser, “Reliable fabrication of 3 nm gaps between nanoelectrodes by electron-beam lithography”, *Nanotechnology* **2012**, *23*, 125302.
- [123] H. Duan, H. Hu, H. K. Hui, Z. Shen, J. K. W. Yang, “Free-standing sub-10 nm nanostencils for the definition of gaps in plasmonic antennas”, *Nanotechnology* **2013**, *24*, 185301.

- [124] Q. Q. Shu, W. G. Ma, “Barrier parameter variation in Al-Al<sub>2</sub>O<sub>3</sub>-metal tunnel junctions”, *Appl. Phys. Lett.* **1992**, *61*, 2542–2544.
- [125] P. Dawson, D. G. Walmsley, H. A. Quinn, A. J. L. Ferguson, “Observation and explanation of light-emission spectra from statistically rough Cu, Ag, and Au tunnel junctions”, *Phys. Rev. B* **1984**, *30*, 3164–3178.
- [126] N. Kroo, Z. Szentirmay, J. Felszerfalvi, “Role of junction plasmons in light emission of MOM diodes”, *Opt. Commun.* **1986**, *56*, 345–350.
- [127] R. K. Jain, S. Wagner, D. H. Olson, “Stable room temperature light emission from metal-insulator-metal junctions”, *Appl. Phys. Lett.* **1978**, *32*, 62–64.
- [128] K. Arya, R. Zeyher, “Light emission from tunnel junctions: The role of multiple scattering of surface polaritons”, *Phys. Rev. B* **1983**, *28*, 4080–4089.
- [129] J. Giergiel, C. E. Reed, J. C. Hemminger, S. Ushioda, “Surface-plasmon-polariton mode conversion on rough interfaces”, *Phys. Rev. B* **1987**, *36*, 3052–3058.
- [130] J. B. D. Soole, C. D. Ager, “The slow-mode surface plasmon in planar metal-oxide-metal tunnel junctions”, *Journal of Applied Physics* **1989**, *65*, 1133–1139.
- [131] N. Kroó, Z. Szentirmay, J. Félserfalvi, “Surface plasmon dispersion relation of gold determined by MOM tunnel structures”, *Physics Letters A* **1982**, *88*, 90–92.
- [132] M. Hanisch, A. Otto, “Light emission from rough tunnel junctions in UHV”, *J. Phys.: Condens. Matter* **1994**, *6*, 9659–9659.
- [133] P. Dawson, D. G. Walmsley, “Light emission from nominally smooth Ag tunnel junctions”, *Surface Science* **1986**, *171*, 135–145.
- [134] Q. Q. Shu, Z. R. Zu, J. W. Lu, “Light emission excited by hot electrons in MgF<sub>2</sub> thin-film devices”, *Journal of applied physics* **1989**, *66*, 6193–6195.
- [135] M.-X. Wang, Y.-W. Zhang, H.-W. Cheng, C.-X. Sun, “Study on the relation between surface roughness and the light emission spectrum of an Au-Al<sub>2</sub>O<sub>3</sub>-Al tunnel junction”, *Appl. Surf. Sci.* **2001**, *173*, 362–367.
- [136] S. L. McCarthy, J. Lambe, “Enhancement of light emission from metal-insulator-metal tunnel junction”, *Appl. Phys. Lett.* **1977**, *30*, 427–429.
- [137] Q. Q. Shu, W. J. Wen, S. J. Xu, “Light emission from high bias Al-AlO<sub>x</sub>-Au tunnel junctions”, *J. Appl. Phys.* **1988**, *65*, 373–375.
- [138] A. J. L. Ferguson, D. G. Walmsley, H. P. Hagan, R. J. Turner, P. Dawson, “Spectral dependence of light output from LEIT devices on electrode morphology”, *Journal of Physics: Condensed Matter* **1989**, *1*, 7931.
- [139] J. Kirtley, T. N. Theis, J. C. Tsang, “Light emission from tunnel junction on gratings”, *Phys. Rev. B* **1981**, *24*, 5650–5663.
- [140] J. R. Kirtley, T. N. Theis, J. C. Tsang, “Diffraction-grating-enhanced light emission from tunnel junctions”, *Appl. Phys. Lett.* **1980**, *37*, 435–437.
- [141] P. D. Sparks, T. Sjodin, B. W. Reed, J. Stege, “Light emission from the slow mode of tunnel junctions on short period diffraction grating”, *Phys. Rev. Lett.* **1992**, *68*, 2668–2671.

- [142] A. Adams, J. C. Wyss, P. K. Hansma, “Possible Observation of local plasmon modes Excited by electrons tunneling through junctions”, *Phys. Rev. Lett.* **1979**, *42*, 912–915.
- [143] A. Adams, P. K. Hansma, “Light emission from small metal particles and thin films excited by tunneling electrons”, *Phys. Rev. B* **1981**, *23*, 3597–3601.
- [144] M. J. Bloemer, J. G. Mantovani, J. P. Goudonnet, D. R. James, R. J. Warmack, T. L. Ferrell, “Observation of driven surface-plasmon modes in metal particulates above tunnel junction”, *Phys. Rev. B* **1987**, *35*, 5947–5954.
- [145] R. W. Rendell, D. J. Scalapino, B. Mühlischlegel, “Role of local plasmon modes in light emission from small-particle tunnel junctions”, *Physical Review Letters* **1978**, *41*, 1746.
- [146] S. Ushioda, J. E. Rutledge, R. M. Pierce, “Prism-coupled light emission from tunnel junctions”, *Physical review letters* **1985**, *54*, 224.
- [147] J. Watanabe, A. Takeuchi, Y. Uehara, S. Ushioda, “Prims-coupled light emission from tunnel junctions containing interface roughness: Experiment”, *Phys. Rev. B* **1988**, *38*, 12959–12965.
- [148] M. Connolly, A. Ferguson, P. Dawson, I. Tamm, D. Walmsley, “Fast mode surface plasmon damping on tunnel junction structures”, *Surface Science* **1991**, *245*, 225–231.
- [149] R. J. Walters, R. V. A. Loon, I. Brunets, J. Schmitz, A. Polman, “A silicon-based electrical source of surface plasmon polaritons”, *Nature Materials* **2010**, *9*, 21–25.
- [150] J. Moreland, A. Adams, P. K. Hansma, “Efficiency of light emission from surface plasmons”, *Phys. Rev. B* **1982**, *25*, 2297–2300.
- [151] J. Watanabe, Y. Uehara, J. Murota, S. Ushioda, “Light emission from Si-metal-oxide-semiconductor tunnel junctions”, *Jpn. J. Appl. Phys. Part 1 - Regul. Pap. Short Notes Rev. Pap.* **1993**, *32*, 99–104.
- [152] E. Cartier, J. C. Tsang, M. V. Fischetti, D. A. Buchanan, “Light emission during direct and Fowler-Nordheim tunneling in ultra thin MOS-tunnel junctions”, *Microelectronic Engineering* **1997**, *36*, 103–106.
- [153] N. Asli, S. V. Gastev, I. V. Grekhov, P. Seegebrecht, A. F. Shulekin, S. E. Tyaginov, M. I. Vexler, H. Zimmermann, “Al/SiO<sub>2</sub>(2.0-2.5 nm)/p-Si tunnel junction as a light emitter”, *Microelectronic Engineering* **1999**, *48*, 79–82.
- [154] N. Asli, S. V. Gastev, I. V. Grekhov, P. Seegebrecht, A. F. Shulekin, S. E. Tyaginov, M. I. Vexler, H. Zimmermann, “Luminescence measurements on MOS tunnel diodes as a method of finding the photon emission rates in silicon”, *Materials Science in Semiconductor Processing* **2000**, *3*, 539–543.
- [155] M. X. Wang, J. H. Yu, C. X. Sun, “Light emission characteristics and negative resistance phenomenon of Si-based metal/insulator/semiconductor tunnel junction”, *Appl. Surf. Sci.* **2000**, *161*, 9–13.
- [156] N. Asli, A. F. Shulekin, P. D. Yoder, M. I. Vexler, I. V. Grekhov, P. Seegebrecht, “Impact of oxide damage on the light emission properties of MOS-tunnel structures”, *Solid-State Electronics* **2004**, *48*, 731–737.

- [157] J. Seidel, T. Gohler, S. Grafstrom, L. M. Eng, “Near-field optical characterization of surface-plasmon-mediated light emission from electrically biased metal-insulator-semiconductor tunnel junctions”, *Appl. Phys. Lett.* **2008**, *92*, 103123.
- [158] A. Tatarog̃lu, ş. Altındal, M. Bülbül, “Temperature and frequency dependent electrical and dielectric properties of Al/SiO<sub>2</sub>/p-Si (MOS) structure”, *Microelectronic Engineering* **2005**, *81*, 140–149.
- [159] L. Mao, H. Zhang, C. Tan, M. Xu, “The effect of transition region on the direct tunneling current and Fowler-Nordheim tunneling current oscillations in ultrathin MOS structures”, *Microelectronics Reliability* **2002**, *42*, 175–181.
- [160] G.-H. Lee, Y.-J. Yu, C. Lee, C. Dean, K. L. Shepard, P. Kim, J. Hone, “Electron tunneling through atomically flat and ultrathin hexagonal boron nitride”, *Applied Physics Letters* **2011**, *99*, 243114.
- [161] L. Britnell, R. V. Gorbachev, R. Jalil, B. D. Belle, F. Schedin, M. I. Katsnelson, L. Eaves, S. V. Morozov, A. S. Mayorov, N. M. R. Peres, A. H. Castro Neto, J. Leist, A. K. Geim, L. A. Ponomarenko, K. S. Novoselov, “Electron Tunneling through Ultrathin Boron Nitride Crystalline Barriers”, *Nano Letters* **2012**, *12*, 1707–1710.
- [162] M. Parzefall, P. Bharadwaj, A. Jain, T. Taniguchi, K. Watanabe, L. Novotny, “Antenna-coupled photon emission from hexagonal boron nitride tunnel junctions”, *Nature Nanotechnology* **2015**, *10*, 1058–1063.
- [163] D. Shafir, H. Soifer, B. D. Bruner, M. Dagan, Y. Mairesse, S. Patchkovskii, M. Y. Ivanov, O. Smirnova, N. Dudovich, “Resolving the time when an electron exits a tunnelling barrier”, *Nature* **2012**, *485*, 343–346.
- [164] W. Du, T. Wang, H.-S. Chu, C. A. Nijhuis, “Highly efficient on-chip direct electronic-plasmonic transducers”, *Nature Photonics* **2017**, *11*, 623–627.
- [165] N. Cazier, M. Buret, A. V. Uskov, L. Markey, J. Arocas, G. Colas Des Francs, A. Bouhelier, “Electrical excitation of waveguided surface plasmons by a light-emitting tunneling optical gap antenna”, *Optics Express* **2016**, *24*, 3873.
- [166] C. Karnetzky, P. Zimmermann, C. Trummer, C. Duque Sierra, M. Wörle, R. Kienberger, A. Holleitner, “Towards femtosecond on-chip electronics based on plasmonic hot electron nano-emitters”, *Nature Communications* **2018**, *9*, 2471.
- [167] S. F. Tan, L. Wu, J. K. W. Yang, P. Bai, M. Bosman, C. A. Nijhuis, “Quantum Plasmon Resonances Controlled by Molecular Tunnel Junctions”, *Science* **2014**, *343*, 1496–1499.
- [168] J. U. Ahamed, T. Sanbongi, S. Katano, Y. Uehara, “Prism-Coupled Scanning Tunneling Microscope Light Emission Spectroscopy of Au Film Covered with Self-Assembled Alkanethiol Monolayer”, *Japanese Journal of Applied Physics* **2010**, *49*, 08LB09.
- [169] T. Lutz, C. Große, C. Dette, A. Kabakchiev, F. Schramm, M. Ruben, R. Gutzler, K. Kuhnke, U. Schlickum, K. Kern, “Molecular Orbital Gates for Plasmon Excitation”, *Nano Letters* **2013**, *13*, 2846–2850.

- [170] B. Rogez, R. Horeis, E. Le Moal, J. Christoffers, K. Al-Shamery, G. Dujardin, E. Boer-Duchemin, “Optical and Electrical Excitation of Hybrid Guided Modes in an Organic Nanofiber–Gold Film System”, *The Journal of Physical Chemistry C* **2015**, *119*, 22217–22224.
- [171] C. Chen, P. Chu, C. A. Bobisch, D. L. Mills, W. Ho, “Viewing the Interior of a Single Molecule: Vibronically Resolved Photon Imaging at Submolecular Resolution”, *Physical Review Letters* **2010**, *105*, 217402.
- [172] M. C. Chong, G. Reecht, H. Bulou, A. Boeglin, F. Scheurer, F. Mathevet, G. Schull, “Narrow-Line Single-Molecule Transducer between Electronic Circuits and Surface Plasmons”, *Physical Review Letters* **2016**, *116*, 036802.
- [173] M. C. Chong, L. Sosa-Vargas, H. Bulou, A. Boeglin, F. Scheurer, F. Mathevet, G. Schull, “Ordinary and Hot Electroluminescence from Single-Molecule Devices: Controlling the Emission Color by Chemical Engineering”, *Nano Letters* **2016**, *16*, 6480–6484.
- [174] C. Große, A. Kabakchiev, T. Lutz, R. Froidevaux, F. Schramm, M. Ruben, M. Etzkorn, U. Schlickum, K. Kuhnke, K. Kern, “Dynamic Control of Plasmon Generation by an Individual Quantum System”, *Nano Letters* **2014**, *14*, 5693–5697.
- [175] K. Braun, X. Wang, A. M. Kern, H. Adler, H. Peisert, T. Chassé, D. Zhang, A. J. Meixner, “Superluminescence from an optically pumped molecular tunneling junction by injection of plasmon induced hot electrons”, *Beilstein Journal of Nanotechnology* **2015**, *6*, 1100–1106.
- [176] W. Du, T. Wang, H.-S. Chu, L. Wu, R. Liu, S. Sun, W. K. Phua, L. Wang, N. Tomczak, C. A. Nijhuis, “On-chip molecular electronic plasmon sources based on self-assembled monolayer tunnel junctions”, *Nature Photonics* **2016**, *10*, 274–280.
- [177] X. Chen, M. Roemer, L. Yuan, W. Du, D. Thompson, E. del Barco, C. A. Nijhuis, “Molecular diodes with rectification ratios exceeding 10<sup>5</sup> driven by electrostatic interactions”, *Nature Nanotechnology* **2017**, *12*, 797–803.
- [178] T. Böhler, J. Grebing, A. Mayer-Gindner, H. v. Löhneysen, E. Scheer, “Mechanically controllable break-junctions for use as electrodes for molecular electronics”, *Nanotechnology* **2004**, *15*, S465–S471.
- [179] L. Yuan, L. Jiang, C. A. Nijhuis, “The Drive Force of Electrical Breakdown of Large-Area Molecular Tunnel Junctions”, *Advanced Functional Materials* **2018**, *28*, 1801710.
- [180] I. Bâldea, “Important issues facing model-based approaches to tunneling transport in molecular junctions”, *Physical Chemistry Chemical Physics* **2015**, *17*, 20217–20230.
- [181] G. Schull, “Nano-optics: Launching plasmons with molecules”, *Nature Photonics* **2016**, *10*, 208–209.
- [182] A. R. Garrigues, L. Yuan, L. Wang, S. Singh, E. del Barco, C. A. Nijhuis, “Temperature dependent charge transport across tunnel junctions of single-molecules and self-assembled monolayers: a comparative study”, *Dalton Transactions* **2016**, *45*, 17153–17159.

- [183] A. Dathe, *Development of sensors based on optically and electrically excited plasmon resonances in hybrid metallic nanostructures*, Technische Universität Bergakademie Freiberg, Freiberg, **2014**.
- [184] J. Junesch, T. Sannomiya, A. B. Dahlin, “Optical Properties of Nanohole Arrays in Metal–Dielectric Double Films Prepared by Mask-on-Metal Colloidal Lithography”, *ACS Nano* **2012**, *6*, 10405–10415.
- [185] K. M. McPeak, S. V. Jayanti, S. J. P. Kress, S. Meyer, S. Iotti, A. Rossinelli, D. J. Norris, “Plasmonic Films Can Easily Be Better: Rules and Recipes”, *ACS Photonics* **2015**, *2*, 326–333.
- [186] M. J. Dodge in *Handbook of Laser Science and Technology, Vol. Optical Materials: Part 2*, CRC Press, Boca Raton, **1986**, p. 30.
- [187] M. A. Green, “Self-consistent optical parameters of intrinsic silicon at 300K including temperature coefficients”, *Solar Energy Materials and Solar Cells* **2008**, *92*, 1305–1310.
- [188] M. N. Polyanskiy, Refractive index database, **2018**, <https://refractiveindex.info>.
- [189] L. Gao, F. Lemarchand, M. Lequime, “Refractive index determination of SiO<sub>2</sub> layer in the UV/Vis/NIR range: spectrophotometric reverse engineering on single and bi-layer designs”, *Journal of the European Optical Society: Rapid Publications* **2013**, *8*.
- [190] F.-C. Chiu, “A Review on Conduction Mechanisms in Dielectric Films”, *Advances in Materials Science and Engineering* **2014**, *2014*, 1–18.
- [191] B. V. Van Zeghbroeck, *Principles of semiconductor devices and heterojunctions*, OCLC: 456836708, Prentice Hall ; Pearson Education [distributor, Upper Saddle River, N.J.; London, **2010**.
- [192] A. Gehring, S. Selberherr, “Modeling of Tunneling Current and Gate Dielectric Reliability for Nonvolatile Memory Devices”, *IEEE Transactions on Device and Materials Reliability* **2004**, *4*, 306–319.
- [193] G. Casados-Cruz, M. Reyes-Barranca, J. Moreno-Cadenas, “A simple method for determination of Fowler–Nordheim tunnelling parameters”, *International Journal of Electronics* **2011**, *98*, 655–666.
- [194] N. M. R. J. Zhao, “Fowler-Nordheim tunneling in thin SiO<sub>2</sub> films”, *Smart Materials and Structures* **1992**, *1*, 197.
- [195] A. Latreche, “An Accurate Method for Extracting the Three Fowler-Nordheim Tunnelling Parameters Using IV Characteristic”, *Microelectronics and Solid State Electronics* **2013**, *2*, 59–64.
- [196] Y. Chiou, J. Gambino, M. Mohammad, “Determination of the Fowler–Nordheim tunneling parameters from the Fowler–Nordheim plot”, *Solid-State Electronics* **2001**, *45*, 1787–1791.
- [197] A. Rostami, M. Leilaieoun, S. Golmohammadi, H. R. Saghai, “Modeling of Metal–Insulator–Semiconductor Dualband Si/SiO<sub>2</sub> Multi-Quantum Well UV Detectors”, *International Journal of Optomechatronics* **2012**, *6*, 275–288.

- [198] J. G. Simmons, “Generalized Formula for the Electric Tunnel Effect between Similar Electrodes Separated by a Thin Insulating Film”, **1963**, *34*, 1793–1803.
- [199] Y.-C. Yeo, T.-J. King, C. Hu, “Metal-dielectric band alignment and its implications for metal gate complementary metal-oxide-semiconductor technology”, *Journal of Applied Physics* **2002**, *92*, 7266–7271.
- [200] K. M. Lang, D. A. Hite, R. W. Simmonds, R. McDermott, D. P. Pappas, J. M. Martinis, “Conducting atomic force microscopy for nanoscale tunnel barrier characterization”, *Review of Scientific Instruments* **2004**, *75*, 2726–2731.
- [201] C. Zhu, R. H. Byrd, P. Lu, J. Nocedal, “Algorithm 778: L-BFGS-B: Fortran subroutines for large-scale bound-constrained optimization”, *ACM Transactions on Mathematical Software* **1997**, *23*, 550–560.
- [202] D. M. Pozar, *Microwave engineering*, Addison-Wesley, Reading, Mass, **1990**, 726 pp.
- [203] B. A. Boukamp, “Impedance Spectroscopy, Strength and Limitations”, *tm - Technisches Messen* **2004**, *71*, 454–459.
- [204] M. R. Beversluis, A. Bouhelier, L. Novotny, “Continuum generation from single gold nanostructures through near-field mediated intraband transitions”, *Physical Review B* **2003**, *68*, 115433.
- [205] R. K. Pearson, *Mining Imperfect Data: Dealing with Contamination and Incomplete Records*, Society for Industrial and Applied Mathematics, **2005**.
- [206] J. A. Dionne, L. A. Sweatlock, H. A. Atwater, A. Polman, “Planar metal plasmon waveguides: frequency-dependent dispersion, propagation, localization, and loss beyond the free electron model”, *Phys. Rev. B* **2005**, *72*, 075405.
- [207] T. Christensen, W. Yan, A.-P. Jauho, M. Soljačić, N. A. Mortensen, “Quantum Corrections in Nanoplasmonics: Shape, Scale, and Material”, *Physical Review Letters* **2017**, *118*, 157402.
- [208] C. Ciraci, R. T. Hill, J. J. Mock, Y. Urzhumov, A. I. Fernandez-Dominguez, S. A. Maier, J. B. Pendry, A. Chilkoti, D. R. Smith, “Probing the Ultimate Limits of Plasmonic Enhancement”, *Science* **2012**, *337*, 1072–1074.
- [209] K. J. Savage, M. M. Hawkeye, R. Esteban, A. G. Borisov, J. Aizpurua, J. J. Baumberg, “Revealing the quantum regime in tunnelling plasmonics”, *Nature* **2012**, *491*, 574–577.
- [210] W. Zhu, R. Esteban, A. G. Borisov, J. J. Baumberg, P. Nordlander, H. J. Lezec, J. Aizpurua, K. B. Crozier, “Quantum mechanical effects in plasmonic structures with subnanometre gaps”, *Nature Communications* **2016**, *7*, 11495.
- [211] A. I. Fernández-Domínguez, S. I. Bozhevolnyi, N. A. Mortensen, “Plasmon-Enhanced Generation of Nonclassical Light”, *ACS Photonics* **2018**, *5*, 3447–3451.
- [212] C. Sönnichsen, B. M. Reinhard, J. Liphardt, A. P. Alivisatos, “A molecular ruler based on plasmon coupling of single gold and silver nanoparticles”, *Nature Biotechnology* **2005**, *23*, 741–745.



- [213] A. Dathe, M. Ziegler, U. Hübner, W. Fritzsche, O. Stranik, “Electrically Excited Plasmonic Nanoruler for Biomolecule Detection”, *Nano letters* **2016**, *16*, 5728–5736.
- [214] S. Dominguez-Medina, S. McDonough, P. Swanglap, C. F. Landes, S. Link, “In Situ Measurement of Bovine Serum Albumin Interaction with Gold Nanospheres”, *Langmuir* **2012**, *28*, 9131–9139.
- [215] S. Dominguez-Medina, J. Blankenburg, J. Olson, C. F. Landes, S. Link, “Adsorption of a Protein Monolayer via Hydrophobic Interactions Prevents Nanoparticle Aggregation under Harsh Environmental Conditions”, *ACS Sustainable Chemistry & Engineering* **2013**, 833–842.
- [216] L. Chalet, F. J. Wolf, “The properties of streptavidin, a biotin-binding protein produced by Streptomyces”, *Archives of Biochemistry and Biophysics* **1964**, *106*, 1–5.
- [217] J. Vörös, “The Density and Refractive Index of Adsorbing Protein Layers”, *Biophysical Journal* **2004**, *87*, 553–561.
- [218] C. Novo, A. M. Funston, I. Pastoriza-Santos, L. M. Liz-Marzan, P. Mulvaney, “Influence of the medium refractive index on the optical properties of single gold triangular prisms on a substrate”, *Journal of Physical Chemistry C* **2008**, *112*, 3–7.
- [219] B. M. Reinhard, M. Siu, H. Agarwal, A. P. Alivisatos, J. Liphardt, “Calibration of Dynamic Molecular Rulers Based on Plasmon Coupling between Gold Nanoparticles”, *Nano Letters* **2005**, *5*, 2246–2252.
- [220] S. Boroviks, C. Wolff, J. Linnet, Y. Yang, F. Todisco, A. S. Roberts, S. I. Bozhevolnyi, B. Hecht, N. A. Mortensen, “Interference in edge-scattering from monocrystalline gold flakes”, *Optical Materials Express* **2018**, *8*, 3688.
- [221] T. Hutter, F. M. Huang, S. R. Elliott, S. Mahajan, “Near-Field Plasmonics of an Individual Dielectric Nanoparticle above a Metallic Substrate”, *The Journal of Physical Chemistry C* **2013**, *117*, 7784–7790.
- [222] M. Thiele, J. Z. E. Soh, A. Knauer, D. Malsch, O. Stranik, R. Müller, A. Csáki, T. Henkel, J. M. Köhler, W. Fritzsche, “Gold nanocubes – Direct comparison of synthesis approaches reveals the need for a microfluidic synthesis setup for a high reproducibility”, *Chemical Engineering Journal* **2016**, *288*, 432–440.
- [223] M. Parzefall, L. Novotny, “Light at the End of the Tunnel”, *ACS Photonics* **2018**, *5*, 4195–4202.
- [224] D. Nečas, P. Klapetek, “Gwyddion: an open-source software for SPM data analysis”, *Open Physics* **2012**, *10*.
- [225] N. Sultanova, S. Kasarova, I. Nikolov, “Dispersion Properties of Optical Polymers”, *Acta Physica Polonica A* **2009**, *116*, 585–587.

## Abbreviations

<b>AC</b>	<b>A</b> lternating <b>C</b> urrent
<b>ACF</b>	<b>A</b> uto <b>C</b> orrelation <b>F</b> unction
<b>AFM</b>	<b>A</b> tom <b>F</b> orce <b>M</b> icroscopy
<b>ALD</b>	<b>A</b> tom <b>L</b> ayer <b>D</b> eposition
<b>AOI</b>	<b>A</b> n <b>g</b> le of <b>I</b> ncidence
<b>CCD</b>	<b>C</b> harge <b>C</b> oupled <b>D</b> evice
<b>DC</b>	<b>D</b> irect <b>C</b> urrent
<b>DF</b>	<b>D</b> ark- <b>F</b> ield
<b>ECB</b>	<b>E</b> lectron <b>C</b> onduction <b>B</b> and
<b>EVB</b>	<b>E</b> lectron <b>V</b> alence <b>B</b> and
<b>FEM</b>	<b>F</b> inite <b>E</b> lements <b>M</b> ethod
<b>FIB</b>	<b>F</b> ocussed <b>I</b> on <b>B</b> eam
<b>FN</b>	<b>F</b> owler- <b>N</b> ordheim (conduction)
<b>FP</b>	<b>F</b> renkel- <b>P</b> oole (conduction)
<b>FWHM</b>	<b>F</b> ull <b>W</b> idth <b>H</b> alf <b>M</b> aximum
<b>HVB</b>	<b>H</b> ole <b>V</b> alence <b>B</b> and
<b>IMI</b>	<b>I</b> nsulator- <b>M</b> etal- <b>I</b> nsulator
<b>LAR</b>	<b>L</b> east <b>A</b> bsolute <b>R</b> esiduals
<b>LEIT</b>	<b>L</b> ight <b>E</b> mission by <b>I</b> nelastic <b>T</b> unneling
<b>LETJ</b>	<b>L</b> ight <b>E</b> mitting <b>T</b> unneling <b>J</b> unction
<b>LSPR</b>	<b>L</b> ocalized <b>S</b> urface <b>P</b> lasmon <b>R</b> esonance
<b>MIM</b>	<b>M</b> etal- <b>I</b> nsulator- <b>M</b> etal
<b>MIS</b>	<b>M</b> etal- <b>I</b> nsulator- <b>S</b> emiconductor
<b>PVD</b>	<b>P</b> hysical <b>V</b> apor <b>D</b> eposition
<b>QE</b>	<b>Q</b> uantum <b>E</b> fficiency
<b>QSN</b>	<b>Q</b> uantum <b>S</b> hot <b>N</b> oise
<b>ROI</b>	<b>R</b> egion of <b>I</b> nterest
<b>SAM</b>	<b>S</b> elf- <b>A</b> ssembled <b>M</b> onolayer
<b>SEM</b>	<b>S</b> canning <b>E</b> lectron <b>M</b> icroscopy
<b>SNR</b>	<b>S</b> ignal-to- <b>N</b> oise <b>R</b> atio
<b>SPP</b>	<b>S</b> urface <b>P</b> lasmon <b>P</b> olariton
<b>STM</b>	<b>S</b> canning <b>T</b> unneling <b>M</b> icroscopy
<b>TAT</b>	<b>T</b> rap <b>A</b> ssisted <b>T</b> unneling
<b>TE</b>	<b>T</b> hermionic <b>E</b> mission

## Physical Constants

speed of light	$c$	$=$	$2.997\,924\,58 \times 10^8 \text{ m} \cdot \text{s}^{-1}$
planck constant	$h$	$=$	$6.626\,069\,57 \times 10^{-34} \text{ J} \cdot \text{s}$
		$=$	$4.135\,667\,51 \times 10^{-15} \text{ eV} \cdot \text{s}$
reduced planck constant	$\hbar$	$=$	$1.054\,571\,80 \times 10^{-34} \text{ J} \cdot \text{s}$
		$=$	$6.582\,119\,51 \times 10^{-16} \text{ eV} \cdot \text{s}$
vacuum permittivity	$\varepsilon_0$	$=$	$8.854\,187\,81 \times 10^{-12} \text{ F} \cdot \text{m}^{-1}$
elementary charge	$e$	$=$	$1.602\,176\,57 \times 10^{-19} \text{ A} \cdot \text{s}$
electron rest mass	$m_0$	$=$	$9.109\,389\,97 \times 10^{-31} \text{ kg}$
Boltzmann constant	$k_B$	$=$	$1.380\,648\,52 \times 10^{-23} \text{ J} \cdot \text{K}^{-1}$
		$=$	$8.617\,330\,25 \times 10^{-5} \text{ eV} \cdot \text{K}^{-1}$
Fowler-Nordheim constants	$a$	$=$	$1.541\,4 \times 10^{-6} \text{ A} \cdot \text{eV} \cdot \text{V}^{-2}$
		$=$	$6.830\,9 \times 10^9 \text{ eV}^{3/2} \cdot \text{Vm}^{-1}$
pi	$\pi$	$=$	$3.141\,592\,65$

# Symbols

$\omega$ angular frequency	$t$ time	$Z$ impedance
$\varepsilon$ permittivity	$\lambda$ wavelength	$X$ reactance
$\delta$ decay length	$\lambda_{\text{SPP}}$ propagation length	$L$ inductivity
$r_s$ radius of sphere	$\alpha$ polarizability	$C$ capacitance
$C_{\text{sca}}$ scattering cross-section	$C_{\text{abs}}$ absorption cross-section	$R$ resistance
$V_g$ gate voltage/bias	$\omega_c$ spectral cut-off	$f$ frequency
$\eta_{\text{exc}}$ excitation efficiency	$\eta_{\text{ant}}$ antenna efficiency	$Y$ residual
$\Gamma_{\text{el}}$ tunneling rate (elastic)	$\Gamma_{\text{inel}}$ tunneling rate (inelastic)	$\sigma_{\text{rms}}$ surface roughness
$P_{\text{r}}$ radiative process	$P_{\text{nr}}$ non-radiative process	$A_{\text{F}}$ amplification factor
$S$ size/area	$t_{\text{ox}}$ oxide thickness	$A_{\text{R}}$ amplification ratio
$\vartheta$ angle	$n$ refractive index	$c$ concentration
$r_j$ reflection coefficient	$t_j$ transmission coefficient	$\mu$ mean value
$I$ tunneling current	$J$ tunneling current density	$S$ Poynting vector
$m^*$ effective mass	$\phi_{\text{B}}$ potential barrier	$s$ separation (particle-film)
$\chi$ electron affinity	$\gamma_r$ rate of emission	$\lambda_{\text{cog}}$ center of gravity wavelength
$E$ electric field	$H$ magnetic field	$P$ optical power
$R$ reflection	$T$ transmission	$A$ absorption
$y_{\text{BG}}$ background emission	$y_{\text{DE}}$ direct emission	$y_{\text{PAR}}$ particle mediated emission

# A | Materials & Protocols

The following Appendix summarizes information on utilized materials and setups. Hardware specifications, calibration procedures as well as measurement protocols are given.

## A.1 Optical Spectroscopy Setup and Calibration

Spectral characteristics of LETJ as described in Chapter 5 were recorded with a setup as shown in Fig. A.1 and components as listed in Tab. A.2. A large core optical fiber (3) with 200  $\mu\text{m}$  diameter was clamped and placed perpendicular with 1 mm distance from the sample surface. On the other end, a Czerny-Turner-Spectrometer (1) with two ports was connected - one port leading to the CCD detector (2), the other to a light bulb, serving for projection of the detection spot size and location on the sample surface. Samples were contacted with a self-built micro-contacter (see Fig. A.6), placed and positioned with a x-y microscopy stage (5). Spectra were obtained by integration over a whole junction. Power supply and logging of the tunneling current was controlled by a source meter (4). Triggering of the measurement parameters was handled by self-written software in LabVIEW. The spectrometer utilized an implemented grating (150 gr/mm) with spectral range of 400 - 900 nm and a blaze wavelength of 650 nm and the entrance slit was set to 50  $\mu\text{m}$ .

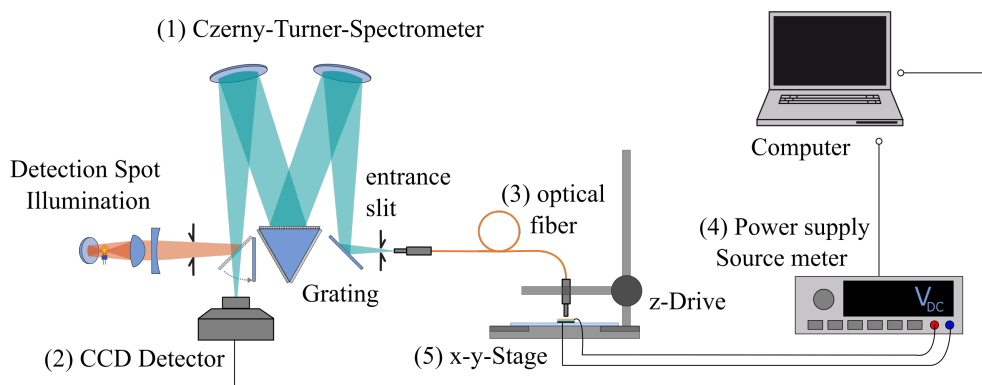


FIGURE A.1: Illustration of the experimental optical setup for detection of spectral characteristics of LETJ.

TABLE A.2: Implemented devices in the optical spectroscopy setup

	<i>Device</i>	<i>Model / Series</i>	<i>Company</i>	<i>Country</i>
(1)	Spectrometer	SpectraPro 2300i	Princeton Instruments	Trenton, US-NJ
(2)	CCD detector	PIXIS 256	Princeton Instruments	Trenton, US-NJ
(3)	Optical fiber	M24L02 - 200 $\mu\text{m}$	Thorlabs Inc.	Newton, US-NJ
(4)	Source meter	2400	Keithley Instruments	Solon, US-OH
(5)	x-y stage	EK14	Märzhäuser	Wetzlar, GER

Calibration of the spectrometer was done with two standards. Wavelength calibration was performed with a spectral tube (Helium-Neon, 3B-scientific) with well defined, narrow peaks from atomic transitions in the UV/VIS region as shown in Fig. A.3. The wavelength dependent detection efficiency was calibrated afterwards by the emitted spectrum of a broad-banded halogen light source (HCA, Kaiser Optical Systems) in the sample position to calculate a look-up table for intensity corrections.

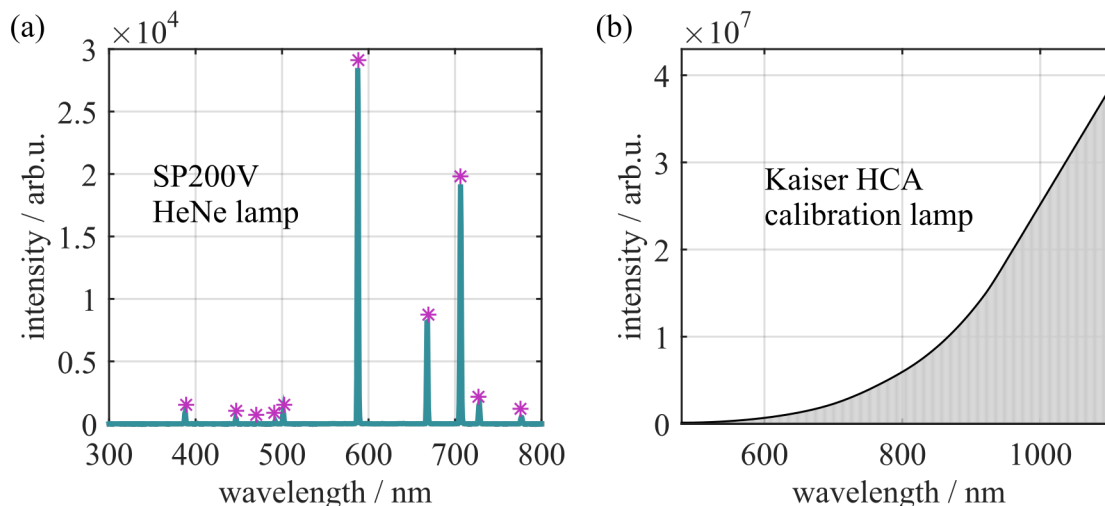


FIGURE A.3: (a) Helium-Neon arc lamp (SP200V) spectrum for calibration of the spectrometer wavelengths. (b) calibrated white-light source (HCA, Kaiser) spectrum for correction of the setup quantum efficiency.

## A.2 Optical Imaging Setup and Procedure

Imaging and spectral characterization of particles as described in Chapter 6 were conducted with a setup as illustrated in Fig. A.4. An optical microscope (3) with upright white light illumination (4) and darkfield configuration was coupled to a Czerny-Turner spectrometer as described in APP. A.1. By assembly of the optical large core fiber into the microscope image plane and termination with a 100  $\mu\text{m}$  pinhole, the detection spot was scaled by the selected objective. The two main microscope ports were used for emission imaging with a sCMOS-camera (1) and a Sagnac interferometer (2) for hyper-spectral imaging. Power supply and logging of the tunneling current was controlled by a source meter (5). Triggering of the measurement parameters was handled by self-written

software in LabVIEW. Depending on the experiment, different microscope objectives were used in the course of this work, such as a 20x (EC Epiplan 20x/0.4 HD, Zeiss) in Section 6.3.1, a 50x (LD EC Epiplan-Neofluar 50x 0.55 HD DIC, Zeiss) in Section 6.4, and a 63x water immersion (N-Achroplan W, 63x, NA 0.9, Zeiss) in Section 6.4.6.

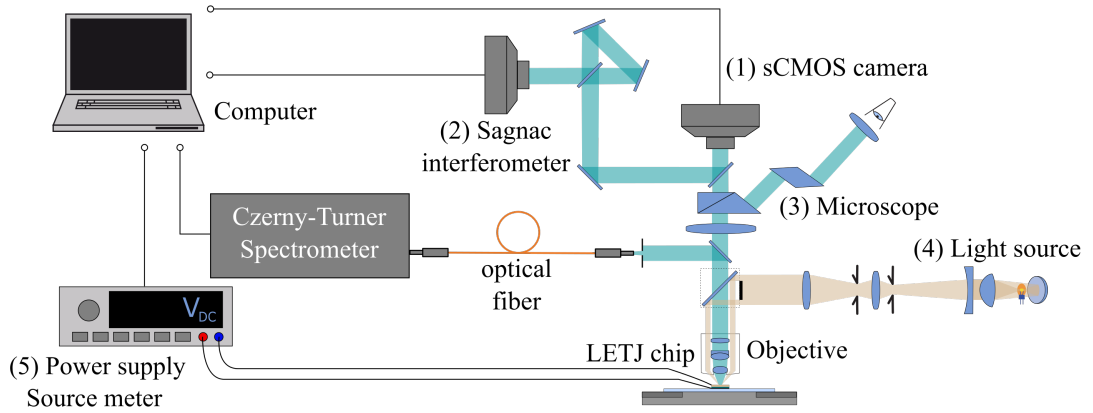


FIGURE A.4: Experimental setup for imaging and spectral characterization of LETJ structures.

Experiments in Section 6.4 were deployed after the same protocol to ensure comparability of the results. First, the sample was measured in darkfield illumination to locate the immobilized nanostructures on the underlying tunneling junction. Images were taken with  $100 \times 0.003 \text{ s}$  (accumulations  $\times$  exposure). The external light source was switched off and integration set to the LETJ integration time ( $6 \times 10 \text{ s}$ ). The LETJ power supply was turned on ( $I(t)$ - $V(t)$  logged) and acquisition of the LETJ image was triggered. After LETJ emission imaging, another darkfield image was acquired with the first setting to cross-check for drifts or structural changes.

TABLE A.5: List of utilized devices in the optical imaging system.

<i>Device</i>	<i>Model / Series</i>	<i>Company</i>	<i>Country</i>
(1) sCMOS camera	Orca Flash V4	Hamamatsu	Hamamatsu, JAP
(2) Sagnac Interferometer	SD-301-VDS	ASI	Carlsbad, US-CA
(3) Microscope	Axiomager Z1.m	Carl-Zeiss GmbH	Jena, GER
(4) Light Source	HAL100	Carl-Zeiss GmbH	Jena, GER
(5) Source Meter	2400	Keithley Instruments	Solon, US-OH

Contacting of LETJ samples was done with a self-designed micro-contacter as depicted in Fig. A.6. The main aims were to ensure reliable electrical contacting and a very low mounting height for usage in a microscope. The baseplate is equivalent to the size of an microscopy slide ( $2.6 \times 7.6 \text{ cm}$ ). Set-screws allowed fine-positioning of the spring loaded wires while they were electrically isolated by polymer slider cubes. The sample table (black) holds the chip at an elevated position which provides flat contacting of the junctions and simultaneous imaging within the working distance of a microscope objective.

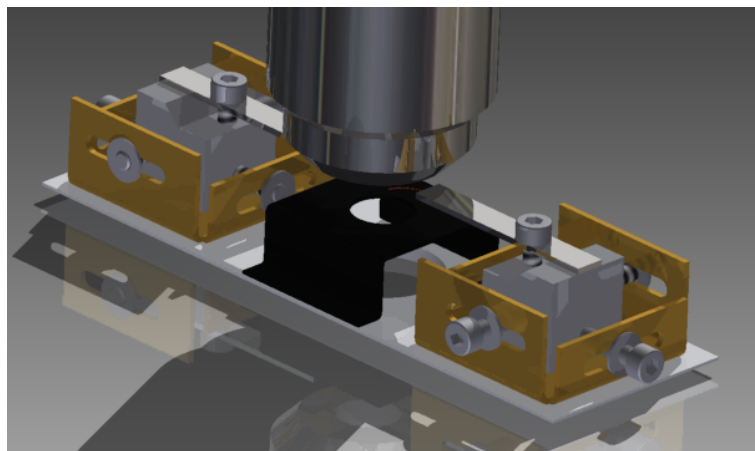


FIGURE A.6: Design of the self-designed micro-contacter for usage in an optical microscope.

Scaling information of the sCMOS Camera was determined by measurement of a calibration standard with  $10\ \mu\text{m}$  fine scale (see Fig. A.7). The obtained image was cross-sectioned perpendicular to the scalebars and smoothed by a moving average filter (width = 10 pixel). The resulting graph was inverted to exclude influences of borders and all determined minima (MATLAB: peakfinder.m) were averaged. As depicted in the figure, the scaling information of the utilized 100xLD objective is around 152 pixel/div. Thus  $s = 15.2\ \text{pixel}/\mu\text{m}$ .

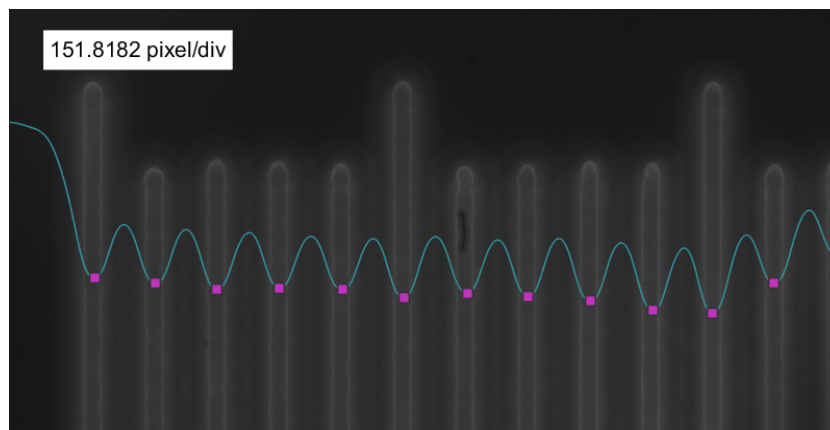


FIGURE A.7: Determination of the magnification at the camera was done with a calibration standard. Each bar has a distance of  $10\ \mu\text{m}$ . A horizontal pixel line coinciding with the image features was selected, averaged over 20 pixels and the dip positions calculated. This mean pixel distance between dips corresponds to the real distance (151.8 pixel) per division for a 100x Objective.

TABLE A.8: List of other utilized devices and setups

	<i>Device</i>	<i>Model / Series</i>	<i>Company</i>	<i>Country</i>
(1)	AFM	Dimension Icon	Bruker	Billerica, US-MA
(2)	SEM	JSM-6700F	JEOL GmbH	Freising, GER



TABLE A.9: Utilized Software for experiments, data analysis and graphics

<i>Software</i>	<i>Version</i>	<i>Company</i>
LabVIEW	2010 Full Development System	National Instruments
MATLAB	2014b	MathWorks
DipImage	2.8	non-commercial
Multiphysics	4.3b	COMSOL
Gwyddion	2.49	non-commercial
Anaconda Navigator	1.6.8	non-commercial
Spyder	3.2.3	non-commercial
Inkscape	0.91	non-commercial
Inventor	2014, Student	Autodesk
TexStudio	2.12.10	non-commercial

### A.3 AFM Scan Parameters & Analysis

Atomic force microscopy data as depicted in Section 6.4 were deployed with constant scanning parameters as follows:

- definition region of interest (ROI) from LETJ images and the sample layout,
- relocalization of ROI in AFM setup,
- tips: Tap300-G, Budgetsensors,  $f = 300 \text{ kHz}$ ,  $k = 40 \text{ Nm}^{-1}$ ,
- tip velocity  $15 \mu\text{ms}^{-1}$ ,
- amplitude setpoint lowered by 3 digital steps after tip engage,
- piezo z-range restricted to  $2 \mu\text{m}$  during scan, after engaging the surface,
- 1024 samples/line,

and data a analysis procedure as follows:

- the software "Gwyddion"[\[224\]](#) was used for AFM metrology:
- minimum of data shifted to zero,
- correction of horizontal line artifacts,
- data was leveled by 2D-plane fitting defined by 3 points (point radius 20 px),
- shift global minimum of data to zero,
- optional: stretching of color range to enhance contrast,
- set colormap to "NT-MDT" or "Rainbow2".

## A.4 Synthesis of mono-crystalline Goldplates

Lab protocol for the chemical synthesis of mono-crystalline goldplates as used in Section 6.4.3. The resulting flakes are several micrometer in lateral dimensions and 100 nm in height on average.

- **solution I:** 30 ml 0.833 mM TSC, heating in water bath to 50°C (diluted 25 mM stock)
- **solution II:** 20 ml H<sub>2</sub>AuCl<sub>4</sub> [1.25 mM] and CTAB [7.5 mM] heated in water bath to 50°C (deep orange solution)
- add solution II to solution I under continuous stirring in 50°C water bath
- orange reaction mixture decolorizes with increasing temperature
- heat to 82°C within 30 min, constant for 10 min
- cool to 62°C, constant for 10 min
- cool down (1-2 h) to room temperature and transfer into 50 ml tube
- solution yellow/golden color → big plates precipitate at the bottom
- ultrasonication 5 min to redisperse the pellet
- take 1 ml and centrifuge at 3000 rpm for 5 min
- take out 900 µl and add 200 µl of water (final CTAB concentration should be 1 mM)
- redisperse by shaking and ultrasonication
- store for 3 days, undisturbed protected from light → precipitation of Au-Plates
- take out supernatant (40 ml) (get rid of small NPs)
- redisperse in ≈ 5 ml CTAB [3 mM]
- again precipitation of Au-Plates is observed
- take out the supernatant (5 ml)
- redisperse in ≈ 50 ml CTAB [2 mM]
- again precipitation of Au-Plates is observed
- take out the supernatant (50 ml)
- redisperse in ≈ 2 ml CTAB [2 mM] → 25x concentrated

## B | Supporting Data

This appendix lists supporting data on conducted experiments in the course of this work. Detailed descriptions of the context are given in the main text and are linked to the respective figure in here.

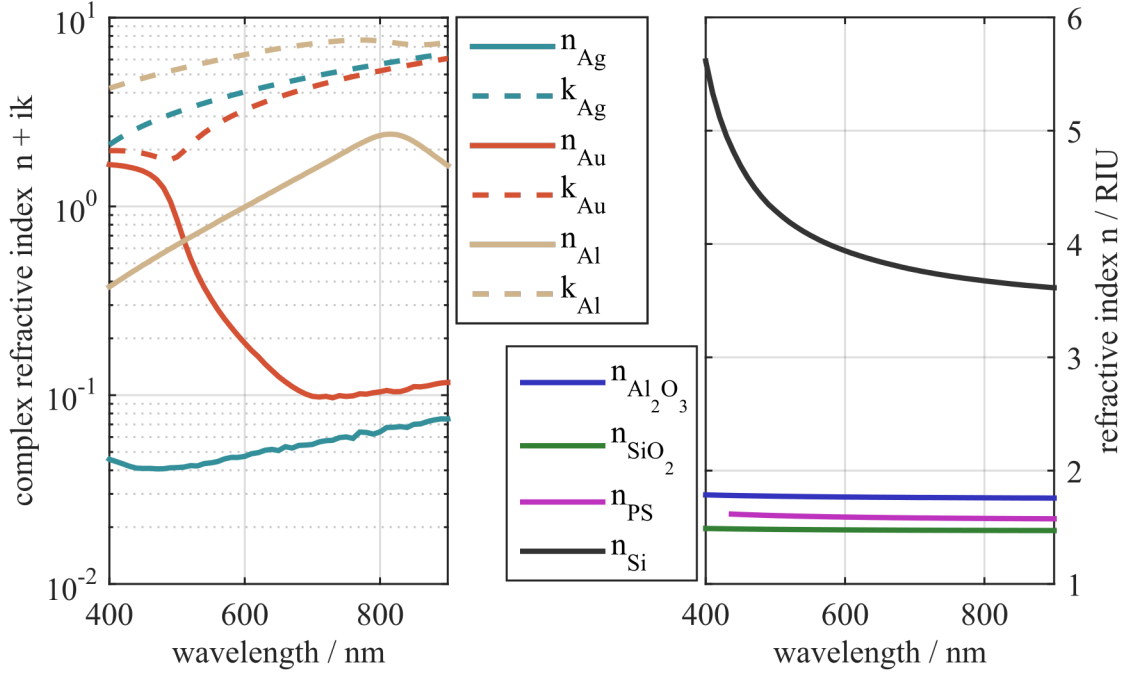


FIGURE B.1: Complex refractive index data of gold, silver and aluminum from [185] as used for calculations and real valued refractive indices of polystyrene[225], silicon[187], silicondioxide[189] and alumina[186]

- Information on the refractive indices of various materials were obtained via the refractiveindex.info webpage[188].

TABLE B.2: Refractive index values at 700 nm wavelength of the different dielectrics and metals as implemented in this work taken from literature referring to Fig.B.1

<i>material</i>	<i>n@700 nm</i>	<i>material</i>	<i>n@700 nm</i>	<i>k@700 nm</i>
Si	3.77	Au	0.10	4.31
SiO <sub>2</sub>	1.47	Ag	0.05	4.87
PS	1.58	Al	1.56	7.27
Al <sub>2</sub> O <sub>3</sub>	1.76			

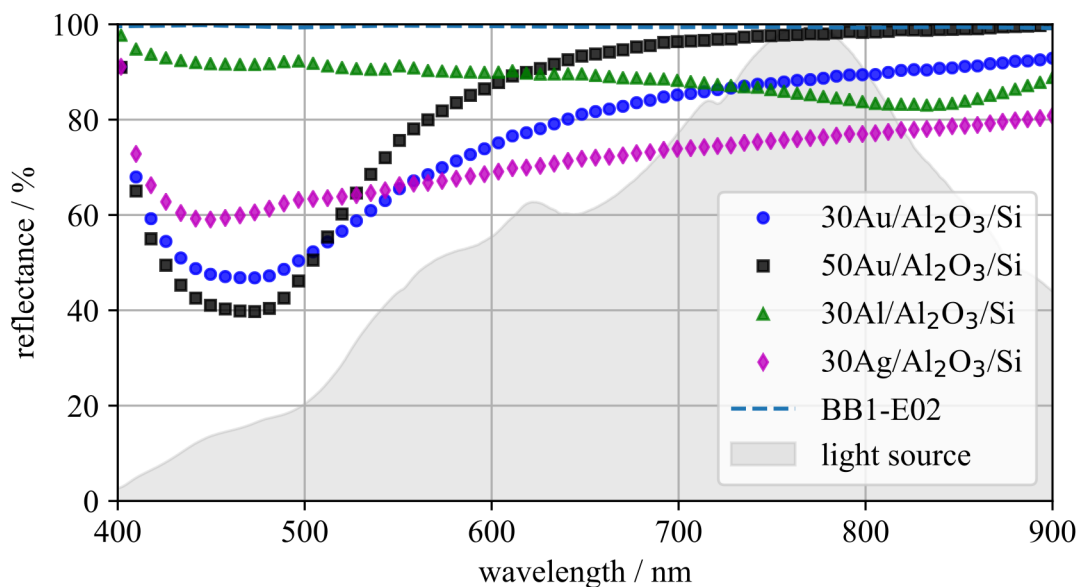


FIGURE B.3: Reflection measurements on LETJ chips with different electrode material and thickness. The dotted curves correspond to experimentally determined reflectance spectra. For gold, the characteristic drop in reflectance for shorter wavelengths is observed, while the thickness of the film increases the overall reflectance as shown by two gold junctions with 30 nm ( $\bullet$ ) and 50 nm ( $\blacksquare$ ). Aluminum ( $\blacktriangle$ ) exhibits a constant reflectance over the observed spectral range, whereas silver electrodes ( $\blacklozenge$ ) suffer strongly from oxidation. The spectrum of the light source is shown by the grey area and the reference mirror (BB1-E02) by the dotted line.

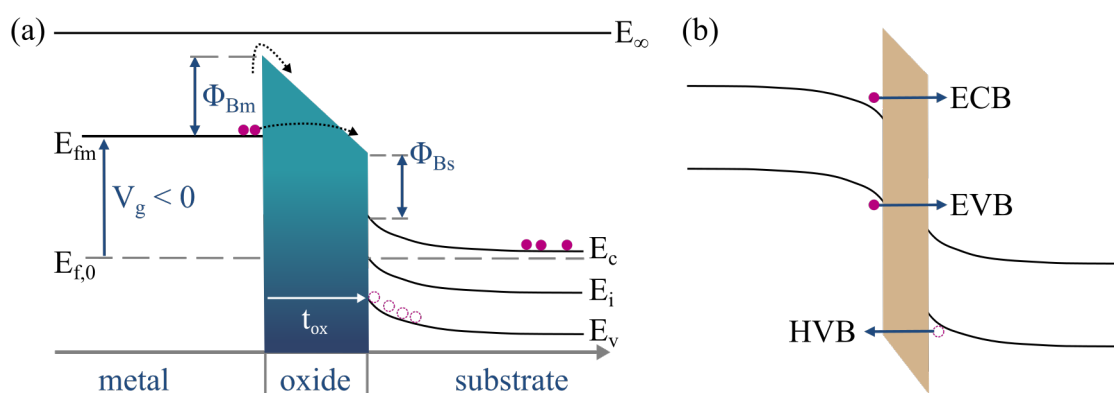


FIGURE B.4: (a) MOS structure in inversion state by application of a sample bias  $V_g < 0$ . (b) Scheme of charge carrier transitions often used for classification of dominant conduction mechanisms in tunneling junctions. Depicted is an exemplary semiconductor/oxide/semiconductor stack allowing tunneling of electrons from the conduction band (ECB), from the valence band (EVB) and tunneling of holes from the valence band (HVB).

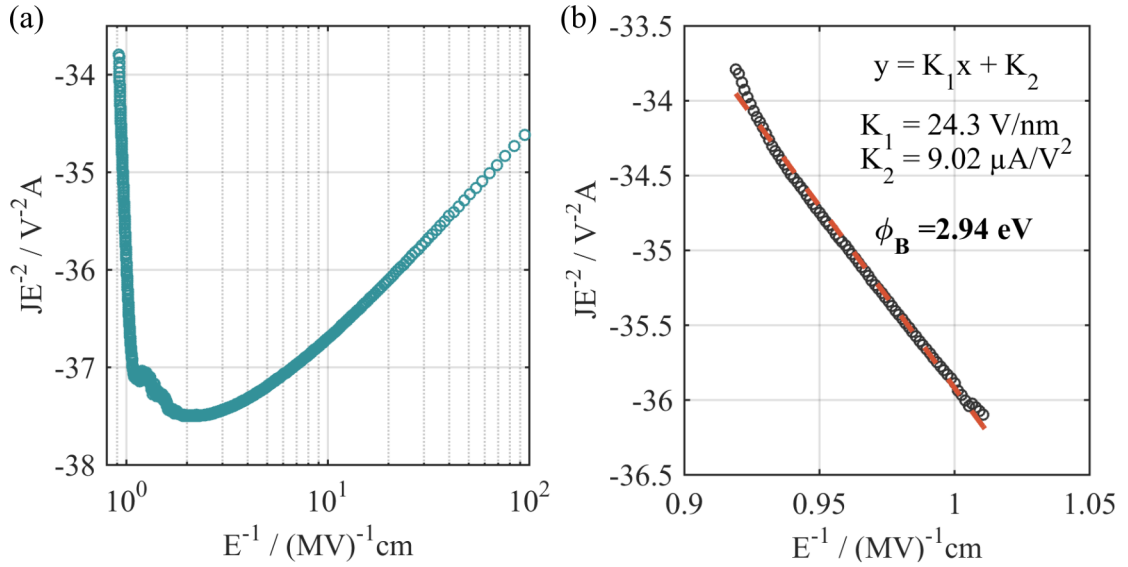


FIGURE B.5: (a) Fowler-Nordheim ( $\ln(JE^2)$  vs.  $1/E$ ) plot of an Au / 10 SiO<sub>2</sub> / Si junction. The minimum indicates the transition to Fowler-Nordheim tunneling. (b) Linear section of the FN-plot at highest fields is suitable for extraction of the tunneling barrier height by linear regression. Calculated as given in the Script C.3.

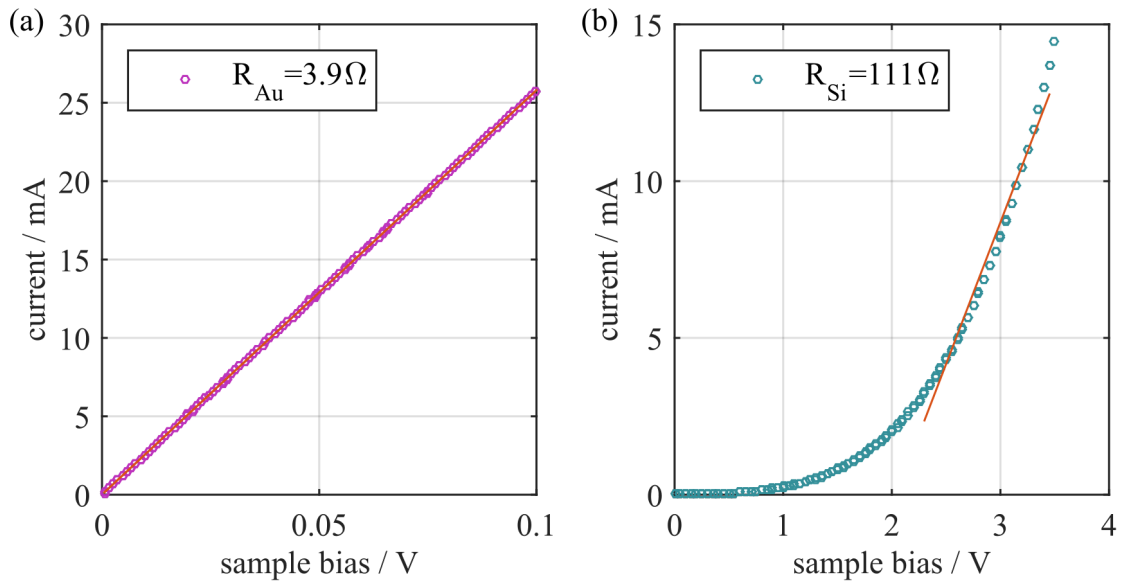


FIGURE B.6: I-V characteristics of the wirings and contact pad resistance (a) as well as the double Schottky contact which is created, if two ground pads are connected (b) as measures of reference.

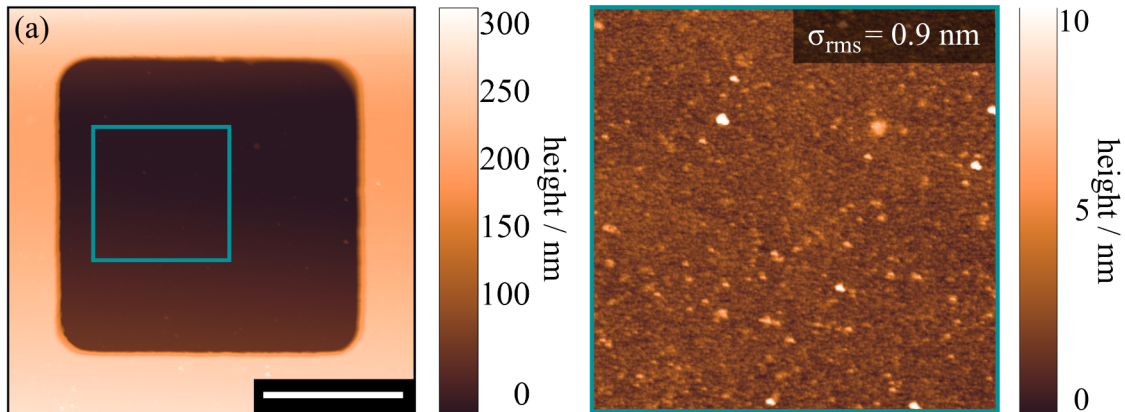


FIGURE B.7: AFM image of a T10-type junction with a 30 nm gold film. The inset was used to calculate the surface roughness of the electrode and was determined to  $\sigma_{\text{RMS}} = 0.9 \text{ nm}$ . Scalebar:  $5 \mu\text{m}$ .

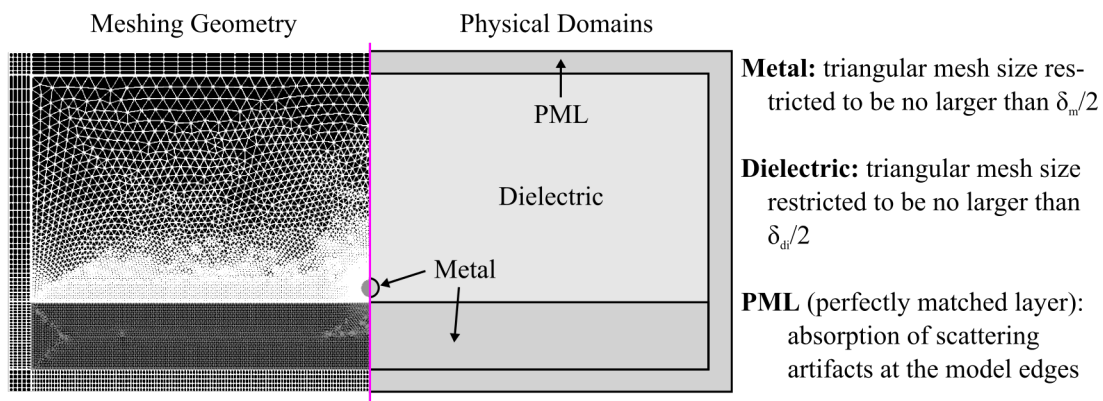


FIGURE B.8: General geometry of the model for numerical simulations by finite element methods. The maximal size of the triangular mesh (left) of all physical domains was selected according to the penetration depth of the materials ( $\delta_m/2 < 13 \text{ nm}$  |  $\delta_d/2 < 100 \text{ nm}$ ). Outer boundaries were expanded by a distribution meshed perfectly matched layer (PML) which serves for absorption to minimize scattering and reflection artifacts at the finite edges of the domains.

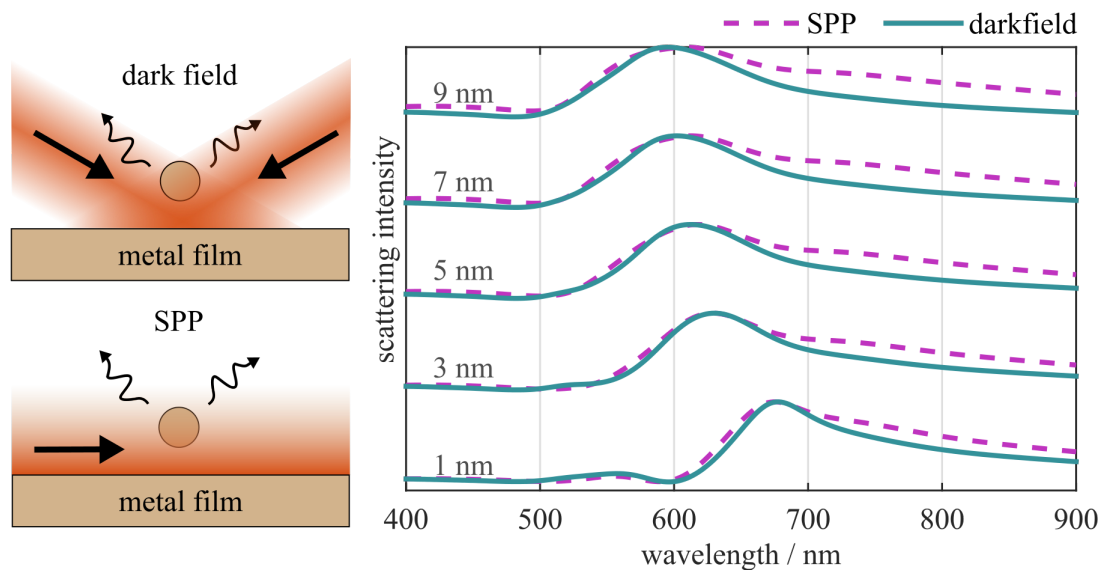


FIGURE B.9: left/top - two different types of excitation where simulated to model the optical response. External excitation by a plane wave at a non-zero angle as present in far-field illumination (e.g. darkfield-microscopy). left/bottom - Input of a propagating SPP along the boundary. This refers to near-field excitations where local sources generate propagating surface plasmons, which interact with nearby nanostructures. right - Comparison of the two models for different particle-film separations.

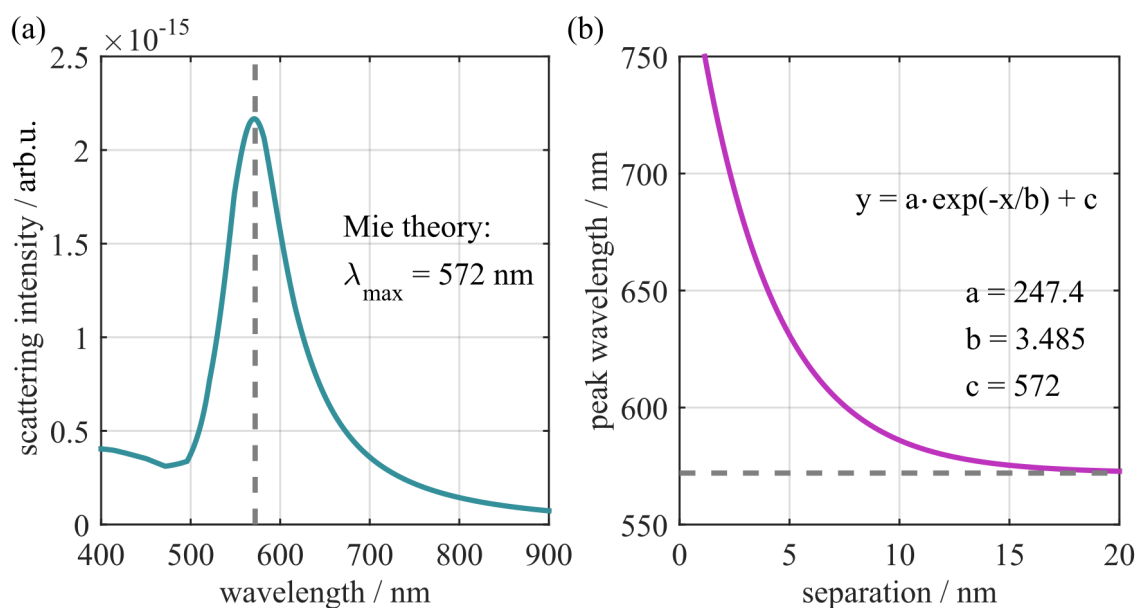


FIGURE B.10: (a) Scattering spectrum of a gold sphere ( $r_s = 50$  nm) in a surrounding medium  $n_m = 1.4$  as calculated by Mie theory, resulting in a peak wavelength  $\lambda_{\max} = 572$  nm. (b) Gap mode function describing the resonance shift of the bonding-mode in dependency of the particle-film separation by a mono-exponential fit with offset  $c = \lambda_{\max}$ .

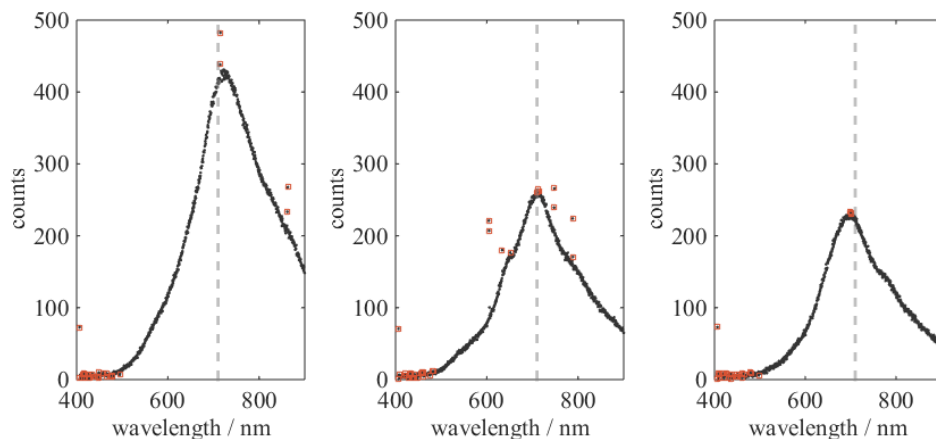


FIGURE B.11: Emission spectra of LETJ ( $r_s = 40$  nm) gold nanoparticles adsorbed on the surface for three different particle functionalizations. Citrate stabilized (left), BSA capped (middle) and BSA-IgG capped (right) particles increase the gap between the junction electrode and particles, resulting in a spectral shift. The intensities decrease accordingly due to weakened coupling, while additional uncertainties in the particle concentration play into the overall intensity. Outliers in the spectra were removed with a Hampel filter and are marked in orange.

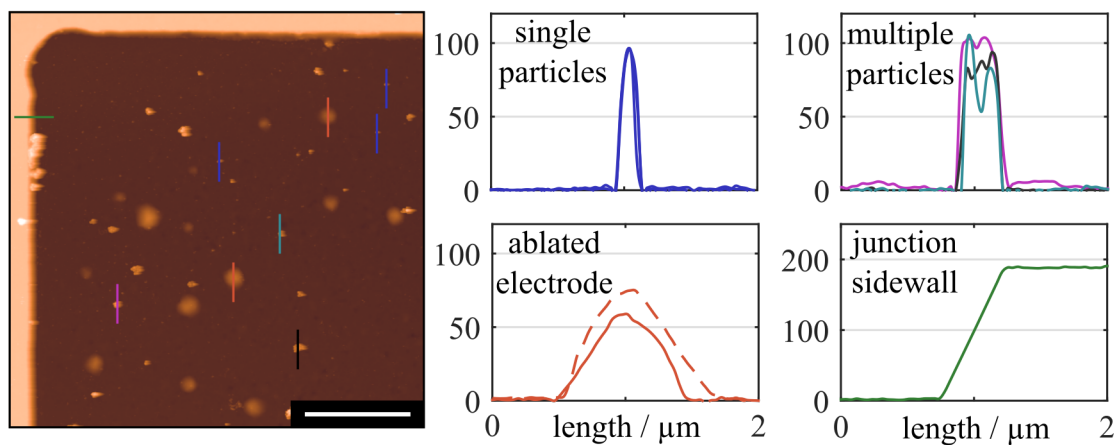


FIGURE B.12: AFM scan ( $20 \times 20 \mu\text{m}$ ) of a T100 junction incorporating nanoparticles ( $r_s = 50$  nm). Different extracted height profiles (indicated by lines in scan image) are depicted for single particles, multiple particle agglomerations, ablated electrode regions and the junction sidewall.



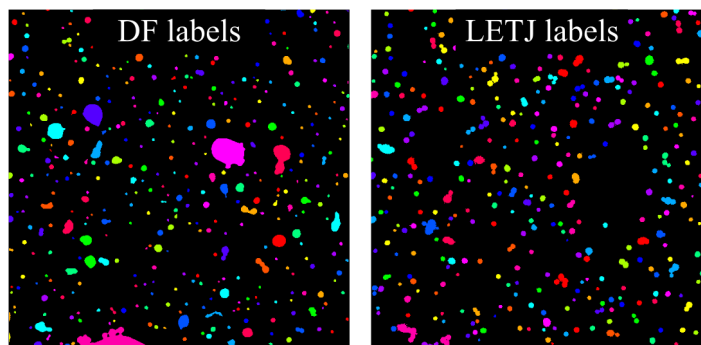


FIGURE B.13: Determined mask regions labeling the particles in DF and LETJ excitation. Thresholding at a fixed value was used to identify the regions. Single pixel objects were removed and image dilation to obtain closed domains.

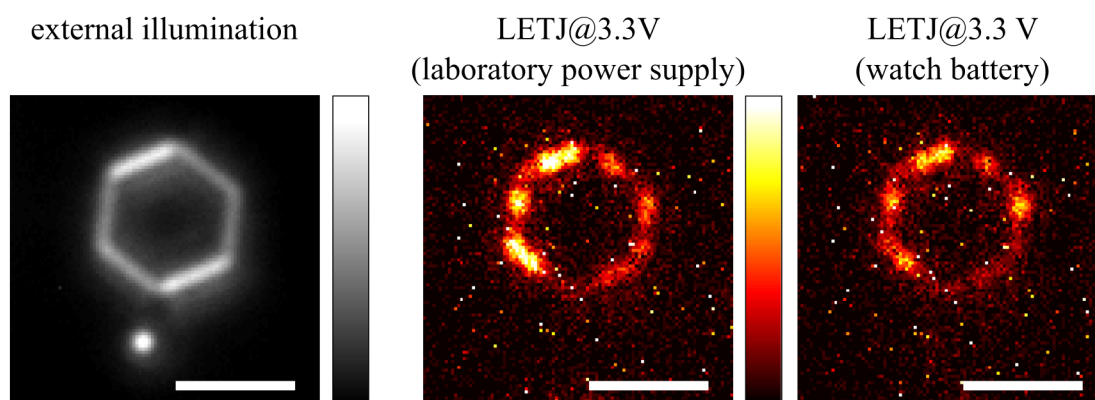


FIGURE B.14: Three consecutive measurements on scattering of an hexagonal goldflake imaged by external illumination in darkfield-configuration and two approaches of LETJ voltage sources, i.e. a laboratory power supply and a simple watch battery. Both biased at 3.3 V. DF range:  $[0, 2^{12}]$ , LETJ range:  $[0, 100]$ , Scalebar: 5  $\mu\text{m}$ .

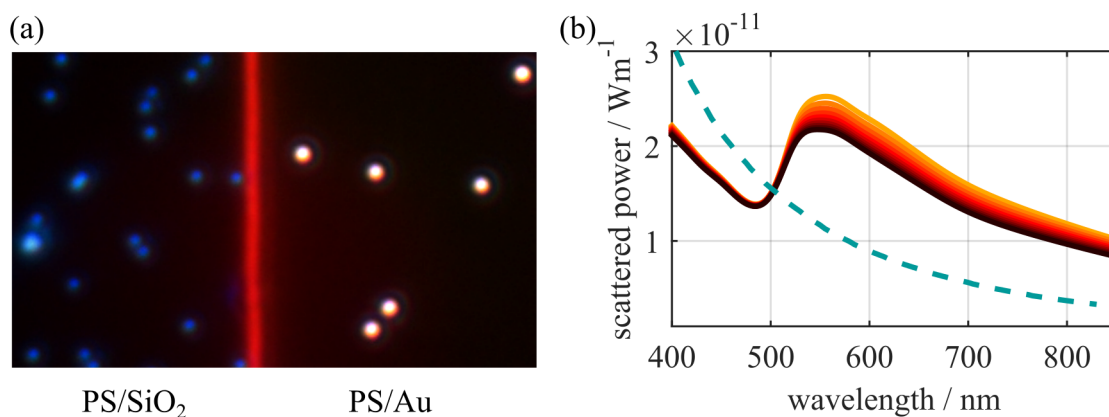


FIGURE B.15: (a) PS particles with radius 50 nm on a glass substrate (left) and on a 200 nm gold film (right) (b) simulated spectra of such dielectric particles on the glass substrate decay according to the scatterers  $\lambda^{-4}$  dependency, whereas the particles on gold the gold film exhibit a scattering peak at wavelength 550 nm corresponding to the gold film bulk plasmon.

- page intentionally left blank -

# C | Programming Scripts

Excerpt of developed functions for extraction of characteristic parameters in LETJ. Scripts C.1 and C.2 are meant for data handling and outlier detection. Script C.3 describes a function for extraction of tunneling barrier information from Fowler-Nordheim I-V curves and Script C.4 a function for intermediate I-V curves as described in Section 4.3. Script C.5 shows a fitting function for impedance data as handled in Section 4.4.

SCRIPT C.1: Python code snippet with the loadmatfile function for data import from a MATLAB '.mat' file containing the proprietary 'struct' datatype

```
1 import scipy
2 import tkinter as tk
3 from tkinter import filedialog
4
5 def loadmatfile():
6
7     root = tk.Tk()
8     root.withdraw()
9
10    file_path = filedialog.askopenfilename()
11
12    matfile = scipy.io.loadmat(file_path, struct_as_record=False, squeeze_me=True)
13    content = matfile.keys()
14
15    return content, matfile
```

SCRIPT C.2: Python code snippet to toss outliers from experimental data if they differ by at least of a factor  $m$  from the median

```
1 import numpy as np
2
3 def reject_outliers(data, m):
4
5     d = np.abs(data - np.median(data))
6     mdev = np.median(d)
7     s = d/mdev if mdev else 0.
8
9     return data[s<m], data[s>m]
```

SCRIPT C.3: MATLAB code for fitting of Fowler-Nordheim characteristics and estimation of the junction potential barriers  $\phi_A$  and  $\phi_B$

---

```

1  function [Finvc,FNc,FNcfit,Ifit,phiA,phiB] = FNconv(V,I,t_ox,S)
2
3  Finv = t_ox./V;    %convert to inverse el. field
4  FN = log(I./S.*(Finv.^2)); % y-axis of FN plot
5
6  FN(isinf(Finv)) = [];    % remove implausible inf values
7  Finv(isinf(Finv)) = []; % remove implausible inf values
8
9  thres = t_ox;    % set termination threshold
10 flag = 0;
11 ii = 1;
12 while flag == 0    % crop FN curve to linear part
13     thres = thres-0.001*t_ox;
14     Finvc = Finv(Finv<thres);
15     FNc = FN(Finv<thres);
16
17     X = [ones(length(FNc),1), Finvc];
18     [beta,~,~,~,stats] = regress(FNc,X);
19     R(ii) = stats(1);
20     if (stats(1) > 0.995) % R^2 threshold for linfit
21         flag = 1;
22     else
23         if (length(Finvc) < 10)
24             flag = 1;
25         end
26     end;
27     ii=ii + 1;
28 end
29
30 %% fit FN plot to data
31 FNcfit = Finvc*beta(2)+beta(1);
32 FNfit = Finv*beta(2)+beta(1);
33 Ifit = S.*exp(FNfit)./Finv.^2;
34
35 A = exp(beta(1));
36 B = -beta(2);
37
38 %% Latreche et al.
39 r_ox = 0.5;
40 a = 1.5414*10^-6; %A eV/V^2
41 b = 6.8309*10^9; % eV^{3/2} V/m
42
43 phiA = a/(r_ox*A);
44 phiB = (B./b).^ (2/3) .* (r_ox).^ (-1/3);
45
46 end

```

---

SCRIPT C.4: Python code snippet to calculate and fit the IV-characteristics of LETJ samples in the regime of direct tunneling. Parameters are the barrier height  $\phi_B$ , thickness  $t_{ox}$ , area  $S$  and effective mass  $m_{eff}$

```
1 import numpy as np
2 import scipy.optimize as opti
3 import scipy.constants as const
4
5 def IVsim2(V, phib, t_ox, S, meff):
6
7     return ((const.e/const.h)**2*(2*meff*const.m_e*const.e*phib/t_ox)**(0.5)\
8             *np.exp(-2*t_ox/const.hbar*np.sqrt(2*const.m_e*meff*const.e*phib))\
9             *(V+(t_ox*np.sqrt(2*const.m_e*meff/const.e)*V**2)/(24*const.hbar*phib**(1.5))\
10            +t_ox**2*const.m_e*meff*const.e*V**3/(12*const.hbar**2*phib)))
11
12 def IVfit2(V, Iexp, phib, t_ox, S, meff, x, bnds):
13
14     popt, pcov = opti.curve_fit(IVsim2, V, Iexp, p0 = x, method = 'trf',\
15                                sigma = Iexp**2, bounds = bnds, ftol = 1E-3)
16     Icalc = IVsim2(V,popt[0],popt[1],popt[2],popt[3])
17
18     return popt,Icalc
```

SCRIPT C.5: Python script for impedance simulation 'Zsim()' and fitting 'Zfit()' to experimental data of electronic elements described by an equivalent circuit as user defined in variable 'Zcalc'.

```

1 import numpy as np
2 import scipy.optimize as optimize
3
4 ## fit equivalent circuit parameters to experimental impedance data
5 def Zfit(f,Zexp,p0,bnds):
6
7     def distance(x): # parameter to minimize
8         Zcalc = Zsim(f,x)
9         rsq = np.sum(np.sum((np.abs(Zcalc)-np.abs(Zexp))**2)) # normfit
10        return rsq
11
12    res = optimize.minimize(distance,p0,method='L-BFGS-B',tol=1e-30,
13                           bounds=bnds, options={'maxfun':200,'maxiter':100})
14    Zcalc = Zsim(f,res.x)
15    return res,Zcalc
16
17 ## simulate circuit at frequency f with intial parameters p0
18 def Zsim(f,p0): #p0 being the element respective parameter
19
20    def R(p,f): # describes a resistor with p=resistance
21        z = p * np.ones(np.size(f))
22        return z
23
24    def C(p,f): # describes a capacitor with p=capacitance
25        z = 1j*2*np.pi*f*p
26        z = 1/z
27        return z
28
29    def L(p,f): # describes an inductance with p=inductance
30        z = 1j*2*np.pi*f*p
31        return z
32
33    def S(z1,z2): # describes a series connection of 2 components
34        z = z1 + z2
35        return z
36
37    def P(z1,z2): # describes of parallel connection of 2 components
38        z=1/(1/z1 + 1/z2)
39        return z
40
41    # total equivalent circuit impedance 'Zcalc' is built
42    ZP = P(P(R(p0[0],f),C(p0[1],f)),C(p0[2],f))
43    Zcalc = S(ZP,S(R(p0[3],f),L(p0[4],f)))
44
45    return Zcalc

```

## D | Personal Information

## List of Peer-Reviewed Publications

- [1] M. Ziegler, **A. Dathe**, K. Pollok, U. Hübner, D. Wang, "Surface plasmon-induced UV-NIR broadband light trapping in silver-silica composite structures", *Nat. Mat.*, **2019**, in preparation
- [2] S. Trautmann, **A. Dathe**, A. Csáki, M. Thiele, R. Müller, W. Fritzsche, O. Stranik, "Time-Resolved Study of Site-Specific Corrosion in a Single Crystalline Silver Nanoparticles", *Nanoscale Res Lett*, **2019**, 14:240.
- [3] **A. Dathe**, T. Heitkamp, I. Pérez, H. Sielaff, A. Westphal, S. Reuter, R. Mrowka, M. Börsch, "Observing monomer: dimer transitions of neurotensin receptors 1 in single SMALPs by homoFRET and in an ABELtrap", *Single Molecule Spectroscopy and Superresolution Imaging XII*, **2019**, 108840N.
- [4] A. Pittner, S. Wendt, D. Zopf, **A. Dathe**, N. Grosse, A. Csáki, W. Fritzsche, O. Stranik, "Fabrication of micro-patterned plasmonic substrates by piezo-dispensing of colloidal nanoparticles", *Anal. Bioanal. Chem.*, **2019**, 411(8), 1537-1547.
- [5] D. Zopf, A. Pittner, **A. Dathe**, N. Grosse, A. Csáki, K. Arstila, J.J. Toppari, W. Schott, D. Dontsov, G. Uhlrich, W. Fritzsche, O. Stranik, "Plasmonic nanosensor array for multiplexed DNA-based pathogen detection", *ACS Sensors*, **2019**, 4(2), 335-343.
- [6] S. Thamm, N. Slesiona, **A. Dathe**, A. Csáki, W. Fritzsche, "AFM-Based Probing of the Flexibility and Surface Attachment of Immobilized DNA Origami", *Langmuir*, **2018**, 34(49), 15093-15098.
- [7] S. Das, J. Preiß, J. Plentz, U. Brückner, M. von der Lühe, O. Eckhardt, **A. Dathe**, F.H. Schacher, E. Täuscher, U. Ritter, A. Csáki, G. Andrä, B. Dietzek, M. Presselt, "Controlling Intermolecular Interactions at Interfaces: Cases of Supramolecular Tuning of Fullerene's Electronic Structure", *Adv. Energy Mater.* **2018**, 8, 21512-21521.
- [8] G. Schmidl, G. Jia, A. Gawlik, J. Kreuzsch, F. Schmidl, J. Dellith, **A. Dathe**, Z.-H. Lin, J.-S. Huang, J. Plentz, "Fabrication of self-assembled spherical Gold Particles by pulsed UV Laser Treatment", *Sci. Rep* **2018**, 8, 9830–9839.
- [9] S. Trautmann, M. Richard-Lacroix, **A. Dathe**, H. Schneidewind, J. Dellith, W. Fritzsche, V. Deckert, "Plasmon response evaluation based on image-derived arbitrary nanostructures", *Nanoscale* **2018**, 10, 9830–9839.
- [10] C. Heck, J. Prinz, **A. Dathe**, V. Merk, O. Stranik, "Gold Nanolenses Self-Assembled by DNA Origami", *ACS Photonics* **2017**, 4, 1123–1130.
- [11] G. Schmidl, J. Dellith, N. Teller, A. Bochmann, S. Teichert, O. Stranik, **A. Dathe**, V. Tympel, F. Schmidl, E. Kessler, T. Wieduwilt, W. Fritzsche, "Confocal sputtering of (111) orientated smooth gold films for surface plasmon resonance approaches", *Vacuum* **2017**, 138, 55–63.



- [12] **A. Dathe**, M. Ziegler, U. Hübner, W. Fritzsche, und O. Stranik, "Electrically Excited Plasmonic Nanoruler for Biomolecule Detection", *Nano Lett.* **2016**, *16*, 5728–5736.
- [13] D. Zopf, J. Jatschka, **A. Dathe**, N. Jahr, W. Fritzsche, und O. Stranik, "Hyperspectral imaging of plasmon resonances in metallic nanoparticles", *Biosens. Bioelectron.* **2016**, *81*, 287–293.
- [14] J. Jatschka, **A. Dathe**, A. Csáki, W. Fritzsche, und O. Stranik, "Propagating and localized surface plasmon resonance sensing — A critical comparison based on measurements and theory", *Sens. Bio-Sens. Res.* **2016**, *7*, 62–70.
- [15] G. Schmidl, J. Dellith, A. Dellith, N. Teller, D. Zopf, G. Li, **A. Dathe**, G. Mayer, U. Hübner, M. Zeisberger, O. Stranik, W. Fritzsche, "Silicon template preparation for the fabrication of thin patterned gold films via template stripping", *J. Micromechanics Microengineering* **2015**, *25*, 125005.
- [16] A. Csáki, M. Thiele, J. Jatschka, **A. Dathe**, D. Zopf, O. Stranik, W. Fritzsche, "Plasmonic nanoparticle synthesis and bioconjugation for bioanalytical sensing", *Eng. Life Sci.* **2015**, *15*, 266–275.

## List of Patents

- [1] T. Henkel, F. Garwe, G. Mayer, A. Csaki, W. Fritzsche, U. Hübner, **A. Dathe**, G. Schmidl, *Anordnung und Verfahren für die Erfassung von Änderungen der optischen Weglänge in einem Nano-Kapillarkanal*, patent, DAKZ: 10 2017 105 113.9, issued March 10, 2017.

## List of Conference Talks

- [1] **A. Dathe**, U. Hübner, M. Ziegler, O. Stranik, W. Fritzsche, "Tunneling junctions as source of electrically excited surface plasmons for sensing applications", Anacapri, Italy, 2017.
- [2] **A. Dathe**, U. Hübner, M. Ziegler, O. Stranik, W. Fritzsche, "Electrically-Driven Plasmon Resonances in Nanostructures: A new Tool for Biosensing", *Molecular Plasmonics*, Jena, Germany, 2015.
- [3] **A. Dathe**, M. Ziegler, U. Hübner, O. Stranik, W. Fritzsche, "Hybrid Metallic Nanostructures as Sensors Based on Electrically Excited Plasmons", *3M-Nano*, Taipeh, Taiwan, 2014.

- page intentionally left blank -

# Acknowledgements

I would like to express my sincere gratitude towards all the people whose generous support throughout the last years have made this work possible.

Prof. Dr. Thomas Pertsch for his willingness to supervise the dissertation and his calm, friendly and helpful manner to approach things. Adj. Prof. Dr. Wolfgang Fritzsche as the head of the workgroup *Nano Biophotonics* at the Leibniz-IPHT is thanked for his unwavering support, the freedom and autonomy in my schedule and tasks as well as the opportunity to travel to different international universities for several research stays.

I would like to particularly thank my colleague Dr. Ondrej Stranik for his weekly support since my master thesis and the many fruitful discussions, hints and directives he gave to keep me on track. Dr. Andrea Csáki is thanked for her assiduous attitude, the strong support in the organization of the research stays as well as the backing of the groups students no matter the issue.

Some of the results presented here have been obtained with the help of others. I am very grateful to Prof. Dr. Jussi Toppari for the opportunity to stay at the NanoScience Center in Jvaskylä, Finland for one month and his willingness to share his expertise, programs and labs for impedance and IV-spectroscopy for the whole time and of course for his warm, friendly kind nature which made me feel very welcome and in good hands.

Dr. Joachim Bollmann and Prof. Dr. Yvonne Joseph contributed with the highly doped silicon wafer and with their help during my studies. A special thanks goes to Dr. Uwe Huebner, Mario Ziegler and Sebastian Goerke who always managed and adapted the fabrication of the thin film stacks for the light emitting tunneling junctions in laborious effort concerning my sometimes altering, shorttermed wishes.

Also Dr. Jan Dellith and Dr. Andrea Dellith are thanked for the FIB lamellas and Franka Jahn for the SEM images of various nanostructures. Prof. Dr. Michael Börsch as my current contractor contributed decisively to the work by giving me a lot of freedom in my working schedule and by being very understanding for the double load of working hours to finish this thesis.

Of course, the versatile support by my office, group mates and fellow PhD students was extremely important over the years - ranging from brainstorming in the coffee breaks, discussions on programming or help in several experiments to going for lunch, having a beer or just a good laugh together during one of the manifold freetime activities. With this, Matthias, Jacqueline, Sophie, David, Isa, Steffen, Stefanie, Andy, Andreas: I really enjoyed working with you and the whole group of Nano Biophotonics and am indebted to you all for shifting everything into the right perspectives and lifting my mood day by day. One of the highlights among these experiences was the sailing trip with Matthias Urban which fulfilled my long-awaited plan to set sails myself.

A special thanks goes to all people who helped me during the part of writing this thesis either by discussions of the overall content proof-reading or cross-checking of references.

---

Over the years, many of my friends helped me in various ways, particularly by just listening to my rants on misplanned experiments and by turning my perspective from small issues to the overall picture in life. I would like to thank my girlfriend Nicole for her support, love and lasting endurance especially when I was pulling countless all-nighters or was typing through the weekends.

I am grateful beyond words to my parents, who helped with their unflagging support and by being always caring, loving and understanding. Same goes for my brother, his wife, my little nephew and niece who always find the right words to remind me what is important. You can't imagine how much I am indebted to you. This thesis is dedicated to you.

# Declaration of Authorship

I, André Dathe, declare that this thesis titled, 'Large Scale Tunneling Junctions for Electrically Driven Plasmonics' and the work presented in it are my own. I confirm that:

- This work was done wholly or mainly while in candidature for a research degree at this University.
- Where any part of this thesis has previously been submitted for a degree or any other qualification at this University or any other institution, this has been clearly stated.
- Where I have consulted the published work of others, this is always clearly attributed.
- Where I have quoted from the work of others, the source is always given. With the exception of such quotations, this thesis is entirely my own work.
- I have acknowledged all main sources of help.
- Where the thesis is based on work done by myself jointly with others, I have made clear exactly what was done by others and what I have contributed myself.

---

Place, Date

---

Signature

- page intentionally left blank -